



The University of
Nottingham

**Synthesis of Low-Coordinate *m*-Terphenyl
Metal Complexes: Structural, Electronic
and Magnetic Studies**

Andrew J. Valentine, MSci (Hons)

Thesis submitted to the School of Chemistry at the
University of Nottingham for the degree of Doctor of Philosophy

September 2019

Declaration

The research described in this thesis was carried out at the University of Nottingham between September 2015 and September 2019, under the joint supervision of Prof. Deborah L. Kays and Prof. Jonathan McMaster. All of the work is my own unless otherwise stated, and has not previously been submitted for any degrees at this or any other university.

Andrew J. Valentine

Abstract

This work aims to expand the library of low-coordinate *m*-terphenyl metal complexes suitable for electronic investigation. Herein, the synthesis of a series of *para*-substituted *m*-terphenyl ligands is reported, featuring a range of different electron-donating and -withdrawing groups. The effects of ligand architecture are then studied with respect to the structural, electronic and magnetic properties of the metal complexes.

The synthesis of a series of *para*-functionalised *m*-terphenyl iodide ligand precursors, R-Ar-I, **3.2** – **3.8**, is first described, with characterisation by X-ray crystallography and NMR spectroscopy. Lithiation of these compounds affords a series of *para*-substituted *m*-terphenyl lithium complexes [R-Ar-Li]₂, **3.9** – **3.13**, which, despite being structurally similar, possess different electronic environments at their lithium ions, as evidenced by ⁷Li NMR spectroscopy. From these lithium precursors, a number of two-coordinate *m*-terphenyl metal complexes is prepared, including the Group 12 diaryls (R-Ar)₂M (M = Zn, Cd, Hg), **4.1** – **4.12**, and the iron diaryls (R-Ar)₂Fe, **5.1** – **5.5**. For each metal series, X-ray crystallography shows that the complexes are structurally invariant, with little change in C–M–C bond lengths and angles as the *para*-group is varied. However, a combination of ¹H, ¹³C, ¹¹³Cd and ¹⁹⁹Hg NMR spectroscopies reveals electronic differences both on the ligand framework and at the Group 12 metal centre. For the iron complexes, additional electronic analysis is performed by IR, UV/Vis and X-ray photoelectron spectroscopies, as well as cyclic voltammetry. Furthermore, the magnetic properties of **5.1** – **5.5** are examined by SQUID magnetometry to determine their single-molecule magnet behaviour. Finally, the reactivity of the iron diaryls towards small molecules is probed, with attempts to bind an infrared-active handle to the metal centre to study its electronic properties via analysis of the IR stretching frequencies.

Acknowledgements

First and foremost, I am greatly thankful to my supervisors Prof. Deborah Kays and Prof. Jonathan McMaster for their continued support and guidance throughout my PhD. I would like to thank Dr Ana Geer and Dr Laurence Taylor for their knowledge and assistance in the laboratory, as well as my project students Katherine Wood and Emily Trew for their contributions to this research. Thanks also go to all members of the Kays group for their friendship and advice during my time in Lab B46. I would like to thank all staff at Nottingham who have assisted with analytical experiments: Dr William Lewis for X-ray crystallography; Dr Stephen Davies for cyclic voltammetry, EPR and MCD spectroscopy; Prof. Jonathan McMaster for MCD spectroscopy; Dr Huw Williams, Mr Kevin Butler and Mr Shazad Aslam for NMR spectroscopy; Dr Mick Cooper for mass spectrometry; Dr Emily Smith for X-ray Photoelectron Spectroscopy; Dr Andy Teale for DFT calculations; Dr Tong Liu for elemental analysis. Thanks also to Dr Maria Gimenez at the University of Santiago de Compostela, Spain, for SQUID magnetometry measurements. Finally, I am grateful to the University of Nottingham for having had the opportunity to pursue this PhD research project.

Contents

Declaration.....	ii
Abstract.....	iii
Acknowledgements.....	iv
Contents	v
Abbreviations.....	ix
Chapter I – Introduction.....	1
1.1 Background.....	2
1.2 Introduction.....	6
1.2.1 Traditional Bulk Magnetism.....	6
1.2.2 Single-Molecule Magnets.....	7
1.2.3 Single-Ion Magnets.....	12
1.2.4 Bulky Ligand Systems.....	14
1.2.5 The <i>m</i> -Terphenyl Ligand.....	17
1.2.6 Synthesis of <i>m</i> -Terphenyl Ligands.....	23
1.2.7 <i>m</i> -Terphenyl Metal Complexes.....	25
1.2.8 Applications of <i>m</i> -Terphenyl Complexes.....	29
1.3 Research Objectives.....	34
1.4 Analytical Methods.....	35
1.4.1 Hammett Constants.....	35
Chapter II – General Experimental.....	36
2.1 General Experimental Techniques.....	37
2.1.1 Manipulation of Air-Sensitive Compounds.....	37
2.2 Analytical Measurements.....	38
2.2.1 X-ray Crystallography.....	38
2.2.2 NMR Spectroscopy.....	39
2.2.3 IR Absorption Spectroscopy.....	40
2.2.4 Mass Spectrometry.....	40
2.2.5 Elemental Analysis.....	40
2.2.6 UV/Vis Absorption Spectroscopy.....	41
2.2.7 Cyclic Voltammetry.....	41
2.2.8 Electron Paramagnetic Resonance Spectroscopy.....	41
2.2.9 X-ray Photoelectron Spectroscopy.....	42

2.2.10 SQUID Magnetometry.....	43
2.2.11 Magnetic Circular Dichroism Spectroscopy.....	43
2.3 Preparation of Solvents and Reagents.....	44
2.3.1 Solvent Preparation.....	44
2.3.2 Reagent Preparation.....	44
Chapter III – Ligand Synthesis	45
3.1 Introduction.....	46
3.2 Discussion.....	48
3.2.1 <i>m</i> -Terphenyl Iodides	48
3.2.1.1 Synthesis	48
3.2.1.2 Crystallographic Analysis.....	59
3.2.1.3 NMR Analysis	62
3.2.2 <i>m</i> -Terphenyl Lithium Complexes.....	65
3.2.2.1 Synthesis	65
3.2.2.2 Crystallographic Analysis.....	66
3.2.2.3 NMR Analysis	71
3.3 Conclusions.....	80
3.4 Future Work.....	81
3.5 Experimental.....	82
3.5.1 Grignard Synthesis: 2,6-Xyl	82
3.5.1.1 (2,6-Dimethylphenyl)magnesium bromide (3.1).....	82
3.5.2 Ligand Synthesis: <i>t</i> -Bu.....	82
3.5.2.1 2,6-Dibromo-4- <i>t</i> -butylaniline (3.2b).....	82
3.5.2.2 1-Iodo-2,6-dibromo-4- <i>t</i> -butylbenzene (3.2c).....	83
3.5.2.3 <i>t</i> -Bu-Ar-I (3.2).....	84
3.5.2.4 [<i>t</i> -Bu-Ar-Li] ₂ (3.9).....	85
3.5.3 Ligand Synthesis: SiMe ₃	86
3.5.3.1 3,5-Dichloro-1-trimethylsilylbenzene (3.3b).....	86
3.5.3.2 Me ₃ Si-Ar-I (3.3).....	87
3.5.3.3 [Me ₃ Si-Ar-Li] ₂ (3.10)	88
3.5.4 Ligand Synthesis: H.....	88
3.5.4.1 H-Ar-I (3.4).....	88
3.5.4.2 [H-Ar-Li] ₂ (3.11).....	89
3.5.5 Ligand Synthesis: Cl.....	90

3.5.5.1 Cl-Ar-I (3.5).....	90
3.5.5.2 [Cl-Ar-Li] ₂ (3.12).....	91
3.5.6 Ligand Synthesis: CF ₃	91
3.5.6.1 1-Iodo-2,6-dichloro-4-trifluoromethylbenzene (3.6b).....	91
3.5.6.2 F ₃ C-Ar-I (3.6)	92
3.5.6.3 [F ₃ C-Ar-Li] ₂ (3.13)	93
3.5.7 Ligand Synthesis: OMe.....	94
3.5.7.1 MeO-Ar-I (3.7)	94
3.5.8 Ligand Synthesis: Double Ligand.....	95
3.5.8.1 3,5-Dichloriodobenzene (3.8b).....	95
3.5.8.2 3,3',5,5'-Tetrachlorobiphenyl (3.8c)	96
3.5.8.3 I-Ar-Ar-I (3.8).....	96
Chapter IV – Group 12 Complexes.....	98
4.1 Introduction.....	99
4.2 Discussion	102
4.2.1 <i>m</i> -Terphenyl Zinc, Cadmium and Mercury Complexes	102
4.2.1.1 Synthesis	102
4.2.1.2 Crystallographic Analysis.....	103
4.2.1.3 NMR Analysis	112
4.2.1.4 Cyclic Voltammetry.....	118
4.3 Conclusions.....	119
4.4 Future Work	120
4.5 Experimental.....	121
4.5.1 Metal Complex Synthesis: Group 12 (M = Zn, Cd, Hg)	121
4.5.1.1 (<i>t</i> -Bu-Ar) ₂ M (M = Zn, 4.1; Cd, 4.2; Hg, 4.3).....	121
4.5.1.2 (Me ₃ Si-Ar) ₂ M (M = Zn, 4.4; Cd, 4.5; Hg, 4.6).....	122
4.5.1.3 (Cl-Ar) ₂ M (M = Zn, 4.7; Cd, 4.8; Hg, 4.9).....	123
4.5.1.4 (F ₃ C-Ar) ₂ M (M = Zn, 4.10; Cd, 4.11; Hg, 4.12)	124
Chapter V – Open-Shell Complexes.....	126
5.1 Introduction.....	127
5.2 Discussion	130
5.2.1 <i>m</i> -Terphenyl Iron Complexes	130
5.2.1.1 Synthesis	130
5.2.1.2 Crystallographic Analysis.....	131

Abbreviations

2,2,2-crypt	4,7,13,16,21,24-hexaoxa-1,10-diazabicyclo[8.8.8]hexacosane
2,6-Xyl	2,6-Xylyl, 2,6-Me ₂ C ₆ H ₃ ⁻
3,5-Xyl	3,5-Xylyl, 3,5-Me ₂ C ₆ H ₃ ⁻
Å	Angstrom, 10 ⁻¹⁰ m
Ar	Aryl
ASAP	Atmospheric solids analysis probe
ATR	Attenuated total reflectance
br	broad (NMR, infrared)
CHN	Carbon/hydrogen/nitrogen content (elemental analysis)
CIF	Crystallographic information file
COSY	Correlated spectroscopy
COT	Cyclooctatetraenyl, C ₈ H ₈ ²⁻
Cp	Cyclopentadienyl, C ₅ H ₅ ⁻
CV	Cyclic voltammetry
DCM	Dichloromethane, CH ₂ Cl ₂
d	doublet (NMR)
Dcp	Dichlorophenyl, 2,6-Cl ₂ C ₆ H ₃ ⁻
DEPT	Distortionless enhancement by polarisation transfer
DFT	Density functional theory
Dipp	Diisopropylphenyl, 2,6- <i>i</i> -Pr ₂ C ₆ H ₃ ⁻
DOSY	Diffusion ordered spectroscopy
Dppe	Ethylenebis(diphenylphosphine), Ph ₂ P-C ₂ H ₄ -PPh ₂
EI	Electron ionisation
en	ethylenediamine, C ₂ H ₄ (NH ₂) ₂

EPR	Electron paramagnetic resonance
eq.	equivalents
ESI	Electrospray ionisation
Et	Ethyl, CH ₃ CH ₂ ⁻
Fc	Ferrocene
FD	Field desorption
FTIR	Fourier transform infrared spectroscopy
GC	Gas chromatography
h	hour
H ₂ valdien	N1,N3-bis(3-methoxysalicylidene) diethylenetriamine
HMBC	Heteronuclear multiple bond correlation
HOESY	Heteronuclear Overhauser NMR spectroscopy
HOMO	Highest occupied molecular orbital
HR	High-resolution
HSQC-ME	Heteronuclear single quantum coherence - multiplicity edited
<i>i</i>	<i>iso</i>
<i>i</i> -Pr	<i>iso</i> -Propyl, Me ₂ CH ⁻
IR	Infrared
<i>J</i>	Coupling constant (NMR)
L	Ligand
LUMO	Lowest unoccupied molecular orbital
M	Metal
m	multiplet (NMR); medium (infrared)
Me	Methyl, CH ₃ ⁻
Mes	Mesityl, 2,4,6-Me ₃ C ₆ H ₂ ⁻

Mes*	Supermesityl, 2,4,6- <i>t</i> -Bu ₃ C ₆ H ₂ ⁻
MS	Mass Spectrometry
<i>n</i>	<i>normal</i> ; number (aggregation/solvent)
<i>n</i> -Bu	<i>n</i> -Butyl, PrCH ₂ ⁻
Naph	1-Naphthyl, C ₁₀ H ₇ ⁻
2-Naph	2-Naphthyl, C ₁₀ H ₇ ⁻
NHC	N-heterocyclic carbene
NMR	Nuclear magnetic resonance
Ph	Phenyl
Pmp	Pentamethylphenyl, 2,3,4,5,6-Me ₅ C ₆ ⁻
ppm	parts per million
q	quartet (NMR)
R	<i>para</i> -Substituent
R'	Molecular fragment
s	second (time); singlet (NMR); strong (infrared)
<i>s</i>	<i>secondary</i>
sh	shoulder (infrared)
<i>s</i> -hexane	<i>secondary</i> -hexane
SQUID	Superconducting quantum interference device
t	triplet (NMR)
<i>t</i>	<i>tert</i>
<i>t</i> -Bu	<i>tert</i> -Butyl, Me ₃ C ⁻
THF	Tetrahydrofuran
Tmp	Trimethylphenyl, 2,4,5-Me ₃ C ₆ H ₂ ⁻
Tol	Tolyl, 4-MeC ₆ H ₄ ⁻

Tripp	Triisopropylphenyl, 2,4,6- <i>i</i> -Pr ₃ C ₆ H ₂ ⁻
UV/Vis	Ultraviolet/visible
w	weak (infrared)
XPS	X-ray photoelectron spectroscopy
XRD	X-ray diffraction
Xyl	Xylyl, Me ₂ C ₆ H ₃ ⁻
$\Delta v_{1/2}$	Half-height peak width
χ	Magnetic susceptibility
χ_M	Molar magnetic susceptibility
δ	Chemical shift (NMR)
λ	Wavelength
η	Hapticity
κ	Denticity
μ	Bridging
μ_{eff}	Effective magnetic moment
μ_B	Bohr magneton
π	Pi (orbital symmetry)
σ	Sigma (orbital symmetry)
σ_{para}	<i>para</i> -substituent Hammett constant
ν	frequency
$\bar{\nu}$	Wavenumber, 1/ λ

Chapter I

Introduction

1.1 Background

With the emergence of the digital era, modern society has been revolutionised by technological advancements and the accessibility of information, which, in turn, has transformed the global economy, business and everyday life. As reliance on computational devices has become commonplace, the execution of tasks has grown faster, cheaper and more efficient, while many disciplines, such as communication, manufacturing and medicine, have benefited tremendously. These advantages, combined with the prospect of increased commercial profit, will continue to fuel the development of new and improved technologies for the foreseeable future.

Crucial to the efforts to advance computational power is the requirement to enhance data processing speeds and information storage capacities. Over the past three decades, a rapid growth of globally stored information has already been witnessed, having increased from an estimated 2.6 to 4600 (optimally compressed) exabytes between 1986 and 2014.^{1,2} Moreover, the current pace of data creation amounted to a staggering 33 zettabytes in just 2018 alone.^{3,4} The majority of data is recorded digitally, over 99% in 2007, using devices that exploit magnetic, semiconductor or optical technologies.² Here, traditional magnetic materials are generally composed from metals, such as iron, nickel and cobalt, or, alternatively, metal oxides and alloys. They host a variety of important applications, for instance in old CRT televisions, magnetic coolers and MRI machines, and have become invaluable in chemical research, notably for NMR spectroscopy. Consequently, magnets are responsible for a multi-billion dollar industry each year, noting a permanent magnet market value of about \$15 billion in 2015.⁵

However, arguably the most essential use of magnets is for information storage, for example in computer hard drives, floppy disks, magnetic tapes, and credit cards.⁶ Such devices are typically manufactured from magnetically-coated polycrystalline materials like iron(III) oxide or cobalt alloys, which are composed from nanoscale particles of varying shape and size.⁷ Assemblies of these nanoparticles form small magnetic regions across the surface, each possessing their own magnetic dipole, where the relative orientations of the magnetisation can be used to store binary data.⁸ Importantly, the inhomogeneity of the particles means that several hundred of them are required to store 1 bit.⁹ This information can be encoded using read-and-write heads, which scan over a material's surface to adjust its magnetisation by applying a local magnetic field.¹⁰ Data can similarly be retrieved by measuring the magnetisation at the regions. Yet, despite these advances, the physical limitations of magnetic materials continue to impose restrictions on the density of data stored within. Efforts have therefore focused on the miniaturisation of these devices in a 'top-down' approach to design smaller and smaller traditional magnets with higher overall information storage capacities.¹¹

For many years, miniaturisation was achieved via the simple down-scaling of magnetic components, enabled by making improvements to the read-and-write heads. Originally, the heads operated using an electromagnetic induction technique, but the demand for increased data storage led to the development thin-film heads in the 1980s, allowing information storage capacities to rise by 30% annually. This grew to 60% in 1991 with the introduction of the magnetoresistive head (MR) and a climb to 100% by 2000 when the giant magnetoresistive head (GMR) was established. Thereafter, despite the launch of the tunnel magnetoresistive head (TMR) in 2006, growth rates have since declined to 40% and then 13% due to higher technologies challenges (**Fig. 1.1**).¹²⁻¹⁶

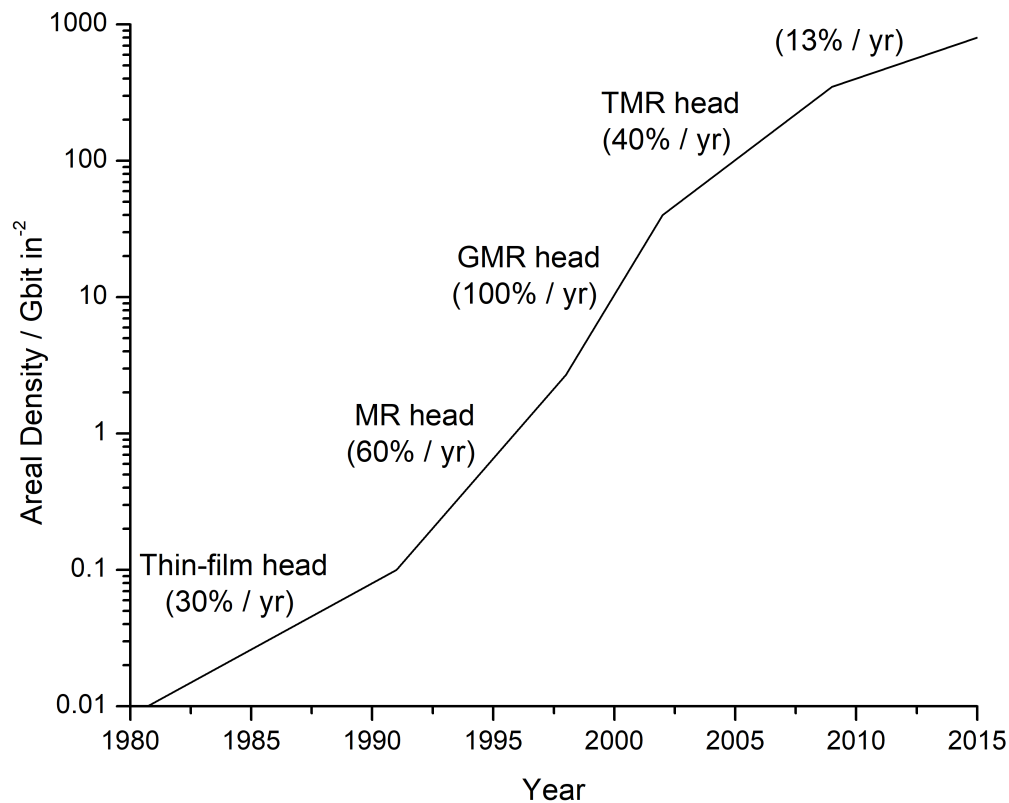


Fig. 1.1 Annual growth in areal density (Gbit/in²) for HDD magnetic recording devices, defined by the number of bits stored per unit of disk surface area.^{12,16}

Clearly, miniaturisation cannot continue indefinitely; a threshold for particle size of approximately 10 nm has been identified (**Fig. 1.2**).^{11,17} While this is partially due to the requirement for more advanced and expensive fabrication methods, the main limitation of the ‘top-down’ approach relates to the superparamagnetic effect.¹⁸ This states that, as nanoparticles decrease in size, their internal energy becomes comparable to the thermal energy of the system. The effects of temperature therefore become dominant, and this results in a random re-orientation and flipping of the magnetic spins such that the overall magnetisation averages to zero. Consequently, at room temperature, any stored information is lost.¹⁹

1.2 Introduction

1.2.1 Traditional Bulk Magnetism

Magnetism arises when the movement of charged particles generates a magnetic field. In atoms, it specifically results from a combination of the nuclear spin, the electron spin and the electron orbital motion. These contributions, responsible for a material's magnetic behaviour, can broadly be divided into five categories (**Fig. 1.3**):²²

1. Diamagnetism is observed when all electron spins are paired such that the overall spin averages to zero. Such materials are weakly repelled by a magnetic field.
2. Paramagnetism occurs for open-shell systems with unpaired electrons. Each spin acts independently of its neighbours and is randomly orientated. Application of a magnetic field causes spin alignment and attraction of the material to the field.
3. Ferromagnetism involves systems with unpaired electrons that exhibit long-range, cooperative ordering of their spins, such that they are all aligned parallel in one direction, even in the absence of a magnetic field. This generates a large magnetic moment that causes materials like iron to be attracted to a magnetic field.
4. Antiferromagnetism again requires unpaired electrons but, in this case, all the spins adopt an antiparallel (opposite directions) configuration that is repeated through the lattice. Consequently, the magnetic moment averages to zero.
5. Ferrimagnetism similarly involves unpaired electrons in an antiparallel alignment, but with more spins orientated in one direction, producing a magnetic moment.

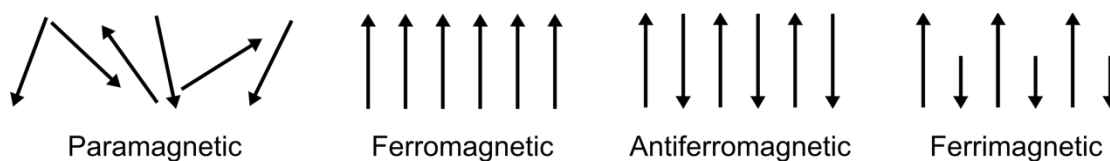


Fig 1.3 Electron spin configurations of different magnetic materials.

1.2.2 Single-Molecule Magnets

Magnetism of a fundamentally different nature to that found in traditional bulk materials is exhibited by a relatively new class of organometallic compounds called single-molecule magnets (SMMs). These are individual molecules of about 1.5 nm diameter that, on application of a magnetic field, show directional magnetisation of purely molecular origin.²³ Crucially, provided the temperature is low enough, this magnetisation will persist for a long duration after removal of the external field due to slow spin relaxation.²⁴

Such compounds typically consist of multiple paramagnetic transition metal or lanthanide ions that are linked together via organic bridging groups. Here, the metal centres within the molecule contain unpaired electrons that couple together through intramolecular interactions to give a magnetic core with a large overall ground state spin, S . The role of the organic linkers is to surround this metal core and protect it from forming close-contacts with neighbouring molecules. Thus, unlike for traditional bulk materials, no intermolecular interactions or long-range ordering is required for the magnetisation to persist, such that all molecules are independent and identical.^{25–27}

The magnetic phenomena experienced by SMMs can be explained in terms of an energy barrier for re-orientation of the magnetisation, U . This barrier arises when a molecule's ground spin state, S , undergoes zero-field splitting (ZFS) into its M_s energy sublevels in the absence of an applied magnetic field (**Fig. 1.4a**); the degeneracy of S is said to be lifted.²⁸ Here, each M_s sublevel corresponds to a different orientation of the spin, relative to the molecular plane, where $M_s = +S$ and $-S$ can be considered as 'spin up' and 'spin down' respectively.²⁹

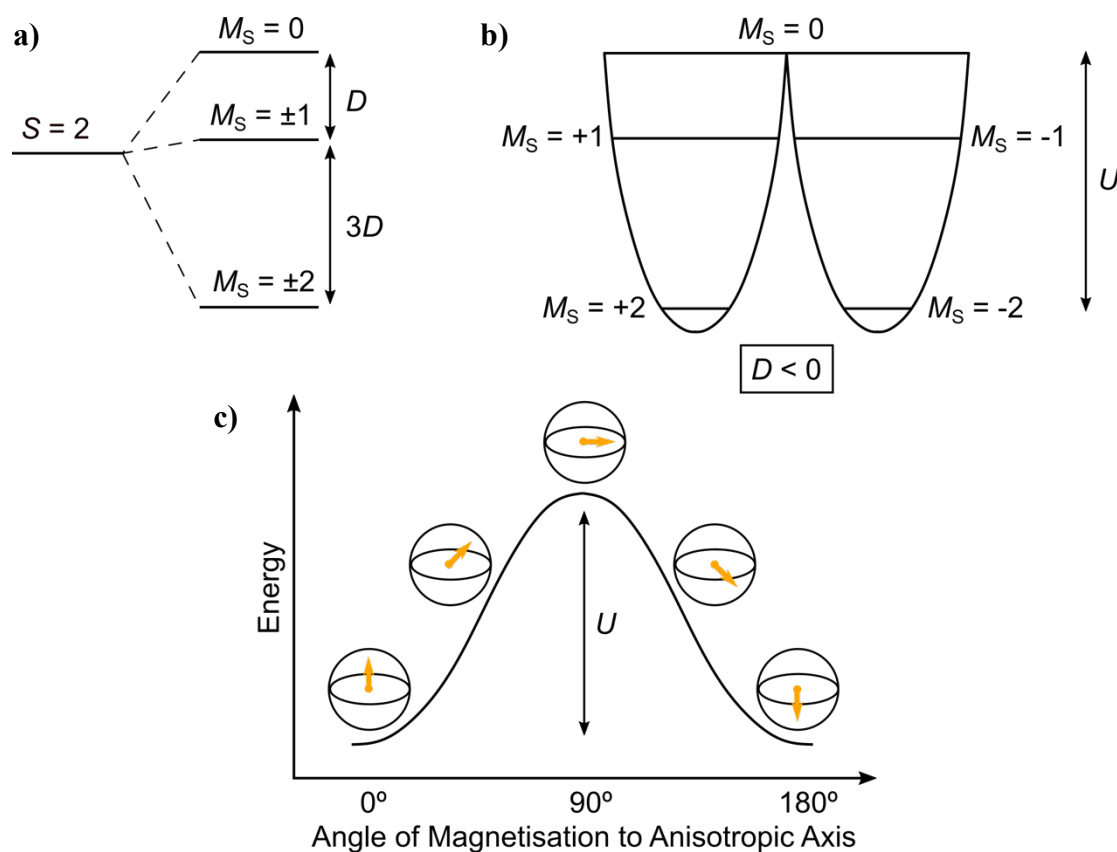


Fig. 1.4 Diagrams of a) the zero-field splitting for an $S = 2$ state, b) its double-well energy curve, and c) the energy preference for easy-axis anisotropy.^{28,29}

In general, zero-field splitting occurs for low symmetry complexes whose electronic states are symmetry-separated, allowing them to mix via spin-orbit coupling. It is expressed by a ZFS parameter with an axial term, D , and a transverse term, E . In SMMs, the axial parameter, D , should be negative; this produces a magnetically bi-stable system where larger M_s states fall at lower energies than smaller M_s states. A double-well potential energy curve can be used to illustrate this concept (**Fig. 1.4b**). The diagram highlights the two energy minima at $M_s = \pm 2$ within which the magnetic spins can be trapped, plus a maximum at $M_s = 0$ showing the spin reversal energy barrier, U , between the $+M_s$ to $-M_s$ states.^{28,30} Such a system is described as having easy-axis anisotropy, since the most favourable spin orientation occurs when the spins are aligned parallel to the principal axis of the magnetic anisotropy (**Fig. 1.4c**).³¹

Application of an external magnetic field parallel to this principal axis causes alignment of the spins in the field's direction. Consequently, the double-well energy curve becomes skewed; the two equally-populated wells observed at zero-field (**Fig. 1.5a**) are shifted in energy such that the $-M_s$ states are stabilised while the $+M_s$ states are destabilised, owing to the Zeeman effect.^{32,33} This increases the population of the $-M_s$ states until, at magnetic saturation, only the $M_s = -S$ sublevel remains populated and all the spins are orientated in the direction of the external field (**Fig. 1.5b**). Here, the bulk sample is magnetised.³¹ Upon removal of the field, the system relaxes back to its thermal equilibrium by overcoming the spin reversal energy barrier, U (**Fig. 1.5c**). However, in practice, due to the occurrence of alternate relaxation pathways like quantum tunnelling,³⁴ the measured barrier is often lower than this intrinsic U value.^{35,36} Hence, an effective energy barrier, U_{eff} , is generally quoted.

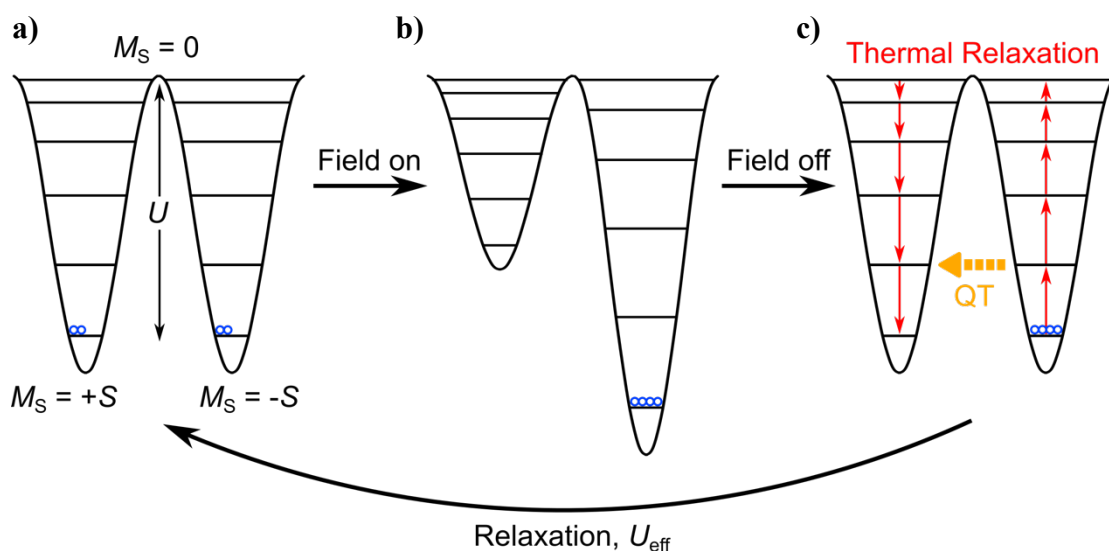


Fig. 1.5 The double-well energy curve showing a) zero-field splitting of the two equally-populated wells, b) application of an external magnetic field to stabilise and populate the $-M_s$ states, and c) removal of the field to cause thermal relaxation or quantum tunnelling (QT) back to the equilibrium state.^{32,33}

Importantly for SMMs, this energy barrier, U , must remain larger than the thermal energy, $K_B T$, of the system to prevent thermal inversion of the spins.³⁷ To achieve this, cooling to a specific blocking temperature, T_B , is required. Under these conditions, application of an external field traps the aligned spins in a fixed orientation such that, on removal of the field, the magnetisation is retained for a long duration. If slow enough, the relaxation can then be studied using a SQUID magnetometer. In principle, such materials could be implemented in data storage devices by assigning binary coding to each M_s spin state, ensuring a large U_{eff} barrier to prevent information loss.³⁸ However, despite recent progress,^{39–41} SMMs are yet to find real-world applications due to the unfeasibly low blocking temperatures required.

Therefore, when designing new SMMs, it is evident that attaining a large U energy barrier is essential. The size of this barrier is dictated by both the ground state spin value, S , and the axial ZFS parameter, D , according to the relationships:³⁵

$$U = |D| \cdot S^2 \quad (\text{Integer spin systems})$$

$$U = |D| \cdot (S^2 - 1/4) \quad (\text{Half-integer spin systems})$$

Originally, research was focused on high nuclearity complexes containing many paramagnetic ions, in an effort to maximise the ground spin state, S . For example, the first SMM $[\text{Mn}_{12}\text{O}_{12}(\text{OAc})_{16}(\text{H}_2\text{O})_4] \cdot 2\text{AcOH} \cdot 4\text{H}_2\text{O}$ (Mn_{12}OAc) had four octahedral Mn(IV) ($S = 3/2$) ions (total $S = 6$), surrounded by the antiparallel spins of eight Jahn-Teller distorted octahedral Mn(III) ($S = 2$) ions (total $S = 16$) (**Fig. 1.6a**).^{42–45} Antiferromagnetic coupling of these metals via the bridging oxygen (O^{2-}) atoms gave a total spin of $S = 10$ (**Fig. 1.6b**). Magnetic studies revealed the complex to have a high U_{eff} of 60 K, where $U = 72$ K, $D = -0.5 \text{ cm}^{-1}$ and $T_B \approx 3$ K.^{45–47}

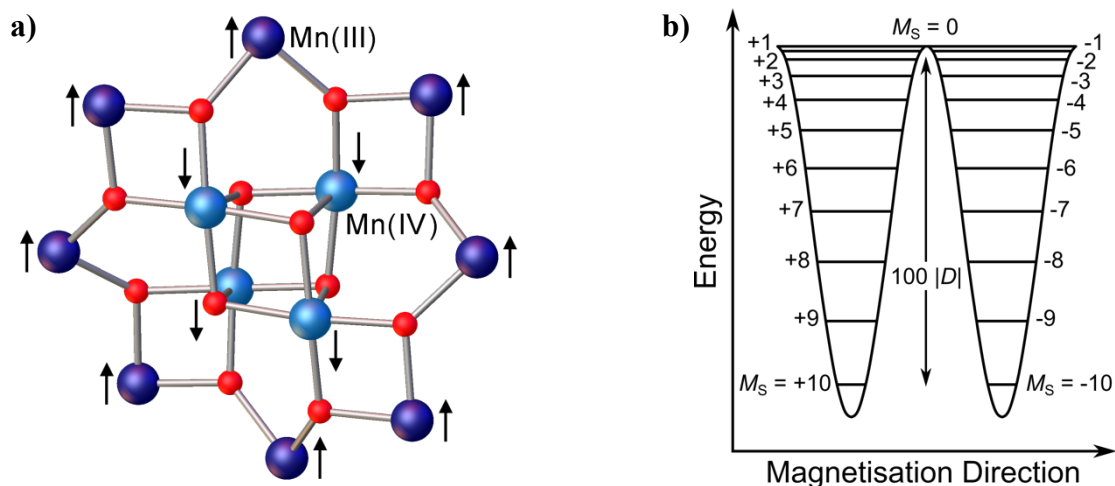


Fig. 1.6 Diagrams for Mn₁₂OAc showing a) the spin alignments in the Mn₁₂ core, and b) the double-well energy curve for the $S = 10$ ground state under zero-field.^{18,48}

However, later attempts at making polynuclear SMMs with improved magnetic properties proved futile; increasing the nuclearity (spin) was ineffective at enlarging the U_{eff} barrier.⁴⁹ The reason for this originates from the inverse relationship between the spin, S , and the axial ZFS parameter, D .^{32,50} This means that, although incorporating many paramagnetic ions into a complex may increase its spin, doing so may be detrimental to the overall U_{eff} barrier since the ZFS term diminishes. In simpler terms, this can be ascribed to anisotropy effects, in which the magnetic spins for each of a complex's individual ions are not aligned in the same direction as one another.⁵¹ Consequently, their anisotropies cancel out, and the axial ZFS parameter, D , decreases. Thus, in order to avoid this anisotropy problem associated with polynuclear SMM complexes, recent research has shifted towards the development of mononuclear SMMs, known as single-ion magnets (SIMs).

1.2.3 Single-Ion Magnets

Containing just one metal centre, single-ion magnets (SIMs) are the smallest sized SMMs attainable and have been subject to considerable scientific interest over the past decade.⁵² Early efforts to develop SIMs with large U energy barriers were limited by the size of the spin, S , offered by the complex's single metal centre. To counteract this, research shifted towards systems with large axial ZFS parameters, D , and high magnetic anisotropies. Lanthanide compounds were initially investigated due to their strong, unquenched, orbital angular momenta that increases the axial ZFS term, D .⁵³

However, since 2013, interest in SIMs of the 3d transition metals has been renewed following the discovery of a linear iron(I) complex $[\text{Fe}(\text{C}\{\text{SiMe}_3\}_3)_2]^-$ ($S = 3/2$) with a notably high relaxation barrier, $U_{\text{eff}} = 325.2$ K (**Fig. 1.7a**).^{54,55} Its magnetic behaviour results from the low coordination number; the weaker crystal field of two-coordinate complexes gives a smaller energy gap between the ground and excited states, leading to better mixing and unquenched orbital angular momentum. Specifically, $3d_{z^2}$ – $4s$ mixing causes stabilisation of the iron $3d_{z^2}$ orbital (**Fig. 1.7b**) to generate anisotropy.⁵⁶ In other words, the strong ligand field that quenches the orbital angular momentum in high-coordinate complexes is removed and the ZFS term, D , is increased.^{46,54} Moreover, the d^7 iron(I) system features a Kramers ion (a half-integer spin) for which quantum tunnelling is minimised.^{54,57}

Another important aspect of two-coordinate SIMs is their linearity. As the geometry of these complexes is bent away from the ideal angle of 180° , the d-orbitals suffer a loss of degeneracy which, in turn, can quench the orbital angular momentum and diminish the ZFS term, D .⁵⁸

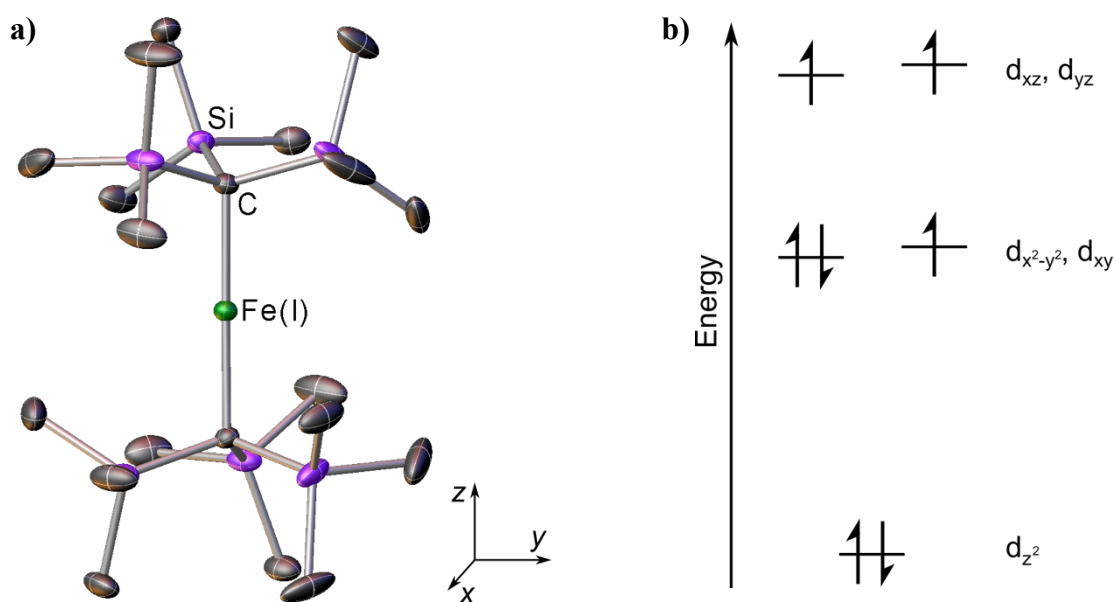


Fig. 1.7 Diagrams for $[\text{Fe}(\text{C}\{\text{SiMe}_3\}_2)]^-$ showing a) the anion's crystal structure and b) the splitting of its 3d-orbital energy levels.⁵⁴ Ellipsoids set at 45% probability. Hydrogen atoms and the counter-cation are omitted.

To further develop the understanding of single-ion magnets and, on a broader scale, the general field of molecular magnetism, future research will require the synthesis of novel two-coordinate linear complexes suitable for magnetic studies. Here, sterically-bulky ligand systems must be carefully chosen to enforce geometries that optimise the orbital angular momentum and give large relaxation barriers, U_{eff} . A variety of different metals from lanthanides to d-block elements can also be investigated. The unique advantage of using transition metals is the ability of their valence d-electrons to couple between ions, such that, by linking together many individual SIM units, highly anisotropic (uniaxial) polymetallic chains could be formed with large spin values.⁴⁶ This has been attempted using lanthanide complexes like $\text{Ln}(\text{COT})_2$ (COT = cyclooctatetraenyl) to build multi-decker species, however their magnetic properties resemble those of the individual SIMs due to the inability of their core-like 4f-orbitals to couple.^{59,60}

1.2.4 Bulky Ligand Systems

Advancements in the field of organometallic chemistry have borne witness to an extensive number of sterically demanding ligands designed for the stabilisation of two-coordinate transition metal complexes.⁶¹ Early studies employed systems featuring heteroatom donors, such as amido (N) and alkoxo (O) ligands, since these coordinated to the d-block ions with greater success than their carbon analogues.^{62,63} Originally, the instability of the carbon complexes was justified by their weaker metal-carbon σ -bonding.⁶⁴ However, this was later ascribed to β -hydride elimination; a low-energy kinetic effect which causes facile decomposition of transition metal alkyls.⁶⁵ It was therefore not until 1985 when the first two-coordinate transition metal-carbon complex, $\text{Mn}(\text{C}\{\text{SiMe}_3\}_3)_2$, was crystallographically characterised (**Fig. 1.8**).⁶⁶

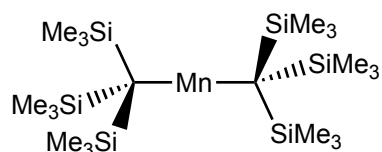


Fig. 1.8 Chemical structure of the two-coordinate complex $\text{Mn}(\text{C}\{\text{SiMe}_3\}_3)_2$.⁶⁶

Following the development of alkyl systems, the role of σ -bonded aryl ligands for the stabilisation of two-coordinate transition metal complexes was explored. Again, similar problems were encountered with *ortho*-hydrogen abstraction, causing synthetic complications like metal reduction and biphenyl formation.⁶⁵ In addition, early reports indicated that some metal diaryls were prone to oligomerisation, particularly those containing small phenyl ligands; an example being $[\text{MnPh}_2]_\infty$, which exhibits a long polymeric chain-like structure (**Fig. 1.9**).⁶⁷

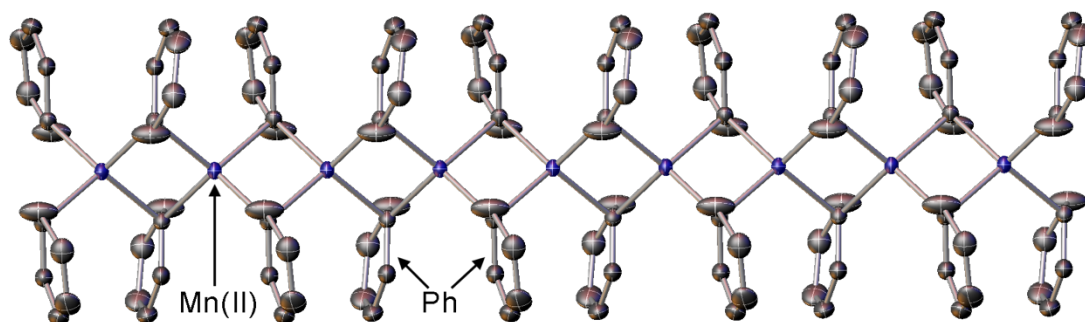


Fig. 1.9 Crystal structure of the $[\text{MnPh}]_{\infty}$ chain stabilised by small phenyl ligands.⁶⁷ Ellipsoids set at 50% probability and hydrogen atoms are omitted.

Despite this, if the steric bulk of the ligand is increased, specifically via the incorporation of bulky *ortho*-substituents onto the aryl ring, then the formation of low-coordinate complexes becomes possible. For instance, in the prior example, utilisation of the larger mesityl ligands, instead of phenyls, gives a smaller complex; $[\text{MnMes}_2]_3$ (Mes = 2,4,6- $\text{Me}_3\text{C}_6\text{H}_2$) is produced as a linear trimer (**Fig. 1.10a**).⁶⁸ In fact, by further increasing the steric bulk through use of the Tripp ligand, the $[\text{MnTripp}_2]_2$ (Tripp = 2,4,6-*i*- $\text{Pr}_3\text{C}_6\text{H}_2$) dimer can be isolated (**Fig. 1.10b**).⁶⁹ Ultimately, a monomer can be obtained by using the even bulkier supermesityl ligand, Mes*, which yields $[\text{MnMes}^*_2]$ (Mes* = 2,4,6-*t*- $\text{Bu}_3\text{C}_6\text{H}_2$) as a two-coordinate species (**Fig. 1.10c**).⁷⁰

Owing to their effective stabilisation of two-coordinate transition metal complexes, these *ortho*-substituted aryl ligands continue to be utilised in organometallic synthesis featuring increasingly bulkier designs. Here, an important example studied within this research is the *m*-terphenyl ligand.

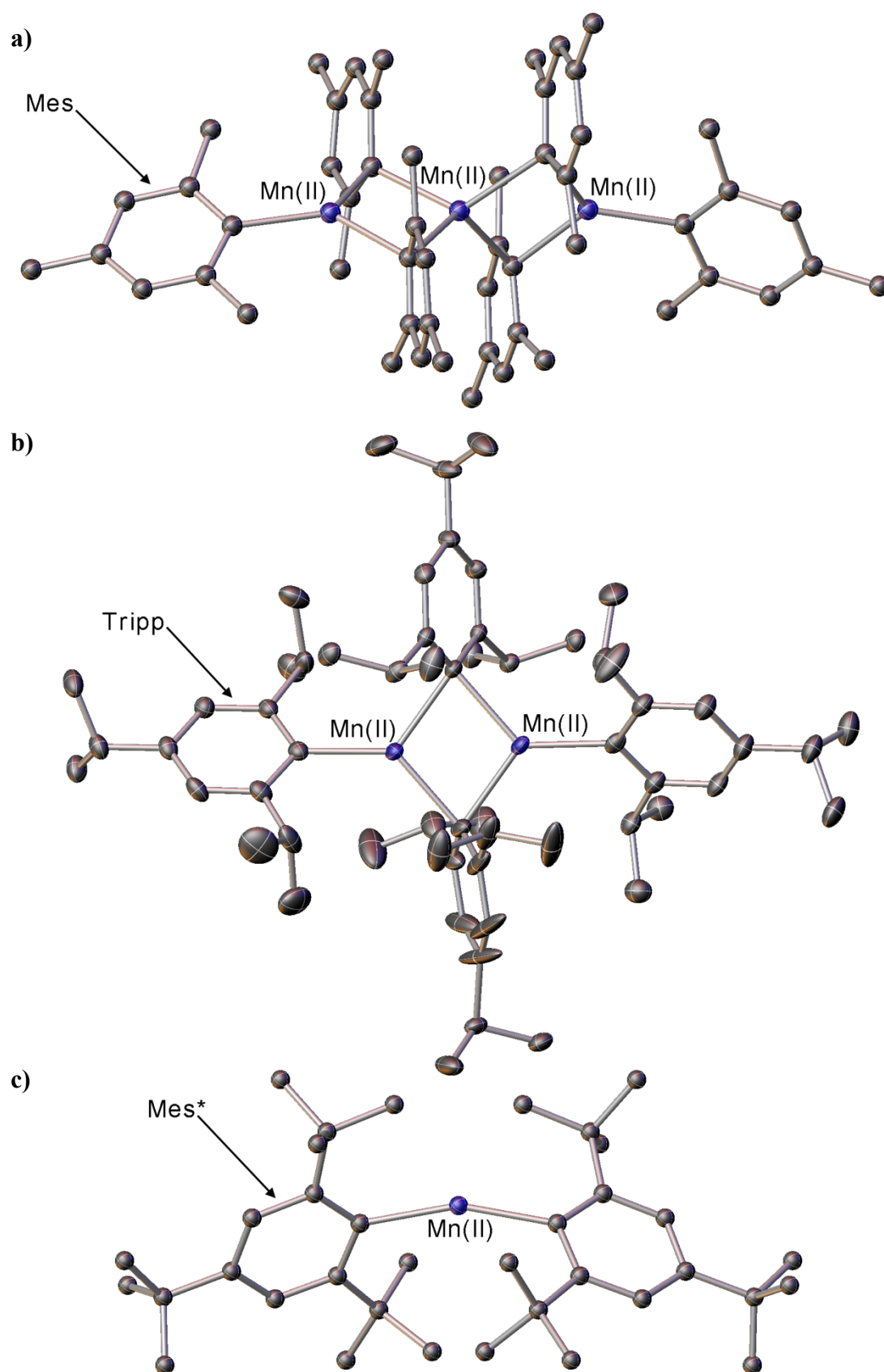


Fig. 1.10 Crystal structures of the a) trimer $[\text{MnMes}_2]_3$, b) dimer $[\text{MnTripp}_2]_2$, and c) monomer $[\text{MnMes}^*_2]$, obtained by increasing the ligand bulk.^{68–70} Ellipsoids set at 20%, 50% and 15% probability. Hydrogens and solvent molecules are omitted.

1.2.5 The *m*-Terphenyl Ligand

The *m*-terphenyl ligand has general formula $2,6\text{-Ar}_2\text{C}_6\text{H}_3^-$ and consists of a central aromatic ring that is di-substituted by two flanking aryl groups, positioned *meta* to one another (**Fig. 1.11**). Between these resides the *ipso*-carbon, which binds to the metal centre in a monodentate fashion via the formation of a M–C σ -bond. The flanking aryl groups adopt an orthogonal geometry relative to the central ring that, on complexation, creates a protective steric pocket around the metal to shield it from forming higher coordination numbers. This enables the stabilisation of coordinatively unsaturated metal complexes with unusual bonding modes and geometries.⁷¹

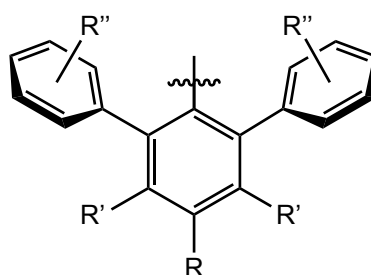


Fig. 1.11 General structure of the *m*-terphenyl (usually R, R', R'' = alkyl or aryl).

The customisable nature of these ligands enables the steric and electronic properties of the metal complex to be tailored via structural substitution, either on the central ring, R and R', or on the flanking aryl groups, R''. To quantify their steric bulk, methods have been developed in place of the Tolman cone angle, whose ability to describe phosphine systems is inadequate for modelling non-conical ligands where the bulk is directed towards the metal.⁷² Instead, a percent buried volume, $\%V_{\text{Bur}}$, term has been defined: for a metal-centred sphere of radius, r , this measures the volume of the sphere buried by overlap with the ligand (**Fig. 1.12**).^{73–76} It represents the space around the metal occupied by the ligand, where bulkier systems give larger $\%V_{\text{Bur}}$, and depends upon the metal-ligand bond length, d , and a predefined, optimised, sphere radius, r .

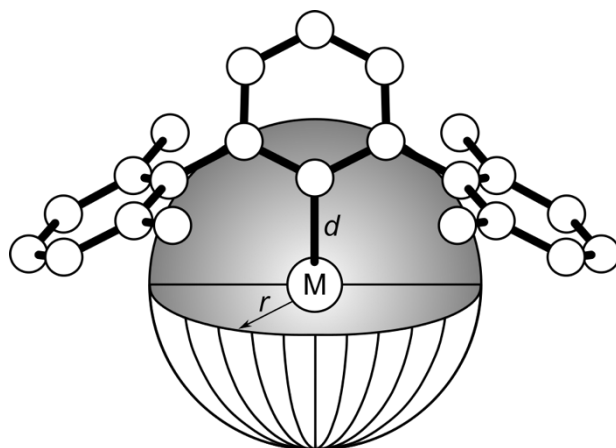


Fig. 1.12 Representation of the metal-centred sphere of radius, r , used to calculate the percent buried volume, $\%V_{\text{Bur}}$, of the m -terphenyl ligand, for a metal (M) complex with metal-ligand bond length, d .

Although $\%V_{\text{Bur}}$ was originally introduced for N-heterocyclic carbenes (NHCs), the term has recently been applied to the m -terphenyl framework.⁷⁷ Specifically, for a series of two-coordinate manganese diaryls $(2,6\text{-Ar}_2\text{C}_6\text{H}_3)_2\text{Mn}(\text{THF})_n$ ($\text{Ar} = 2,6\text{-Xyl}$ $\{n = 0\}$, Mes $\{n = 0\}$, Tmp $\{n = 1\}$; $2,6\text{-Xyl} = 2,6\text{-Me}_2\text{C}_6\text{H}_3$; $\text{Tmp} = 2,4,5\text{-Me}_3\text{C}_6\text{H}_2$) featuring different flanking aryl groups substituted at the R'' position (**Fig. 1.11**), the $\%V_{\text{Bur}}$ term of the m -terphenyl ligand decreases from Mes (42.7) to 2,6-Xyl (42.0) to Tmp (37.5) respectively, with $r = 3.5 \text{ \AA}$. This indicates a reduction of steric bulk in the coordination sphere, notably for Tmp, where removal of an *ortho*-methyl group causes the greatest loss of steric shielding at the metal centre.⁷⁷

Topographic steric maps can similarly be used to describe the bulk of a ligand by taking a cross-section of its structure to render a 2D surface profile, where contour lines depict areas of varying steric bulk.⁷⁸ This has proven useful in reactivity studies for mapping ligand-substrate interaction surfaces, or the shape of a catalytic pocket.⁷⁹ These steric plots have been computed for the m -terphenyl ligands of the abovementioned manganese complexes $(2,6\text{-Ar}_2\text{C}_6\text{H}_3)_2\text{Mn}(\text{THF})_n$ (**Fig. 1.13**).⁷⁷

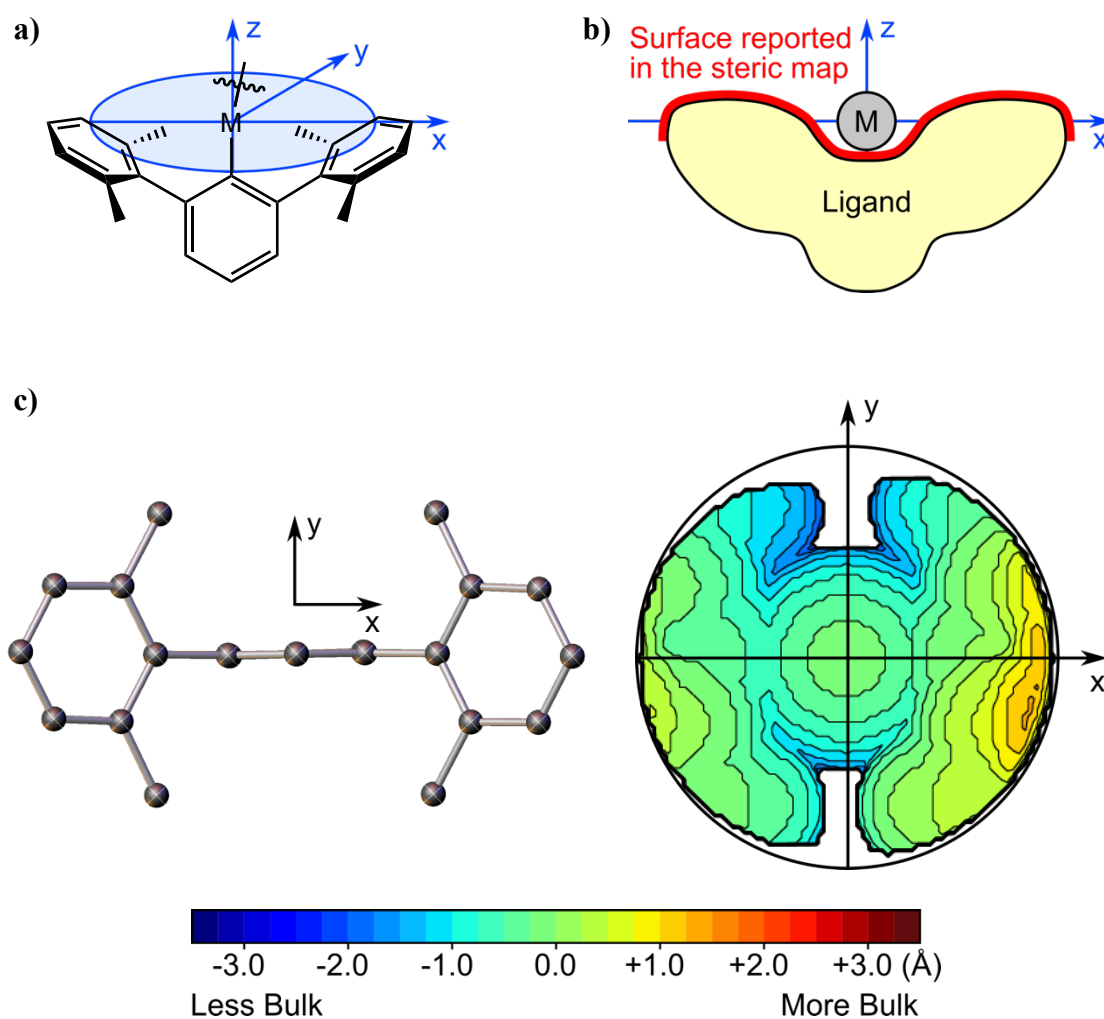


Fig. 1.13 Diagrams showing a) an *m*-terphenyl complex with a cross-section through its metal (M) centre, b) the surface of the ligand reported in the steric map, and c) the steric map of the *m*-terphenyl ligand in $(2,6\text{-Ar}_2\text{C}_6\text{H}_3)_2\text{Mn}$ (Ar = 2,6-Xyl) with a sphere radius of 3.5 Å, a mesh spacing of 0.10 Å, and with hydrogens included.^{77,78}

Clearly, modification of the *m*-terphenyl framework via substitution at the R, R' or R'' positions (**Fig. 1.11**) can cause significant changes to the steric bulk in the vicinity of the coordination sphere. As a consequence, the impact of these ligand alterations upon the structural and electronic properties of the resulting metal complexes, specifically on their bonding modes and geometries, has become a central research theme in *m*-terphenyl chemistry. Examples of these studies are described over the following pages.

Substitution of the *m*-terphenyl flanking groups, at the R'' position (**Fig. 1.11**), alters the steric environment at the coordination sphere and, thus, impacts the size of the steric pocket encapsulating the metal. This has been shown by a series of two-coordinate Group 12 diaryls $(2,6\text{-Ar}_2\text{C}_6\text{H}_3)_2\text{M}$ ($\text{M} = \text{Zn}, \text{Cd}, \text{Hg}$; $\text{Ar} = 2,6\text{-Xyl}, 3,5\text{-Xyl}, \text{Pmp}$; $3,5\text{-Xyl} = 3,5\text{-Me}_2\text{C}_6\text{H}_3$; $\text{Pmp} = 2,3,4,5,6\text{-Me}_5\text{C}_6$), where structural modification of the flanking rings was studied (**Fig. 1.14**).^{80,81} Here, near-linear C–M–C bond angles were reported for the bulkier 2,6-Xyl [$177.1(2)\text{--}179.9(3)^\circ$] and Pmp [$175.78(12)\text{--}180.0(0)^\circ$] derivatives, both of which feature *ortho*-methyl substituents, whereas narrower angles were found for the less sterically-hindered 3,5-Xyl group [$171.18(5)\text{--}176.4(2)^\circ$], whose *meta*-methyl substituents are situated further from the coordination sphere. The absence of these *ortho*-methyls was suggested to allow for easier rotation of the flanking rings that, in turn, enables the complex to bend. Moreover, the 3,5-Xyl derivatives exhibit extra secondary contacts between the flanking *ortho*-hydrogens and the metal.

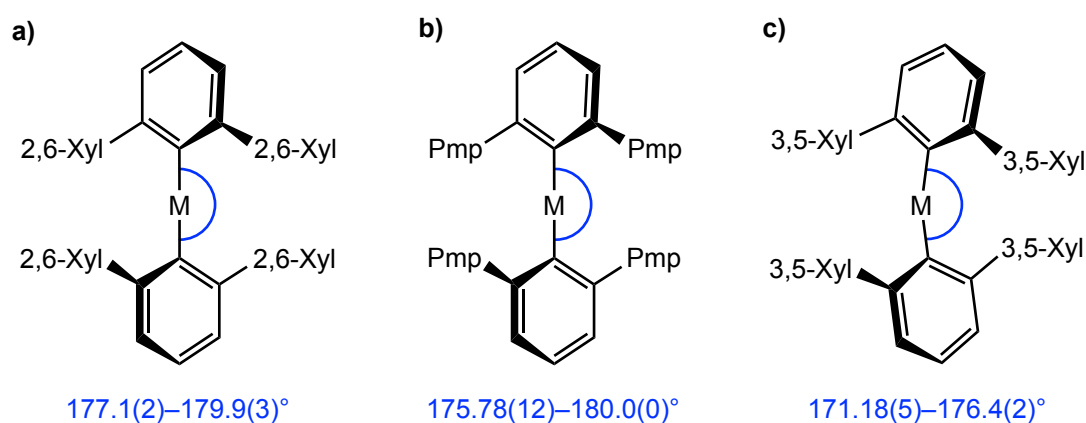


Fig. 1.14 Structures and C–M–C bond angles for a series of Group 12 *m*-terphenyl complexes $(2,6\text{-Ar}_2\text{C}_6\text{H}_3)_2\text{M}$ ($\text{M} = \text{Zn}, \text{Cd}, \text{Hg}$; $\text{Ar} = 2,6\text{-Xyl}, 3,5\text{-Xyl}, \text{Pmp}$).^{80,81}

Nonetheless, there are limitations to the amount of steric bulk that can be incorporated on the flanking rings; until recently,^{82,83} the Mes* *m*-terphenyl iodide, $2,6\text{-Mes}^*\text{C}_6\text{H}_3\text{I}$, possibly the bulkiest known, could not be prepared due to synthetic difficulties.⁸⁴

Alternatively, the *m*-terphenyl can be functionalised on its central ring, at the R or R' positions (**Fig. 1.11**). Here, the addition of bulky R' groups via *meta*-substitution forces the flanking groups to move closer to the metal in order to minimise steric clash. This reduces the bite angle, defined as the angle between the vectors linking the two flanking ring centroids to the central ring *ipso*-carbon (**Fig. 1.15a**).⁸⁵ For example, the bite angle of an *m*-terphenyl iodide, 2,6-Mes₂C₆H₃I, [158.12(13)°] becomes narrower following *meta*-substitution with *i*-Pr groups to give 2,6-Mes₂-3,5-*i*-Pr₂C₆H₃I [155.92(5)°].⁸⁶ The incorporation of such ligands into a metal complex can therefore increase the steric pressure exerted on the coordination sphere that, in turn, can cause major distortions of its structure. This has been demonstrated by an *m*-terphenyl gallium complex, where *meta*-substitution with *i*-Pr groups causes the bite angle of the unsubstituted dimeric species [(2,6-Dipp₂C₆H₃)Ga]₂ (Dipp = 2,6-*i*-Pr₂C₆H₃) [158.13(8)°] to close; the greater steric crowding prevents Ga–Ga bond formation and drives the complex to adopt a monomeric geometry [(2,6-Dipp₂-3,5-*i*-Pr₂C₆H₃)Ga:] [150.4(3)°] (**Fig. 1.15b**).^{85,87,88} *Meta*-substitution has also been noted to increase the rigidity of a complex by hindering the rotation of its flanking aryls which, practically, can encourage crystal growth.⁸⁹

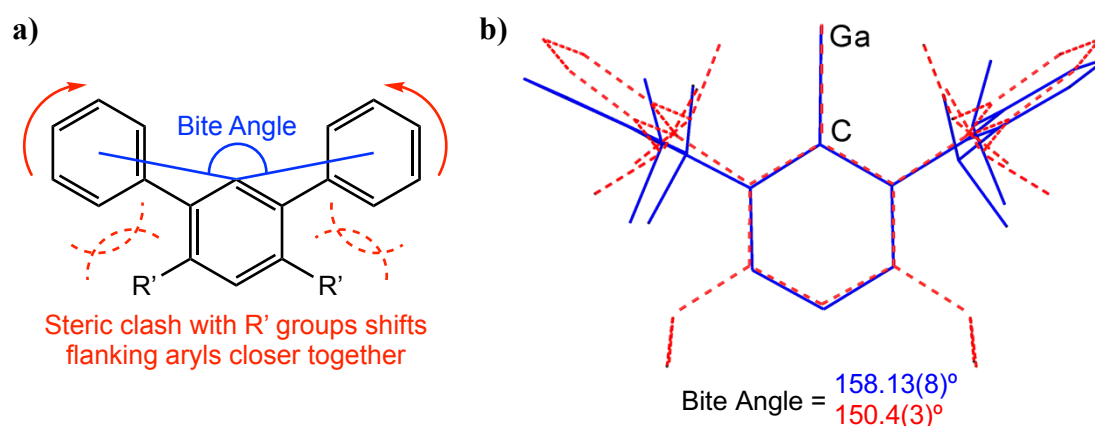
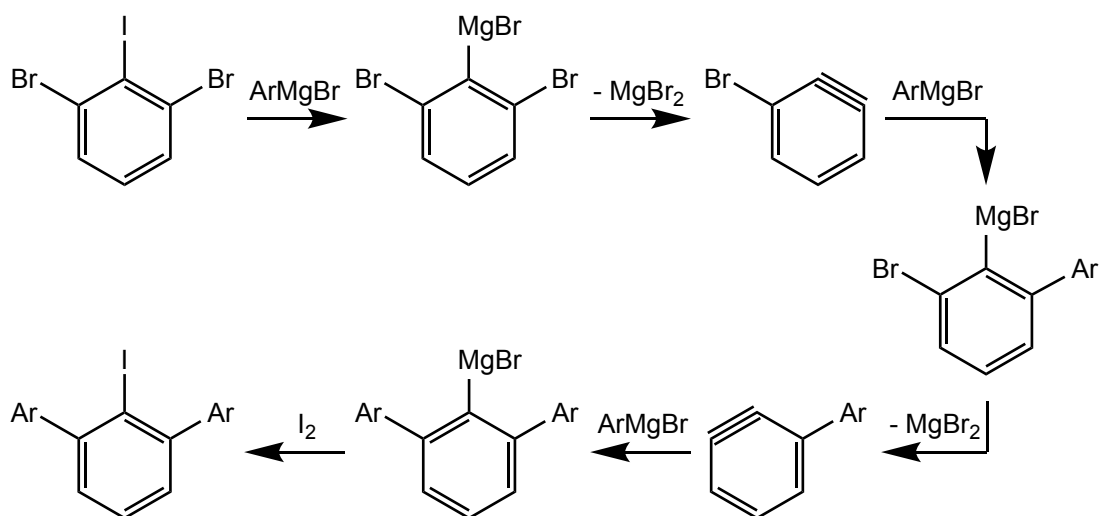


Fig. 1.15 Diagrams of a) the bite angle for an *m*-terphenyl, and b) the overlaid crystal structures of [(2,6-Dipp₂C₆H₃)Ga]₂ (blue) and [(2,6-Dipp₂-3,5-*i*-Pr₂C₆H₃)Ga:] (red), where *meta*-substitution produces a narrower bite angle and prevents dimerisation.⁸⁵

Substitution of the *m*-terphenyl at its *para*-position, R, (**Fig. 1.11**) with electron-donating or -withdrawing groups, has received relatively less attention, limited mostly to a handful of main group compounds.^{85,89–94} This concept is generally considered to induce electronic changes at the metal centre, while minimising structural variations owing to steric effects. For instance, the ¹¹⁹Sn NMR spectra for the functionalised tin hydrides [(2,6-Dipp₂-4-R-C₆H₂)Sn(μ -H)]₂ (R = H, *t*-Bu, OMe) show a downfield shift with greater electron-donating strength of the *para*-group (657, 667 and 687 ppm for H, *t*-Bu and OMe, respectively), despite adopting similar crystallographic structures.⁹⁰ However, in other cases, the observed electronic shifts are accompanied by structural distortions. For a series of Group 14 diaryls (2,6-Mes₂-4-R-C₆H₂)₂M (M = Ge, Sn, Pb; R = H, SiMe₃, Cl), electron-withdrawing groups not only cause upfield ¹¹⁹Sn NMR shifts (1891, 1971 and 1975 ppm for Cl, H and SiMe₃, respectively) and hypsochromic UV/Vis shifts (when M = Ge: 583, 573 and 566 nm for SiMe₃, H and Cl, respectively), but also cause bent C–M–C angles in the germanium derivative.^{91,92} This bending due to electron-withdrawal was ascribed to increased s-electron character of the germanium lone pair, resulting in a greater energy separation of the frontier orbitals and the observed spectroscopic shifts. Despite this, the structural changes of *para*-substitution could arguably be a consequence of crystal packing effects, rather than electronics. This possibility was debated for the distannyne [(2,6-Dipp₂C₆H₃)Sn]₂, whose Sn–Sn multiple-bond [2.6675(4) Å] is lengthened by adding SiMe₃ *para*-groups to yield the single-bonded [(2,6-Dipp₂-4-SiMe₃-C₆H₂)Sn]₂ [3.0577(2) Å].^{93,94} Alternatively, *para*-substitution may produce no significant structural or electronic differences. Such was the case for the quintuply-bonded arylchromium dimer [(2,6-Dipp₂-4-R-C₆H₂)Cr]₂ (R = H, SiMe₃, OMe, F).⁸⁹ Further research is therefore required to fully understand the effects of *para*-substitution, particularly for transition metal complexes.

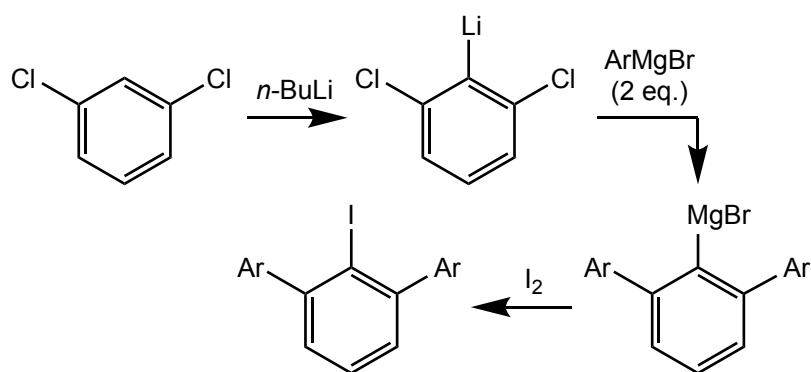
1.2.6 Synthesis of *m*-Terphenyl Ligands

The synthesis of an *m*-terphenyl ligand was first reported by Hart *et al.* in 1986, where 1,3-dibromo-2-iodobenzene was reacted with three equivalents of an aryl Grignard (Scheme 1.1).⁹⁵ The mechanism proceeds via two benzyne intermediates, which are formed and captured sequentially, to produce an *m*-terphenyl Grignard that can be quenched with an electrophile like iodine. This yields an air-stable *m*-terphenyl iodide.



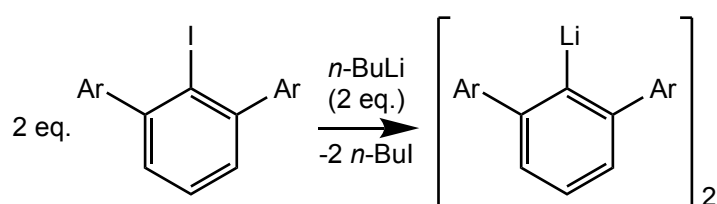
Scheme 1.1 First reported synthesis of an *m*-terphenyl iodide.⁹⁵

An alternative, more efficient route was later published by Hart *et al.* in 1996, where 1,3-dichlorobenzene was lithiated via a chloride-directed *ortho*-lithiation using *n*-butyllithium, followed by the addition of just two equivalents of an aryl Grignard reagent (Scheme 1.2).⁹⁶ Here, the mechanism proceeds via the formation of similar benzyne intermediates. The resultant *m*-terphenyl Grignard was again quenched with iodine to yield an air-stable *m*-terphenyl iodide. The benefits of this method include the easier preparation of the aryl halide starting material as well as the requirement for one equivalent less of the aryl Grignard reagent.



Scheme 1.2 Alternative synthesis of an *m*-terphenyl iodide.⁹⁶

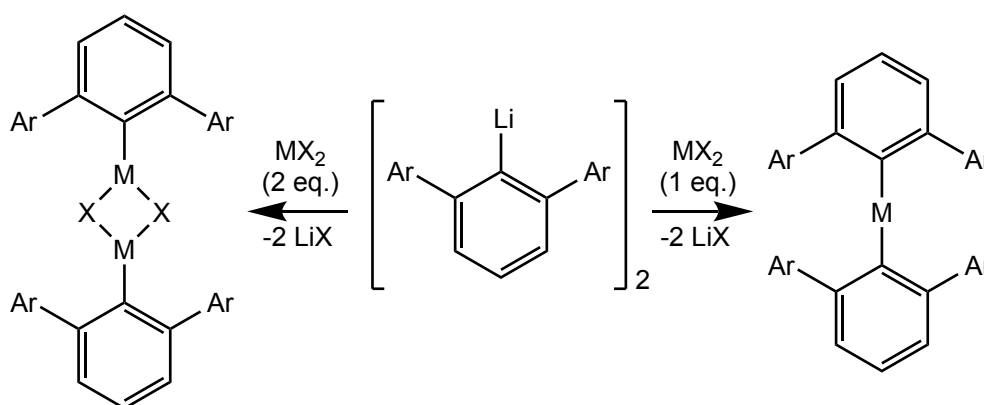
The resultant *m*-terphenyl iodide can be lithiated via the addition of *n*-butyllithium to yield an air- and moisture-sensitive *m*-terphenyl lithium complex (**Scheme 1.3**).^{97–100} These salts generally exist in dimeric form, although structural changes can be imposed by modification of the flanking aryl groups. For example, by increasing the steric bulk, the aggregation state of 2,6-Ar₂C₆H₃Li shifts from a dimer (Ar = Mes),⁹⁷ to a more crowded dimer (Ar = Dipp),⁹⁸ to a monomer stabilised by a coordinated benzene molecule (Ar = Tripp).^{98,101,102} In any case, these lithium salts can be employed as precursors for the synthesis of low-coordinate metal complexes.



Scheme 1.3 General synthesis of the dimeric *m*-terphenyl lithium complexes.

1.2.7 *m*-Terphenyl Metal Complexes

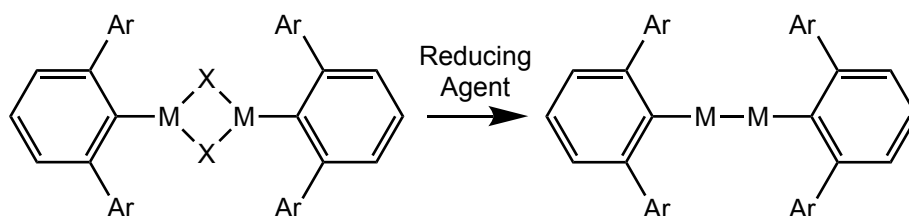
Low-coordinate metal complexes can be prepared via the metathesis reaction of an *m*-terphenyl lithium salt with a metal halide (MX_2). Here, the reagent stoichiometry dictates the product formed; heteroleptic or homoleptic species can be produced using either two equivalents or one equivalent of metal halide, respectively (**Scheme 1.4**).



Scheme 1.4 General synthesis of heteroleptic (left) and homoleptic (right) complexes.

Heteroleptic *m*-terphenyl complexes usually exist as halide-bridged dimers of the form $[(2,6\text{-Ar}_2\text{C}_6\text{H}_3)\text{M}(\mu\text{-X})]_2$ (M = metal; Ar = aryl; X = halide), including the transition metal systems $[(2,6\text{-Dipp}_2\text{C}_6\text{H}_3)\text{M}(\mu\text{-X})]_2$ (M = Cr or Co, X = Cl; M = Fe, X = Br).^{103,104} However, dimerisation can be blocked, as illustrated by a series of Group 12 complexes, whose zinc and cadmium derivatives were characterised to be iodide-bridged dimers $[(2,6\text{-Dipp}_2\text{C}_6\text{H}_3)\text{M}(\mu\text{-I})]_2$ (M = Zn, Cd), whereas the mercury analogue was found to adopt a monomeric structure $[(2,6\text{-Dipp}_2\text{C}_6\text{H}_3)\text{Hg}(\text{I})]$.¹⁰⁵ This was suggested to be a consequence of relativistic effects that reduce the dimerisation energy of the mercury species. Alternatively, halide-bridged dimers can be isolated as solvated lithium adducts $[(2,6\text{-Dipp}_2\text{C}_6\text{H}_3)\text{M}(\mu\text{-I})(\text{LiOEt}_2)]_2$ (M = Mn, Fe, Co) that possess a distorted cubane $\text{Li}_2\text{M}_2\text{I}_4$ core, afforded via the incomplete elimination of LiI .¹⁰³

Halide-bridged dimers can be used as precursors for the preparation of dinuclear M–M bonded complexes, via a two-electron reduction process to give $[(2,6\text{-Ar}_2\text{C}_6\text{H}_3)\text{M}]_2$ (M = metal; Ar = aryl) (**Scheme 1.5**).



Scheme 1.5 General synthesis of dinuclear M–M bonded complexes.

Specifically, chemical reduction of the halide compounds $[(2,6\text{-Dipp}_2\text{C}_6\text{H}_3)\text{M}(\mu\text{-X})]_2$ (M = Cr or Co, X = Cl; M = Fe, X = Br) with potassium graphite (KC_8) yields the dimeric metal(I) series $[(2,6\text{-Dipp}_2\text{C}_6\text{H}_3)\text{M}]_2$.^{104,106} Here, the chromium derivative features a short Cr–Cr quintuple bond [1.8351(4) Å], whereas the iron and cobalt species exhibit longer Fe–Fe [2.5151(9) Å] and Co–Co [2.8033(5) Å] distances, indicating their weaker M–M bonding (**Fig. 1.16**). Similarly, reduction of the Group 12 halides $[(2,6\text{-Dipp}_2\text{C}_6\text{H}_3)\text{M}(\text{I})]_n$ (M = Zn or Cd, $n = 2$; M = Hg, $n = 1$) with sodium (Zn), sodium hydride (Cd) or KC_8 (Hg) produces metal(I) dimers $[(2,6\text{-Dipp}_2\text{C}_6\text{H}_3)\text{M}]_2$ with near-linear C–M–M–C cores.¹⁰⁵

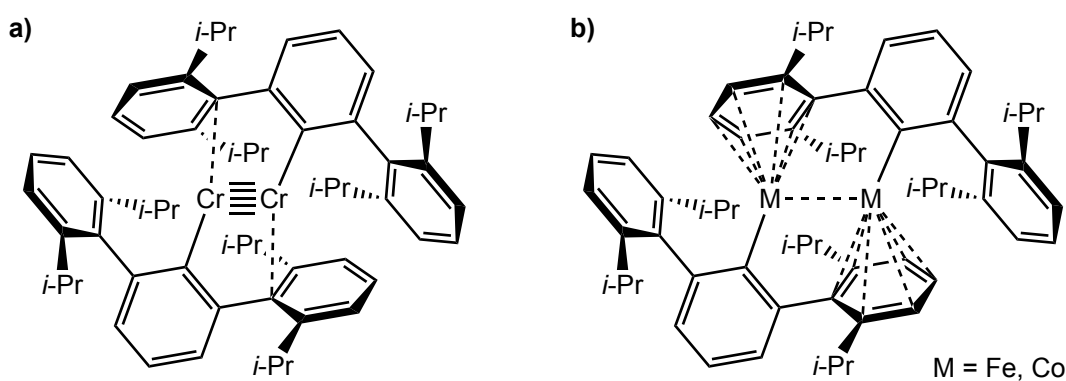


Fig. 1.16 Structures of the metal(I) dimers $[(2,6\text{-Dipp}_2\text{C}_6\text{H}_3)\text{M}]_2$ showing a) the short quintuple bond when M = Cr, and b) the longer bond when M = Fe or Co.^{104,106}

Homoleptic *m*-terphenyl complexes, on the other hand, prepared by reacting the lithium precursor with just one equivalent of metal halide (**Scheme 1.4**), generally adopt a monomeric, two-coordinate structure $(2,6\text{-Ar}_2\text{C}_6\text{H}_3)_2\text{M}$ (M = metal; Ar = aryl). For example, the transition metal diaryls $(2,6\text{-Mes}_2\text{C}_6\text{H}_3)_2\text{M}$ (M = Mn, Fe, Co) exhibit isomorphous geometries that are distorted from the idealised D_{2d} symmetry.¹⁰⁷ These complexes deviate from linearity, and present a range of C–M–C bond angles [162.8(1)–173.0(1)°]; this bending is possibly due to the formation of weak M⋯C contacts between the metal centre and the *ipso*-carbons of the ligand's flanking rings. Notably, this was the first example of a homoleptic, two-coordinate cobalt(II) diaryl to feature a Co–C σ -bond. Following this, an analogous series of transition metal diaryls $(2,6\text{-Dipp}_2\text{C}_6\text{H}_3)_2\text{M}$ (M = Mn, Fe, Co) was reported (**Fig. 1.17**), where the incorporation of the bulkier Dipp flanking groups caused increased bending of the C–M–C bond angles [159.34(6)–160.19(9)°].^{58,69,108} The linearity of two-coordinate metal complexes therefore varies with ligand architecture.

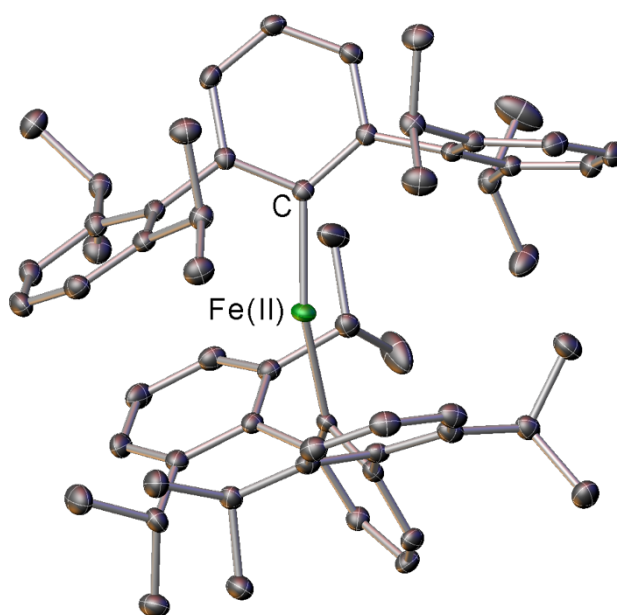


Fig. 1.17 Crystal structure of the homoleptic iron(II) diaryl $(2,6\text{-Dipp}_2\text{C}_6\text{H}_3)_2\text{Fe}$. Ellipsoids set at 45% probability and hydrogen atoms are omitted.¹⁰⁸

The d-orbital splitting pattern for two-coordinate transition metal complexes differs for systems of linear ($D_{\infty h}$) and nonlinear (C_{2v}) geometries.^{109–111} This model is based upon an idealised ML_2 molecule, considering only the local symmetry at the metal and its two directly bonded atoms. For strictly linear coordination ($D_{\infty h}$), the $3d_{z^2}$ orbitals sit at highest energy, the $3d_{xz}$ and $3d_{yz}$ orbitals fall below at intermediate energy, while the degenerate $3d_{x^2-y^2}$ and $3d_{xy}$ orbitals lie at lowest energy (**Fig. 1.18a**), assuming no complicating effects like π -bonding. Upon bending to a 90° angle, these orbitals split and shift in energy (**Fig. 1.18b**). Note that, in reality, the symmetry of the idealised ML_2 system may be lowered due to the complex nature of the bulky ligands employed, which can lead to further splitting of the energy states.¹⁰⁹ The d^1 – d^9 electron configurations of these two-coordinate complexes generally favour a high-spin arrangement. It is thus possible for a d^6 metal, like iron(II), to generate a large orbital angular momentum that could induce interesting single-molecule magnet behaviour.

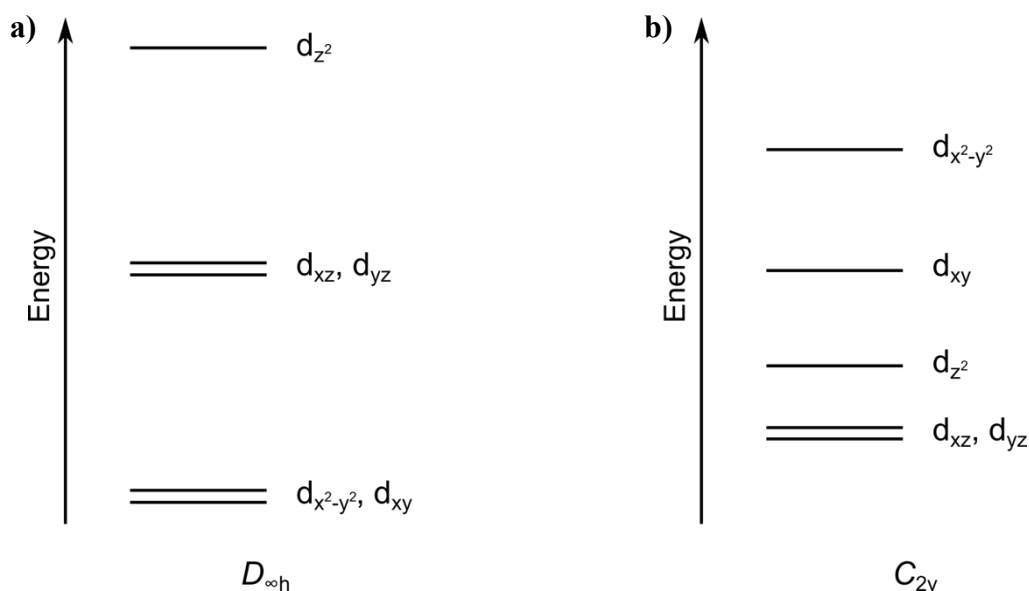
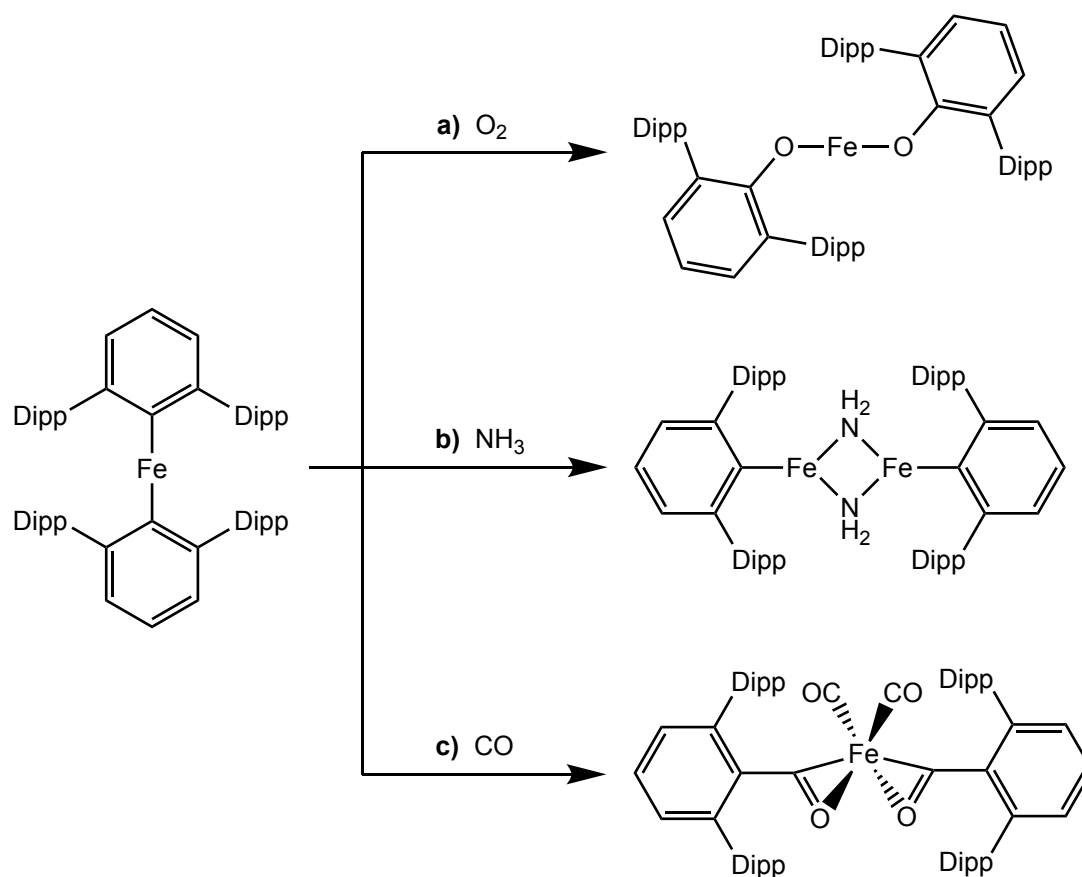


Fig. 1.18 Diagrams showing the d-orbital splitting for two-coordinate complexes with a) linear ($D_{\infty h}$) geometries, and b) nonlinear (C_{2v}) geometries.¹⁰⁹

1.2.8 Applications of *m*-Terphenyl Complexes

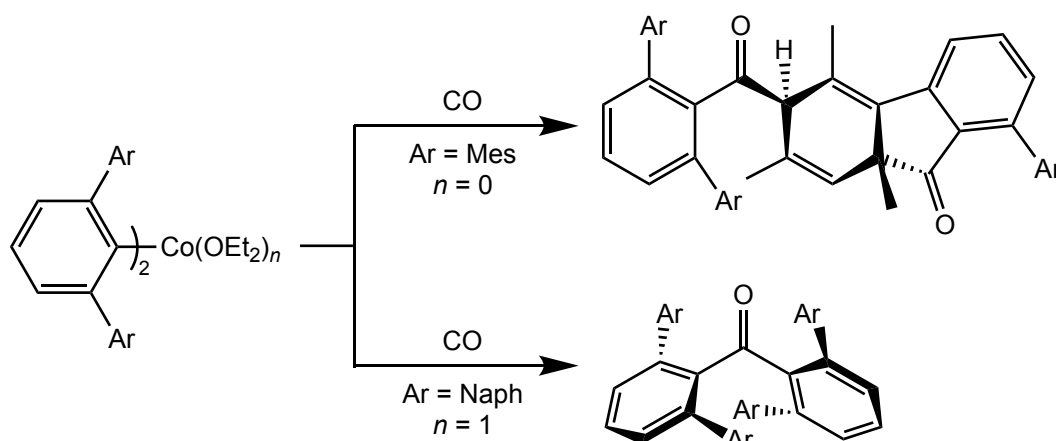
A range of applications for low-coordinate transition metal aryl complexes has been proposed, including as cross-coupling catalysts,^{112–114} as transmetallation reagents,¹¹⁵ as alkyne and olefin polymerisation catalysts,^{116–120} as dopants for quantum dot preparation,^{121–123} and for the preparation of nanoparticles with controlled morphologies.^{124–126} For the *m*-terphenyl complexes, particular interest has been focused on their small molecule reactivity and catalytic activity, as well as their unique magnetic properties that render them potential candidates for single-ion magnetism.

The small molecule reactivity of the *m*-terphenyl iron complex $(2,6\text{-Dipp}_2\text{C}_6\text{H}_3)_2\text{Fe}$, for instance, has been investigated towards dioxygen, ammonia and carbon monoxide. In the first scenario, the reaction with excess dry O_2 at $-100\text{ }^\circ\text{C}$ yields the linear iron(II) aryloxy $(2,6\text{-Dipp}_2\text{C}_6\text{H}_3\text{O})_2\text{Fe}$ via oxygen insertion into each of the Fe–C σ -bonds (**Scheme 1.6a**).¹⁰⁸ Here, the formation of an iron(III) species was not observed due to difficulty of oxidising the electron deficient iron(II) centre; this is a consequence of the highly electronegative ligands. In the second example, the addition of dry NH_3 affords the amido-bridged complex $[(2,6\text{-Dipp}_2\text{C}_6\text{H}_3)\text{Fe}(\mu\text{-NH}_2)]_2$, whose mechanism likely proceeds via the initial coordination of ammonia, followed by N–H bond cleavage and arene elimination of $2,6\text{-Dipp}_2\text{C}_6\text{H}_4$, with dimerisation of the final amido species (**Scheme 1.6b**).¹²⁷ In the third case, the reaction with dry CO produces an acyl-carbonyl complex $(\eta^2\text{-}\{2,6\text{-Dipp}_2\text{C}_6\text{H}_3\}\text{CO})_2\text{Fe}(\text{CO})_2$ via insertion of CO into each of the Fe–C σ -bonds and coordination of two CO molecules to the iron centre (**Scheme 1.6c**).¹⁰⁸ This six-coordinate species adopts an approximate octahedral geometry with an 18-electron configuration, and displays considerable Fe–CO backbonding.



Scheme 1.6 The small molecule reactivity of the *m*-terphenyl iron complex (2,6-Dipp₂C₆H₃)₂Fe towards a) dioxygen, b) ammonia, and c) carbon monoxide.^{108,127}

The reactivity of carbon monoxide towards the analogous *m*-terphenyl cobalt complex (2,6-Ar₂C₆H₃)₂Co(OEt₂)_{*n*} (Ar = Mes {*n* = 0}, Naph {*n* = 1}; Naph = 1-naphthyl) has also been studied, where variation of the flanking aryl groups affects the product formed.¹²⁸ Here, treatment of dry CO with the mesityl species (Ar = Mes) produces a keto-fluorenone featuring two stereogenic centres, whereas the naphthyl derivative (Ar = Naph) yields a rare example of a tetra *ortho*-substituted benzophenone (**Scheme 1.7**). These sterically-encumbered ketones both result from CO insertion, involving Co–C bond breaking and C–C bond forming processes with concomitant elimination of Co₂(CO)₈.



Scheme 1.7 The reactivity of the *m*-terphenyl cobalt diaryls $(2,6\text{-Ar}_2\text{C}_6\text{H}_3)_2\text{Co}(\text{OEt}_2)_n$ (Ar = Mes $\{n = 0\}$, Naph $\{n = 1\}$) towards carbon monoxide.¹²⁸

Another example is the reaction of the *m*-terphenyl iron complex $(2,6\text{-Mes}_2\text{C}_6\text{H}_3)_2\text{Fe}$ with the Zintl phase precursor K_4Ge_9 , in the presence of both ethylenediamine (en) and 2,2,2-crypt (4,7,13,16,21,24-hexaoxa-1,10-diazabicyclo[8.8.8]hexacosane) to produce $[\text{K}(2,2,2\text{-crypt})]_3[\text{Fe}@\text{Ge}_{10}] \cdot 2\text{en}$ featuring an endohedral Zintl ion $[\text{Fe}@\text{Ge}_{10}]^{3-}$. This ion exhibits a pentagonal prismatic 10-atom germanium cage with an encapsulated interstitial iron atom (**Fig. 1.19**), which is remarkable for a substituent-free Group 14 cluster.¹²⁹ It is formed via the reductive cleavage of the two Fe–C bonds, using the solvated electrons present in the ethylenediamine solution of K_4Ge_9 .

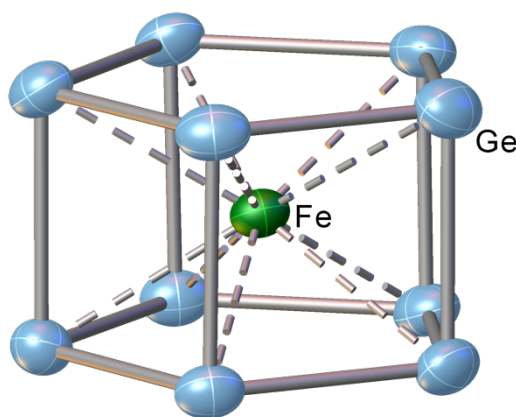
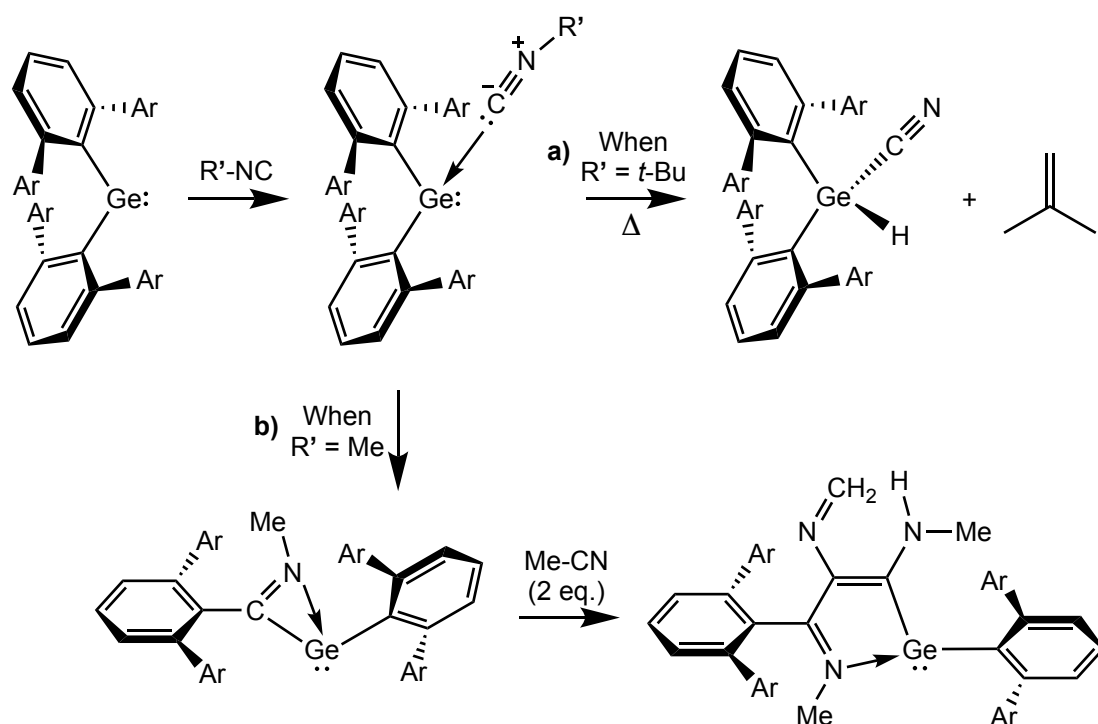


Fig. 1.19 Crystal structure of $[\text{Fe}@\text{Ge}_{10}]^{3-}$. Ellipsoids set at 40% probability.¹²⁹

The small molecule reactivity of an *m*-terphenyl germanium diaryl $(2,6\text{-Mes}_2\text{C}_6\text{H}_3)_2\text{Ge}$ towards functionalised isocyanides, $\text{R}'\text{-NC}$ ($\text{R}' = t\text{-Bu, Me}$), has also been investigated, where variation of the R' substituent affects the product formed. In the first scenario, the addition of *t*-butyl isocyanide ($\text{R}' = t\text{-Bu}$) initially yields a Lewis adduct product $[(2,6\text{-Mes}_2\text{C}_6\text{H}_3)_2\text{Ge}(\text{CN-}t\text{-Bu})]$ via isocyanide coordination; upon mild heating, this undergoes C–H bond activation to form a germanium(IV) hydride/cyanide species $[(2,6\text{-Mes}_2\text{C}_6\text{H}_3)_2\text{Ge}(\text{H})(\text{CN})]$, with the elimination of isobutene via *t*-Bu–N bond cleavage (**Scheme 1.8a**).¹³⁰ In the second case, the use of methyl isocyanide ($\text{R}' = \text{Me}$) yields a similar coordination complex $[(2,6\text{-Mes}_2\text{C}_6\text{H}_3)_2\text{Ge}(\text{CN-Me})]$, which isomerises to give the η^2 -bonded species $[(2,6\text{-Mes}_2\text{C}_6\text{H}_3\text{-}\{\text{Me-N}\}\text{C})\text{Ge}(2,6\text{-Mes}_2\text{C}_6\text{H}_3)]$ via migratory insertion of the MeCN carbon into a Ge–C bond. Here, sequential isocyanide insertions result in the formation of an azagermacyclopentadienyl product $[(\text{MeN}\{2,6\text{-Mes}_2\text{C}_6\text{H}_3\}\text{C}\{\text{H}_2\text{CN}\}\text{C}\{\text{MeHN}\}\text{C})\text{Ge}(2,6\text{-Mes}_2\text{C}_6\text{H}_3)]$ (**Scheme 1.8b**).¹³¹



Scheme 1.8 The reactivity of the *m*-terphenyl germanium complex $(2,6\text{-Ar}_2\text{C}_6\text{H}_3)_2\text{Ge}$ ($\text{Ar} = \text{Mes}$) with either a) *t*-butyl isocyanide, or b) methyl isocyanide.^{130–132}

The magnetic properties of the *m*-terphenyl complexes are of further interest for the development of new single-ion magnets with record-breaking relaxation barriers, U_{eff} , and blocking temperatures, T_{B} . This results from the extensive orbital contributions in linear, two-coordinate systems that yield large effective magnetic moments, μ_{eff} .¹³³ For example, above 50 K, the high-spin ($S = 2$) iron(II) diaryl (2,6-Dipp₂C₆H₃)₂Fe displays a greater magnetic moment ($\chi_{\text{M}}T = 4.5 \text{ emu K mol}^{-1}$, $\mu_{\text{eff}} = 6.0 \mu_{\text{B}}$) than its spin-only value ($\chi_{\text{M}}T = 3.0 \text{ emu K mol}^{-1}$, $\mu_{\text{eff}} = 4.9 \mu_{\text{B}}$); this was attributed to the degeneracy of its 3d_{x²-y²} and 3d_{xy} orbitals (**Fig. 1.18a**) that generates unquenched orbital angular momentum.¹³⁴ However, magnetic quenching can be induced by bending the geometry of a two-coordinate system away from linearity. This has been shown for the amido *m*-terphenyl iron(II) species (2,6-Ar₂C₆H₃-{H}N)₂Fe (Ar = Dipp, Tripp, Mes), whose linear Dipp and Tripp compounds [N–Fe–N = 180(0)°] give higher magnetic moments ($\chi_{\text{M}}T = 3.8$ and $3.5 \text{ emu K mol}^{-1}$, $\mu_{\text{eff}} = 5.5$ and $5.3 \mu_{\text{B}}$, for Dipp and Tripp respectively) than the more bent Mes derivative [N–Fe–N = 140.9(2)°] ($\chi_{\text{M}}T = 2.9 \text{ emu K mol}^{-1}$, $\mu_{\text{eff}} = 4.8 \mu_{\text{B}}$).^{135–137} The complexes also exhibited lower magnetic saturation values ($M_{\text{sat}} = 2.74$, 2.14 and $1.93 \mu_{\text{B}}$ for Dipp, Tripp and Mes respectively) than expected for a spin-only ($S = 2$) system ($M_{\text{sat}} = g \cdot S = 4 \mu_{\text{B}}$)²⁹ due to their random orientations and high anisotropies.¹³⁵ Here, magnetic relaxation barriers, U_{eff} , could only be measured for the Dipp (156.8 K) and Tripp (149.6 K) species.¹³⁵ A diminished magnetic moment has similarly been reported for a bent *m*-terphenyl cobalt diaryl (2,6-Dipp₂C₆H₃)₂Co.⁵⁸ Alternatively, magnetic quenching can occur due to the formation of metal–ligand secondary contacts with the ligand’s flanking groups. For instance, in the iron complex (Mes*)₂Fe, the low magnetic moment ($\mu_{\text{eff}} = 4.8\text{--}5.2 \mu_{\text{B}}$) has been ascribed to the presence of Fe⋯H anagostic interactions [2.18–2.23 Å] with the *ortho*-substituted *t*-Bu groups of the mesityl ligands.^{70,138}

1.3 Research Objectives

This research project aims to expand the library of low-coordinate *m*-terphenyl metal complexes suitable for electronic investigation. It describes the design and synthesis of a new series of *para*-substituted *m*-terphenyl ligands featuring electron-donating and -withdrawing groups, whose electronic strengths are quantified by literature Hammett constants, σ_{para} .¹³⁹ In all cases, the same flanking aryl groups are employed to minimise structural variations due to steric effects. The influence of the ligand architecture is then studied with respect to the structural, electronic and magnetic properties of the resulting metal complexes.

Firstly, the synthesis of the *para*-substituted *m*-terphenyl iodide ligand precursors is described, following routes adapted from those in *Chapter 1.2.6*. Secondly, the iodide compounds are lithiated to afford a series of *para*-substituted *m*-terphenyl lithium complexes. From these, the two-coordinate metal diaryl complexes are synthesised via salt metathesis reactions, similar to those in *Chapter 1.2.7*, featuring zinc, cadmium, mercury and iron. All of the metal complexes are then characterised by crystallographic and NMR spectroscopic methods, notably ⁷Li, ¹¹³Cd and ¹⁹⁹Hg NMR to study the electronic properties at the metal centre. For the iron complexes, additional electronic analysis is performed by IR, UV/Vis and X-ray photoelectron spectroscopies, as well as cyclic voltammetry. Furthermore, the magnetic properties of the iron systems are examined by direct current (dc) and alternating current (ac) susceptibility measurements using a SQUID magnetometer. Finally, the small molecule reactivity of the two-coordinate iron complexes is probed, with attempts to bind an infrared-active handle to the metal centre through which the electronics could be measured via analysis of the shifting vibrational wavenumbers.

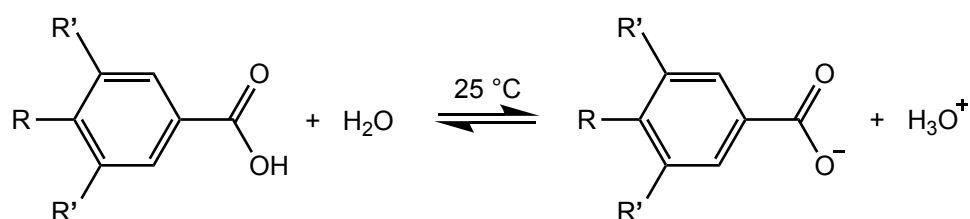
1.4 Analytical Methods

1.4.1 Hammett Constants

The electron-donating and -withdrawing strengths of the *m*-terphenyl *para*-substituents can be quantified using literature Hammett constants, σ_{para} , in order to correlate their electronic effects with any observed experimental trends.¹³⁹ The Hammett constants, σ , for *para*- and *meta*-substituents, R, are derived from the reversible deprotonation of functionalised benzoic acids in water at 25 °C (**Scheme 1.9**), by relating the measured equilibrium constants for the substituted derivatives, K_R , with those of the unsubstituted (R = H) derivatives, K_H , using the Hammett linear free-energy equation:¹⁴⁰

$$\log(K_R/K_H) = \sigma \cdot \rho$$

In this equation, the reaction constant, ρ , measures the sensitivity of the reaction to the electronic substituent effects. Relative to hydrogen, large negative σ -values correspond to strong electron-donating power, while large positive σ -values correspond to strong electron-withdrawing power.



Scheme 1.9 Equilibrium for the deprotonation of functionalised benzoic acids in water at 25 °C showing the *para*- and *meta*-substituents, R and R'.

Chapter II

General Experimental

2.1 General Experimental Techniques

2.1.1 Manipulation of Air-Sensitive Compounds

The compounds synthesised are renowned for their highly air- and moisture-sensitive nature and thus require handling under strictly anaerobic and anhydrous conditions through the use of standard Schlenk line and glove box techniques. The Schlenk line apparatus comprises a dual manifold of thick-walled Pyrex glass, where one line is attached to an inert gas cylinder (usually argon at *ca.* 0.5 bar) and the other to a dynamic vacuum (*ca.* 10^{-4} mbar), both of which are linked via four two-way stopcocks. The vacuum was achieved using an Edwards RV5 dual-stage rotary vane mechanical vacuum pump with an Edwards Pirani10 thermal conductivity vacuum gauge. A liquid dinitrogen cooled trap was also employed to prevent volatiles from damaging the pump. The line was connected via neoprene tubing to reaction vessels, such as thick-walled glass Schlenk tubes (with ground glass joints lubricated by Dow Corning high-vacuum silicone grease) or Young's tap ampoules. All glassware was oven-heated overnight (*ca.* 80–100 °C), assembled, attached to the vacuum line, and flame-dried with a Bunsen burner until a vacuum of *ca.* 10^{-3} mbar was maintained. After cooling, the vessels were exposed to a minimum of three refill/evacuation cycles then sealed under inert gas. Liquids and solutions were transferred using stainless steel or Teflon cannulae with rubber Suba-Seal septa. A stainless steel MBraun UNIlab glove box, fitted with a strengthened viewing panel and neoprene gloves, was used for the storage and manipulation of air- and moisture-sensitive compounds and NMR solvents. An inert dinitrogen atmosphere was maintained inside the glove box via constant circulation of the gas through a copper-based catalyst to keep O₂ and H₂O levels below 0.1 ppm. Equipment was admitted into the glove box through an ante-chamber purged using four refill/evacuation cycles.

2.2 Analytical Measurements

2.2.1 X-ray Crystallography

Air-sensitive crystallographic samples were quickly transferred under dinitrogen flow from a Schlenk tube to a microscope slide and coated in Fomblin PFPE (YR-1800 perfluoropolyether oil). A suitable crystal was mounted on a MiTeGen MicroMount™ and cooled under a dinitrogen cryostream using an open flow cryostat.¹⁴¹ X-ray diffraction data was measured on one of three Agilent SuperNova diffractometers (either using graphite-monochromated Mo-K α radiation, $\lambda = 0.71073 \text{ \AA}$, ω scans; or using mirror-monochromated Cu-K α radiation, $\lambda = 1.54184 \text{ \AA}$, ω scans), equipped with either an Atlas, AtlasS2 or TitanS2 CCD area detector. Alternatively, X-ray diffraction data was measured on a Rigaku Oxford Diffraction XtalLab Pro diffractometer equipped with a copper MM07 rotating anode X-ray source and a Pilatus 200K-A CCD area detector. Cell parameters were refined for each data set from the observed positions of all strong reflections, and absorption corrections were applied via a Gaussian numerical method with beam profile correction (CrysAlisPro).¹⁴² The structures were solved by direct or iterative methods and all non-hydrogen atoms were refined by full-matrix least-squares on all unique F^2 values with anisotropic displacement parameters, except for certain disordered atoms that could not be refined anisotropically so were instead refined isotropically, as discussed in their .cif files. Hydrogen atoms were refined using constrained geometries and riding thermal parameters. In some instances, Platon SQUEEZE¹⁴³ was applied to disordered solvent molecules that could not be modelled sensibly. Software used includes OLEX2¹⁴⁴ for molecular graphics, SHELXT¹⁴⁵ for structure solution and SHELXL¹⁴⁶ for structure refinement. All structural images were generated in OLEX2.¹⁴⁴ CIF files were checked using CheckCIF¹⁴⁷ and by Dr William Lewis at the University of Nottingham.

2.2.2 NMR Spectroscopy

Air-sensitive NMR samples were prepared in the glove box under dinitrogen and sealed inside Young's tap modified borosilicate glass NMR tubes. NMR spectra were recorded on either Bruker DPX300, DPX400, AV400, AV(III)400, AV(III)500 spectrometers. Chemical shifts are quoted in ppm relative to TMS (for ^1H , $^{13}\text{C}\{^1\text{H}\}$ and $^{29}\text{Si}\{^1\text{H}\}$ NMR), to CFCl_3 (for $^{19}\text{F}\{^1\text{H}\}$ NMR), to a 1.0 M $\text{LiCl}/\text{D}_2\text{O}$ solution (for $^7\text{Li}\{^1\text{H}\}$ NMR), and to CdMe_2 and HgMe_2 (for ^{113}Cd and ^{199}Hg NMR, respectively) using 0.1 M $\text{Cd}(\text{ClO}_4)_2/\text{D}_2\text{O}$ and 1.0 M $\text{Hg}(\text{ClO}_4)_2/\text{D}_2\text{O}$ solutions as internal calibrants. DOSY experiments were performed on a Bruker AV(III)400HD spectrometer using the PFGSE (Pulsed-Field Gradient Spin-Echo) NMR Diffusion method. The variation in intensity (integral) of a selected ^1H NMR signal (I) is related to the gradient strength (g) by the equation: $\ln(I/I_0) = -(\gamma g \delta)^2 D [\Delta - (\delta/3)]$, where D is the diffusion coefficient, γ is the gyromagnetic ratio of the proton (4257.7 Hz G^{-1}), δ (small delta) is the length of the gradient pulse, and Δ (big delta) is the delay between the midpoints of the gradients. For all data recorded, experimental values of $\delta = 2 \text{ ms}$ and $\Delta = 200 \text{ ms}$ were used, and the gradient was varied across 32 spectra (following a `dstebpgp3s` sequence). Data analysis was carried out with TopSpin¹⁴⁸ software by plotting straight-line graphs of $\ln(I)$ versus g^2 to deduce the diffusion coefficients, D . Hydrodynamic radii, r_s , were then calculated, assuming a spherical system, using the Stokes-Einstein equation: $r_s = (kT/6\pi\eta D)$, where k is the Boltzmann constant, T is the absolute temperature, η is the solvent viscosity, and D is the diffusion coefficient. Two-dimensional ^7Li - ^1H HOESY experiments were performed by Huw Williams on a Bruker AV(III)600 spectrometer using echo and anti-echo quadrature detection running a 64 point T1 acquisition and 64 scans with a recycling delay of 3 s.^{149,150}

2.2.3 IR Absorption Spectroscopy

Air-sensitive IR samples were measured as solutions inside a sealed cell fitted with KBr windows. The solutions were prepared using dry, degassed solvents under an inert atmosphere, either within the glove box under dinitrogen, or on the Schlenk line by direct transferal via syringe into a cell pre-purged with argon. IR spectra were recorded on a Bruker Alpha FTIR instrument in the region of 500–4000 cm^{-1} , then the solvent background was subtracted with the OPUS¹⁵¹ software. Air-stable samples were recorded on the same instrument using either a ‘Platinum’ ATR attachment for solid samples, or two KBr discs for liquids.

2.2.4 Mass Spectrometry

Air-sensitive mass spectrometry compounds were prepared within the glove box under dinitrogen, then sealed inside glass capillary tubes under argon on the Schlenk line. In-house spectra were recorded by Dr Mick Cooper at the University of Nottingham on a JEOL AccuTOF GCX mass spectrometer via direct probe FD or EI methods using either polyethylene glycol or perfluorotributylamine as mass calibrants, respectively. Alternatively, samples were measured by the EPSRC National Mass Spectrometry Facility at Swansea University on a Xevo G2-S ASAP mass spectrometer via an atmospheric solids analysis probe (positive mode). Air-stable spectra were recorded at the University of Nottingham on a self-service Bruker microTOF mass spectrometer via the ESI method, using sodium formate as a mass calibrant.

2.2.5 Elemental Analysis

Elemental analysis (CHN) samples were measured by either Tong Liu at the University of Nottingham, or by Mr Stephen Boyer at the London Metropolitan University.

2.2.6 UV/Vis Absorption Spectroscopy

Air-sensitive UV/Vis samples were prepared within the glove box under dinitrogen as solutions of known concentration inside a Young's tap modified 10 mm quartz cell. After initially measuring the solvent background, the UV/Vis spectra were recorded on a Perkin Elmer Lambda 16 spectrometer over a wavelength range of 290–900 nm, with a data interval of 1 nm.

2.2.7 Cyclic Voltammetry

Air-sensitive CV samples were prepared within the glove box under dinitrogen as 1.0 mM solutions in THF containing 0.5 M [ⁿBu₄N][BF₄] electrolyte. The solutions were sealed inside a single-compartment electrochemical cell that functioned as a three-electrode system comprising of glassy carbon working and counter electrodes, alongside a Hg/Hg₂Cl₂ reference electrode (SCE) that was chemically isolated from the sample solution via a bridge tube containing electrolyte solution and fitted with a porous Vycor frit. CV experiments were carried out in conjunction with Dr E. Stephen Davies at the University of Nottingham using an Autolab PGSTAT320N potentiostat. Redox potentials are referenced to the ferrocenium-ferrocene (Fc⁺/Fc) couple by an internal calibration.

2.2.8 Electron Paramagnetic Resonance Spectroscopy

Air-sensitive EPR samples were prepared on the Schlenk line under argon by direct transferal via syringe into a Young's tap modified Wilmad quartz EPR tube. Continuous wave X band EPR spectra were recorded on a Bruker EMX spectrometer in conjunction with Dr E. Stephen Davies at the University of Nottingham. EPR spectra simulations were performed using the WINEPR SimFonia¹⁵² software package.

2.2.9 X-ray Photoelectron Spectroscopy

Air-sensitive XPS samples were prepared within the glove box under dinitrogen as a lightly-ground crystalline solid placed in a thin, full-coverage layer on top of a stainless steel Kratos sample stub, using double-sided tape to stick the sample in position. The stub was sealed inside a Kratos air-sensitive transport device, which itself was sealed inside an air-tight plastic box, then was carried to the nearby Nanoscale and Microscale Research Centre (nmRC) for XPS analysis by Dr Emily Smith at the University of Nottingham. Spectra were recorded on a Kratos Axis Ultra DLD spectrometer employing a focused, monochromated Al-K α source ($h\nu = 1486.6$ eV), hybrid (magnetic/electrostatic) optics, a hemispherical analyser, plus a triple channel plate and delay line detector (DLD). X-ray incident and collection angles of *ca.* 30° and 0° were used respectively (relative to the surface normal). X-ray gun power was set to 120 W. All spectra were measured using an entrance aperture of 300 x 700 μm with a pass energy of 80 eV for wide scans and 20 eV for high-resolution scans. As quoted by the manufacturer (Kratos), the absolute error in the binding energies is ± 0.1 eV. Charge neutralisation was applied at 2.0 A filament current and 3.6 V balance plate voltage. Sample stubs were earthed via the instrument stage to the UHV chamber. The Kratos air-sensitive transport device was inserted into the XPS spectrometer then the sample was introduced into the preparation chamber, where initial pumping down to a pressure of *ca.* 10^{-7} mbar was performed. The sample was next transferred to the main analytical vacuum chamber where the pressure was lowered to *ca.* 10^{-9} mbar. Spectra were acquired at room temperature, with collection times of 20 mins for wide-scans and 20, 10, 5, 5, 3 and 2 mins for high-resolution scans of Fe, C, Si, F, O and I, respectively. Energy step sizes used were 1.0 eV for wide-scans and 0.1 eV for high-resolution scans. The resulting XPS data was processed using the CasaXPS¹⁵³ software package.

2.2.10 SQUID Magnetometry

Air-sensitive SQUID samples were prepared within the glove box under dinitrogen by grinding a crystalline sample into a powder, then weighing a known amount of the solid into an NMR tube. On top of this, a known amount of eicosane was added. The NMR tube was inserted into an air-tight adapter and cycled onto the Schlenk line. Under argon, the NMR tube was gently heated to melt the eicosane and immobilise the sample. Once cooled, the NMR tube was flame-sealed under vacuum. The sample was posted to Dr Maria Gimenez at the University of Santiago de Compostela, Spain, for magnetic analysis.

2.2.11 Magnetic Circular Dichroism Spectroscopy

The air-sensitive MCD sample was prepared within the glove box under dinitrogen as a 3.2 mM solution in dichloromethane containing 0.4 M [ⁿBu₄N][BF₄]. This solution was injected via syringe into a cell constructed of two quartz discs separated by a rubber O-ring with a path length of *ca.* 1 mm. The cell was removed from the glove box and immediately frozen in liquid nitrogen. MCD spectra were recorded on an instrument employing a JASCO J-810 spectropolarimeter adapted to incorporate an Oxford Instruments Spectromag SM4000 magnetocryostat. Measurements were collected at magnetic fields up to 7 T and temperatures down to 5 K. To correct for circular dichroism contributions owing to strain effects, the spectra recorded at +B fields were subtracted from the spectra recorded at -B fields.

2.3 Preparation of Solvents and Reagents

2.3.1 Solvent Preparation

All solvents for air-sensitive synthesis were pre-dried, either by passing through a drying column containing 4 Å molecular sieves (*s*-hexane), or alternatively by refluxing over molten potassium (toluene and benzene), sodium/benzophenone (THF), calcium hydride (dichloromethane), or a sodium-potassium alloy (diethyl ether) for a minimum of three days. All solvents were stored in ampoules over a potassium mirror (*s*-hexane, toluene and benzene) or activated 4 Å molecular sieves (THF and dichloromethane) and were degassed *in vacuo* prior to use. Benzene-*d*₆ was dried over molten potassium in a sealed ampoule at 90 °C for five days, before vacuum transfer to an ampoule containing a potassium mirror with degassing via three freeze-pump-thaw cycles.

2.3.2 Reagent Preparation

Solid reagents were dried *in vacuo* and liquid reagents were dried over 4 Å molecular sieves, both of which were stored in the glove box before use. The transition metal halide adducts FeCl₂(THF)_{1.5} and CoBr₂(DME) (where DME = 1,2-dimethoxyethane) were prepared following minor modification of the literature methods.^{154,155} Nitric oxide gas was kindly provided by Mr Neil Barnes and, after three refill/evacuation cycles, was added directly to the reaction ampoule without additional purification. All other reagents and solvents were acquired commercially and used as received unless otherwise stated.

Chapter III

Ligand Synthesis

3.1 Introduction

The development of novel sterically bulky ligand systems has become a central research theme for the stabilisation of low-coordinate metal complexes whose sophisticated structural, electronic and magnetic properties continue to push the frontiers of organometallic chemistry. One important example is the *m*-terphenyl ligand, which has been well established in the literature for enabling the isolation of low-coordinate main group and transition metal complexes.^{71,101,102,107,156,157} Although a plethora of *m*-terphenyl frameworks has been designed, studies have largely been structurally focused, aimed at investigating the effects of steric bulk on the geometries, bonding modes, and reactivities of the resulting compounds.^{80,83,84,86,128,158–163} For instance, the crystallographic structures for a series of *m*-terphenyl lithium complexes can be varied depending on the steric constraints imposed by the flanking *ortho*-aryl substituents; via increasing their steric bulk, the aggregation state of $2,6\text{-Ar}_2\text{C}_6\text{H}_3\text{Li}$ shifts from a dimer,⁹⁷ to a more crowded dimer,⁹⁸ to a monomer stabilised by a coordinated benzene molecule,⁹⁸ for Ar = Mes, Dipp and Tripp respectively (**Fig. 3.1**).^{101,102}

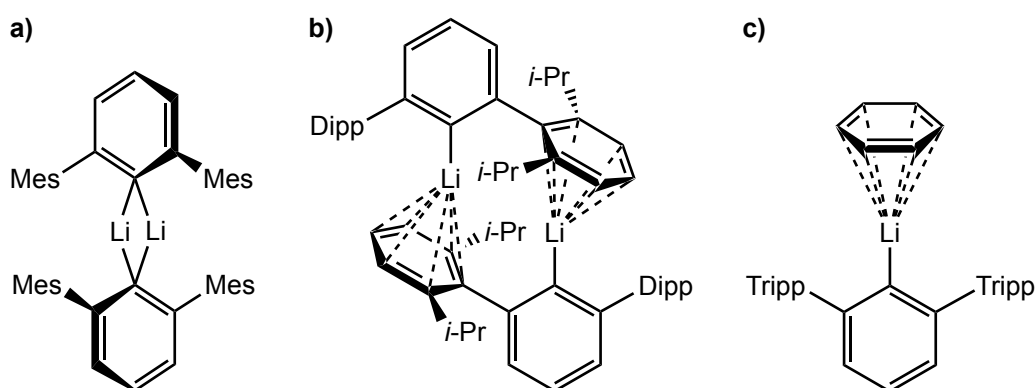


Fig. 3.1 Solid-state structures of a) the $[2,6\text{-Mes}_2\text{C}_6\text{H}_3\text{Li}]_2$ dimer, b) the more crowded $[2,6\text{-Dipp}_2\text{C}_6\text{H}_3\text{Li}]_2$ dimer, and c) the benzene-stabilised $[2,6\text{-Tripp}_2\text{C}_6\text{H}_3\text{Li}(\text{C}_6\text{H}_6)]$ monomer.^{97,98,101,102}

However, comparatively less work has been reported on the electronic nature of such low-coordinate *m*-terphenyl systems, with studies limited mainly to a handful of main group complexes.^{85,90,92–94} Moreover, of the few electronically-substituted *m*-terphenyl ligands described in the literature, none have been applied to the transition metals, except for chromium in the quintuply-bonded Cr–Cr dimer [(2,6-Dipp₂-4-R-C₆H₂)Cr]₂ (R = H, SiMe₃, OMe, F).⁸⁹ Even their lithium precursors, although structurally characterised, have not yet been studied from an electronic viewpoint. Thus, it is the objective of this research to develop a toolbox of novel *m*-terphenyl ligands featuring *para*-substituents, R, of varying electron-donating and -withdrawing strengths, in order to investigate the effects of substitution upon their metal complexes (**Fig. 3.2**).

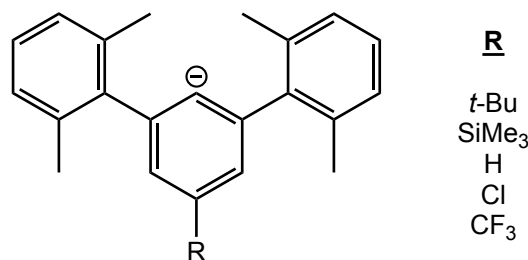


Fig. 3.2 General structure of the *para*-substituted *m*-terphenyl ligands discussed within this body of research.

Herein, a series of *para*-substituted *m*-terphenyl iodide ligand precursors and their lithium complexes are discussed, with structural and electronic elucidation provided through crystallographic and NMR chemical shift analyses. Specifically, ⁷Li NMR is employed to assess the electronics directly at the metal centre. Most importantly, this lays the groundwork for the subsequent synthesis of their transition metal complexes, with the eventual aim to determine the ideal electronic environment for optimised reactivity and single-molecule magnet behaviour.

3.2 Discussion

3.2.1 *m*-Terphenyl Iodides

3.2.1.1 Synthesis

A series of *para*-functionalised *m*-terphenyl iodide ligand precursors **3.2** – **3.8** has been synthesised, featuring a range of electron-donating and -withdrawing groups (Fig. 3.3). These are aimed at investigating the significance of *para*-substitution on the bonding, geometry, electronics and magnetism of their resulting metal complexes. Compounds **3.2**, **3.3** and **3.5** – **3.8** are novel and, until now, have not been previously reported.¹⁶⁴

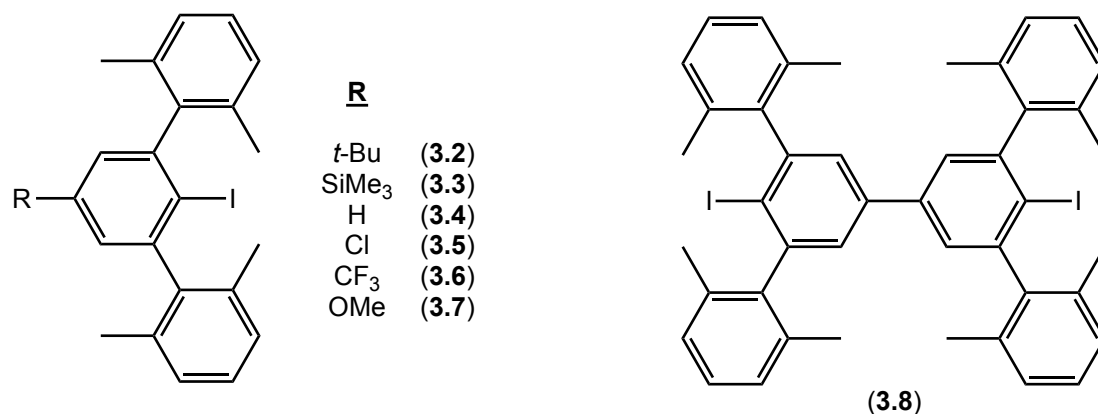
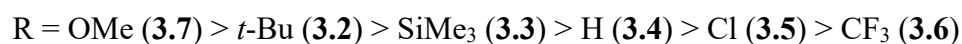


Fig. 3.3 The reported series of *para*-substituted *m*-terphenyl iodides, R-Ar-I, featuring R = *t*-Bu (**3.2**), SiMe₃ (**3.3**), H (**3.4**), Cl (**3.5**), CF₃ (**3.6**) and OMe (**3.7**), along with the double *m*-terphenyl iodide, I-Ar-Ar-I (**3.8**), where Ar = 2,6-(2,6-Xyl)₂C₆H₂.

The general structure of the *m*-terphenyl unit used in this research, R-Ar-I, was chosen such that only the *para*-substituent, R, would vary across the series, while the core aromatic framework, Ar-I, would remain unaltered. Thus, it was necessary to select the most ideal flanking aryl group that could be incorporated consistently in all compounds. For this, the 2,6-Xyl group (2,6-Xyl = 2,6-Me₂C₆H₃) was employed due to its ability to yield near-linear complexes with a high tendency to crystallise. Furthermore, metal complexes of the unsubstituted (R = H) *m*-terphenyl ligand with the 2,6-Xyl group have already been studied, allowing their comparison with the results discussed hereafter.⁸¹

The substituents, R, were incorporated at the *para*-position of the central aryl ring; this location provides a balance between closeness to the metal centre such that electronic effects can be transferred through the conjugated aromatic network, while minimising steric effects by ensuring the *para*-substituent is directed away from the coordination sphere. Moreover, the symmetrical nature of the *para*-position aids with the synthesis, availability of precursors, and simplifies the analysis of their NMR spectra. A total of six different *para*-substituents, R, have been studied, with varying electronic strengths ranging from electron-donating to electron-withdrawing in the following order:



These electronic strengths can be quantified using literature Hammett constants σ_{para} , where, relative to a proton, large negative σ_{para} values correspond to strong electron-donating power and large positive σ_{para} values indicate strong electron-withdrawing power. Hammett constants for the *para*-substituents discussed in this research are listed in **Table 3.1** below; these prove to be a valuable tool for identifying trends in the electronic properties from the experimental measurements.¹³⁹ For a more detailed discussion of Hammett constants, refer to *Chapter 1.4.1*.

Table 3.1 Hammett constants, σ_{para} , for the *para*-substituents discussed hereafter.¹³⁹

R group	Hammett constant, σ_{para}
OMe	-0.27
<i>t</i> -Bu	-0.20
SiMe ₃	-0.07
H	0.00
Cl	0.23
CF ₃	0.54

These *para*-substituents control electron density either by inductive effects, mesomeric effects, or through a combination of both. For example, inductive effects are observed in the electron-rich *t*-Bu and SiMe₃ groups where electron density is donated through a σ -bond to the ligand, and also in the electron-deficient CF₃ group where electron density is withdrawn. In contrast, mesomeric effects occur via π -bonding for substituents with p-orbitals available to conjugate into the delocalised aromatic system by resonance. For this reason, despite the inductive withdrawal associated with the electronegative oxygen atom, the OMe group becomes strongly electron-donating. The halogen substituents demonstrate a similar balance between inductive withdrawal and mesomeric donation; at the extremes, fluorine ($\sigma_{para} = 0.06$) and iodide ($\sigma_{para} = 0.18$) weakly withdraw electron density, whereas chlorine and bromine (both $\sigma_{para} = 0.23$) each exhibit comparatively stronger withdrawal strengths.¹³⁹ Hence, of the halogens, the optimal *para*-substituent for this research was the Cl group. Therefore, a total of six *para*-substituents were investigated, of which five (**3.2** – **3.6**) were successfully carried forwards for metal complex synthesis.

The final double *m*-terphenyl iodide ligand precursor, I-Ar-Ar-I, **3.8**, features an identical *m*-terphenyl unit at its *para*-position, presenting the possibility to form polymetallic complexes by attaching a metal at either end of this ligand (**Fig. 3.4**). Since the monomeric analogues exhibit single-molecule magnet behaviour by themselves, linking these units together could create single-chain magnets with a higher overall magnetic anisotropy, assuming that their spins align uniaxially along the chain. Hence, a synthetic route towards this compound was also explored.

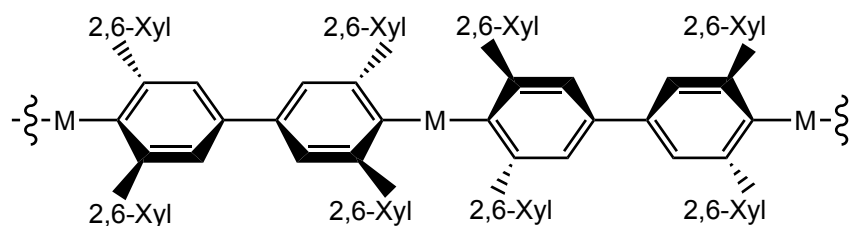
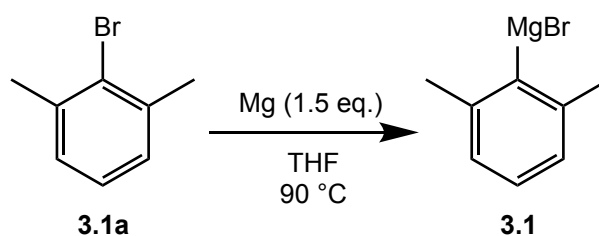


Fig. 3.4 Proposed polymetallic complexes derived from the double *m*-terphenyl iodide ligand, I-Ar-Ar-I, **3.8**, where M is a transition metal.

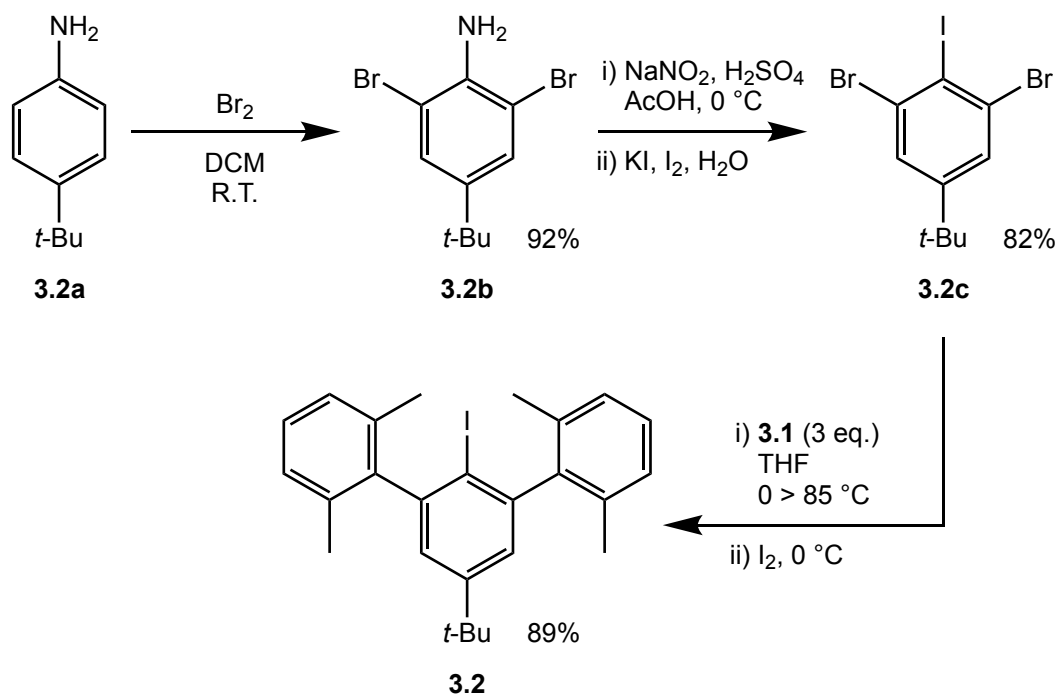
The design of all the *para*-substituted *m*-terphenyl iodides followed a two-step process; firstly, the *para*-functionalised core was synthesised then, secondly, the 2,6-Xyl flanking groups were attached. Here, the 2,6-Xyl groups were prepared via a reaction between 2,6-Xyl bromide (**3.1a**) and metallic magnesium, involving an oxidative insertion of the magnesium into the carbon-halogen bond (**Scheme 3.1**). The resultant product **3.1** was isolated, then added directly to subsequent reactions without purification or characterisation.



Scheme 3.1 Synthesis of the 2,6-Xyl flanking group Grignard reagent, **3.1**.

However, before coupling this flanking group to the *para*-functionalised ligand core, the appropriate *para*-substituted central aryl precursor had to be synthesised. To prepare compounds **3.2** – **3.8**, different synthetic routes were employed, some of which were adapted from previously reported literature methods.

The *t*-butyl *m*-terphenyl iodide, **3.2**, was synthesised using a multi-step process (Scheme 3.2). Firstly, the commercially available 4-*t*-butylaniline, **3.2a**, was brominated via an electrophilic aromatic substitution reaction that occurs at the *ortho*-positions due to the activating effect of the amine group.¹⁶⁵ The product, **3.2b**, was then converted to an iodide, **3.2c**, using a Sandmeyer reaction.¹⁶⁶ This involved the initial reaction of sodium nitrite with sulfuric acid to generate a NO^+ cation, which was then attacked by the amine to form an aryl diazonium salt.¹⁶⁷ Importantly, to prevent decomposition of this unstable salt via the potentially explosive loss of N_2 , low temperatures of $0\text{ }^\circ\text{C}$ were required. The diazonium salt was finally displaced by potassium iodide in a nucleophilic aromatic substitution to give **3.2c**. All compounds were purified by flash column chromatography through a silica plug and all steps were high yielding ($> 82\%$).

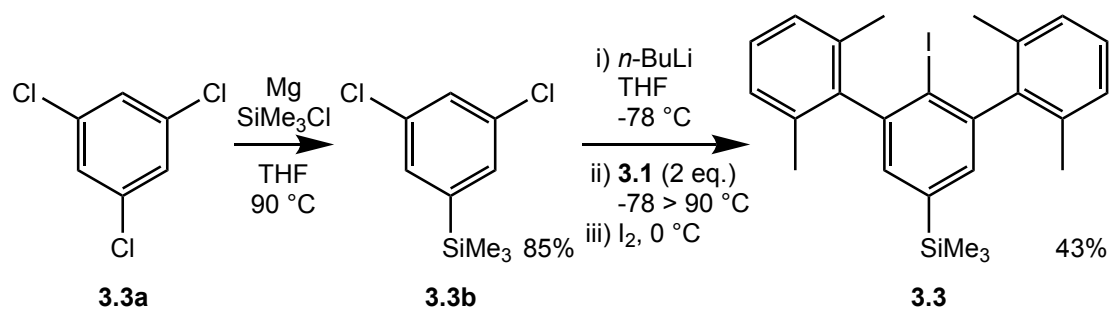


Scheme 3.2 Synthesis of the *t*-butyl *m*-terphenyl iodide, **3.2**.

The *t*-butyl aryl core, **3.2c**, was then coupled to the 2,6-Xyl flanking groups by direct addition of the Grignard reagent, **3.1**, via methods similar to those reported by Hart and Power.^{90,95} This “old-style” route requires three equivalents of Grignard reagent, as opposed to two equivalents for the “new-style” method, as discussed previously in *Chapter 1.2.6*. The addition initially underwent a halogen-metal exchange that occurs preferentially at iodine, rather than at bromine, and then proceeded via two benzyne intermediates to form an *m*-terphenyl Grignard. This was quenched with iodine to yield the final *para*-substituted *t*-butyl *m*-terphenyl iodide, *t*-Bu-Ar-I, **3.2**.

Two main problems were encountered during the purification of **3.2**: firstly, the presence of residual 2,6-Xyl-I impurity in the crude mixture and, secondly, a black coloured dye that was not observed in the NMR spectra. The first issue was addressed by heating the crude product to 150 °C under vacuum to remove the volatile impurity, corresponding to the disappearance of the methyl peak at 2.48 ppm in the ¹H NMR spectrum. For the latter, multiple decolourisation techniques were investigated. The addition of decolourising charcoal was met with varying success but was ineffective on a large scale, while sublimation at 260 °C proved successful but was too low yielding. Flash column chromatography through a silica plug was found to be a better approach, since the black colour remained at the baseline while the off-white product carried through in petroleum ether. Recrystallisation with boiling ethanol finally allowed the pure product of **3.2** to be isolated as white crystalline needles with a total yield of 89%. Purity was confirmed by ¹H and ¹³C NMR spectroscopy and by elemental analysis.

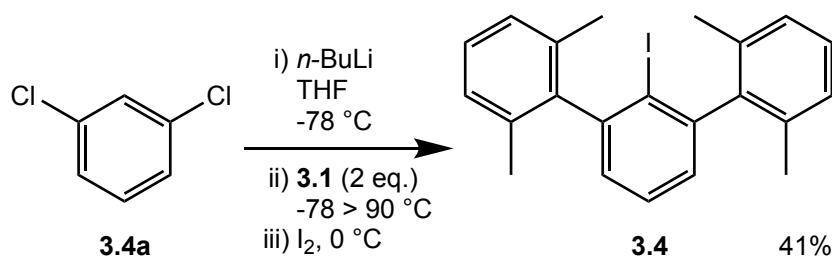
The trimethylsilyl *m*-terphenyl iodide, Me₃Si-Ar-I, **3.3**, was synthesised by a different route (**Scheme 3.3**). Firstly, a Grignard reaction was performed on the commercially available 1,3,5-trichlorobenzene, **3.3a**, then trimethylchlorosilane was added to yield **3.3b**, which was purified by distillation at 45 °C under vacuum.¹⁶⁸



Scheme 3.3 Synthesis of the trimethylsilyl *m*-terphenyl iodide, **3.3**.

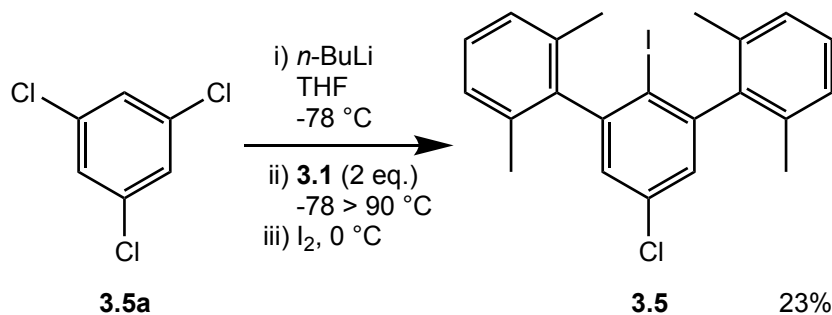
The trimethylsilyl aryl core, **3.3b**, was then coupled to the 2,6-Xyl flanking groups using a newer procedure than the “old-style” route employed for the *t*-butyl compound. This “new-style” method is more economical because, rather than wasting a third equivalent of Grignard reagent, an extra lithiation step is used; again, this is described in *Chapter 1.2.6*.⁹⁶ The reaction of **3.3b** proceeded via a chloride-directed *ortho*-lithiation by the slow addition of *n*-butyllithium at $-78\text{ }^\circ\text{C}$ under argon.^{90,92} Here, low temperatures were employed to prevent lithium-halogen exchange and the decomposition of the lithiated intermediate. Once lithiated, two equivalents of 2,6-Xyl Grignard, **3.1**, were added to form an *m*-terphenyl Grignard via two benzyne intermediates. This *m*-terphenyl Grignard was quenched with iodine to yield the final *para*-substituted trimethylsilyl *m*-terphenyl iodide, Me₃Si-Ar-I, **3.3**, in a moderate yield of 43%. Purity was confirmed by ¹H, ¹³C and ²⁹Si NMR spectroscopy and elemental analysis.

The previously reported unsubstituted *m*-terphenyl iodide, H-Ar-I, **3.4**, was synthesised in a similar manner by lithiation of 1,3-dichlorobenzene, **3.4a**, followed by the addition of the Grignard reagent, **3.1**, to yield **3.4** in 41% yield (Scheme 3.4). Purity was confirmed by ^1H and ^{13}C NMR spectroscopy, and agreed with the literature values.^{80,81}



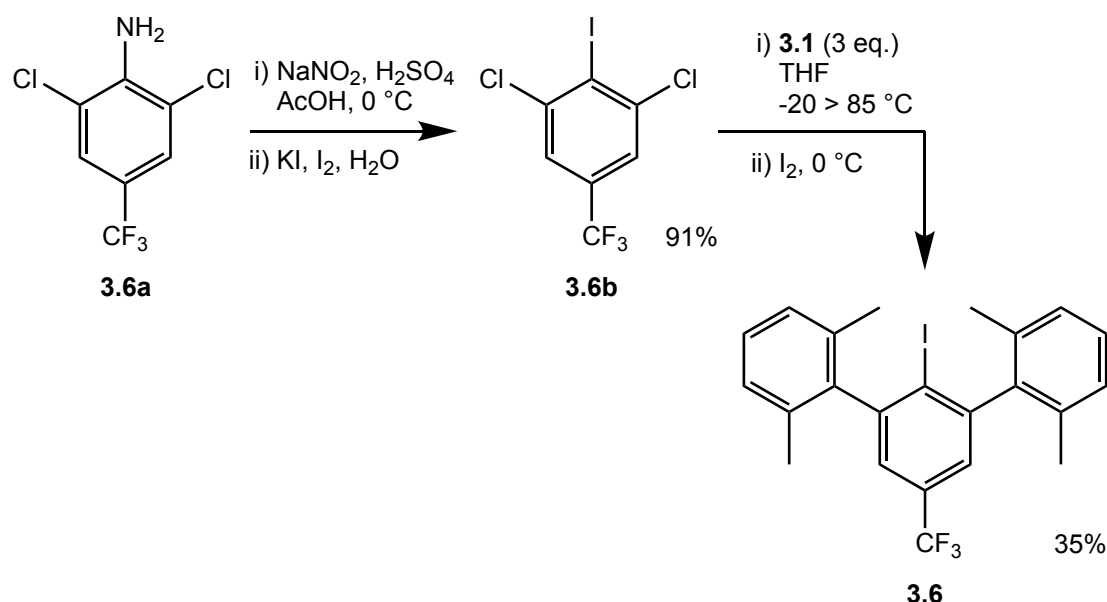
Scheme 3.4 Synthesis of the unsubstituted *m*-terphenyl iodide, **3.4**.

The chloro *m*-terphenyl iodide, Cl-Ar-I, **3.5**, was synthesised by the lithiation of 1,3,5-trichlorobenzene, **3.5a**, with addition of the 2,6-Xyl Grignard reagent, **3.1**, to yield **3.5** in 23% yield (Scheme 3.5).⁹² Purity was confirmed by ^1H and ^{13}C NMR spectroscopy. The low yield obtained for this reaction was likely due to purification problems; recrystallisation of the compound from a range of solvents was unsuccessful, except from diethyl ether via slow evaporation of the solvent over five days. However, a small portion of the resultant crystals were coated in a sticky, orange oil that proved difficult to remove by washing and, therefore, resulted in a loss of yield.



Scheme 3.5 Synthesis of the chloro *m*-terphenyl iodide, **3.5**.

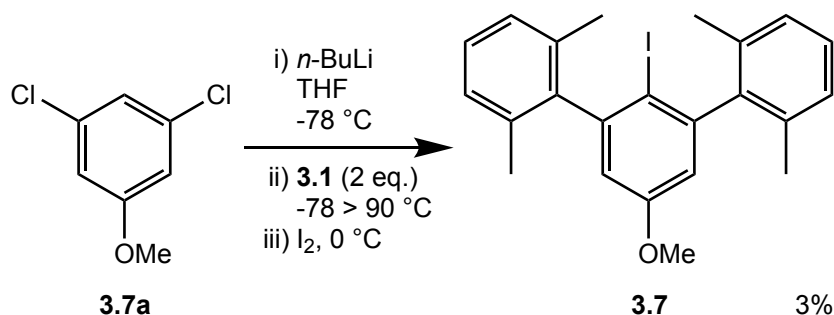
The trifluoromethyl *m*-terphenyl iodide, F₃C-Ar-I, **3.6**, was synthesised via a multi-step process similar to that employed for the *t*-butyl compound (**Scheme 3.6**). In this case, 2,6-dichloro-4-trifluoromethylaniline, **3.6a**, was converted to an iodide, **3.6b**, using a Sandmeyer reaction, then the product was coupled with three equivalents of the 2,6-Xyl Grignard reagent, **3.1**, via the “old-style” method.^{89,95,169} Again, quenching with iodine gave the *para*-substituted trifluoromethyl *m*-terphenyl iodide, F₃C-Ar-I, **3.6**, in 35% yield. Purity was confirmed by ¹H, ¹³C and ¹⁹F NMR spectroscopy.



Scheme 3.6 Synthesis of the trifluoromethyl *m*-terphenyl iodide, **3.6**.

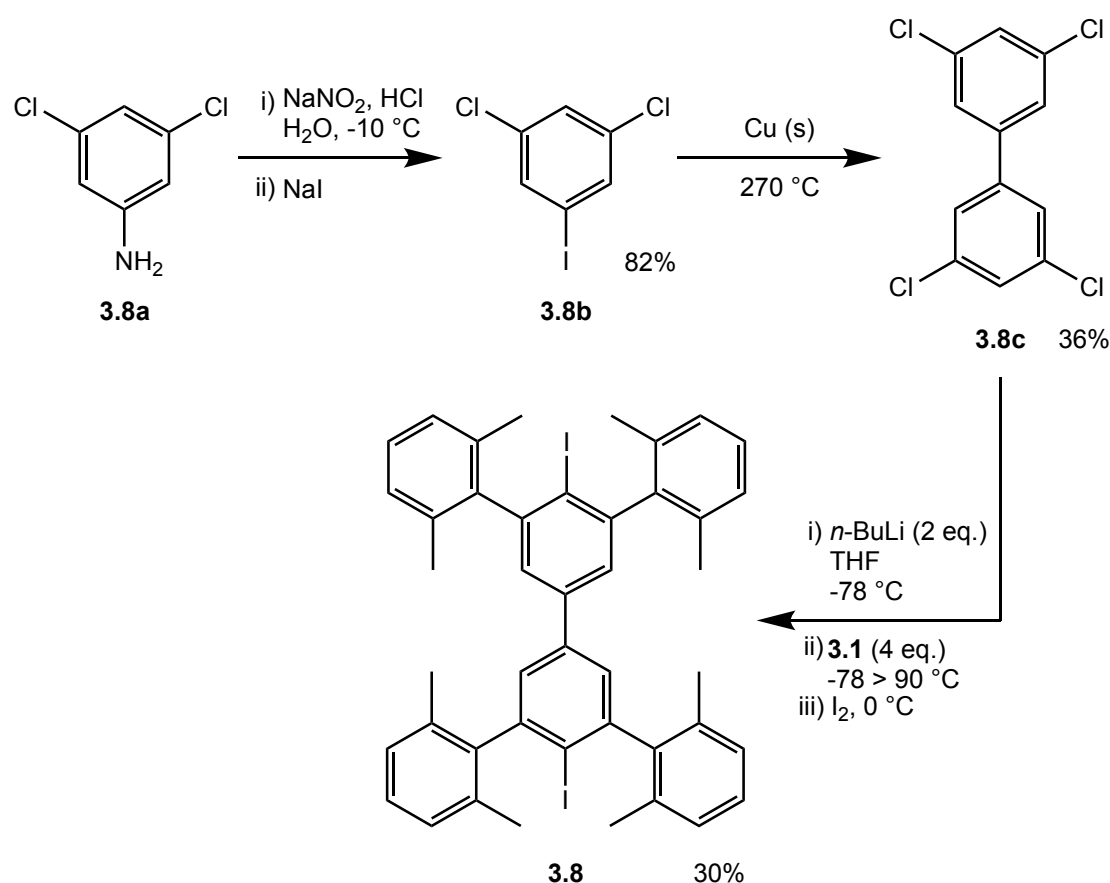
The methoxy *m*-terphenyl iodide, MeO-Ar-I, **3.7**, was synthesised by the lithiation of 3,5-dichloroanisole, **3.7a**, with the subsequent addition of the Grignard reagent, **3.1**, followed by quenching with iodine (**Scheme 3.7**).⁹⁰ However, **3.7** was only obtained in a 3% yield. Originally, this low yield was suspected to be a problem with the lithiation step; when the *n*-butyllithium was added too quickly, the reaction mixture unexpectedly turned purple. This could suggest that the methoxy group competes with the *ortho*-directing chloride groups causing interference with the lithiation process or,

alternatively, that an intensely coloured radical was produced. Either way, the slower addition of the *n*-butyllithium was found to circumvent this problem. Regardless, low yields were still repeatedly obtained, partially due to difficulties with the purification process and, for this reason, **3.7** was determined to be unviable as a ligand precursor. Therefore, the methoxy-substituted *m*-terphenyl iodide **3.7** was not pursued any further in this research.



Scheme 3.7 Synthesis of the methoxy *m*-terphenyl iodide, **3.7**.

The final double *m*-terphenyl iodide ligand precursor, I-Ar-Ar-I, **3.8**, was synthesised by a multi-step process (**Scheme 3.8**). Here, 3,5-dichloroaniline, **3.8a**, was converted to the iodide, **3.8b**, using a Sandmeyer reaction.¹⁷⁰ The individual iodide units, **3.8b**, were then linked together via a solid-state Ullmann coupling with copper at 270 °C to give the tetrachlorobiphenyl **3.8c** in 36% yield.¹⁷¹ This low yield can partly be attributed to purification difficulties; the product was filtered through Celite to remove the copper species, recrystallised from boiling cyclohexane and, finally, sublimed at 170 °C under vacuum. The tetrachlorobiphenyl **3.8c** was then doubly-lithiated via the “new-style” method, which required two equivalents of *n*-butyllithium, with the subsequent addition of four equivalents of the 2,6-Xyl Grignard reagent, **3.1**.⁹⁶ After quenching with iodine, the final double *m*-terphenyl iodide, I-Ar-Ar-I, **3.8**, was obtained in 30% yield. Purity was confirmed by ¹H and ¹³C NMR spectroscopy and by elemental analysis.



Scheme 3.8 Synthesis of the double *m*-terphenyl iodide, **3.8**.

In total, seven *para*-functionalised *m*-terphenyl iodide ligand precursors **3.2** – **3.8** were prepared, all of which were obtained on a large enough scale to be feasible for future metal complex synthesis, with the exception of **3.7** that was too low-yielding to be practically carried forwards in this research. Despite this, compounds **3.2** – **3.8** have been characterised crystallographically, and by ^1H and ^{13}C NMR analyses, enabling a comparative study of their structural and electronic properties as the *para*-substituent is varied across the series of these *m*-terphenyl iodides.

3.2.1.2 Crystallographic Analysis

The structural properties of the *para*-substituted *m*-terphenyl iodides **3.2** – **3.8** were analysed by X-ray crystallography. The compounds were recrystallised from either ethanol (**3.2**, **3.4**, **3.6** and **3.7**), diethyl ether (**3.3** and **3.5**) or a toluene-hexane mix (**3.8**) as white crystals. All compounds were crystallographically characterised, except for H-Ar-I (**3.4**) which has previously been reported.^{80,81} Single crystal X-ray data of R-Ar-I, where R = *t*-Bu (**3.2**), SiMe₃ (**3.3**), Cl (**3.5**), CF₃ (**3.6**), OMe (**3.7**), Ar-I (**3.8**), reveals that all molecules adopt the same core aromatic structure, differing only by the *para*-substituent (**Fig. 3.5/3.6**). Similar C–I bond distances are observed across the series [C(1)–I(1) = 2.107(2), 2.121(6), 2.103(3)–2.110(3), 2.103(4)–2.110(4), 2.11(3)–2.13(3), and 2.092(9) Å, for **3.2** – **3.3** and **3.5** – **3.8** respectively] which are comparable to **3.4** [2.106(4) Å] and literature *m*-terphenyl iodides, including 2,6-Ar₂C₆H₃I (Ar = Ph, Mes, Dipp, Tripp, Pmp, Tol; Tol = 4-MeC₆H₄).^{86,172–177} Also, all C–C bond lengths within the central aromatic ring are comparable [1.379(7)–1.408(8) Å]. However, bond lengths from the central ring to the *para*-substituent do vary; while the C–CF₃ bond [1.492(6)–1.496(7) Å] is shorter than the C–CMe₃ bond [1.535(4) Å], the C–Cl [1.738(4)–1.740(4) Å] and C–SiMe₃ [1.887(6) Å] bonds are significantly longer.

The dihedral angles between the planes of the central C(1)-aryl ring and the *ortho*-2,6-Xyl flanking groups for **3.2** [87.79(9)° and 89.74(9)°], **3.3** [80.2(2)° and 81.8(2)°], **3.5** [82.74(12)–87.28(13)°], **3.6** [82.91(15)–88.23(16)°], **3.7** [79.9(11)–86.9(10)°] and **3.8** [85.7(4)° and 87.7(4)°] are all near-orthogonal and only vary within a 10° range. This range is marginal in comparison to related *m*-terphenyl iodides where the flanking aryl differs; for example, the dihedral angle is significantly narrower for 2,6-(3,5-Xyl)₂C₆H₃I [65.59°], likely due to the different steric bulk.^{80,81} In contrast, the

angles reported here are consistent with the unsubstituted analogue **3.4** [$89.50(9)^\circ$].^{80,81} Therefore, keeping the 2,6-Xyl group constant across the series seemingly limits the dihedral angle to a 10° range, where any minor deviations within this are likely due to crystal packing effects, secondary contacts or intermolecular interactions, such as the weak CH- π bonding observed in **3.3** [$\text{H}(18)\cdots\text{C}(7)$ centroid = $2.794(3)$ Å, $\text{C}(18)\cdots\text{C}(7)$ centroid = $3.722(7)$ Å, $\angle\text{C}(18)\text{--H}(18)\cdots\text{C}(7)$ centroid = $165.6(5)^\circ$]. These effects likely overshadow any potential structural changes caused by the *para*-substituents.

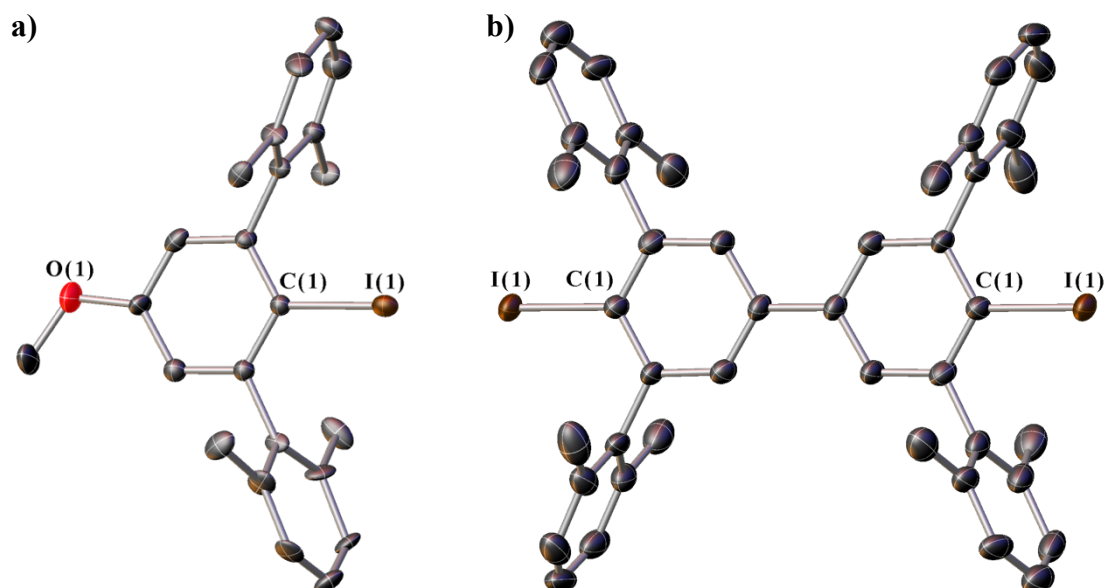


Fig. 3.5 Crystal structures of the *m*-terphenyl iodides, R-Ar-I, where a) R = OMe (**3.7**) and b) R = Ar-I (**3.8**). Ellipsoids set at 50% probability. Hydrogen atoms and residual solvent molecules are omitted for clarity.

In summary, the crystallographic structures of the *m*-terphenyl iodides **3.2** – **3.8** show little structural variation as the *para*-substituent is changed, except for minor deviations in the dihedral angle between the C(1)-aryl ring and the *ortho*-2,6-Xyl flanking groups. However, although structurally similar, further research of these compounds is required to understand the effects of *para*-functionalisation on their electronic properties.

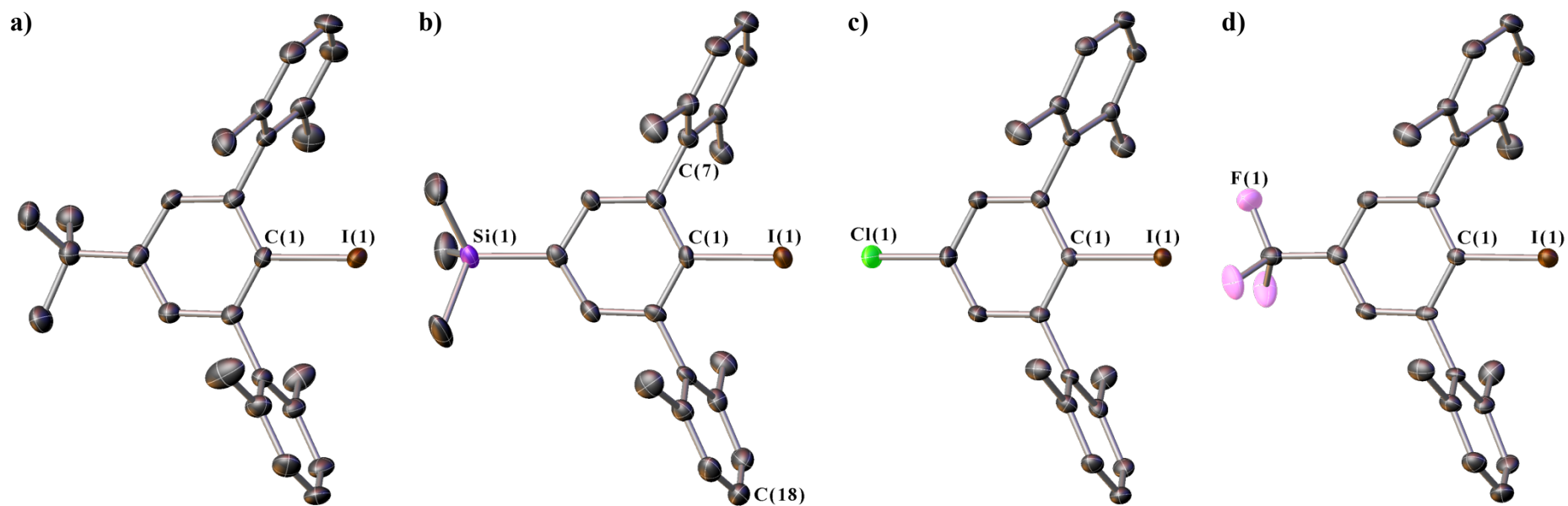


Fig. 3.6 Crystal structures of the *m*-terphenyl iodides, R-Ar-I, where a) R = *t*-Bu (**3.2**), b) R = SiMe₃ (**3.3**), c) R = Cl (**3.5**) and b) R = CF₃ (**3.6**). Ellipsoids set at 50% probability. Hydrogen atoms omitted for clarity. When necessary, only one molecule from the asymmetric unit is shown. The unsubstituted analogue, R = H (**3.3**), is reported elsewhere.^{80,81}

3.2.1.3 NMR Analysis

The electronic properties of the *para*-substituted *m*-terphenyl iodides **3.2** – **3.8** were studied by ^1H and ^{13}C NMR spectroscopies. To aid with this, the *m*-terphenyl framework has been assigned a numbering scheme (**Fig. 3.7**). In all cases but **3.4**, the ^1H NMR shows four characteristic peaks: a weak singlet for the *meta*-hydrogens (H-3) on the central ring, a strong singlet for the methyl groups (H-9) on the 2,6-Xyl rings, and two slightly broadened signals, a doublet (H-7) and a triplet (H-8), also on the 2,6-Xyl rings, whose coupling displays the roofing phenomenon (**Fig. 3.7**).¹⁷⁸ Here, the broadening of these peaks could potentially arise from hindered rotation of the flanking aryl groups due to a steric clash with the iodine atom. Additional singlets are observed for **3.2**, **3.3** and **3.7** owing to the *t*-Bu, SiMe₃ and OMe groups respectively. In comparison, for the unsubstituted **3.4**, the extra proton on the central ring couples to the *meta*-hydrogens (H-3) to yield another doublet-triplet pair.

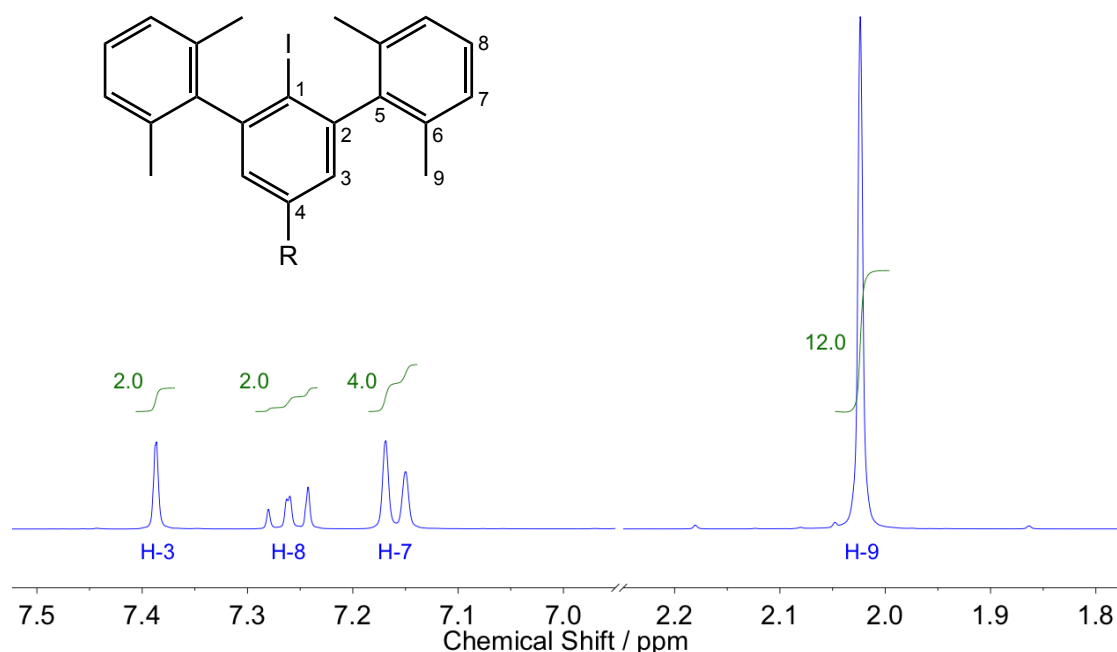


Fig. 3.7 General ^1H NMR spectrum of the *para*-substituted *m*-terphenyl iodides, showing the numbering scheme used for the NMR assignments.

To understand the effects of *para*-substitution on the electronics of **3.2** – **3.8**, their ^1H NMR spectra can be compared. Regarding the 2,6-Xyl flanking groups, the peaks for H-7 (7.15–7.17 ppm), H-8 (7.24–7.26 ppm) and H-9 (2.02–2.11 ppm) remain essentially unshifted across the series. Evidently, the change of *para*-substituent does not appear to influence the electronics of the flanking aryl rings; this is possibly due to their distance from the *para*-group and their disconnect from the conjugated aromatic core. However, for the *meta*-hydrogens on the central ring, measurable peak shifts are noted (H-3 = 7.16, 7.23, 7.14, 7.17, 7.39, 6.73 and 7.40 ppm for **3.2** – **3.8** respectively), see **Table 3.2**. Although no apparent electronic trends are observed, the two extremes, **3.6** (CF_3) and **3.7** (OMe), suggest that increased electron-donating character causes an upfield peak shift corresponding to greater shielding of the *meta*-hydrogens, H-3.

A similar approach can be used to analyse the ^{13}C NMR spectra of **3.2** – **3.8**, which were assigned with the aid of DEPT, HSQC-ME and HMBC techniques. In all cases, nine peaks are observed, corresponding to each of the carbons in the *m*-terphenyl framework, including the *ipso*-carbon (C-1) that is shifted upfield due to shielding from the iodine.^{179–182} Additional peaks are noted for **3.2**, **3.3**, **3.6** and **3.7** owing to the *t*-Bu, SiMe_3 , CF_3 and OMe groups respectively. Notably, the CF_3 analogue **3.6** exhibits splitting of its peaks into quartets via ^{13}C - ^{19}F coupling (for C-10: $^1J_{\text{CF}} = 272.7$ Hz; for C-4: $^2J_{\text{CF}} = 32.6$ Hz; and for C-3: $^3J_{\text{CF}} = 3.6$ Hz).¹⁸³ Again, a comparison of the 2,6-Xyl flanking group peaks reveals that C-5 (143.6–145.3 ppm), C-6 (135.5–135.8 ppm), C-7 (127.4–127.7 ppm), C-8 (127.7–128.4 ppm) and C-9 (20.4–20.6 ppm) remain essentially unshifted for **3.2** – **3.8**. In contrast, with the exception of C-2, the carbon peaks on the central ring shift considerably, see **Table 3.2** below. Here, the largest shifts are noted for C-4 (129.1–160.5 ppm), possibly because this carbon is closest to the

para-substituent, while smaller shifts are observed for C-1 (95.5–111.8 ppm) and C-3 (113.6–132.3 ppm). As for the ^1H NMR spectra, it is difficult to deduce any reliable trends, notably for C-3 and C-4. However, a general downfield shift is found for C-1 as electron-withdrawing character of the *para*-substituent is increased. This provides evidence that *para*-functionalisation does influence the electronic properties within the central ring of the *m*-terphenyl iodide, most importantly at the *ipso*-position.

Table 3.2 ^1H and ^{13}C NMR chemical shifts, δ , for R-Ar-I (**3.4** – **3.8**), where R is the *para*-substituent, for relevant atoms on the *m*-terphenyl iodides. The flanking aryl atoms remain unshifted so have been omitted.

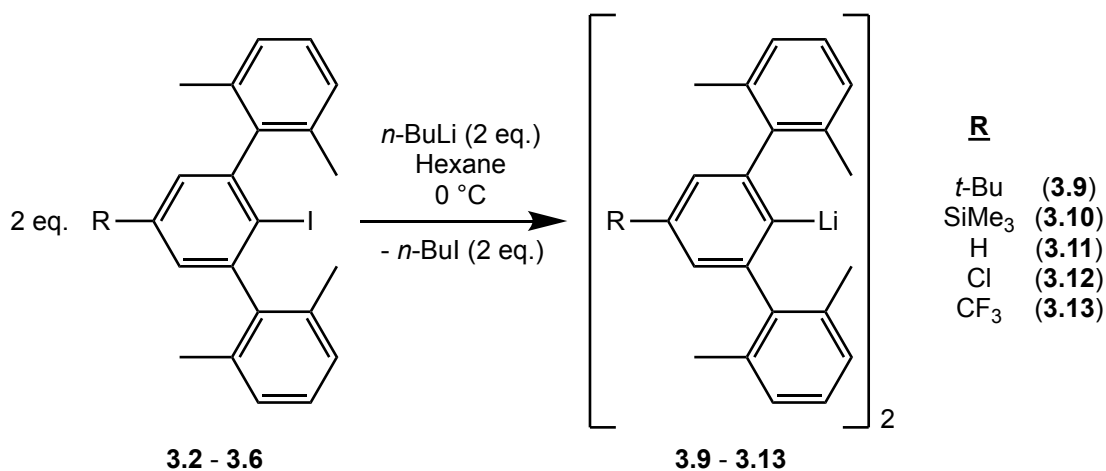
R-Ar-I	R Group	^1H and ^{13}C NMR Chemical Shifts, δ (ppm)						
		H-3	H-9	C-1	C-2	C-3	C-4	C-9
3.2	<i>t</i> -Bu	7.16	2.06	102.4	146.6	125.0	152.6	20.5
3.3	SiMe ₃	7.23	2.05	107.7	146.3	132.3	141.7	20.6
3.4	H	7.14	2.06	106.9	147.3	127.8	129.1	20.5
3.5	Cl	7.17	2.07	104.7	148.9	127.7	135.2	20.4
3.6	CF ₃	7.39	2.02	111.8	148.5	124.3	131.7	20.5
3.7	OMe	6.73	2.06	95.5	148.1	113.6	160.5	20.4
3.8	Ar-I	7.40	2.11	106.3	148.1	125.8	140.4	20.6

In summary, although the *m*-terphenyl iodides **3.2** – **3.8** are structurally very similar, both ^1H and ^{13}C NMR spectroscopies reveal significant electronic differences. While *para*-substitution has negligible effect on the chemical shifts associated with the 2,6-Xyl flanking groups, the electronic properties are transferred through the conjugated central ring to the *ipso*-carbon. Since the *ipso*-position is where a metal should bind, this is promising for future work and provides reason to carry out the next step of lithiation on all *m*-terphenyl iodides, except for the low-yielding OMe compound **3.7**.

3.2.2 *m*-Terphenyl Lithium Complexes

3.2.2.1 Synthesis

The *para*-substituted *m*-terphenyl iodide ligand precursors, R-Ar-I, **3.2** – **3.6**, were lithiated following a lithium-halogen exchange reaction via the addition of excess *n*-butyllithium at 0 °C to produce the *m*-terphenyl lithium complexes, [R-Ar-Li]₂, (Ar = 2,6-(2,6-Xyl)₂C₆H₂; R = *t*-Bu, **3.9**; SiMe₃, **3.10**; H, **3.11**; Cl, **3.12**; CF₃, **3.13**), as pure white powders (**Scheme 3.9**). A range of yields was obtained (38%, 60%, 99%, 100% and 95% for **3.2** – **3.6** respectively) and purity was confirmed by ¹H and ⁷Li NMR spectroscopies. The low yield of **3.9** can be ascribed to the greater solubility of the *t*-Bu complex in hexane, which was used to wash the product, as well as the formation of an unknown side-product likely to be an inorganic salt.



Scheme 3.9 General synthesis of the *m*-terphenyl lithium complexes, **3.9** – **3.13**.

Lithiation of the double *m*-terphenyl iodide, I-Ar-Ar-I, **3.8**, failed to yield any major products. However, a crystal structure was obtained for the decomposition product, a doubly protonated ligand, H-Ar-Ar-H, suggesting that lithiation did occur. Refinement of the experimental conditions is thus required for future studies of this system, but it was decided not to pursue the compound any further in this research.

3.2.2.2 Crystallographic Analysis

To analyse the structural properties of the *para*-substituted *m*-terphenyl lithium complexes **3.9** – **3.13**, all samples were recrystallised from *s*-hexane and characterised crystallographically, except for [H-Ar-Li]₂ (**3.11**) that has previously been reported.¹⁰⁰ Single crystal X-ray data of [R-Ar-Li]₂ (R = *t*-Bu, **3.9**; SiMe₃, **3.10**; Cl, **3.12**; CF₃, **3.13**) reveals that all molecules adopt a dimeric structure featuring two anionic *m*-terphenyl units linked together by two lithium cations, which bridge the ligands via their *ipso*-carbons to form a planer Li₂C₂ core (**Fig. 3.8/3.9**). Relevant bond lengths and angles are given in **Table 3.3**. Similar Li₂C₂ cores are observed across the series, with Li(1)⋯Li(2) distances of 2.304(4)–2.333(4) Å, C_{*ipso*}⋯C_{*ipso*} distances between 3.686(2)–3.702(3) Å, and C_{*ipso*}–Li–C_{*ipso*} angles in the range of 114.59(13)–116.66(15)° [Σ_{Li-C-Li-C} = 360°]. Furthermore, all C_{*ipso*}–Li bond lengths occur within a narrow range [2.159(3)–2.1986(18) Å] and are comparable to the unsubstituted analogue **3.11** [2.143(5)–2.187(6) Å] and other *m*-terphenyl lithium dimers in the literature.^{80,97,100}

Table 3.3 Relevant bond lengths (Å) and angles (°) for the planar Li₂C₂ core of the *m*-terphenyl lithium complexes, [R-Ar-Li]₂ (**3.9** – **3.13**), featuring *para*-substituent, R. The unsubstituted analogue, R = H (**3.11**), is reported elsewhere.¹⁰⁰

Li ₂ C ₂ Core	Bond Lengths (Å) and Angles (°)			
	3.9 (R = <i>t</i> -Bu)	3.10 (R = SiMe ₃)	3.12 (R = Cl)	3.13 (R = CF ₃)
Li(1)–C(1)	2.186(4)	2.173(4)	2.188(7)	2.1986(18)
Li(1)–C(23) ^a	2.177(3)	2.186(5)	2.186(7)	-
Li(2)–C(1)	2.159(3)	2.192(5)	2.174(6)	2.1759(18)
Li(2)–C(23) ^a	2.172(4)	2.186(4)	2.176(6)	-
Li(1)⋯Li(2)	2.304(4)	2.318(6)	2.316(8)	2.333(4)
C(1)⋯C(23)	3.686(2)	3.702(3)	3.695(4)	3.700(2)
C(1)–Li(1)–C(23) ^a	115.32(15)	116.30(19)	115.3(3)	114.59(13)
C(1)–Li(2)–C(23) ^a	116.66(15)	115.48(19)	116.3(3)	116.48(13)

^a For **3.13**, C(23) = C(1) due to only half the molecule in the asymmetric unit.

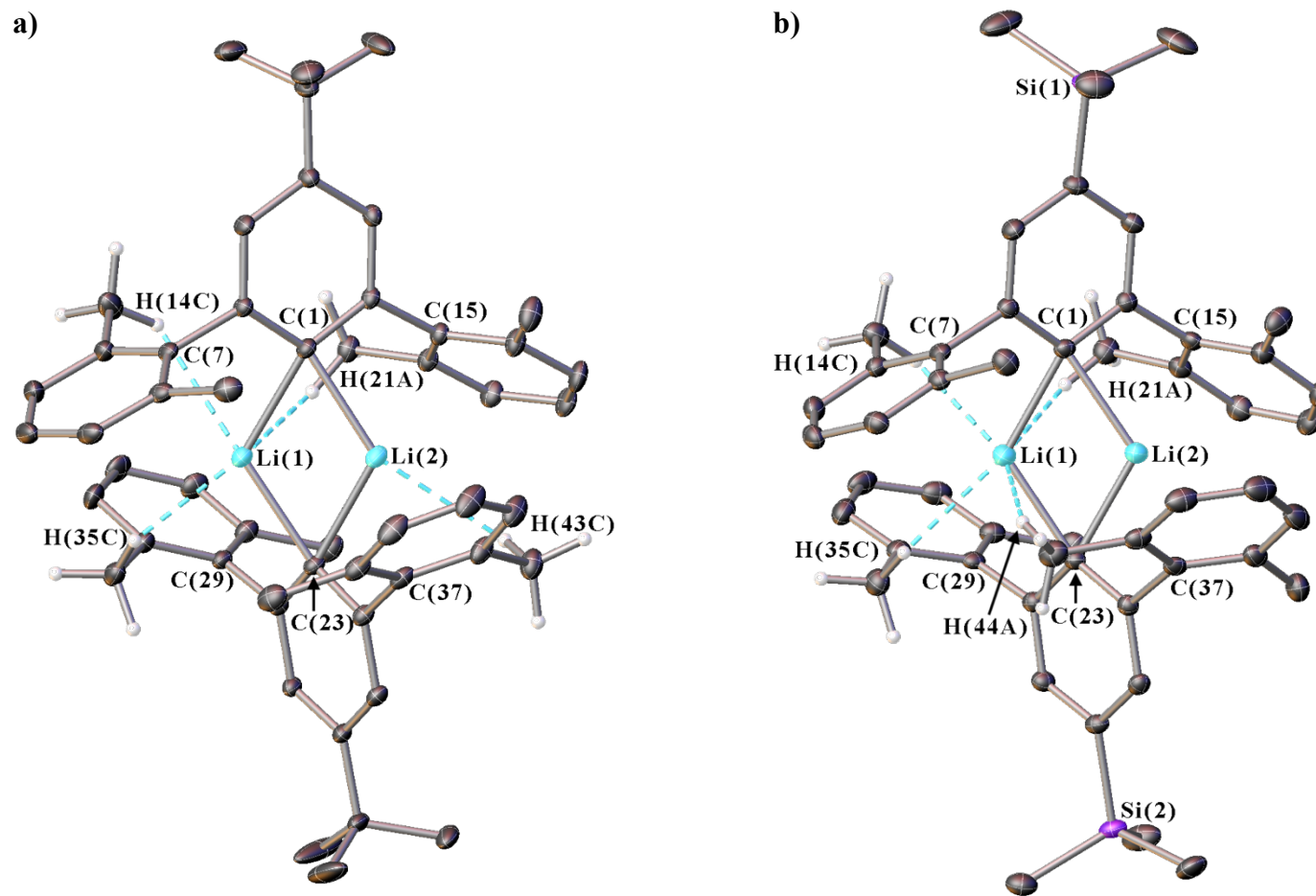


Fig. 3.8 Crystal structures of the *m*-terphenyl lithium complexes, $[\text{R-Ar-Li}]_2$, where a) $\text{R} = t\text{-Bu}$ (**3.9**) and b) $\text{R} = \text{SiMe}_3$ (**3.10**). Dashed lines indicate the short $\text{Li}\cdots\text{H-C}$ anagostic contacts. Ellipsoids set at 20% and 40% probability for **3.9** and **3.10** respectively. All irrelevant hydrogen atoms and residual solvent molecules are omitted for clarity. The unsubstituted analogue, $\text{R} = \text{H}$ (**3.11**), is reported elsewhere.¹⁰⁰

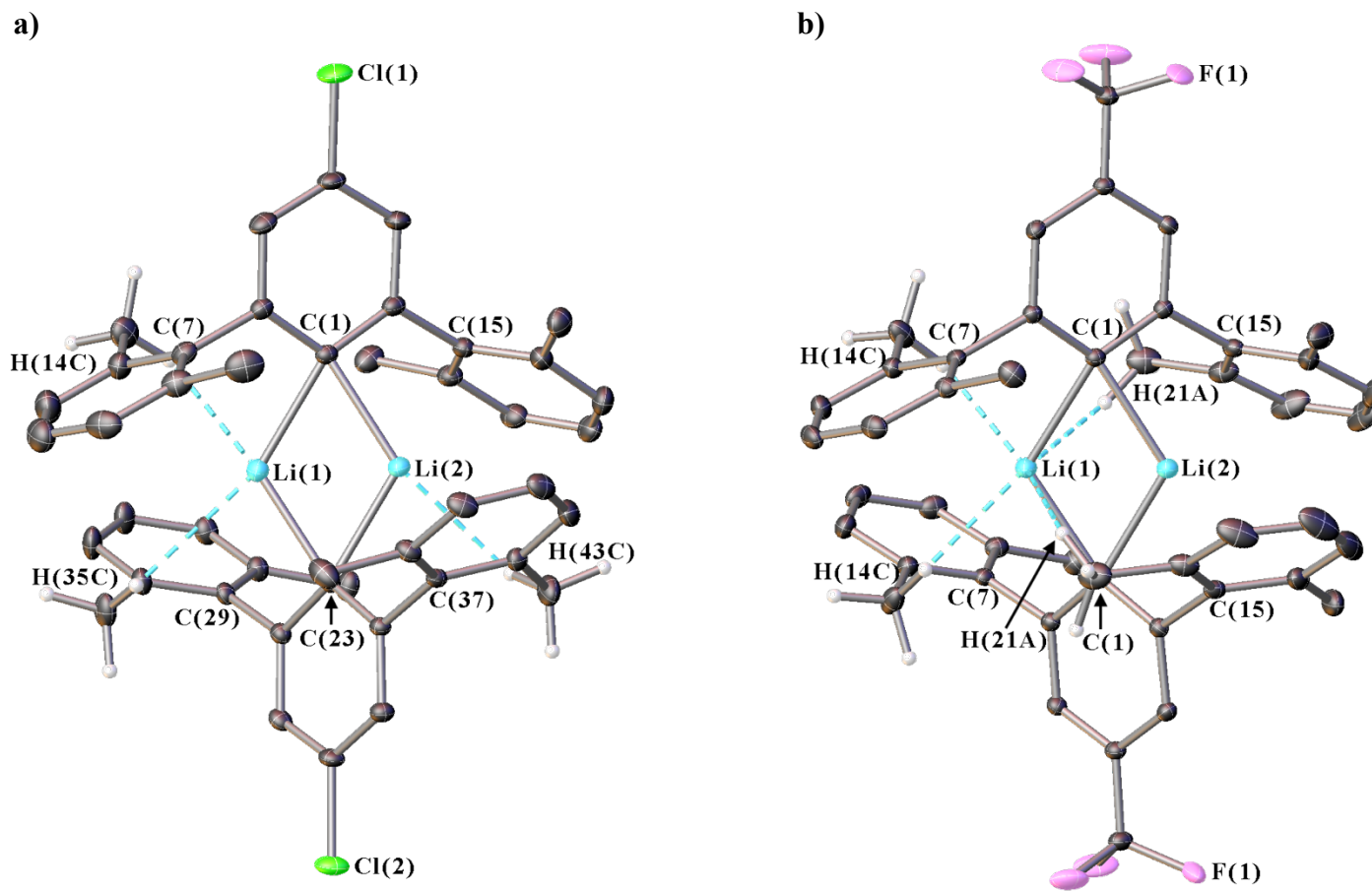


Fig. 3.9 Crystal structures of the *m*-terphenyl lithium complexes, $[\text{R-Ar-Li}]_2$, where a) $\text{R} = \text{Cl}$ (**3.11**) and b) $\text{R} = \text{CF}_3$ (**3.13**). Dashed lines indicate the short $\text{Li}\cdots\text{H-C}$ anagostic contacts. Ellipsoids set at 15% and 25% probability for **3.12** and **3.13** respectively. All irrelevant hydrogen atoms and residual solvent molecules are omitted for clarity. The unsubstituted analogue, $\text{R} = \text{H}$ (**3.11**), is reported elsewhere.¹⁰⁰

Weaker intramolecular interactions are also observed between the lithium ions and the 2,6-Xyl flanking groups; these secondary contacts are *ca.* 0.2–0.7 Å longer than the C_{ipso} –Li bonds in the Li_2C_2 core but remain shorter than the sum of the Van der Waals radii for lithium and hydrogen (3.02 Å) or lithium and carbon (3.52 Å).^{184,185} These contacts are summarised in **Table 3.4**. For **3.9** – **3.13**, the lithium ions interact with the *ipso*-carbons of the flanking aryls [2.4244(15)–2.729(4) Å], and also form multiple $Li \cdots H-C$ anagostic interactions with the hydrogens of the flanking methyl groups [2.327(3)–2.920(3) Å]. Notably, when comparing **3.9** and **3.10** (**Fig 3.8**), rotation of the C(37) flanking aryl appears to cause breakage of the $Li(2) \cdots H(43C)$ contact in **3.9** and formation of a $Li(1) \cdots H(44A)$ contact in **3.10**; the anagostic interaction swaps between methyl groups on either side of the 2,6-Xyl ring. A similar scenario is noted when comparing **3.12** and **3.13** (**Fig 3.9**). Furthermore, in **3.9** – **3.13**, contacts are observed between the lithium ions and the *ortho*-carbons of the flanking rings [$> 2.681(4)$ Å]. These are longer than those reported for $[2,6-(3,5-Xyl)_2C_6H_3Li]_2$ [2.318(6)–2.524(6) Å] due to the greater steric hindrance of the 2,6-Xyl group which restricts rotation of the flanking aryls and, in turn, opposes the formation of these stabilising contacts.^{80,81}

This restricted rotation is further evidenced by the dihedral angles between the planes of the central rings, C(1)-aryl and C(23)-aryl, and their *ortho*- 2,6-Xyl flanking groups. For **3.9** – **3.13**, the flanking groups are near orthogonal [68.41(8)–89.59(12)°] to minimise steric clash of the methyl groups. These angles fall within a narrower range than the less hindered 3,5-Xyl analogue [36.50(12)–83.5(6)°], which highlights how the 2,6-Xyl group is more rotationally constrained.^{80,81} Thus, keeping the 2,6-Xyl group constant minimises the effects of steric variations on the coordination sphere, where any minor deviations are likely due to crystal packing effects or secondary contacts.

Table 3.4 Intramolecular distances (Å) between the lithium ions and 2,6-Xyl flanking groups of the *m*-terphenyl lithium complexes, [R-Ar-Li]₂ (**3.9** – **3.13**), featuring *para*-substituent, R. The unsubstituted analogue, R = H (**3.11**), is reported elsewhere.¹⁰⁰

Li⋯(2,6-Xyl)	Intramolecular Distances (Å)			
	3.9 (R = <i>t</i> -Bu)	3.10 (R = SiMe ₃)	3.12 (R = Cl)	3.13 (R = CF ₃)
Li(1)⋯C(7)	2.654(4)	2.729(4)	2.541(7)	2.6633(14)
Li(1)⋯C(29) ^a	2.694(4)	2.649(3)	2.558(6)	2.6633(14)
Li(2)⋯C(15)	2.541(4)	2.437(4)	2.613(7)	2.4243(15)
Li(2)⋯C(37) ^a	2.504(4)	2.468(5)	2.587(7)	2.4243(15)
Li(1)⋯H(14C)	2.865(3)	2.476(5)	2.770(6)	2.4867(17)
Li(1)⋯H(21A)	2.811(4)	2.920(3)	-	2.8953(9)
Li(1)⋯H(35C) ^a	2.327(3)	2.527(3)	2.832(6)	2.4867(17)
Li(1)⋯H(44A) ^a	-	2.803(3)	-	2.8953(9)
Li(2)⋯H(43C) ^a	2.647(3)	-	2.596(6)	-

^a For **3.13**, C(29) = C(7), C(37) = C(15), H(35C) = H(14C), H(44A) = H(21A), and H(43C) = H(22C) due to only half the molecule in the asymmetric unit.

Dihedral angles can also be measured between the planes of the central rings for the two *m*-terphenyl ligands either side of the lithium ions, C(1)-aryl and C(23)-aryl. For complexes **3.9** – **3.13**, the ligands position themselves near-orthogonal to one another to minimise steric strain, yet the dihedral angles for **3.9** [78.10(6)°], **3.10** [74.90(6)°], **3.12** [73.82(12)°] and **3.13** [67.18(5)°] differ across the series. Here, *para*-substitution seemingly affects the dihedral angle; stronger electron-withdrawing groups appear to decrease the angle. However, the unsubstituted analogue, **3.11**, does not fit this trend [81.43(10)–87.8(5)°], suggesting that this observation could be a coincidence.¹⁰⁰

In summary, the crystal structures of the *m*-terphenyl lithium complexes **3.9** – **3.13** show that varying the *para*-substituent has minimal effect on the structural properties but do reveal the formation of weak Li⋯H–C anagostic contacts between the lithium ions and the flanking methyl groups. However, while structurally similar, further studies are required to probe the electronic properties of these systems.

3.2.2.3 NMR Analysis

Research into the electronic properties of the *para*-substituted *m*-terphenyl lithium complexes **3.9** – **3.13** was achieved by ^1H , ^{13}C and ^7Li NMR spectroscopies. In all cases, the samples were prepared in *d*-benzene and, due to their poor solubilities, were fully saturated, except for **3.9** whose *t*-Bu group enabled dissolution. To provide evidence that the dimeric structures of the solid-state complexes are retained in solution, DOSY experiments were performed; this NMR technique approximates the size of a molecule, its hydrodynamic radius, r_s , from the measured diffusion coefficient, D , assuming a perfectly spherical system. It indicates that larger molecules diffuse more slowly in solution.^{186,187} To mimic a monomeric species, the unsubstituted iodide, H-Ar-I, **3.4**, was analysed, giving a hydrodynamic radius of 3.0 Å. In comparison, the equivalent lithium complex, [H-Ar-Li]₂, **3.11**, gave a larger radius of 4.8 Å, which closely matches the crystallographic diameters (9.4 x 9.9 Å) likely due to its near-spherical shape. The *para*-substituted complexes yield similarly larger radii that, except for **3.13**, exhibit a size increase with bulkier substituents, although these values deviate from the crystal parameters due to the more ellipsoidal shape of the molecules (Fig 3.10).¹⁸⁸ However, the overall increase of hydrodynamic radii for the lithium complexes, **3.09** – **3.13**, compared to the monomeric iodide, **3.4**, suggests that these species are dimeric in *d*-benzene solution. These results are summarised in Table 3.5 below.

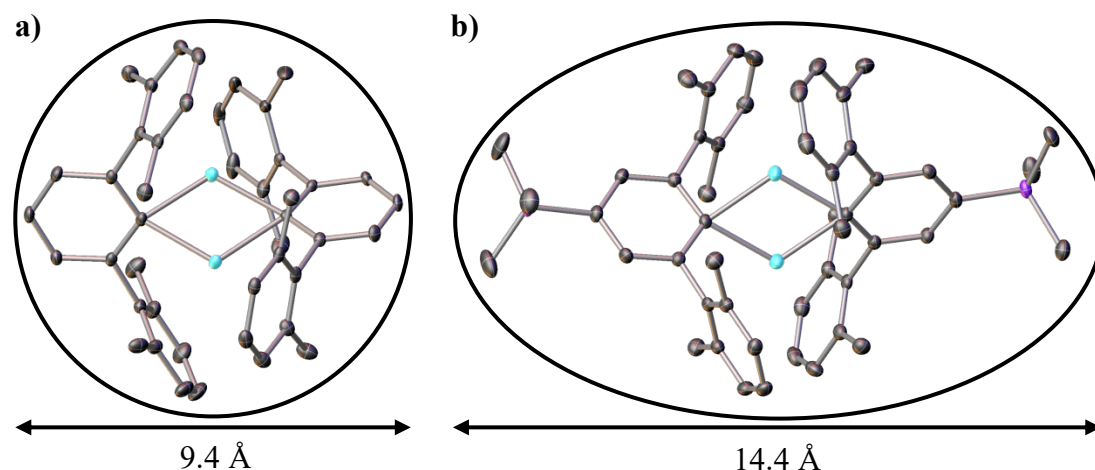


Fig. 3.10 Crystal structures of the *m*-terphenyl lithium complexes, $[\text{R-Ar-Li}]_2$, comparing the length of a) the spherical $\text{R} = \text{H}$ (**3.11**) complex (9.4 Å) against that of b) the ellipsoidal $\text{R} = \text{SiMe}_3$ (**3.10**) complex (14.4 Å). The widths of both are 9.9 Å. Ellipsoids set at 20% and 40% probability for **3.11** and **3.10** respectively. Hydrogen atoms and residual solvent molecules are omitted for clarity.

Table 3.5 Diffusion coefficients, D , and hydrodynamic radii, r_s , obtained from DOSY measurements for the monomeric R-Ar-I (**3.4**) and dimeric $[\text{R-Ar-Li}]_2$ (**3.9** – **3.13**) species, where R is the *para*-substituent. Their crystallographic diameters, d_c , are provided for comparison.

Compound ^a	Diffusion Coefficient, D ($10^{-10} \text{ m}^2 \text{ s}^{-1}$)	Hydrodynamic Radius, r_s (Å)	Crystallographic diameters, d_c (Å)	
			Length ^b	Width ^c
H-Ar-I (3.4)	12.30	3.0	4.9	9.9
$[\text{H-Ar-Li}]_2$ (3.11)	7.54	4.8	9.4	9.9
$[\text{Cl-Ar-Li}]_2$ (3.12)	6.72	5.4	12.8	9.9
$[\text{F}_3\text{C-Ar-Li}]_2$ (3.13)	7.59	4.8	13.4	9.9
$[t\text{-Bu-Ar-Li}]_2$ (3.9)	6.59	5.5	13.6	9.9
$[\text{Me}_3\text{Si-Ar-Li}]_2$ (3.10)	6.27	5.8	14.4	9.9

^a All samples were prepared to be 24 mM in *d*-benzene.

^b Length along the compound measured between $\text{R}\cdots\text{I}$ (**3.4**) and $\text{R}\cdots\text{R}$ (**3.9** – **3.13**), where R is the outermost point of the *para*-substituent.

^c Width across the compound measured between $\text{C}\cdots\text{C}$ for the outermost carbon atoms of the flanking aryl rings on each *m*-terphenyl ligand. All widths averaged at 9.9 Å.

To aid with the analyses of the NMR data, the *m*-terphenyl unit in **3.9** – **3.13** has been assigned a numbering scheme (**Fig. 3.11**). Their ^1H NMR spectra show four characteristic peaks similar to those of the iodide compounds, except that, in some cases, the signals for the aromatic 2,6-Xyl protons (H-7 and H-8) are merged into a broadened singlet. Additional peaks are observed for **3.9**, **3.10** and **3.11** due to the *t*-Bu, SiMe₃ and H groups respectively. Relative to the iodides, all of the resonances are shifted upfield in keeping with the greater shielding provided by the anionic ligands. A comparison of the ^1H NMR spectra across the series reveals three key features. Firstly, akin to the iodide compounds **3.2** – **3.6**, the *meta*-hydrogens on the central rings exhibit small peak shifts (H-3 = 6.85, 7.04, 6.77, 6.78, 6.99 ppm for **3.9** – **3.13**, respectively) with no overall trend, see **Table 3.6** below. Secondly, the 2,6-Xyl aryl protons, H-7 (6.86–7.01 ppm) and H-8 (6.94–7.01 ppm), remain essentially unshifted, reinforcing the concept that *para*-substitution does not influence the chemical shifts associated with the flanking rings. Thirdly, however, unlike the iodides, the 2,6-Xyl methyl protons shift unexpectedly upfield (H-9 = 1.83, 1.81, 1.80, 1.61, 1.55 ppm for **3.9** – **3.13**, respectively) with increased electron-withdrawing strength of the *para*-substituent. In fact, a graph of these chemical shifts, δ , against the corresponding Hammett constants, σ_{para} , reveals a linear correlation (**Fig. 3.12**).¹³⁹ Not only does this contradict the previous observation that *para*-substituents do not appear to affect the chemical shifts associated with the flanking aryls, but it instead suggests that they are directly responsible for these electronic changes. Moreover, this trend proceeds in the opposite direction to that expected; electron-withdrawing groups usually cause a downfield shift but here an upfield shift is observed. This finding is discussed in more depth later in the section.

Table 3.6 ^1H , ^{13}C and ^7Li NMR chemical shifts, δ , for $[\text{R-Ar-Li}]_2$ (**3.9** – **3.13**), where R is the *para*-substituent, for relevant atoms on the *m*-terphenyl lithium complexes. The flanking aryl atoms remain unshifted so have been omitted.

$[\text{R-Ar-Li}]_2$	R Group	^1H , ^{13}C and ^7Li NMR Chemical Shifts, δ (ppm)							
		H-3	H-9	C-1	C-2	C-3	C-4	C-9	Li
3.9	<i>t</i> -Bu	6.85	1.83	168.1	152.0	120.4	148.7	21.8	1.60
3.10	SiMe ₃	7.04	1.81	174.2	151.6	128.1	136.5	21.9	1.47
3.11	H	6.77	1.80	172.7	152.0	123.6	126.3	21.8	1.46
3.12	Cl	6.78	1.61	170.7	153.6	123.6	132.9	21.5	1.10
3.13	CF ₃	6.99	1.55	180.2	152.4	119.5	- ^a	21.5	0.93

^a Peak C-4 for **3.13** not observed (hidden behind *d*-benzene solvent peak).

The ^{13}C NMR spectra of **3.9** – **3.13** were assigned using DEPT, HSQC-ME and HMBC techniques, and show nine peaks representing the carbons in the ligand framework, with additional peaks for **3.9**, **3.10** and **3.13** for the *t*-Bu, SiMe₃ and CF₃ groups respectively. Compared to the iodides, the 2,6-Xyl flanking carbons remain unshifted, and only minor shifts are observed for the central rings, except for the *ipso*-carbons which are shifted downfield (C-1 = 106.9 vs. 172.7 ppm for **3.4** and **3.11** respectively) owing to a large deshielding effect in the plane perpendicular to the C–Li bond.^{97,189–192} In all cases, the *ipso*-carbon NMR resonances were of low intensity and were thus assigned using the HMBC spectra of **3.9** – **3.13**. For the unsubstituted **3.11**, an optimised ^{13}C NMR experiment was performed to achieve better resolution of the *ipso*-carbon peak (**Fig. 3.11**). The results revealed a seven-line splitting pattern (blue) centred at 172.7 ppm with a 1:2:3:4:3:2:1 intensity ratio ($^1J_{^{13}\text{C}^7\text{Li}} = 23.3$ Hz) characteristic of quadrupolar coupling to two ^7Li nuclei (spin: 3/2, abundance: 92.41%), which provides further evidence that the lithium complexes are dimeric in *d*-benzene solution.^{193–196} These findings agree with the simulated spectrum (red), although the ^6Li splitting (spin = 1, abundance = 7.59%) could not be resolved experimentally.

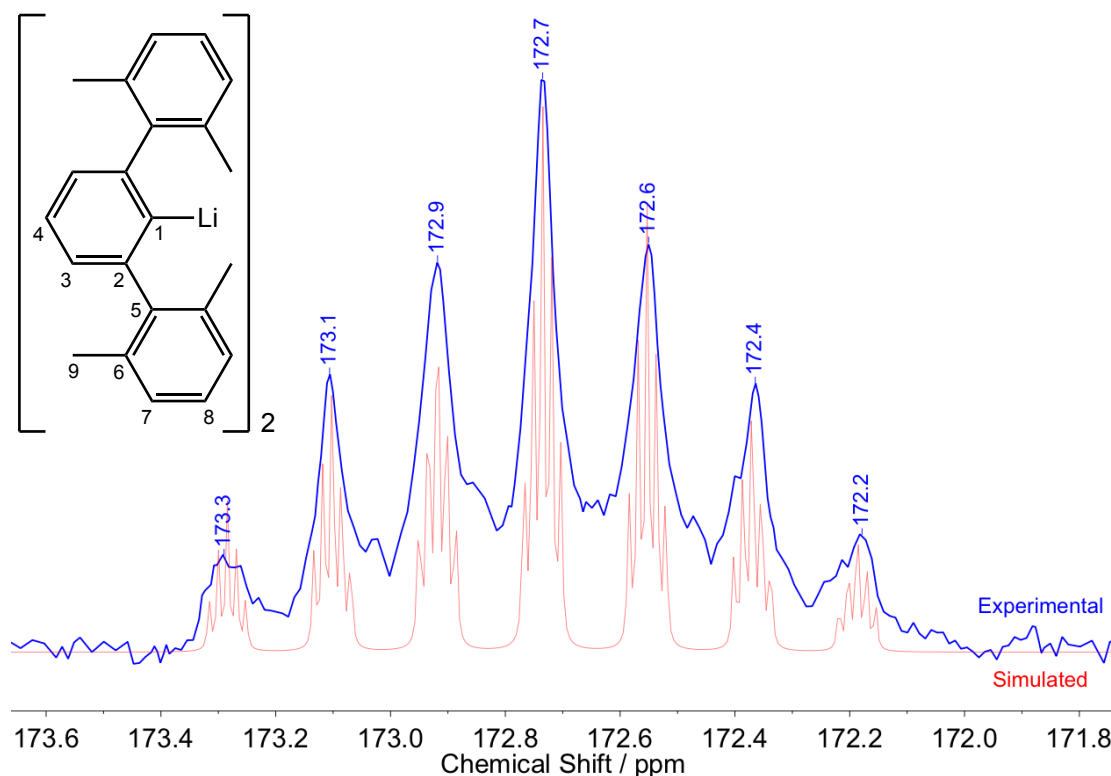


Fig. 3.11 Seven-line splitting pattern of the *ipso*-carbons in the experimental (blue) and simulated (red) ^{13}C NMR spectra of $[\text{H-Ar-Li}]_2$ (**3.11**).

A comparison of the ^{13}C NMR spectra of **3.9**–**3.13** reveals that C-5 (144.8–147.1 ppm), C-6 (136.1–136.4 ppm), C-7 (128.9–129.1 ppm), C-8 (127.3–128.0 ppm) and C-9 (21.5–21.9 ppm) of the 2,6-Xyl flanking groups remain essentially unshifted across the series. The unusual shift observed for the 2,6-Xyl methyl groups in the ^1H NMR is not replicated in the ^{13}C NMR, suggesting only the protons are noticeably affected. Akin to the iodides, the peaks for the central ring carbons shift considerably, except for C-2, see **Table 3.6**. Again, the largest shifts are noted for C-4 (126.3–148.7 ppm), while smaller shifts occur for C-1 (168.1–180.2 ppm) and C-3 (119.5–128.1 ppm). Though no reliable trends can be identified, a general downfield shift is observed for C-1 as electron-withdrawing character of the *para*-substituent is increased. This provides evidence that *para*-functionalisation does influence the electronic properties within the central rings of the *m*-terphenyl lithium complexes, importantly at the *ipso*-carbon.

The ^7Li NMR spectra of **3.9** – **3.13** were recorded. Despite the sensitive nature of ^7Li NMR spectra to the analyte concentration, aggregation and solvent effects, these factors appear to be negligible, possibly due to the steric bulk of the ligands that prevents interaction of the metal centre with the surrounding solvent.^{197–199} This is shown by the soluble *t*-Bu complex, **3.9**, whose ^7Li NMR resonance remains unshifted by varying the analyte concentration (1.60 ppm at 24, 48 and 72 mM, respectively). For all other complexes, saturated samples were used due to their poor solubilities in *d*-benzene. Furthermore, the steric effects of the 2,6-Xyl flanking groups on the lithium ions are assumed to remain consistent throughout the series and, therefore, do not contribute to the shifting of the NMR resonances. This is in contrast to other literature *m*-terphenyl lithium complexes, where changing the flanking groups shifts the ^7Li NMR signal.^{80,81}

In all cases, the ^7Li NMR spectra show a single peak indicating one environment in solution for the two lithium ions of the dimer. The position of these peaks shifts upfield (1.60, 1.47, 1.46, 1.10 and 0.93 ppm for **3.9** – **3.13**, respectively) as electron-withdrawing strength of the *para*-substituent is increased, see **Table 3.6**. In fact, plotting a graph of these chemical shifts, δ , against the Hammett constants, σ_{para} , reveals a linear correlation (**Fig. 3.12**).¹³⁹ This suggests that *para*-substitution directly influences the electronic properties at the lithium centres. Moreover, the trend proceeds in the opposite direction than expected, since electron-withdrawing groups usually deshield the nuclei and cause a downfield shift. Despite this, a similar observation was reported in 1972 for a series of *para*-substituted aryllithiums, $[4\text{-R-C}_6\text{H}_4]_2\text{Li}$ (R = OMe, Me, H, F, Cl, CF₃).^{200–202} However, a Hammett plot of their findings presents outliers; the reported data may be inaccurate due to the debated aggregation state of phenyllithium in solution at the time.^{200–208}

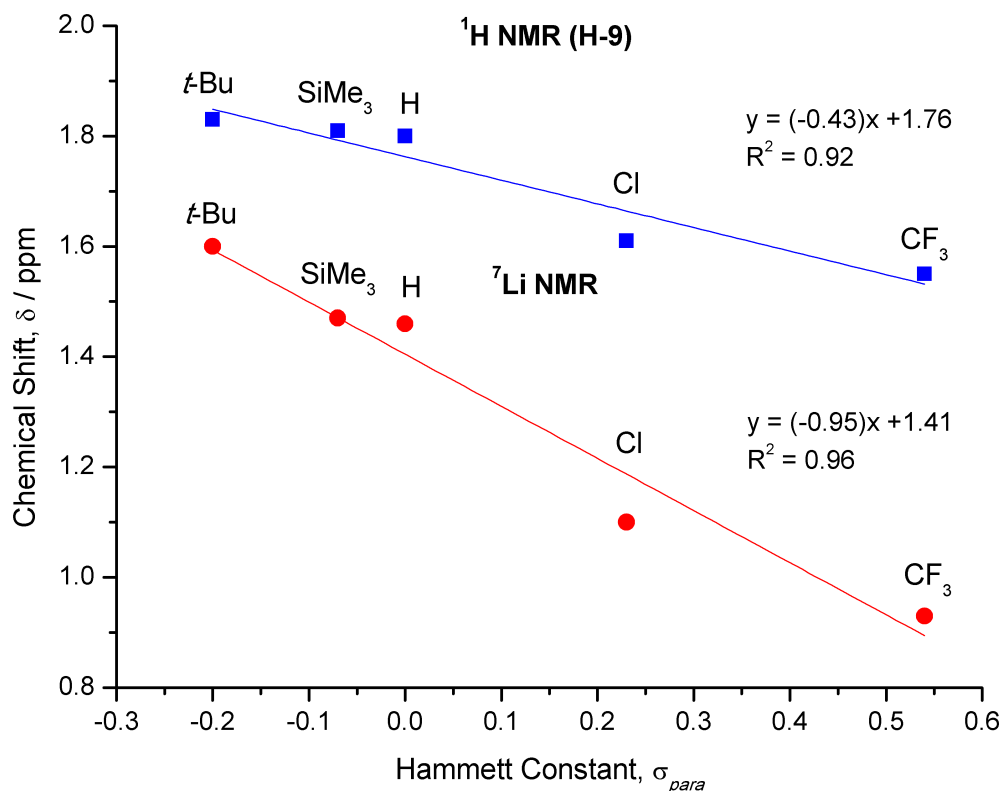


Fig 3.12 Plot of the ^1H (for flanking methyl protons, H-9) and ^7Li NMR chemical shifts, δ , for the *para*-substituted lithium complexes, $[\text{R-Ar-Li}]_2$, **3.9** – **3.13**, versus their corresponding literature Hammett constants, σ_{para} .¹³⁹

These ^7Li NMR results help elucidate the ^1H NMR trend mentioned in **Table 3.6**, where the flanking methyl protons, H-9, were also shifted downfield by electron-withdrawing groups (**Fig. 3.12**). Since all other atoms on the 2,6-Xyl rings remain unshifted by the changing *para*-substituents, this suggests that the electronic effects could instead be transferred to the flanking methyl protons via the lithium atoms. Evidence of this may already have been provided by the crystallographic structures; in the solid-state, weak $\text{Li}\cdots\text{H}-\text{C}$ anagostic interactions were identified between these atoms (**Fig. 3.8/3.9**). In solution, however, this theory is corroborated by two-dimensional ^7Li - ^1H heteronuclear Overhauser NMR spectroscopy (HOESY).^{149,209} This technique reveals short $^7\text{Li}\cdots^1\text{H}$ contacts in **3.9** – **3.13** as evidenced by the intense cross-peak between the lithium ions and the flanking methyl protons, H-9, in each of their 2D NMR spectra (**Fig. 3.13**).

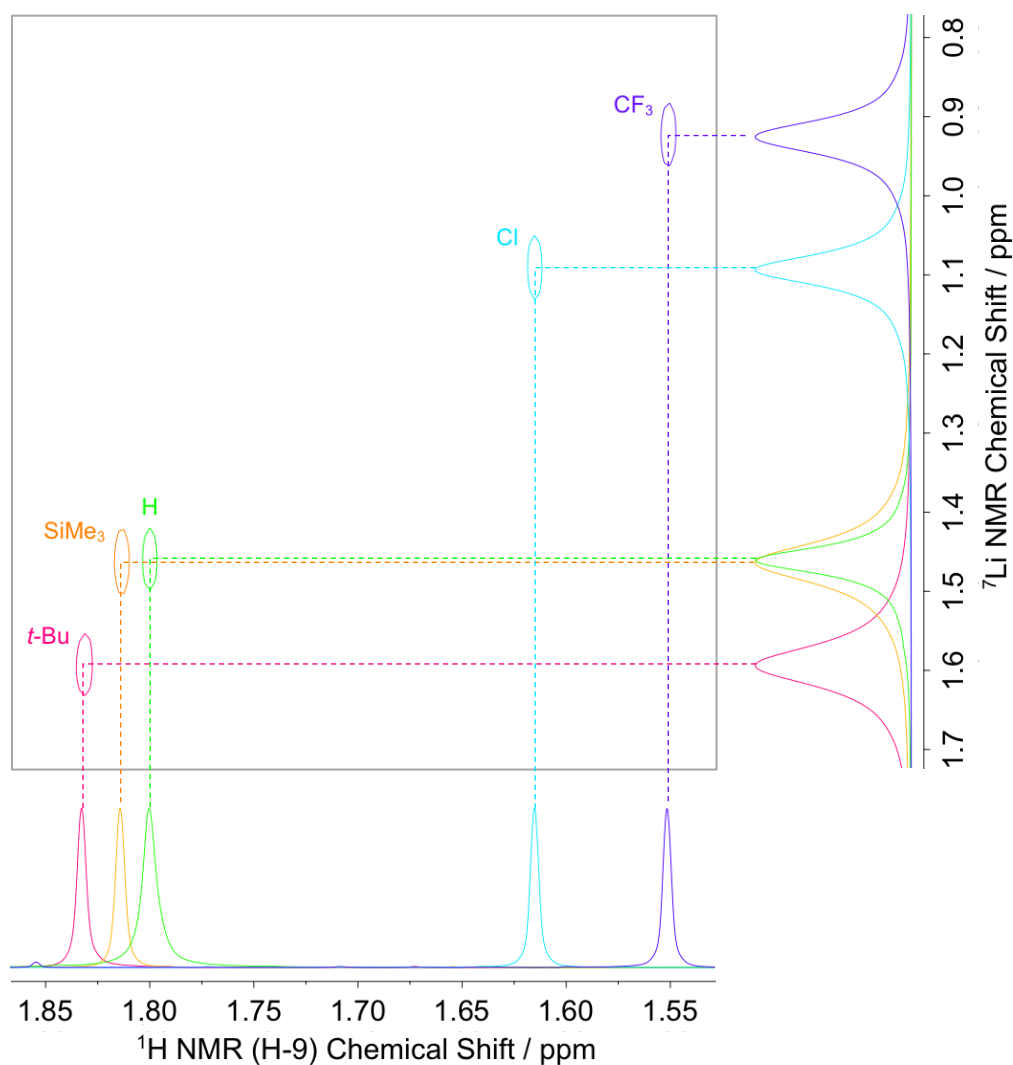


Fig 3.13 Superimposed 2D ${}^7\text{Li}$ - ${}^1\text{H}$ HOESY spectra of the five *m*-terphenyl lithium complexes, $[\text{R-Ar-Li}]_2$, **3.9** – **3.13**, showing strong cross-peaks between the flanking methyl protons, H-9, and the ${}^7\text{Li}$ nuclei.

Similar $\text{Li}\cdots\text{H}$ interactions have been reported for the monomeric $[\text{Mes}^*\text{-Li}]$ species, whose ${}^6\text{Li}$ - ${}^1\text{H}$ HOESY spectrum gave a cross-peak for the *ortho*-*t*-Bu protons, but not for the *para*-*t*-Bu protons.¹⁹⁰ Moreover, the *ortho*- groups (1.61 ppm) occurred at lower field than the *para*-groups (1.56 ppm), owing to the electric field produced by lithium that deshields the protons within close proximity.¹⁹⁰ Comparable findings have been described for other lithium complexes $[\text{Ar-Li}]$ ($\text{Ar} = \text{Naph}, 2\text{-}\{t\text{-BuS}\}\text{C}_6\text{H}_4$).^{210,211}

From this, it is suggested that the electronic effects of the *para*-substituents in complexes **3.9** – **3.13** are relayed through the central *m*-terphenyl ring, onto the lithium ions, then through-space onto the nearby flanking methyl groups. These through-space interactions could possibly arise from an electric field produced by the lithium centres, whose field strength would vary depending on the *para*-substituent. In fact, evidence of similar through-space interactions within the *m*-terphenyl framework has already been reported. Specifically, for a literature series of *m*-terphenyl carboxylic acids (2,6-Ar₂C₆H₃)COOH (Ar = 4-R-C₆H₄; R = OMe, Me, H, F, Cl, Br, C{O}Me), *para*-substitution of their flanking aryl rings influences their measured p*K*_a values, owing to through-space effects.²¹² Another example involves the *m*-terphenyl silane (2,6-Ar₂C₆H₃)SiMe₂H (Ar = 2,6-F₂C₆H₃), whose flanking aryl fluorine atoms couple through-space to the Si–H proton.²¹³ The presence of through-space interactions in complexes **3.9** – **3.13** would therefore explain why both the ¹H and ⁷Li NMR trends proceed in the same direction (**Fig. 3.12**).

However, a computational analysis would be required to fully explain the upfield shifts of the ¹H and ⁷Li NMR spectra as electron-withdrawing power of the *para*-group is increased. It has previously been theorised that *para*-substitution in phenyllithium alters the ionic character of the C–Li bond. Here, electron-withdrawing groups enhance the bond covalency, which increases the availability of C–Li σ-bonded electrons for orbital mixing. This mixing generates paramagnetic circulations of the *ipso*-carbon electrons, whose resultant magnetic anisotropy enables greater shielding of the lithium centres and causes the observed upfield NMR peak shifts.^{200–202}

3.3 Conclusions

A series of *para*-functionalised *m*-terphenyl iodide ligand precursors **3.2** – **3.8** has been reported. Crystallographically, the compounds are structurally similar, with comparable C–I bond lengths and little change in the dihedral angles between their central C(1)-aryl ring and the 2,6-Xyl groups; restricting the flanking group to 2,6-Xyl across the series minimises steric effects at these positions. However, NMR spectroscopy reveals that, while *para*-substitution has negligible effect on the 2,6-Xyl flanking groups, it does cause significant electronic change in the central ring, notably at the *ipso*-carbon. Overall, all iodides were synthesised on a large scale feasible for future metal complex synthesis, except for **3.7** which was too low-yielding to be practically useful.

A series of *para*-substituted *m*-terphenyl lithium complexes **3.9** – **3.13** were then prepared from the iodides, although lithiation of **3.8** failed to yield any substantial products. In the solid-state, the complexes are structurally similar, forming dimers with weak Li···H–C anagostic contacts between the lithium ions and the flanking methyl groups. In solution, the complexes retain these dimeric structures, as shown by DOSY experiments and optimised ¹³C NMR spectroscopy. Furthermore, NMR spectroscopic studies reveal electronic differences both in the ligand framework and at the metal centre, evidenced by the linear correlation of the ⁷Li NMR chemical shifts with the Hammett constants of the *para*-substituents. The flanking methyl protons, H-9, exhibit similar shifts in their ¹H NMR spectra, possibly due to the through-space Li···H interactions observed by ⁷Li-¹H HOESY experiments. In all cases, the NMR trends proceed in the opposite direction to that expected, where electron-withdrawing substituents cause an upfield peak shift. Future computational modelling will therefore be required to elucidate the electronic nature of these lithium complexes.

3.4 Future Work

Aside from performing the aforementioned computational calculations on the lithium complexes **3.9** – **3.13**, a potential future project could be to synthesis a new class of *para*-functionalised *m*-terphenyl ligands substituted with molecular anchors aimed at tethering their metal complexes to solid surfaces. For example, the incorporation of a pyrene moiety at the *para*-position could enable the *m*-terphenyl framework to form π - π stacking interactions with graphene-type surfaces (**Fig. 3.14**).²¹⁴ This is preferable over covalent-tethering, whose demand for harsher reaction conditions could cause decomposition of the metal complexes.²¹⁵ While the primary objective would be to study the surface-binding interactions exhibited by low-coordinate metal complexes, the effects of this tethering upon their small molecule reactivity and catalytic properties would also be of interest.^{216,217}

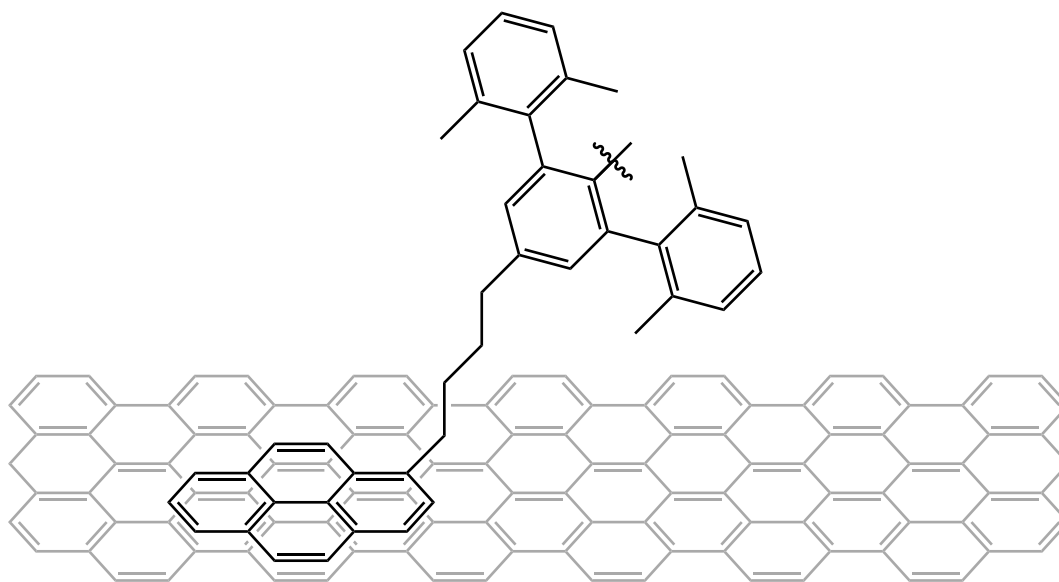


Fig. 3.14 Proposed *m*-terphenyl *para*-substitution with a pyrene group to enable tethering of its metal complexes to graphene-type surfaces via π - π stacking.

3.5 Experimental

3.5.1 Grignard Synthesis: 2,6-Xyl

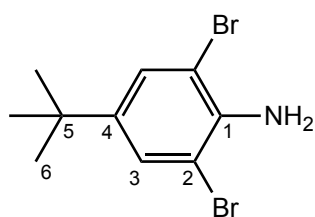
3.5.1.1 (2,6-Dimethylphenyl)magnesium bromide (3.1)



Magnesium turnings (9.85 g, 405 mmol) were activated by stirring in a solution of iodine (*ca.* 50 mg) in acetone (30 mL) for 20 mins, after which time the magnesium was washed with acetone (4 x 20 mL), oven-dried for 10 mins, then gently stirred under vacuum for 16 h. To the magnesium, dry THF (*ca.* 150 mL) was added. This mixture was heated to reflux, then a solution of 2-bromo-1,3-dimethylbenzene (**3.1a**) (50.0 g, 270 mmol) in THF (*ca.* 100 mL) was added dropwise over 1 h. The resultant black mixture was refluxed at 90 °C under argon for 4 h, then was cooled to room temperature and left to settle over 12 h. After this time, the mixture was filtered to give a brown solution of the product **3.1** (*ca.* 56.6 g, 270 mmol) which was stored under argon until its direct use in later reaction steps. This was not characterised due to being a transient reagent.

3.5.2 Ligand Synthesis: *t*-Bu

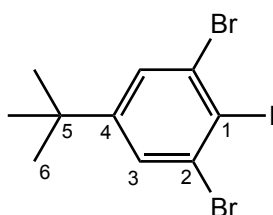
3.5.2.1 2,6-Dibromo-4-*t*-butylaniline (3.2b)



4-*t*-Butylaniline (**3.2a**) (16.0 g, 107 mmol) was dissolved in dichloromethane (250 mL) under argon, then a solution of bromine (13.8 mL, 268 mmol) in dichloromethane (100 mL) was added dropwise. The resultant dark red solution was stirred for 16 h at room temperature. After this, an orange solid had precipitated. The mixture was poured onto deionised water (200 mL) at 0 °C, then aqueous sodium bicarbonate (200 mL, 1 M) was added. The organic layer was separated, and the aqueous phase was washed with diethyl ether (3 x 50 mL), then the organics were combined, dried over MgSO₄, and

filtered. The filtrate was reduced under vacuum to yield a dark red-purple oil that was purified by plug column chromatography on silica gel eluted with petroleum ether (40-60)/dichloromethane 5:1 (v/v) to afford the crude product **3.2b** (30.4 g, 92%) as a red oil. The compound was used directly in the next reaction without further purification. IR $\nu_{\max}(\text{neat})/\text{cm}^{-1}$ 3477(w), 3379(w), 2960(m), 2905(w), 2866(w), 1611(m), 1577(m), 1540(m), 1479(s), 1392(m), 1362(m), 1291(m), 1256(m), 1059(w), 869(m), 731(s), 709(m); $^1\text{H NMR}$ δ_{H} (400 MHz; CDCl_3): 7.34 (2H, s, 2 x H-3), 4.36 (2H, br s, NH_2), 1.21 (9H, s, 9 x H-6); $^{13}\text{C NMR}$ δ_{C} (101 MHz; CDCl_3): 143.0 (C-4), 139.5 (C-1), 128.9 (C-3), 108.8 (C-2), 34.1 (C-5), 31.4 (C-6); HRMS (ESI), m/z : (Found: 305.9490. Calc. for $\text{C}_{10}\text{H}_{13}\text{Br}_2\text{N}_1$: 305.9488.)

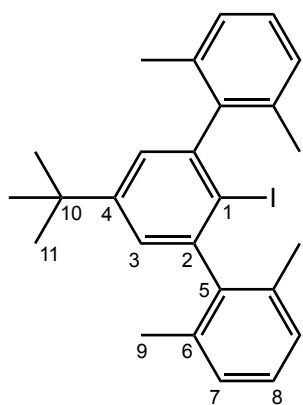
3.5.2.2 1-Iodo-2,6-dibromo-4-*t*-butylbenzene (3.2c)



To a mixture of sodium nitrite (3.75 g, 54.3 mmol) in conc. sulfuric acid (32 mL) kept at 0 °C, a solution of 2,6-dibromo-4-*t*-butylaniline (**3.2b**) (15.0 g, 48.9 mmol) in glacial acetic acid (160 mL) was added slowly. The resultant black slurry was stirred at room temperature for 4 h. After this time, a solution of potassium iodide (58.7 g, 354 mmol) and iodine (13.8 g, 54.3 mmol) in deionised water (120 mL) was added slowly to the reaction mixture. The resultant dark purple mixture was stirred at room temperature for 16 h. The mixture was then carefully poured into an aqueous solution of sodium hydroxide (1.5 L, 30%) to give a cloudy orange mixture that was extracted with ethyl acetate (3 x 400 mL). The combined organics were washed with aqueous sodium thiosulfate (300 mL, 10%), brine (300 mL), and deionised water (300 mL), then were dried over MgSO_4 , and filtered. The filtrate was reduced under vacuum to yield a brown-black oil that was purified by plug column chromatography on silica gel eluted

with petroleum ether (40-60) to afford the crude product **3.2c** (16.8 g, 82%) as an orange liquid. The compound was used directly in the next reaction without further purification. IR $\nu_{\text{max}}(\text{neat})/\text{cm}^{-1}$ 2962(m), 2905(w), 2866(w), 2109(w), 1571(w), 1522(m), 1499(m), 1373(m), 1259(m), 1212(w), 1183(w), 1000(w), 869(m), 768(w), 735(s), 690(w); ^1H NMR δ_{H} (400 MHz; CDCl_3): 7.55 (2H, s, 2 x H-3), 1.28 (9H, s, 9 x H-6); ^{13}C NMR δ_{C} (101 MHz; CDCl_3): 154.6 (C-4), 131.0 (C-2), 128.8 (C-3), 105.1 (C-1), 35.0 (C-5), 31.0 (C-6); HRMS (EI), m/z: (Found: 415.82861. Calc. for $\text{C}_{10}\text{H}_{11}\text{Br}_2\text{I}$: 415.82667.)

3.5.2.3 *t*-Bu-Ar-I (3.2)

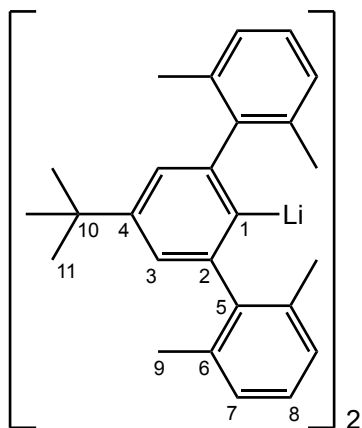


1-Iodo-2,6-dibromo-4-*t*-butylbenzene (**3.2c**) (33.0 g, 79.0 mmol) was dissolved in dry THF (*ca.* 400 mL) at 0 °C under argon. To this, the pre-prepared Grignard of (2,6-dimethylphenyl)magnesium bromide (**3.1**) (*ca.* 53.6 g, 256 mmol) in THF (*ca.* 200 mL) was added dropwise at 0 °C over 1 h. The red solution was then refluxed at 85 °C for 16 h.

After this time, the solution was re-cooled to 0 °C, then iodine (105 g, 413 mmol) was added over 1 h. The mixture was refluxed at 85 °C for 16 h. After this, the solution was cooled to room temperature, and aqueous sodium sulfite (1.7 L, 1 M) was added. The organic layer was separated and the aqueous phase was washed with diethyl ether (3 x 200 mL). The combined organics were washed with aqueous sodium thiosulfate (300 mL, 10%) and deionised water (2 x 100 mL), then were dried over MgSO_4 , and filtered. The filtrate was reduced under vacuum to give a brown oily-solid which was heated at 150 °C under vacuum for 1 h to remove any residual 2,6-Xyl-I impurity from the mixture. The resultant brown solid was purified by plug column chromatography

on silica gel eluted with petroleum ether (40-60) to afford a pale orange-white solid. This solid was recrystallised from boiling ethanol (450 mL) to form crystals on cooling to room temperature. The solid was collected by suction filtration, washing with cold methanol (2 x 100 mL), to yield product **3.2** (33.1 g, 89%) as white crystalline needles. Elemental analysis: (Found: C, 66.5; H, 6.3. Calc. for C₂₆H₂₉I₁: C, 66.7; H, 6.2%); IR $\nu_{\max}(\text{neat})/\text{cm}^{-1}$ 2960(m), 2902(m), 2867(w), 1474(m), 1393(m), 1240(w), 1056(m), 881(m), 768(s); ¹H NMR δ_{H} (400 MHz; CDCl₃): 7.26 (2H, t, *J* 7.5 Hz, 2 x H-8), 7.17 (4H, d, *J* 7.8 Hz, 4 x H-7), 7.16 (2H, s, 2 x H-3), 2.06 (12H, s, 12 x H-9), 1.35 (9H, s, 9 x H-11); ¹³C NMR δ_{C} (101 MHz; CDCl₃): 152.6 (C-4), 146.6 (C-2), 145.3 (C-5), 135.8 (C-6), 127.7 (C-8), 127.4 (C-7), 125.0 (C-3), 102.4 (C-1), 34.9 (C-10), 31.5 (C-11), 20.5 (C-9); HRMS (FD), *m/z*: (Found: 468.1304. Calc. for C₂₆H₂₉I₁: 468.1309.)

3.5.2.4 [*t*-Bu-Ar-Li]₂ (**3.9**)



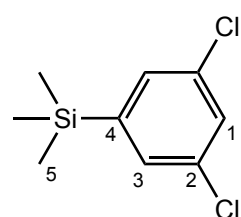
t-Bu-Ar-I (**3.2**) (5.00 g, 10.7 mmol) was dried under vacuum for 16 h. Hexane (*ca.* 70 mL) was added and the white mixture was cooled to 0 °C. Once cooled, *n*-butyllithium (7.7 mL, 2.5 M in hexanes, 19.2 mmol) was added slowly, then the pale yellow solution was stirred for 16 h, allowing to warm to room temperature.

After this time, a white solid impurity had precipitated, which was left to settle for 1 h. The mixture was filtered, and the residue was washed with hexane (2 x 10 mL), to afford a yellow solution that was concentrated to 30 mL under vacuum, causing a white solid to precipitate. This mixture was stirred for 2 h, after which the solid was left to settle for 1 h. The solid was filtered, washed with hexane (5 x 10 mL), and dried under vacuum for 6 h to yield the product **3.9** (1.40 g, 38%) as a white powder. ¹H NMR δ_{H}

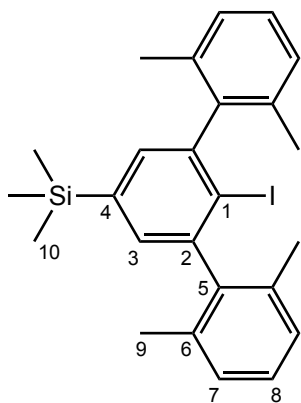
(400 MHz; C₆D₆): 7.01 (12H, s, 8 x H-7 and 4 x H-8), 6.85 (4H, s, 4 x H-3), 1.83 (24H, s, 24 x H-9), 1.23 (18H, s, 18 x H-11); ¹³C NMR δ_C (101 MHz; C₆D₆): 168.1 (m, C-1), 152.0 (C-2), 148.7 (C-4), 147.1 (C-5), 136.4 (C-6), 128.9 (C-7), 127.3 (C-8), 120.4 (C-3), 34.4 (C-10), 31.7 (C-11), 21.8 (C-9); ⁷Li NMR δ_{Li} (155 MHz; C₆D₆): 1.60 (s).

3.5.3 Ligand Synthesis: SiMe₃

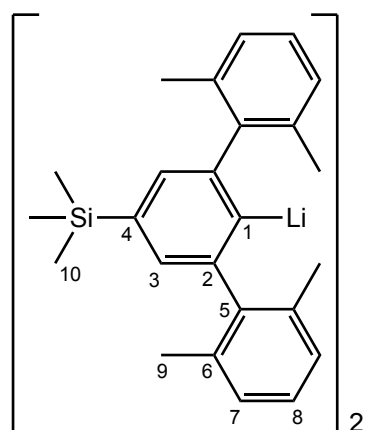
3.5.3.1 3,5-Dichloro-1-trimethylsilylbenzene (3.3b)



Magnesium turnings (6.70 g, 276 mmol) were activated by stirring in a solution of iodine (*ca.* 50 mg) in acetone (30 mL) for 20 mins, after which the magnesium was washed with acetone (4 x 20 mL), oven-dried for 10 mins, then stirred under vacuum over 16 h. To the magnesium, dry THF (*ca.* 100 mL) and trimethylchlorosilane (69.9 mL, 551 mmol) were added. This mixture was then heated as a stirred solution of 1,3,5-trichlorobenzene (**3.3a**) (50.0 g, 276 mmol) in dry THF (*ca.* 100 mL) was added dropwise over 1 h, until the reaction became self-sustaining. The resultant grey mixture was refluxed at 90 °C under argon for 16 h. After this time, the beige mixture was reduced under vacuum, then petroleum ether (40-60) (250 mL) was added and the mixture was filtered. The yellow filtrate was reduced under vacuum to give the crude product as a yellow liquid. This liquid was purified via distillation by heating to 45 °C under vacuum (*ca.* 10⁻⁴ mbar) to collect the product **3.3b** (51.2 g, 85%) as a colourless liquid. IR ν_{max}(neat)/cm⁻¹ 3067(w), 2958(s), 2898(w), 1570(m), 1551(s), 1392(m), 1371(s), 1252(s), 1137(s), 1100(m), 839(s), 797(s), 755(s); ¹H NMR δ_H (400 MHz; CDCl₃): 7.33 (3H, m, 3 x H-1/3), 0.28 (9H, s, 9 x H-5); ¹³C NMR δ_C (101 MHz; CDCl₃): 145.2 (C-4), 134.9 (C-2), 131.4 (C-3), 128.9 (C-1), -1.2 (C-5); ²⁹Si NMR δ_{Si} (79 MHz; CDCl₃): -2.08 (s); HRMS (EI), m/z: (Found: 218.0076. Calc. for C₉H₁₂Cl₂Si₁: 218.0080.)

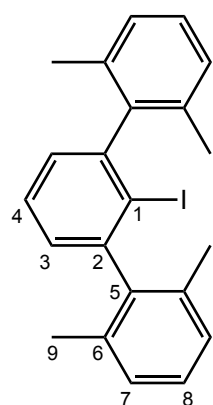
3.5.3.2 *Me₃Si-Ar-I* (**3.3**)

To a solution of 3,5-dichloro-1-trimethylsilylbenzene (**3.3b**) (26.9 g, 123 mmol) in dry THF (*ca.* 250 mL) at $-78\text{ }^{\circ}\text{C}$, *n*-butyllithium (54.0 mL, 2.5 M in hexanes, 135 mmol) was added dropwise over 1 h. The pale yellow mixture was stirred at $-78\text{ }^{\circ}\text{C}$ for 2 h, then the pre-prepared Grignard of (2,6-dimethylphenyl)magnesium bromide (**3.1**) (*ca.* 56.6 g, 270 mmol) in THF (*ca.* 300 mL) was added dropwise at $-78\text{ }^{\circ}\text{C}$ over 1 h. The dark brown solution was warmed to room temperature over 16 h, then was refluxed at $90\text{ }^{\circ}\text{C}$ for 2 h. The solution was cooled to $0\text{ }^{\circ}\text{C}$, and iodine (46.7 g, 184 mmol) was added over 1 h. The dark purple solution was refluxed at $90\text{ }^{\circ}\text{C}$ for 2 h, then was cooled to room temperature and stirred for 16 h. Aqueous sodium sulfite (500 mL, 1 M) was added, then the organic and aqueous phases were separated, washing the aqueous with diethyl ether (3 x 100 mL). The organics were combined, dried over MgSO_4 , filtered, then the filtrate was reduced to dryness to give a beige powder that was recrystallised from hot diethyl ether (300 mL). The crystals were collected by suction filtration, washing with cold methanol (3 x 50 mL), to yield product **3.3** (25.7 g, 43%) as a white crystalline solid. Elemental analysis: (Found: C, 62.0; H, 6.1. Calc. for $\text{C}_{25}\text{H}_{29}\text{Si}_1\text{I}_1$: C, 62.0; H, 6.0%); IR ν_{max} (neat)/ cm^{-1} 3019(w), 2949(w), 2910(w), 1462(w), 1442(w), 1356(w), 1248(m), 1037(w), 860(s), 834(s), 770(s), 694(m); ^1H NMR δ_{H} (400 MHz; CDCl_3): 7.26 (2H, t, *J* 7.5 Hz, 2 x H-8), 7.23 (2H, s, 2 x H-3), 7.17 (4H, d, *J* 7.7 Hz, 4 x H-7), 2.05 (12H, s, 12 x H-9), 0.29 (9H, s, 9 x H-10); ^{13}C NMR δ_{C} (101 MHz; CDCl_3): 146.3 (C-2), 145.1 (C-5), 141.7 (C-4), 135.8 (C-6), 132.3 (C-3), 127.7 (C-8), 127.4 (C-7), 107.7 (C-1), 20.6 (C-9), -1.0 (C-10); ^{29}Si NMR δ_{Si} (79 MHz; CDCl_3): -3.26 (s); HRMS (FD), *m/z*: (Found: 484.1086. Calc. for $\text{C}_{25}\text{H}_{29}\text{Si}_1\text{I}_1$: 484.1078.)

3.5.3.3 $[Me_3Si-Ar-Li]_2$ (**3.10**)

$Me_3Si-Ar-I$ (**3.3**) (5.00 g, 10.3 mmol) was dried under vacuum for 16 h. Hexane (*ca.* 70 mL) was added and the white mixture was cooled to 0 °C. Once cooled, *n*-butyllithium (7.4 mL, 2.5 M in hexanes, 18.6 mmol) was added slowly, then the white mixture was stirred for 16 h, allowing to warm to room temperature. After this

time, the solid was left to settle for 1 h. The solid was filtered, washed with hexane (2 x 10 mL), and dried under vacuum for 16 h to yield the product **3.10** (2.27 g, 60%) as a white powder. 1H NMR δ_H (400 MHz; C_6D_6): 7.04 (4H, s, 4 x H-3), 6.99 (12H, s, 8 x H-7 and 4 x H-8), 1.81 (24H, s, 24 x H-9), 0.21 (18H, s, 18 x H-10); ^{13}C NMR δ_C (101 MHz; C_6D_6): 174.2 (C-1), 151.6 (C-2), 146.7 (C-5), 136.5 (C-4), 136.4 (C-6), 129.0 (C-7), 128.1 (C-3), 127.4 (C-8), 21.9 (C-9), -0.8 (C-10); ^{29}Si NMR δ_{Si} (79 MHz; C_6D_6): -5.58 (s); 7Li NMR δ_{Li} (155 MHz; C_6D_6): 1.47 (s).

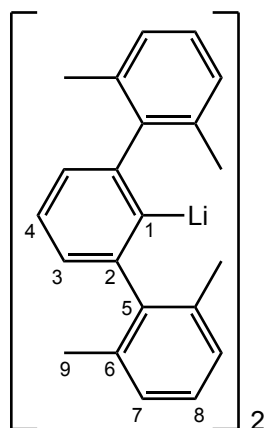
3.5.4 Ligand Synthesis: *H*3.5.4.1 *H-Ar-I* (**3.4**)

To a solution of 1,3-dichlorobenzene (**3.4a**) (18.1 g, 123 mmol) in dry THF (*ca.* 200 mL) at -78 °C, *n*-butyllithium (59.0 mL, 2.5 M in hexanes, 148 mmol) was added dropwise over 1 h. The white mixture was stirred at -78 °C for 1 h, then the pre-prepared Grignard of (2,6-dimethylphenyl)magnesium bromide (**3.1**) (*ca.* 56.6 g, 270 mmol) in THF (*ca.* 200 mL) was added dropwise at -78 °C over

1 h. The brown solution was warmed to room temperature over 16 h, refluxed at 90 °C for 2 h, cooled to 0 °C, then iodine (46.7 g, 184 mmol) was added over 1 h. The purple

mixture was refluxed at 90 °C for 2 h, cooled to room temperature, then aqueous sodium sulfite (500 mL, 1 M) was added. The organic and aqueous phases were separated, and the aqueous was washed with diethyl ether (3 x 100 mL). The organics were combined, dried over MgSO₄, filtered, then the filtrate was dried to give a yellow solid that was recrystallised in boiling ethanol (500 mL). The solid was collected, washing with cold methanol (3 x 50 mL), to give product **3.4** (20.7 g, 41%) as a beige crystalline powder. IR $\nu_{\text{max}}(\text{neat})/\text{cm}^{-1}$ 3037(w), 2968(w), 2933(w), 2911(w), 2852(w), 1579(w), 1457(m), 1385(w), 1163(w), 1079(w), 1012(w), 1001(w), 803(m), 768(s), 734(s), 694(w), 549(w); ¹H NMR δ_{H} (400 MHz; CDCl₃): 7.52 (1H, t, *J* 7.5 Hz, 1 x H-4), 7.26 (2H, t, *J* 7.5 Hz, 2 x H-8), 7.17 (4H, d, *J* 7.7 Hz, 4 x H-7), 7.14 (2H, d, *J* 7.5 Hz, 2 x H-3), 2.06 (12H, s, 12 x H-9); ¹³C NMR δ_{C} (101 MHz; CDCl₃): 147.3 (C-2), 144.8 (C-5), 135.7 (C-6), 129.1 (C-4), 127.8 (C-3), 127.7 (C-8), 127.4 (C-7), 106.9 (C-1), 20.5 (C-9).

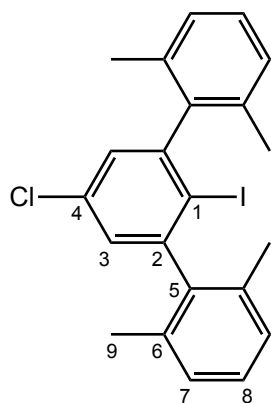
3.5.4.2 [*H-Ar-Li*]₂ (**3.11**)



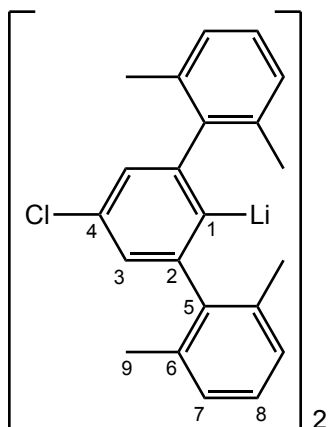
H-Ar-I (**3.4**) (5.00 g, 12.1 mmol) was dried under vacuum for 16 h. Hexane (*ca.* 70 mL) was added and the yellow mixture was cooled to 0 °C, then *n*-butyllithium (7.2 mL, 2.5 M in hexanes, 18.2 mmol) was added slowly. The mixture was stirred for 16 h, warmed to room temperature, then left to settle for 1 h. The solid was filtered, washed with hexane (2 x 10 mL), and dried under vacuum for 16 h to yield product **3.11** (3.49 g, 99%) as a white powder. ¹H NMR δ_{H} (400 MHz; C₆D₆): 7.19 (2H, t, *J* 7.5 Hz, 2 x H-4), 6.98 (12H, s, 8 x H-7 and 4 x H-8), 6.77 (4H, d, *J* 7.5 Hz, 4 x H-3), 1.80 (24H, s, 24 x H-9); ¹³C NMR δ_{C} (126 MHz; C₆D₆): 172.7 (septet, *J* 23.3 Hz, C-1), 152.0 (C-2), 146.4 (C-5), 136.3 (C-6), 129.0 (C-7), 127.4 (C-8), 126.3 (C-4), 123.6 (C-3), 21.8 (C-9); ⁷Li NMR δ_{Li} (155 MHz; C₆D₆): 1.46 (s).

3.5.5 Ligand Synthesis: Cl

3.5.5.1 Cl-Ar-I (3.5)



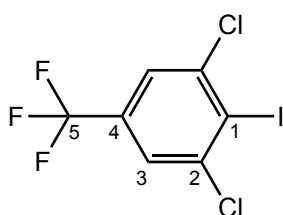
To a solution of 1,3,5-trichlorobenzene (**3.5a**) (22.3 g, 123 mmol) in dry THF (*ca.* 200 mL) at $-78\text{ }^{\circ}\text{C}$, *n*-butyllithium (54.0 mL, 2.5 M in hexanes, 135 mmol) was added dropwise over 1 h. The pale yellow solution was stirred at $-78\text{ }^{\circ}\text{C}$ for 1 h, then the Grignard of (2,6-dimethylphenyl)magnesium bromide (**3.1**) (*ca.* 56.6 g, 270 mmol) in THF (*ca.* 200 mL) was added dropwise at $-78\text{ }^{\circ}\text{C}$ over 1 h. The brown solution was warmed to room temperature over 16 h, then was refluxed at $90\text{ }^{\circ}\text{C}$ for 2 h. The solution was cooled to $0\text{ }^{\circ}\text{C}$, and iodine (46.7 g, 184 mmol) was added over 1 h. The dark purple mixture was refluxed at $90\text{ }^{\circ}\text{C}$ for 2 h, cooled to room temperature, then aqueous sodium sulfite (500 mL, 1 M) was added. The organic and aqueous phases were separated, washing the aqueous with diethyl ether (3 x 100 mL), then the organics were combined, dried over MgSO_4 , and filtered. The filtrate was dried to give an orange oil which was heated under vacuum for 1 h at $80\text{ }^{\circ}\text{C}$ to remove any 2,6-Xyl-I impurity. The crude product was recrystallised in diethyl ether (300 mL) via solvent evaporation over 5 days. The solid was isolated by suction filtration, washing with cold diethyl ether (3 x 50 mL), to give product **3.5** (12.7 g, 23%) as white needles. IR $\nu_{\text{max}}(\text{neat})/\text{cm}^{-1}$ 3055(w), 3021(w), 2942(w), 2912(w), 2852(w), 1583(w), 1561(w), 1461(m), 1440(w), 1379(m), 1296(w), 1110(m), 1001(s), 870(m), 828(w), 777(s), 765(s), 551(w), 474(m); ^1H NMR δ_{H} (400 MHz; CDCl_3): 7.26 (2H, t, J 7.5 Hz, 2 x H-8), 7.17 (2H, s, 2 x H-3), 7.16 (4H, d, J 7.5 Hz, 4 x H-7), 2.07 (12H, s, 12 x H-9); ^{13}C NMR δ_{C} (101 MHz; CDCl_3): 148.9 (C 2), 143.6 (C-5), 135.5 (C-6), 135.2 (C-4), 128.2 (C-8), 127.7 (C-3), 127.6 (C-7), 104.7 (C-1), 20.4 (C-9); HRMS (EI), m/z : (Found: 446.02891. Calc. for $\text{C}_{22}\text{H}_{20}\text{Cl}_1\text{I}_1$: 446.02927.)

3.5.5.2 [Cl-Ar-Li]₂ (3.12)

Cl-Ar-I (**3.5**) (5.00 g, 11.2 mmol) was dried under vacuum for 16 h. Hexane (*ca.* 70 mL) was added and the white mixture was cooled to 0 °C. Once cooled, *n*-butyllithium (8.1 mL, 2.5 M in hexanes, 20.2 mmol) was added slowly, then the white mixture was stirred for 16 h, allowing to warm to room temperature. After this time, the solid was left to settle for 1 h. The solid was filtered, washed with hexane (2 x 10 mL), and dried under vacuum for 16 h to yield the product **3.12** (3.59 g, 98%) as a white powder. ¹H NMR δ_H (400 MHz; C₆D₆): 6.95 (4H, t, *J* 7.5 Hz, 4 x H-8), 6.87 (8H, d, *J* 7.6 Hz, 8 x H-7), 6.78 (4H, s, 4 x H-3), 1.61 (24H, s, 24 x H-9); ¹³C NMR δ_C (101 MHz; C₆D₆): 170.7 (C-1), 153.6 (C-2), 144.8 (C-5), 136.1 (C-6), 132.9 (C-4), 129.0 (C-7), 127.8 (C-8), 123.6 (C-3), 21.5 (C-9); ⁷Li NMR δ_{Li} (155 MHz; C₆D₆): 1.10 (s).

3.5.6 Ligand Synthesis: CF₃

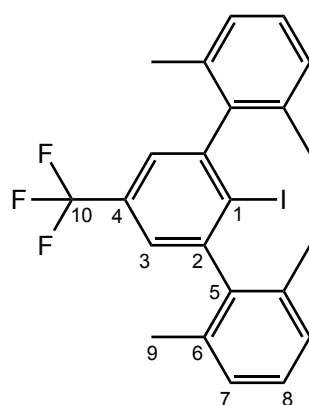
3.5.6.1 1-Iodo-2,6-dichloro-4-trifluoromethylbenzene (3.6b)



To a mixture of sodium nitrite (5.00 g, 72.5 mmol) in conc. sulfuric acid (40 mL) cooled to 0 °C, a stirred solution of 2,6-dichloro-4-trifluoromethylaniline (**3.6a**) (15.0 g, 65.2 mmol) in glacial acetic acid (180 mL) was added slowly. The resultant pale yellow mixture was stirred at room temperature for 4 h. After this time, a solution of potassium iodide (78.6 g, 474 mmol) and iodine (18.4 g, 72.5 mmol) in deionised water (135 mL) was added slowly to the reaction mixture. The resultant black solution was stirred at room temperature for 16 h. The solution was then carefully poured into an aqueous solution of sodium hydroxide (1.5 L, 30%) to give a yellow mixture that was divided

into two fractions. Each fraction was extracted with ethyl acetate (3 x 200 mL), then the organics were combined, dried over MgSO₄, and filtered. The filtrate was reduced under vacuum to yield the crude product **3.6b** (20.2 g, 91%) as a dark red liquid. The compound was used directly in the next reaction without further purification. IR $\nu_{\text{max}}(\text{neat})/\text{cm}^{-1}$ 3080(w), 1595(w), 1555(w), 1379(m), 1303(s), 1259(w), 1197(m), 1171(m), 1133(s), 1102(s), 1014(m), 879(m), 808(m), 706(w), 697(w); ¹H NMR δ_{H} (400 MHz; CDCl₃): 7.57 (2H, s, 2 x H-3); ¹³C NMR δ_{C} (101 MHz; CDCl₃): 141.9 (C-2), 132.5 (q, *J* 34.2 Hz, C-4), 123.9 (q, *J* 3.7 Hz, C-3), 122.7 (q, *J* 273.0 Hz, C-5), 108.9 (C-1); ¹⁹F NMR δ_{F} (376 MHz; CDCl₃): -63.24 (s); HRMS (EI), *m/z*: (Found: 339.85205. Calc. for C₇H₂F₃Cl₂I₁: 339.85248.)

3.5.6.2 F₃C-Ar-I (3.6)

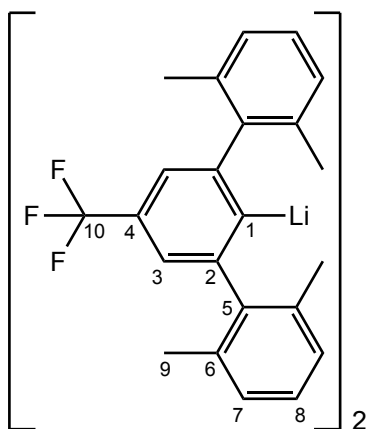


1-Iodo-2,6-dichloro-4-trifluoromethylbenzene (**3.6b**)

(30.0 g, 88.0 mmol) was dissolved in dry THF (*ca.* 200 mL) at -20 °C under argon. To this, the pre-prepared Grignard of (2,6-dimethylphenyl)magnesium bromide (**3.1**) (*ca.* 60.8 g, 290 mmol) in THF (*ca.* 200 mL) was slowly added dropwise at -20 °C. The dark brown mixture was refluxed at 85 °C for 16 h., then was cooled to 0 °C, and iodine (39.6 g, 156 mmol) was added over 1 h. The mixture was stirred at room temperature for 4 h, then aqueous sodium sulfite (300 mL, 1 M) was added. The organic layer was separated and the aqueous phase was washed with diethyl ether (3 x 200 mL), then the organics were combined, dried over MgSO₄, and filtered. The filtrate was reduced under vacuum to give a black oil which was heated at 150 °C under vacuum for 1 h to remove any residual 2,6-Xyl-I impurity from the mixture. The resultant black solid was recrystallised from boiling ethanol (180 mL) to

yield white crystals. These crystals were collected by filtration, washed with cold methanol (3 x 50 mL), and dried under vacuum to yield product **3.6** (14.9 g, 35%). IR $\nu_{\text{max}}(\text{neat})/\text{cm}^{-1}$ 3055(w), 3020(w), 2945(w), 2915(w), 2857(w), 1595(w), 1437(w), 1346(s), 1261(s), 1243(m), 1173(s), 1136(m), 1107(s), 1035(w), 1004(m), 890(m), 777(s), 766(s), 746(m), 699(m), 551(w); ^1H NMR δ_{H} (400 MHz; CDCl_3): 7.39 (2H, s, 2 x H-3), 7.26 (2H, t, J 7.5 Hz, 2 x H-8), 7.16 (4H, d, J 7.6 Hz, 4 x H-7), 2.02 (12H, s, 12 x H-9); ^{13}C NMR δ_{C} (101 MHz; CDCl_3): 148.5 (C-2), 143.6 (C-5), 135.5 (C-6), 131.7 (q, J 32.6 Hz, C-4), 128.4 (C-8), 127.7 (C-7), 124.3 (q, J 3.6 Hz, C-3), 124.1 (q, J 272.7 Hz, C-10), 111.8 (C-1), 20.5 (C-9); ^{19}F NMR δ_{F} (376 MHz; CDCl_3): -62.47 (s); HRMS (EI), m/z : (Found: 480.05619. Calc. for $\text{C}_{23}\text{H}_{20}\text{F}_3\text{I}_1$: 480.05563.)

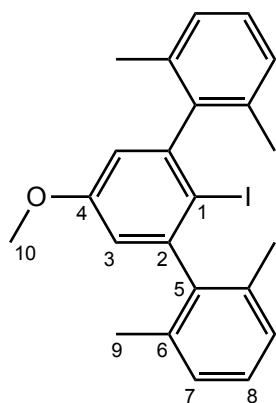
3.5.6.3 [$\text{F}_3\text{C-Ar-Li}$] $_2$ (**3.13**)



$\text{F}_3\text{C-Ar-I}$ (**3.6**) (4.88 g, 10.2 mmol) was dried at 60 °C under vacuum for 3 h. Hexane (*ca.* 80 mL) was added and the mixture was cooled to 0 °C, then *n*-butyllithium (7.3 mL, 2.5 M in hexanes, 18.3 mmol) was added slowly. The white mixture was stirred for 16 h, warmed to room temperature, then left to settle for 1 h. The solid was filtered, washed with hexane (2 x 10 mL), and dried under vacuum for 16 h to yield product **3.13** (3.58 g, 95%) as a white powder. ^1H NMR δ_{H} (400 MHz; C_6D_6): 6.99 (4H, s, 4 x H-3), 6.94 (4H, t, J 7.5 Hz, 4 x H-8), 6.86 (8H, d, J 7.5 Hz, 8 x H-7), 1.55 (24H, s, 24 x H-9); ^{13}C NMR δ_{C} (126 MHz; C_6D_6): 180.2 (m, C-1), 152.4 (C-2), 144.7 (C-5), 136.1 (C-6), 129.1 (C-7), 128.0 (C-8), 126.0 (q, J 271.7 Hz, C-10), 119.5 (q, J 2.8 Hz, C-3), 21.5 (C-9);* ^{19}F NMR δ_{F} (376 MHz; C_6D_6): -61.58 (s); ^7Li NMR δ_{Li} (155 MHz; C_6D_6): 0.93 (s). *C-4 not observed.

3.5.7 Ligand Synthesis: OMe

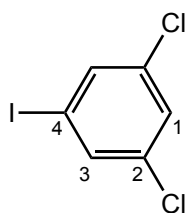
3.5.7.1 MeO-Ar-I (3.7)



To a solution of 3,5-dichloroanisole (**3.7a**) (4.88 g, 27.0 mmol) in dry THF (*ca.* 100 mL) at $-78\text{ }^{\circ}\text{C}$, *n*-butyllithium (10.8 mL, 2.5 M in hexanes, 27.0 mmol) was added dropwise over 1 h. The pale orange solution was stirred at $-78\text{ }^{\circ}\text{C}$ for 1.5 h, then the Grignard of (2,6-dimethylphenyl)magnesium bromide (**3.1**) (*ca.* 11.3 g, 54.0 mmol) in THF (*ca.* 140 mL) was added dropwise at $-78\text{ }^{\circ}\text{C}$ over 0.5 h. The brown solution was warmed to room temperature over 16 h, refluxed at $90\text{ }^{\circ}\text{C}$ for 2 h, cooled to $0\text{ }^{\circ}\text{C}$, then iodine (10.3 g, 40.5 mmol) was added over 1 h. The dark purple mixture was stirred for 1 h. Aqueous sodium sulfite (100 mL, 1 M) was added, then the organic and aqueous phases were separated, washing the aqueous with diethyl ether (3 x 100 mL). The organics were combined, dried over MgSO_4 , filtered, then the filtrate was dried to give a brown oil which was heated at $150\text{ }^{\circ}\text{C}$ under vacuum for 1 h to remove any 2,6-Xyl-I impurity. The crude product was recrystallised in boiling ethanol (100 mL), collected by filtration, washed with cold methanol (2 x 10 mL), and dried to yield product **3.7** (0.41 g, 3%) as a white powder. Elemental analysis: (Found: C, 62.9; H, 5.3. Calc. for $\text{C}_{23}\text{H}_{23}\text{I}_1\text{O}_1$: C, 62.5; H, 5.2%); IR $\nu_{\text{max}}(\text{neat})/\text{cm}^{-1}$ 3053(w), 2935(w), 2911(w), 2851(w), 1568(m), 1460(m), 1393(m), 1326(s), 1201(s), 1174(s), 1027(m), 1003(m), 883(w), 846(m), 776(s), 765(s), 734(m); ^1H NMR δ_{H} (400 MHz; CDCl_3): 7.24 (2H, t, J 7.5 Hz, 2 x H-8), 7.15 (4H, d, J 7.5 Hz, 4 x H-7), 6.73 (2H, s, 2 x H-3), 3.81 (3H, s, 3 x H-10), 2.06 (12H, s, 12 x H-9); ^{13}C NMR δ_{C} (101 MHz; CDCl_3): 160.5 (C-4), 148.1 (C-2), 144.7 (C-5), 135.7 (C-6), 127.8 (C-8), 127.4 (C-7), 113.6 (C-3), 95.5 (C-1), 55.6 (C-10), 20.4 (C-9); HRMS (FD), m/z : (Found: 442.0809. Calc. for $\text{C}_{23}\text{H}_{23}\text{O}_1\text{I}_1$: 442.0788.)

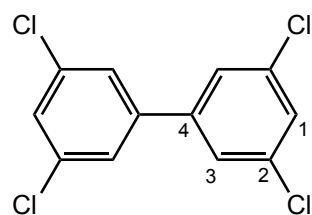
3.5.8 Ligand Synthesis: Double Ligand

3.5.8.1 3,5-Dichloriodobenzene (**3.8b**)



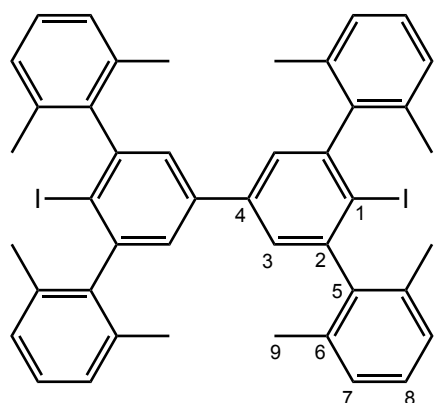
A mixture of 3,5-dichloroaniline (**3.8a**) (19.4 g, 120 mmol) in hydrochloric acid (6M, 200 mL) was cooled to $-10\text{ }^{\circ}\text{C}$, then a solution of sodium nitrite (8.70 g, 126 mmol) in deionised water (40 mL) was added dropwise. The stirred solution was warmed to room temperature over 1 h, after which it was carefully added to a solution of sodium iodide (54.0 g, 360 mmol) in deionised water (360 mL). The resultant dark red mixture was stirred for 16 h. After this time, the product was extracted into dichloromethane (3 x 200 mL), then washed with sodium bisulfite (10%, 500 mL), sodium hydroxide (2M, 500 mL) and brine (300 mL). The organics were dried over MgSO_4 , filtered, then the filtrate was reduced under vacuum to give an oily red solid. The crude product was purified by filtration through silica gel, eluting with hexane:dichloromethane (9:1), to yield product **3.8b** (26.7 g, 82%) as an orange solid. Elemental analysis: (Found: C, 26.3; H, 1.0. Calc. for $\text{C}_6\text{H}_3\text{Cl}_2\text{I}$: C, 26.4; H, 1.1%); IR $\nu_{\text{max}}(\text{neat})/\text{cm}^{-1}$ 3067(m), 1716(w), 1552(s), 1405(s), 1391(s), 1369(m), 1349(m), 1094(m), 845(m), 792(m), 738(m), 657(m); ^1H NMR δ_{H} (400 MHz; CDCl_3): 7.60 (2H, d, J 1.8 Hz, 2 x H-3), 7.33 (1H, t, J 1.8 Hz, 1 x H-1); ^{13}C NMR δ_{C} (101 MHz; CDCl_3): 135.7 (C-3), 135.6 (C-2), 128.5 (C-1), 93.8 (C-4); MS (EI), m/z : 272 (M^+ , 100%), 145 (62), 109 (30), 74 (35); HRMS (EI), m/z : (Found: 271.8660. Calc. for $\text{C}_6\text{H}_3\text{Cl}_2\text{I}$: 271.8651.)

3.5.8.2 3,3',5,5'-Tetrachlorobiphenyl (3.8c)



A mixture containing 3,5-dichloriodobenzene (**3.8b**) (32.5 g, 119 mmol) and copper powder (32.5 g, 511 mmol) was stirred at 270 °C for 16 hours. The resultant brown sludge was allowed to cool, then toluene (300 mL) was added, the mixture was filtered, and the filtrate was reduced under vacuum. The crude product was recrystallised from cyclohexane (150 mL) to give a beige solid that was collected by vacuum filtration. This solid was purified via sublimation at 170 °C under vacuum to give product **3.8c** (6.24 g, 36%) as a white powder. Elemental analysis: (Found: C, 49.2; H, 1.8. Calc. for C₁₂H₆Cl₄: C, 49.4; H, 2.1%); IR $\nu_{\text{max}}(\text{neat})/\text{cm}^{-1}$ 3074(w), 1585(m), 1557(s), 1414(w), 1374(m), 1126(m), 1104(m), 850(s), 805(s), 672(s); ¹H NMR δ_{H} (400 MHz; CDCl₃): 7.40 (4H, d, *J* 1.6 Hz, 4 x H-3), 7.38 (2H, t, *J* 1.7 Hz, 2 x H-1); ¹³C NMR δ_{C} (101 MHz; CDCl₃): 141.5 (C-4), 135.8 (C-2), 128.5 (C-1), 125.7 (C-3); MS (EI), *m/z*: 292 (M⁺, 100%), 220 (46), 150 (14); HRMS (EI), *m/z*: (Found: 291.9189. Calc. for C₁₂H₆Cl₄: 291.9194.)

3.5.8.3 I-Ar-Ar-I (3.8)



To a solution of 3,3',5,5'-tetrachlorobiphenyl (**3.8c**) (6.00 g, 20.5 mmol) in dry THF (*ca.* 200 mL) at -78 °C, *n*-butyllithium (18.1 mL, 2.5 M in hexanes, 42.5 mmol) was added dropwise over 2 h. The resultant cloudy brown mixture was left to stir at -78 °C for 1 h, then the pre-prepared Grignard of (2,6-dimethylphenyl)magnesium bromide (**3.1**) (*ca.* 18.9 g, 90.4 mmol) in THF (*ca.* 200 mL) was added dropwise at -78 °C over 1.5 h. The dark brown mixture

was warmed to room temperature over 16 h, then was refluxed at 90 °C for 2 h. The mixture was cooled to 0 °C, and iodine (20.0 g, 78.8 mmol) was added over 1 h. The dark red solution was stirred for 1 h. Aqueous sodium sulfite (150 mL, 1 M) was added, then the organic and aqueous phases were separated, washing the aqueous with dichloromethane (3 x 100 mL). The organics were combined, dried over MgSO₄, and filtered. The filtrate was reduced under vacuum to give an orange oily solid which was heated at 150 °C under vacuum for 1 h to remove any residual 2,6-Xyl-I impurity from the mixture. Hexane (100 mL) was then added to precipitate a white solid. This solid was collected by filtration, washed with cold hexane (3 x 50 mL), and dried under vacuum to yield product **3.8** (5.09 g, 30%) as a white powder. Elemental analysis: (Found: C, 64.2; H, 4.9. Calc. for C₄₄H₄₀I₂: C, 64.2; H, 4.9%); IR $\nu_{\max}(\text{neat})/\text{cm}^{-1}$ 2916(w), 1581(w), 1462(m), 1438(w), 1385(m), 1086(w), 1002(m), 873(m), 763(s); ¹H NMR δ_{H} (400 MHz; CDCl₃): 7.40 (4H, s, 4 x H-3), 7.26 (4H, t, *J* 7.5 Hz, 4 x H-8), 7.17 (8H, d, *J* 7.5 Hz, 8 x H-7), 2.11 (24H, s, 24 x H-9); ¹³C NMR δ_{C} (101 MHz; CDCl₃): 148.1 (C-2), 144.5 (C-5), 140.4 (C-4), 135.6 (C-6), 128.0 (C-8), 127.5 (C-7), 125.8 (C-3), 106.3 (C-1), 20.6 (C-9).

Note: Elemental analysis and mass spectrometry data has not been reported for the m-terphenyl lithium complexes, 3.9 – 3.13, due to their highly air- and moisture-sensitive nature. This is also the case for other m-terphenyl lithium species previously reported in the literature.^{90,97,98,100,172,218}

Chapter IV

Group 12 Complexes

4.1 Introduction

The stabilisation of low-coordinate Group 12 metal complexes exhibiting novel bonding modes and geometries has been explored through the utilisation of sterically demanding ligands.^{219–224} In contrast to the earliest examples of zinc, cadmium and mercury dialkyl and diaryl complexes,^{225–228} which necessitated secondary stabilising interactions, the bulky *m*-terphenyl framework has since enabled the isolation of strictly two-coordinate Group 12 systems, such as (2,6-Mes₂C₆H₃)₂Zn (**Fig. 4.1**).^{229,230} Other reports include the synthesis of a homologous series of Group 12 M–M bonded species (2,6-Dipp₂C₆H₃)₂M₂ (M = Zn, Cd, Hg)^{105,231} and the formation of a Zn–Zr–Zn unit in [(2,6-Tripp₂C₆H₃)Zn]₂Zr(η⁵-C₅H₅)₂.^{71,232}

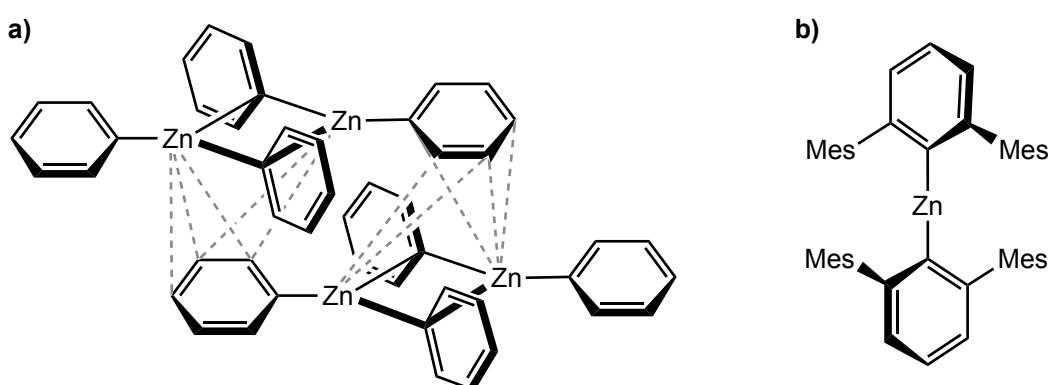


Fig. 4.1 Solid-state structures comparing a) the ‘ZnPh₂’ tetramer stabilised by secondary contacts, and b) the (2,6-Mes₂C₆H₃)₂Zn monomer featuring the bulkier *m*-terphenyl ligand framework.^{225,227,230}

The application of Group 12 organometallic complexes in catalysis has rendered them invaluable reagents for synthesis. Organozinc compounds, for example, have proven useful in organic transformations,^{233,234} alkali-metal-mediated zincation reactions,^{235,236} and copolymerisation reactions.^{237,238} Organocadmium complexes, on the other hand, play a key role as molecular precursors in the synthesis of photoluminescent quantum dots,^{239,240} while organomercurials feature as ligand transmetallation reagents.^{241,242}

Previous work within the Kays group has explored the structural role of the *m*-terphenyl ligand upon three series of two-coordinate Group 12 diaryls $(2,6\text{-Ar}_2\text{C}_6\text{H}_3)_2\text{M}$ (M = Zn, Cd, Hg; Ar = 2,6-Xyl, 3,5-Xyl, Pmp), where subtle changes in the steric pocket around the metal centre were studied.^{80,81} Here, the bulkier 2,6-Xyl and Pmp flanking groups led to near-linear C–M–C bond angles $[175.78(12)\text{--}180.0(0)^\circ]$, whereas the less sterically-hindered 3,5-Xyl group resulted in more bent geometries $[171.18(5)\text{--}176.4(2)^\circ]$. Despite this, the effects of varying the electronic structure of the *m*-terphenyl ligand upon these Group 12 systems has yet to be investigated.

Multiple studies by Power *et al.* have analysed the electronic properties of other metal complexes using *para*-substituted *m*-terphenyl ligands.^{85,93,94} One example features the quintuply-bonded arylchromium dimer, where a set of *para*-functionalised analogues $[(2,6\text{-Dipp}_2\text{-4-R-C}_6\text{H}_2)\text{Cr}]_2$ (R = H, SiMe₃, OMe, F) were prepared to probe the nature of the Cr–Cr bond.⁸⁹ Additional reports include the study of a series of *para*-substituted Group 14 complexes $(2,6\text{-Mes}_2\text{-4-R-C}_6\text{H}_2)_2\text{M}$ (M = Ge, Sn, Pb; R = H, SiMe₃, Cl),^{91,92} and the analysis of the functionalised tin hydrides $[(2,6\text{-Dipp}_2\text{-4-R-C}_6\text{H}_2)\text{Sn}(\mu\text{-H})]_2$ (R = H, SiMe₃, OMe, *t*-Bu).⁹⁰

Therefore, we have applied a similar approach to the syntheses of Group 12 complexes by employing *para*-substituted *m*-terphenyl ligands to study the role of electronic effects on the structures, bonding and properties of their resulting metal complexes. By exploiting the diamagnetic nature of the Group 12 metal(II) species, an NMR handle is provided through which the electronic properties can be studied; this was previously used to differentiate between *syn*- and *anti*-conformers in a series of naphthyl-substituted complexes $(2,6\text{-Naph}_2\text{C}_6\text{H}_3)_2\text{M}$ (M = Zn, Cd·OEt₂, Hg·OEt₂).²⁴³

Herein, four series of novel *para*-substituted, two-coordinate, *m*-terphenyl Group 12 diaryls (R-Ar)₂M (Ar = 2,6-(2,6-Xyl)₂C₆H₂; M = Zn, Cd, Hg; R = *t*-Bu, SiMe₃, Cl, CF₃) are reported, and discussed alongside their unsubstituted (R = H) analogues.⁸⁰ The geometric and electronic structures of these compounds are elucidated through X-ray crystallographic and NMR spectroscopic studies, respectively. Specifically, ¹¹³Cd and ¹⁹⁹Hg NMR spectroscopies are employed to assess the electronics directly at the metal centre. In addition, the synthetic methods adopted for preparing these complexes provide a tool for refining the experimental conditions used in the later syntheses of their transition metal complexes, whose paramagnetic nature restricts the use of NMR characterisation, see *Chapter 5.2.1.3*. The general structure of the ligands used in this research is shown below (**Fig. 4.2**).

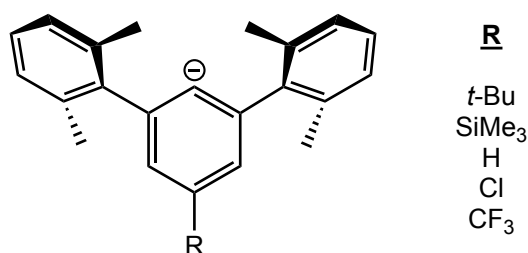


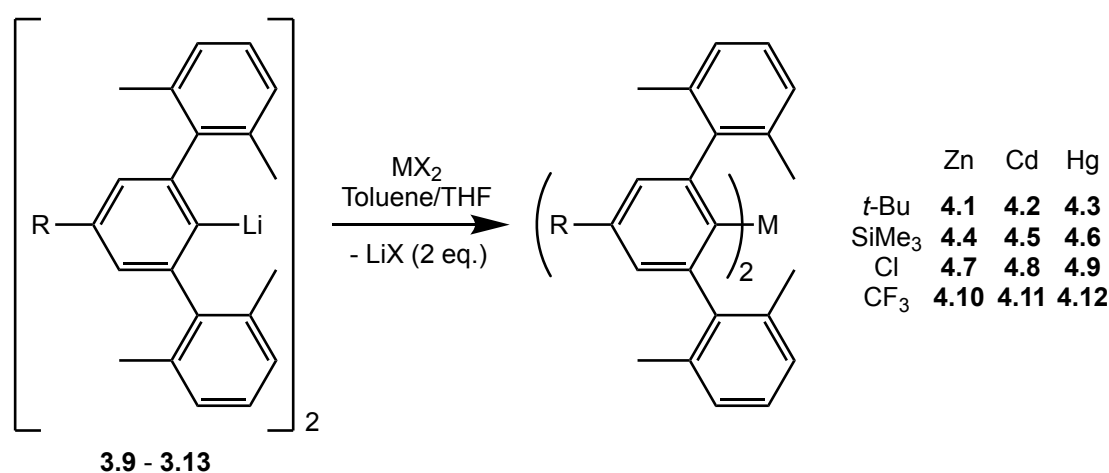
Fig. 4.2 General structure of the *para*-substituted *m*-terphenyl ligands discussed herein for the synthesis of Group 12 metal complexes.

4.2 Discussion

4.2.1 *m*-Terphenyl Zinc, Cadmium and Mercury Complexes

4.2.1.1 Synthesis

The *para*-substituted *m*-terphenyl lithium complexes, $[\text{R-Ar-Li}]_2$, (Ar = 2,6-(2,6-Xyl) $_2$ C $_6$ H $_2$; R = *t*-Bu, **3.9**; SiMe $_3$, **3.10**; Cl, **3.12**; CF $_3$, **3.13**), were reacted with one equivalent of ZnCl $_2$, CdCl $_2$ or HgBr $_2$ in a toluene/THF (10:1) mixture at room temperature to yield the corresponding *m*-terphenyl zinc, cadmium and mercury complexes, (R-Ar) $_2$ M, (Ar = 2,6-(2,6-Xyl) $_2$ C $_6$ H $_2$; M = Zn, Cd, Hg; R = *t*-Bu, **4.1** – **4.3**; SiMe $_3$, **4.4** – **4.6**; Cl, **4.7** – **4.9**; CF $_3$, **4.10** – **4.12**), respectively (Scheme 4.1). All samples were recrystallised from *s*-hexane (**4.1** – **4.6**, **4.10** – **4.12**) or toluene (**4.7** – **4.9**) at –30 °C to give colourless crystals in low to moderate yields, although these yields are of crystalline materials that have not been optimised. Characterisation of **4.1** – **4.12** has been achieved via multinuclear (^1H , ^{13}C , ^{19}F , ^{29}Si , ^{113}Cd , ^{199}Hg) NMR spectroscopy, mass spectrometry, elemental analysis and single crystal X-ray diffraction.



Scheme 4.1 General synthesis of the *m*-terphenyl Group 12 complexes, **4.1** – **4.12**, (MX $_2$ = ZnCl $_2$, CdCl $_2$, HgBr $_2$; M = Zn, Cd, Hg; R = *t*-Bu, SiMe $_3$, Cl, CF $_3$).

4.2.1.2 Crystallographic Analysis

To analyse the structural properties of the *para*-substituted *m*-terphenyl Group 12 complexes **4.1** – **4.12**, the compounds were crystallographically characterised after recrystallisation from *s*-hexane (**4.1** – **4.6**, **4.10** – **4.12**) or toluene (**4.7** – **4.9**) at $-30\text{ }^{\circ}\text{C}$. Single crystal X-ray data for $(\text{R-Ar})_2\text{M}$ ($\text{M} = \text{Zn, Cd, Hg}$; $\text{R} = t\text{-Bu}$, **4.1** – **4.3**; SiMe_3 , **4.4** – **4.6**; Cl , **4.7** – **4.9**; CF_3 , **4.10** – **4.12**) confirms these systems to be two-coordinate and monomeric in the solid-state, each featuring a single metal centre stabilised by two σ -bonded *m*-terphenyl ligands in a quasi-linear geometry (**Fig. 4.3** – **4.6**). Owing to the steric demands of the bulky *m*-terphenyl ligands, the nearest $\text{M}\cdots\text{M}$ separations are $d(\text{Zn}\cdots\text{Zn}) = 9.1\text{ \AA}$ (for **4.4**), $d(\text{Cd}\cdots\text{Cd}) = 10.5\text{ \AA}$ (for **4.8**) and $d(\text{Hg}\cdots\text{Hg}) = 10.5\text{ \AA}$ (for **4.9**). Unlike the 3,5-Xyl analogues, $(2,6\text{-}\{3,5\text{-Xyl}\}_2\text{C}_6\text{H}_3)_2\text{M}$ ($\text{M} = \text{Zn, Cd, Hg}$), no $\text{M}\cdots\text{H}$ interactions are formed to the flanking rings and, in contrast to **3.9** – **3.13** in *Chapter 3.2.1.3*, no $\text{M}\cdots\text{H}$ (methyl) anagostic contacts are observed.⁸⁰ Bond lengths and angles are given in **Table 4.1** ($\text{M} = \text{Zn}$), **Table 4.2** ($\text{M} = \text{Cd}$) and **Table 4.3** ($\text{M} = \text{Hg}$).

For each Group 12 metal, the corresponding series of *para*-substituted complexes show no significant change in M-C bond lengths as the functional group is varied. The Zn-C bond lengths for **4.1** [$\text{Zn(1)-C(1)} = 1.935(4)\text{ \AA}$, $\text{Zn(1)-C(23)} = 1.939(3)\text{ \AA}$], **4.4** [$\text{Zn(1)-C(1)} = 1.954(10)\text{ \AA}$, $\text{Zn(1)-C(23)} = 1.950(10)\text{ \AA}$], **4.7** [$\text{Zn(1)-C(1)} = 1.9419(18)\text{ \AA}$, $\text{Zn(1)-C(23)} = 1.9464(18)\text{ \AA}$, $\text{Zn(2)-C(45)} = 1.9429(18)\text{ \AA}$, $\text{Zn(2)-C(67)} = 1.9367(18)\text{ \AA}$] and **4.10** [$\text{Zn(1)-C(1)} = 1.945(3)\text{ \AA}$, $\text{Zn(1)-C(23)} = 1.948(3)\text{ \AA}$] are all comparable to one another, see **Table 4.1**, and to the unsubstituted analogue $(2,6\text{-}\{2,6\text{-Xyl}\}_2\text{C}_6\text{H}_3)_2\text{Zn}$ [$\text{Zn(1)-C(1)} = 1.949(4)\text{ \AA}$, $\text{Zn(1)-C(23)} = 1.944(4)\text{ \AA}$].^{80,81} These values also reflect other zinc diaryls in the literature, whose Zn-C bond distances range between $1.93\text{--}1.95\text{ \AA}$.^{244–246}

Table 4.1 Relevant bond lengths (Å) and angles (°) for the *m*-terphenyl zinc complexes, (R-Ar)₂Zn (**4.1**, **4.4**, **4.7** and **4.10**), featuring *para*-substituent, R. The unsubstituted analogues, R = H, are reported elsewhere.⁸⁰

M = Zn	Bond Lengths (Å) and Angles (°)			
	4.1 (R = <i>t</i> -Bu)	4.4 (R = SiMe ₃)	4.7 ^a (R = Cl)	4.10 (R = CF ₃)
Zn(1)–C(1)	1.935(4)	1.954(10)	1.9419(18) [1.9429(18)]	1.945(3)
Zn(1)–C(23)	1.939(3)	1.950(10)	1.9464(18) [1.9367(18)]	1.948(3)
C(1)–Zn(1)–C(23)	175.86(14)	176.4(5)	176.11(8) [176.84(8)]	178.79(10)
C(1)-aryl plane ⋯C(23)-aryl plane	83.02(12)	78.0(4)	89.26(6) [83.13(7)]	83.07(10)
C(1)-aryl plane ⋯flanking aryl plane	84.67(14) 76.98(16)	82.4(4) 73.7(4)	69.52(7) 78.65(7) [76.09(7)] [86.30(7)]	83.07(11) 81.95(13)
C(23)-aryl plane ⋯flanking aryl plane	75.16(13) 80.25(18)	83.5(4) 70.4(4)	87.35(7) 83.33(7) [82.85(7)] [78.18(7)]	84.07(11) 88.56(10)

^a For **4.7**, molecule 2 of the asymmetric unit [C(45)–Zn(2)–C(67)] is in square brackets.

A narrow range of M–C bond lengths is similarly observed for the cadmium complexes **4.2**, **4.5**, **4.8** and **4.11** [Cd–C = 2.098(11)–2.121(3) Å] in **Table 4.2**, and for the mercury complexes **4.3**, **4.6**, **4.9** and **4.12** [Hg–C = 2.05(2)–2.101(19) Å] in **Table 4.3**, and mirror the M–C bond lengths of the unsubstituted complexes (2,6-{2,6-Xyl}₂C₆H₃)₂M (M = Cd, Hg) [Cd(1)–C(1) = 2.115(5) Å, Cd(1)–C(23) = 2.228(5) Å and Hg(1)–C(1) = 2.087(6) Å, Hg(1)–C(23) = 2.101(5) Å].^{80,81} These values are comparable to other cadmium and mercury diaryls, whose M–C bond lengths range between 2.11–2.12 Å and 2.07–2.15 Å, respectively.^{228,247–251} In all cases, the M–C bonds initially lengthen down Group 12 as the covalent radius of the metal increases from Zn (1.22 Å) to Cd (1.44 Å), then shortens for Hg as the radius decreases (1.32 Å);²⁵² this is presumably a consequence of relativistic effects and the lanthanide contraction.^{253,254}

Table 4.2 Relevant bond lengths (Å) and angles (°) for the *m*-terphenyl cadmium complexes, (R-Ar)₂Cd (**4.2**, **4.5**, **4.8** and **4.11**), featuring *para*-substituent, R. The unsubstituted analogues, R = H, are reported elsewhere.⁸⁰

M = Cd	Bond Lengths (Å) and Angles (°)			
	4.2 (R = <i>t</i> -Bu)	4.5 (R = SiMe ₃)	4.8 (R = Cl)	4.11 (R = CF ₃)
Cd(1)–C(1)	2.109(3)	2.110(11)	2.120(2)	2.119(3)
Cd(1)–C(23)	2.111(3)	2.098(11)	2.116(2)	2.121(3)
C(1)–Cd(1)–C(23)	176.56(10)	177.5(5)	177.43(9)	179.08(13)
C(1)-aryl plane ···C(23)-aryl plane	81.91(10)	79.5(4)	87.23(8)	80.33(13)
C(1)-aryl plane ···flanking aryl plane	84.31(10)	83.5(4)	86.63(8)	82.06(14)
C(23)-aryl plane ···flanking aryl plane	76.33(10)	83.1(4)	75.65(9)	84.78(13)
	83.97(10)	75.9(4)	79.38(8)	88.63(13)

Table 4.3 Relevant bond lengths (Å) and angles (°) for the *m*-terphenyl mercury complexes, (R-Ar)₂Hg (**4.3**, **4.6**, **4.9** and **4.12**), featuring *para*-substituent, R. The unsubstituted analogues, R = H, are reported elsewhere.⁸⁰

M = Hg	Bond Lengths (Å) and Angles (°)			
	4.3 (R = <i>t</i> -Bu)	4.6 (R = SiMe ₃)	4.9 (R = Cl)	4.12 (R = CF ₃)
Hg(1)–C(1)	2.099(5)	2.101(19)	2.086(3)	2.097(4)
Hg(1)–C(23)	2.097(5)	2.05(2)	2.085(3)	2.100(4)
C(1)–Hg(1)–C(23)	177.34(17)	176.6(8)	177.51(15)	179.38(15)
C(1)-aryl plane ···C(23)-aryl plane	82.18(17)	80.2(7)	87.54(12)	80.97(14)
C(1)-aryl plane ···flanking aryl plane	84.04(18)	83.8(7)	86.47(13)	83.23(15)
C(23)-aryl plane ···flanking aryl plane	77.13(18)	83.3(7)	76.80(14)	85.72(16)
	84.29(19)	76.8(8)	81.74(13)	88.09(15)

The C–M–C angles for **4.1** – **4.12** similarly occur within a narrow range. Specifically, the C–Zn–C angles of complexes **4.1**, **4.4**, **4.7** and **4.10** [175.86(14)–178.79(10)°] are comparable to the C–Cd–C angles of **4.2**, **4.3**, **4.8** and **4.11** [176.56(10)–179.08(13)°] and to the C–Hg–C angles of **4.3**, **4.6**, **4.9** and **4.12** [176.6(8)–179.38(15)°], indicating little variation as the metal is changed. These values reflect the quasi-linear geometries adopted by the Group 12 complexes, and are reminiscent of the C–M–C angles reported for the unsubstituted 2,6-Xyl analogues (2,6-{2,6-Xyl}₂C₆H₃)₂M (M = Zn, Cd, Hg) [177.1(2)–178.79(10)°], but differ from the bent angles observed in the 3,5-Xyl complexes (2,6-{3,5-Xyl}₂C₆H₃)₂M (M = Zn, Cd, Hg) [171.18(5)–176.4(2)°].^{80,81} The C–M–C angles for **4.1** – **4.12** are also similar to those of Mes₂M (M = Zn, Cd, Hg).^{227,228} Regarding the *para*-substituent, the CF₃ complexes, **4.10** – **4.12**, all exhibit more linear C–M–C angles [178.79(10)–179.38(15)°]; however, this could be a consequence of crystal packing effects rather than an electronic influence caused by the *para*-group.

To reduce the steric strain between the *m*-terphenyl ligands in these complexes, the two metal-substituted central aryl rings on each ligand are orientated near orthogonal to one another. Here, torsion angles can be measured between the planes of each of their 6-membered central rings, C(1)-aryl and C(23)-aryl, see **Tables 4.1** – **4.3**. These torsion angles vary depending on the *para*-substituent; those for the *t*-Bu, SiMe₃ and CF₃ complexes [78.0(4)–83.07(10)°] are less perpendicular than those for the Cl analogues [83.13(7)–89.26(6)°], possibly due to crystal packing effects or the steric size of the *para*-group. Furthermore, these angles are also nearer 90° for the unsubstituted complexes (2,6-{2,6-Xyl}₂C₆H₃)₂M (M = Zn, Cd, Hg) [83.6(2)–86.62(18)°].^{80,81} Regarding the metal centre, moving down Group 12 has minimal impact upon the observed torsion angles.

Finally, for **4.1** – **4.12**, the torsion angles between the 6-membered ring planes of the central aryls, C(1)-aryl and C(23)-aryl, and the 2,6-Xyl groups [69.52(7)–88.63(13)°], are shown in **Tables 4.1** – **4.3**. These angles are similar to those of the unsubstituted analogues (2,6-{2,6-Xyl}₂C₆H₃)₂M (M = Zn, Cd, Hg) [80.73(19)–88.4(2)°].^{80,81} In all cases, the 2,6-Xyl flanking groups adopt a near orthogonal orientation such that the steric hindrance of the *ortho*-methyl groups is minimised. This is in contrast to the torsion angles reported for the less rotationally-restricted 3,5-Xyl complexes (2,6-{3,5-Xyl}₂C₆H₃)₂M (M = Zn, Cd, Hg) [40.36(5)–57.8(2)°].⁸⁰ Overall, the measured torsion angles fall within a narrow range which indicates that keeping the 2,6-Xyl groups constant throughout the series minimises the effects of steric variations on the coordination sphere.

In summary, the crystal structures of the *m*-terphenyl Group 12 diaryls **4.1** – **4.12** show little structural variation as the *para*-substituent is changed, which suggests that *para*-functionalisation has little steric influence on the geometries of these complexes. This is presumably because the *para*-group is directed away from the coordination sphere. Furthermore, unlike the lithium complexes **3.9** – **3.13** in *Chapter 3.2.1.3*, M···H–C anagostic interactions are not observed between the metal centre and the flanking methyl groups. However, although structurally similar, further studies are required to probe the electronic properties of these systems.

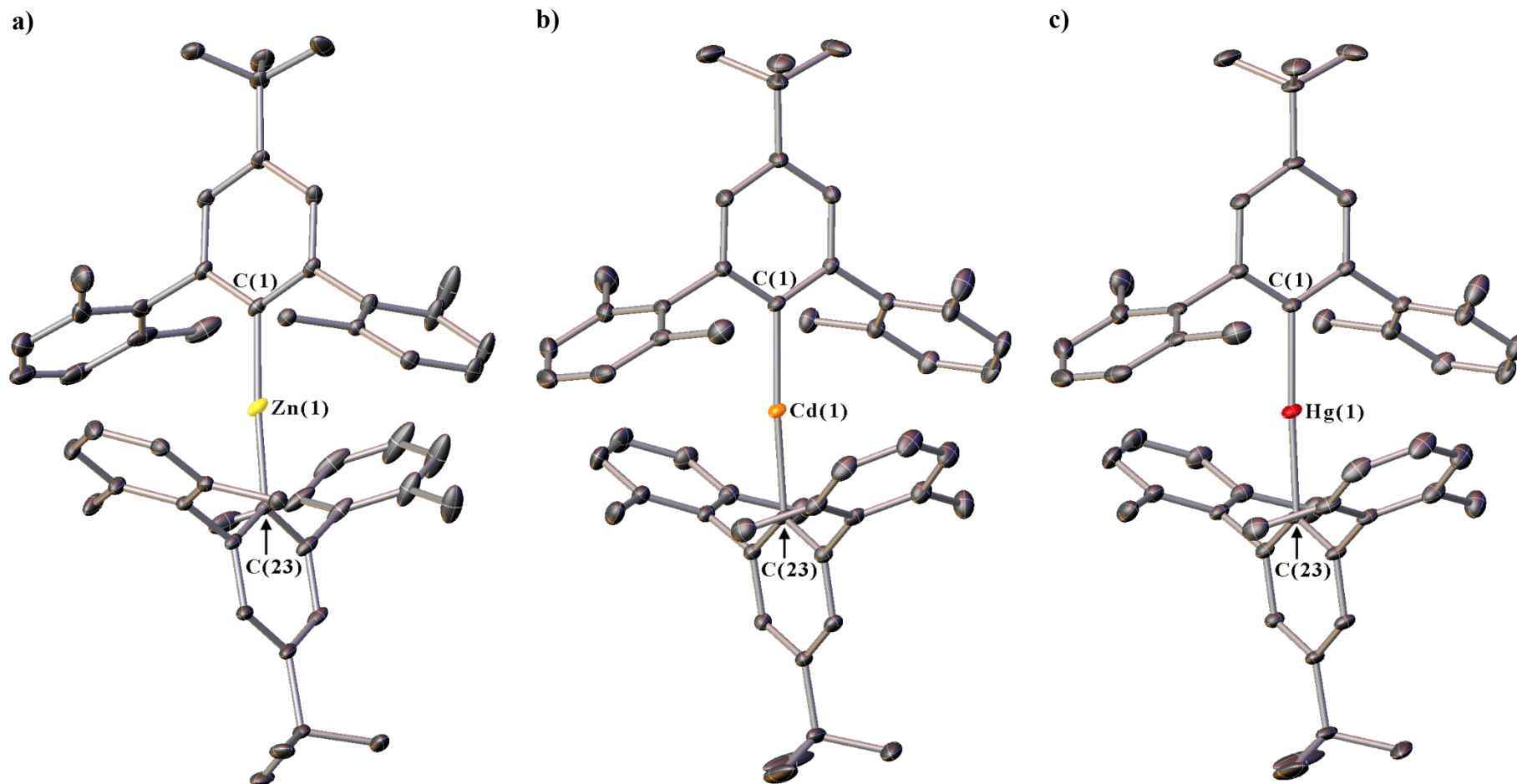


Fig. 4.3 Crystal structures of the *m*-terphenyl Group 12 complexes, (*t*-Bu-Ar)₂M, for a) M = Zn (**4.1**), b) M = Cd (**4.2**) and c) M = Hg (**4.3**). Ellipsoids set at 15%, 30% and 30% probability respectively. Hydrogen atoms and residual solvent molecules are omitted for clarity. When necessary, only one molecule from the asymmetric unit is shown. The unsubstituted analogues, (H-Ar)₂M, are reported elsewhere.⁸⁰

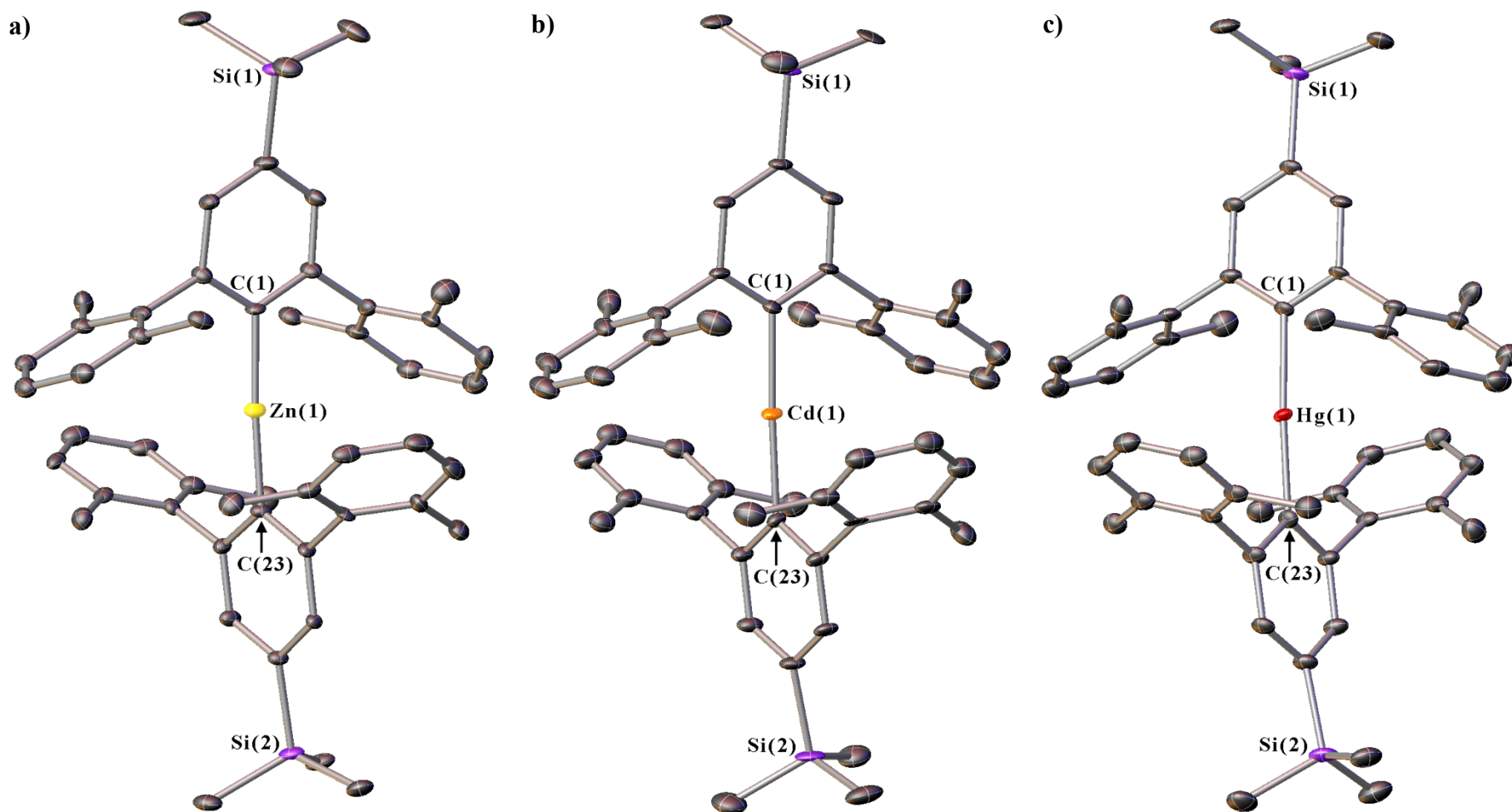


Fig. 4.4 Crystal structures of the *m*-terphenyl Group 12 complexes, $(\text{Me}_3\text{Si-Ar})_2\text{M}$, for a) $\text{M} = \text{Zn}$ (4.4), b) $\text{M} = \text{Cd}$ (4.5) and c) $\text{M} = \text{Hg}$ (4.6). Ellipsoids set at 25%, 50% and 40% probability respectively. Hydrogen atoms and residual solvent molecules are omitted for clarity. When necessary, only one molecule from the asymmetric unit is shown. The unsubstituted analogues, $(\text{H-Ar})_2\text{M}$, are reported elsewhere.⁸⁰

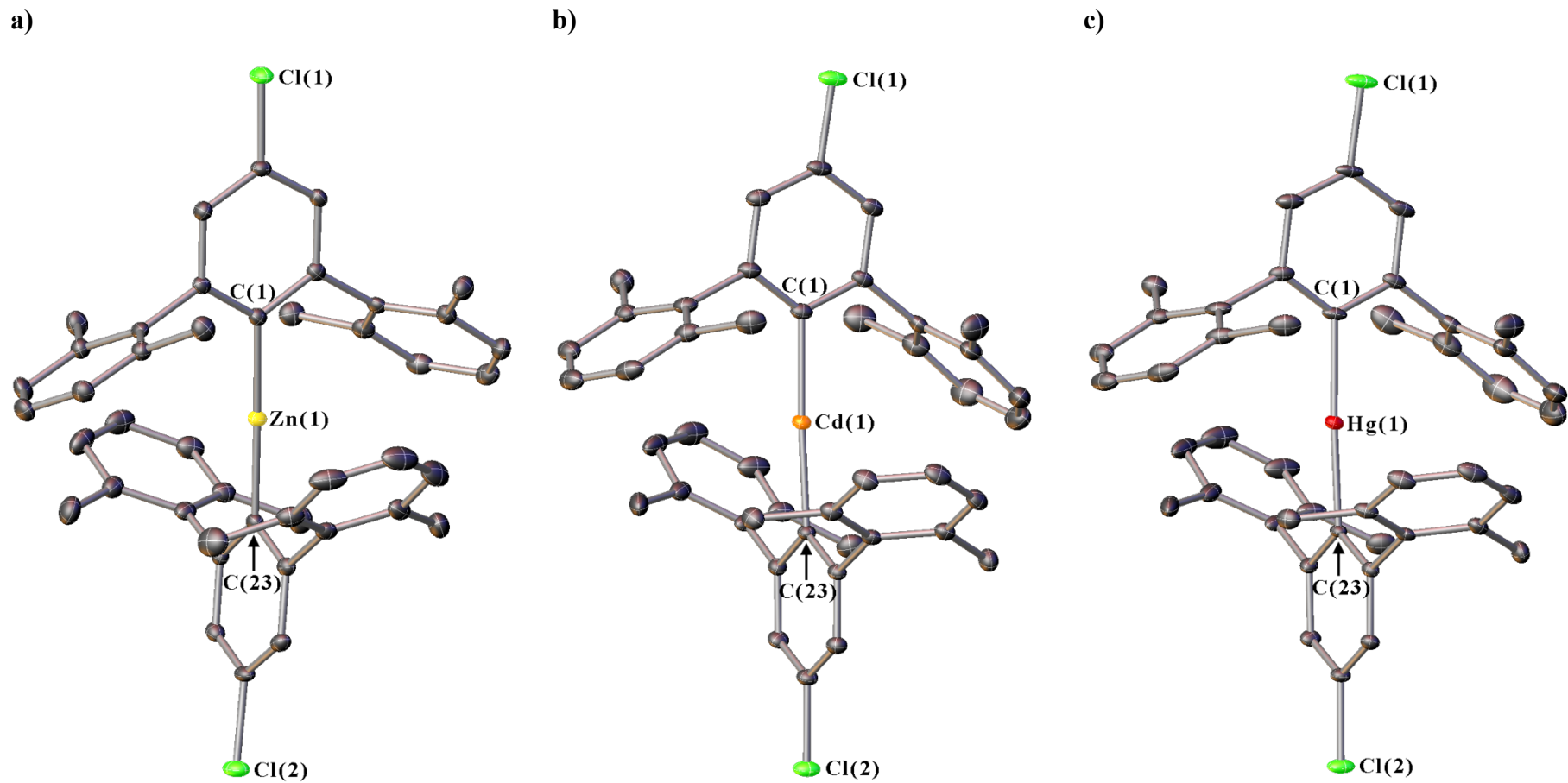


Fig. 4.5 Crystal structures of the *m*-terphenyl Group 12 complexes, (Cl-Ar)₂M, for a) M = Zn (4.7), b) M = Cd (4.8) and c) M = Hg (4.9). Ellipsoids set at 35%, 25% and 20% probability respectively. Hydrogen atoms and residual solvent molecules are omitted for clarity. When necessary, only one molecule from the asymmetric unit is shown. The unsubstituted analogues, (H-Ar)₂M, are reported elsewhere.⁸⁰

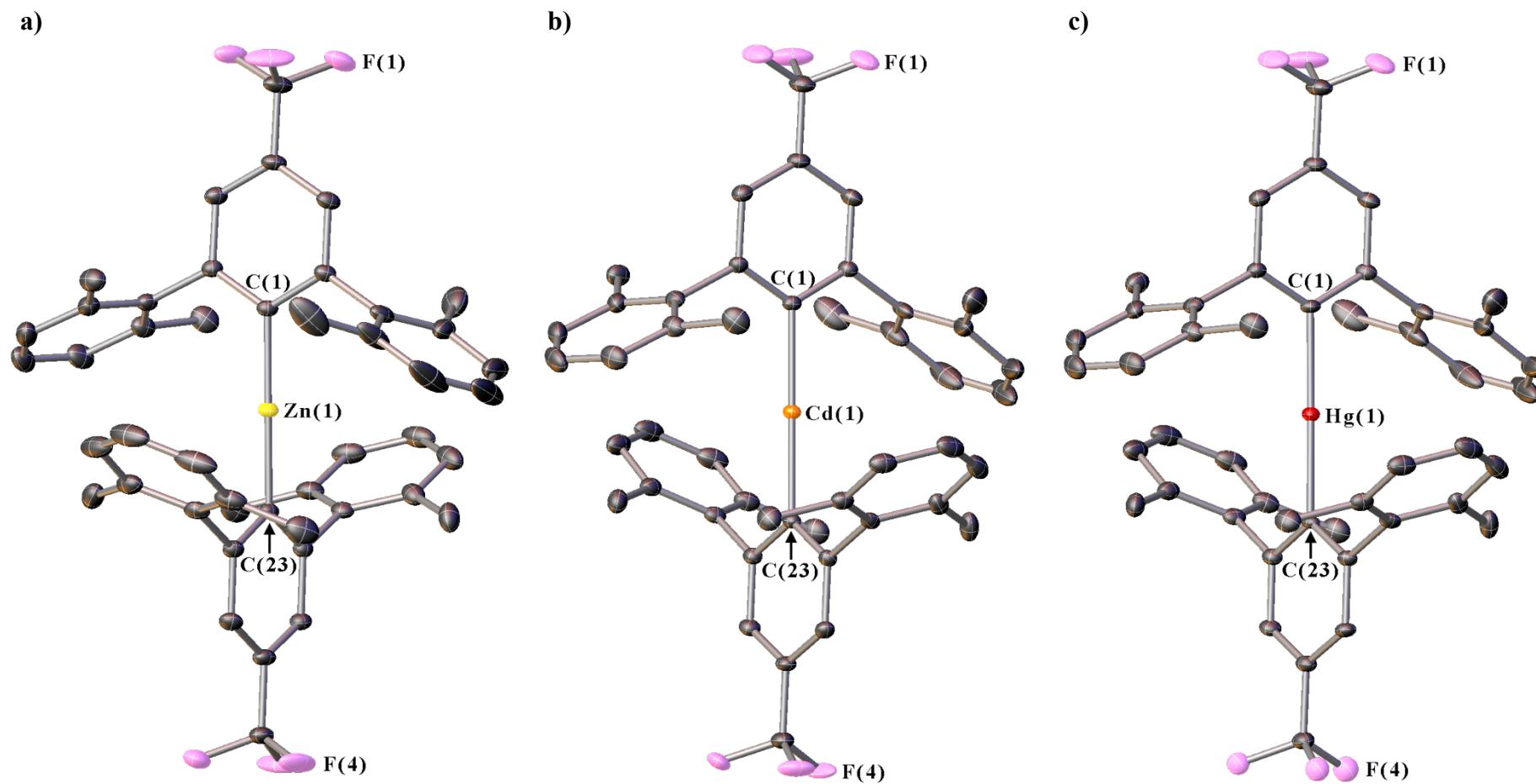


Fig. 4.6 Crystal structures of the *m*-terphenyl Group 12 complexes, $(F_3C-Ar)_2M$, for a) $M = Zn$ (**4.10**), b) $M = Cd$ (**4.11**) and c) $M = Hg$ (**4.12**). Ellipsoids set at 35%, 25% and 20% probability respectively. Hydrogen atoms and residual solvent molecules are omitted for clarity. When necessary, only one molecule from the asymmetric unit is shown. The unsubstituted analogues, $(H-Ar)_2M$, are reported elsewhere.⁸⁰

4.2.1.3 NMR Analysis

The electronic properties of the *para*-substituted *m*-terphenyl Group 12 complexes **4.1** – **4.12** were studied via ^1H , ^{13}C , ^{113}Cd and ^{199}Hg NMR spectroscopies in *d*-benzene, and compared with that of the unsubstituted (R = H) analogues.⁸⁰ Here, the *m*-terphenyl unit has been assigned a numbering scheme (**Fig. 4.7**). Akin to the iodides **3.2** – **3.6** in *Chapter 3.2.1.3*, and the lithium species **3.9** – **3.13** in *Chapter 3.2.2.3*, the ^1H NMR spectra of **4.1** – **4.12** show four characteristic peaks, except that, in some cases, the signals for the aromatic 2,6-Xyl protons (H-7 and H-8) are merged. Additional singlets are observed in **4.1** – **4.6** due to the *t*-Bu or SiMe₃ groups. A comparison of the ^1H NMR spectra for each metal series reveals three features. Firstly, the *meta*-hydrogens, H-3, on the central rings exhibit notable peak shifts as the *para*-substituent is changed but with no overall trend, as well as a clear downfield shift when varying the metal from Zn (6.76–7.14 ppm) to Cd (6.87–7.22 ppm) to Hg (6.92–7.30 ppm), see **Table 4.4**. Secondly, the 2,6-Xyl aryl protons, H-7 (6.88–7.05 ppm) and H-8 (6.98–7.10 ppm), for **4.1** – **4.12** remain relatively unshifted by changing the *para*-group or the metal, suggesting that *para*-substitution has minimal influence on the flanking rings. Thirdly, the 2,6-Xyl methyl protons, H-9, shift upfield with increased electron-withdrawing strength of the *para*-substituent. A plot of the chemical shifts, δ , against the Hammett constants, σ_{para} , reveals a linear correlation (**Fig. 4.9**).¹³⁹ This trend proceeds in the opposite direction to that expected; electron-withdrawing groups usually cause a downfield shift. Although no M···H–C anagostic contacts were noted in the solid-state, see *Chapter 4.2.1.2*, this trend is presumably due to interactions between the metal and flanking methyl groups, like those evidenced by ^7Li - ^1H HOESY spectra for **3.9** – **3.13** in *Chapter 3.2.2.3*. Moreover, exchanging Li for Zn, Cd and Hg appears to have no impact on this trend, as the chemical shifts remain identical regardless of the metal.

The ^{13}C NMR spectra of **4.1** – **4.12** were assigned using DEPT, HSQC-ME and HMBC techniques, and show nine peaks for the carbons of the ligand framework, plus extra peaks for the *t*-Bu, SiMe₃ and CF₃ groups (**Fig. 4.7**). A comparison of the spectra reveals that C-5 (143.2–147.4 ppm), C-6 (135.8–136.4 ppm), C-7 (127.8–128.3 ppm), C-8 (127.1–127.9 ppm) and C-9 (21.2–22.0 ppm) of the 2,6-Xyl groups remain almost unshifted, regardless of the metal or *para*-group. However, the central ring carbons shift considerably, except for C-2, see **Table 4.4**. Here, the largest shifts are noted for the *ipso*-carbons, C-1, likely due to changing the metal; the C-1 peak shifts downfield in *ca.* 10 ppm increments from Zn (148.5–156.8 ppm) to Cd (158.3–167.0 ppm) to Hg (169.1–176.0 ppm). For similar complexes in the literature, this downfield trend has been ascribed to the increased Pauling electronegativity down the Group 12 metals (1.65, 1.69 and 2.00 for Zn, Cd and Hg, respectively).^{80,105,228,251,255–257} However, a computational analysis of the ^{13}C chemical shift tensors for the C_{*ipso*}–M bond would be required to rationalise the trend in **4.1** – **4.12**.^{192,200} Regarding the *para*-substituents, no definitive trends may be identified, although a general downfield shift is observed for C-1 as electron-withdrawing character of the *para*-group is increased, see **Table 4.4**. This suggests that *para*-substitution does affect the electronic properties in the central rings of the *m*-terphenyl Group 12 complexes, most importantly at the *ipso*-position.

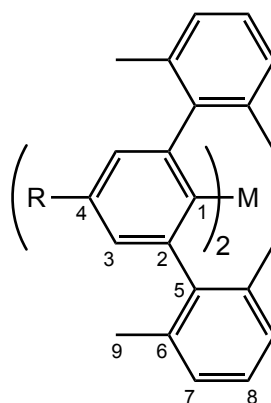


Fig. 4.7 NMR numbering scheme for the complexes (R-Ar)₂M (M = Zn, Cd, Hg).

Table 4.4 ^1H and ^{13}C NMR chemical shifts, δ , for $(\text{R-Ar})_2\text{M}$ (**4.1** – **4.12**), where M is a metal and R is the *para*-substituent, for relevant atoms on the *m*-terphenyl Group 12 complexes. The flanking aryl atoms remain unshifted so have been omitted.

	$(\text{R-Ar})_2\text{M}$	R Group	^1H and ^{13}C NMR Chemical Shifts, δ (ppm)						
			H-3	H-9	C-1	C-2	C-3	C-4	C-9
M = Zn	4.1	<i>t</i> -Bu	6.93	1.83	148.5	149.8	122.4	151.9	21.9
	4.4	SiMe ₃	7.14	1.82	152.8	149.3	130.2	140.7	22.0
	lit. ^a	H	6.76	1.79	152.0	150.0	125.5	128.9	21.8
	4.7	Cl	6.78	1.61	150.2	151.6	125.7	135.4	21.6
	4.10	CF ₃	7.05	1.55	156.8	150.7	122.1	131.5	21.6
M = Cd	4.2	<i>t</i> -Bu	7.02	1.84	158.3	149.4	122.0	151.4	21.5
	4.5	SiMe ₃	7.22	1.82	162.9	149.1	129.7	140.0	21.6
	lit. ^a	H	6.87	1.80	161.9	149.6	125.1	128.4	21.5
	4.8	Cl	6.88	1.63	160.1	151.1	125.4	134.8	21.2
	4.11	CF ₃	7.14	1.56	167.0	150.2	121.7	131.1	21.3
M = Hg	4.3	<i>t</i> -Bu	7.09	1.83	169.1	148.4	123.7	151.4	21.5
	4.6	SiMe ₃	7.30	1.81	173.0	148.1	131.5	140.2	21.5
	lit. ^a	H	6.92	1.78	172.0	148.7	126.8	128.4	21.4
	4.9	Cl	6.92	1.61	170.2	150.1	127.0	134.7	21.2
	4.12	CF ₃	7.20	1.54	176.0	149.3	123.6	131.1	21.2

^a Literature NMR data for the unsubstituted complexes $(\text{H-Ar})_2\text{M}$ (M = Zn, Cd, Hg); original data was revised to ensure correct peak assignments and C₆D₆ referencing.⁸⁰

The ^{113}Cd and ^{199}Hg NMR spectra of **4.2**, **4.5**, **4.8**, **4.11** and **4.3**, **4.6**, **4.9**, **4.12** were recorded in *d*-benzene. Despite the sensitive nature of these NMR spectra to analyte concentration and effects like solvent coordination, such factors appear to be negligible, possibly due to the steric bulk of the ligands preventing interaction of the metal with the surrounding solvent.^{258–260} Nonetheless, all samples were prepared to be about the same concentration. The steric effects of the 2,6-Xyl flanking groups on the metal centre are assumed to remain constant throughout the series and, thus, do not contribute to the variations in the NMR chemical shifts. This is in contrast to $(2,6\text{-Ar}_2\text{C}_6\text{H}_3)_2\text{M}$ (M = Cd, Hg; Ar = 2,6-Xyl, 3,5-Xyl, Pmp), where increasing the steric bulk of the flanking groups causes an upfield shift in their ^{113}Cd and ^{199}Hg NMR spectra.⁸⁰

In all cases, the ^{113}Cd and ^{199}Hg NMR spectra show a single peak indicating one metal environment in solution, in the same region as other literature metal diaryl complexes, see **Table 4.5**.^{243,261–263} The position of these peaks is shifted upfield by the increasing electron-withdrawing strength of the *para*-substituents (**Fig. 4.8**).

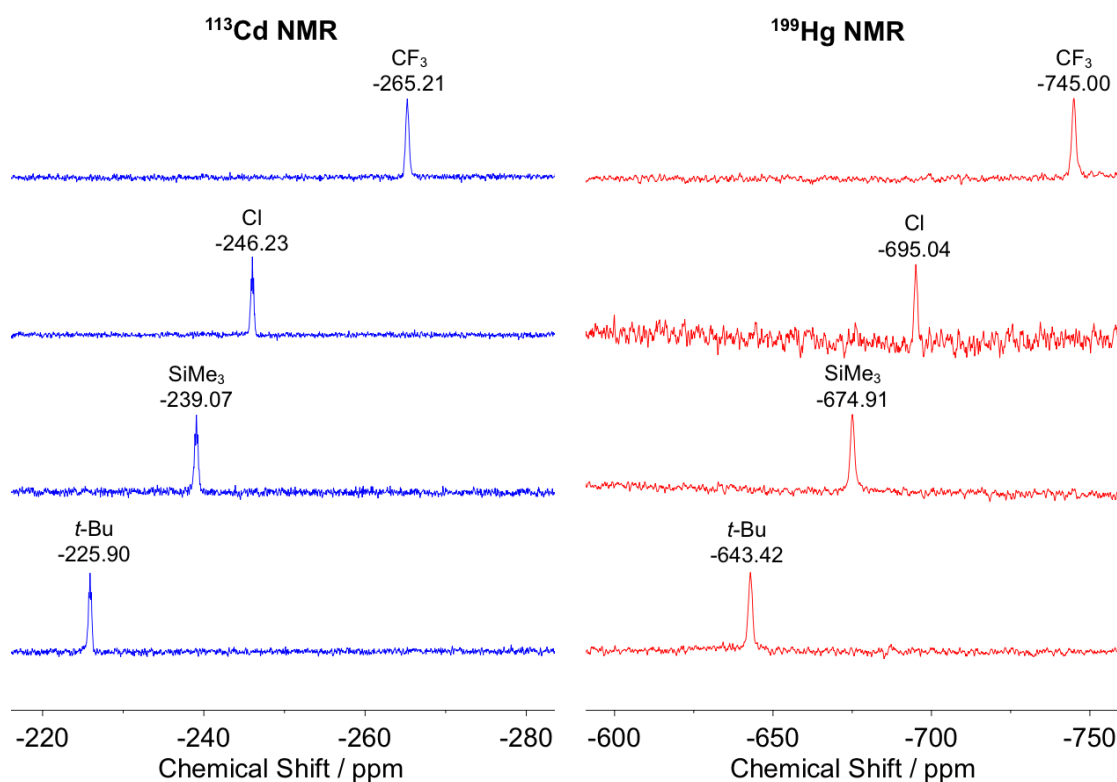


Fig. 4.8 ^{113}Cd and ^{199}Hg NMR spectra of the *m*-terphenyl Group 12 complexes, $(\text{R-Ar})_2\text{M}$ ($\text{M} = \text{Cd}, \text{Hg}$; $\text{R} = t\text{-Bu}, \text{SiMe}_3, \text{Cl}, \text{CF}_3$), showing an upfield peak shift as the electron-withdrawing strength of the *para*-substituent increases.

Plotting a graph of the ^{113}Cd and ^{199}Hg NMR chemical shifts, δ , against the Hammett constants, σ_{para} , reveals a linear correlation for each series (**Fig. 4.9**).¹³⁹ This suggests that the *para*-groups directly influence the electronic properties at the metal centre. Akin to the lithium complexes **3.9** – **3.13** in *Chapter 3.2.2.3*, these trends proceed in the opposite direction to that expected, electron-withdrawing groups usually deshield the nuclei and cause a downfield shift. Similar findings were reported for a series of *para*-substituted mercury diaryls $[\text{4-R-C}_6\text{H}_4]_2\text{Hg}$ ($\text{R} = \text{OMe}, \text{Me}, \text{H}, \text{F}, \text{Cl}, \text{CF}_3$).^{264–266}

Table 4.5 ^{113}Cd and ^{199}Hg NMR chemical shifts, δ , for $(\text{R-Ar})_2\text{M}$ ($\text{M} = \text{Cd}, \text{Hg}$), where R is the *para*-substituent, for the *m*-terphenyl Group 12 complexes.¹³⁹

	$(\text{R-Ar})_2\text{M}$	R Group	Hammett Constant, σ_{para}	NMR Chemical Shifts, δ (ppm)	
				^{113}Cd	^{199}Hg
M = Cd, Hg	4.2, 4.3	<i>t</i> -Bu	-0.20	-225.89	-642.81
	4.5, 4.6	SiMe ₃	-0.07	-239.07	-674.91
	lit. ^a	H	0.00	-239.36	-679.77
	4.8, 4.9	Cl	0.23	-246.03	-695.04
	4.11, 4.12	CF ₃	0.54	-265.21	-745.00

^a Literature NMR data for the unsubstituted complexes $(\text{H-Ar})_2\text{M}$ ($\text{M} = \text{Cd}, \text{Hg}$).⁸⁰

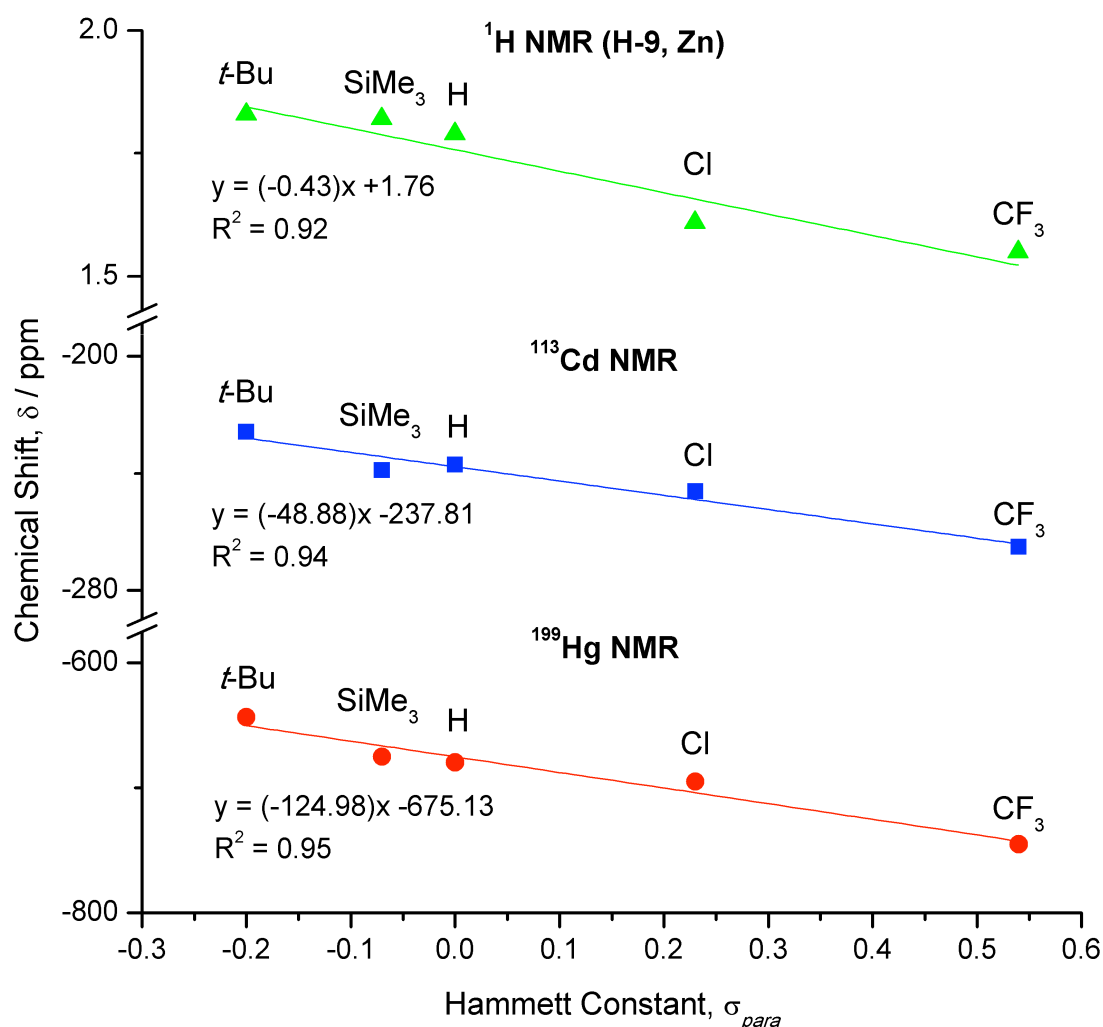


Fig. 4.9 Plot of the ^1H (for flanking methyl protons, H-9), ^{113}Cd and ^{199}Hg NMR chemical shifts, δ , for the *para*-substituted Group 12 complexes $(\text{R-Ar})_2\text{M}$, 4.1 – 4.12, versus their Hammett constants, σ_{para} .¹³⁹ For clarity, the ^1H NMR (H-9) trend is given only for the Zn series; plots for the Cd and Hg series ($R^2 = 0.94$) are identical.

These ^{113}Cd and ^{199}Hg NMR results parallel the trends observed for the flanking methyl protons, H-9, in the ^1H NMR, see **Table 4.4**, where electron-withdrawing groups cause a downfield shift (**Fig. 4.9**). Since all other atoms of the 2,6-Xyl rings remain essentially unshifted by the changing *para*-groups, the electronic effects may instead be transferred to the methyl protons, H-9, by the metal via through-space $\text{M}\cdots\text{H}-\text{C}$ contacts, similar to those for **3.9** – **3.13** in *Chapter 3.2.2.3*.²⁰⁰ These interactions could be caused by an electric field at the metal centre, whose field strength would vary depending on the *para*-substituent. However, computational work would be required to fully explain this.

It has been theorised that the bonding in organomercury compounds involves mainly the Hg 6s orbital,²⁶⁷ since the Hg 6p orbitals are too high in energy to overlap with the ligand orbitals. However, by incorporating electron-donating groups, the ligand orbitals would increase in energy affording better overlap with the Hg 6p orbitals.^{262,268} In doing so, the more diffuse Hg 6p orbitals would become populated, while the compact Hg 6s orbital would be depopulated. Hence, the more diffuse electron density would less effectively shield the metal centre, resulting in the observed downfield shift. Another study similarly describes the importance of p orbital contributions on the NMR chemical shifts for a series of zinc and cadmium complexes.²⁶⁹ Further computational work is necessary to explain the upfield shifts observed for the ^{113}Cd and ^{199}Hg NMR spectra as electron-withdrawing power of the *para*-group is increased.

To conclude, although the *m*-terphenyl Group 12 complexes **4.1** – **4.12** are structurally similar, NMR spectroscopy reveals major electronic differences at the metal centre that depend directly on the *para*-group, with a trend in the reverse direction to that expected. Moreover, these electronic effects are mirrored by the flanking methyl protons, H-9.

4.2.1.4 Cyclic Voltammetry

To further probe the electronic properties of the *para*-substituted *m*-terphenyl Group 12 complexes, cyclic voltammetry was attempted in order to study their redox activity. For this, two mercury complexes were trialled (R-Ar)₂Hg (R = *t*-Bu, **4.3**; CF₃, **4.12**) featuring *para*-groups that lie at the extremes of electron-donating and -withdrawing strength. However, redox processes are not observed for either sample within the range of +1.5 to -3.0 V, relative to Fc⁺/Fc. Notably, their cyclic voltammograms do not exhibit a signal corresponding to a reduction process (Fig. 4.10). This suggests that neither the mercury centre nor the *m*-terphenyl ligand are redox active in these systems; such findings are characteristic of closed-shell Group 12 complexes.

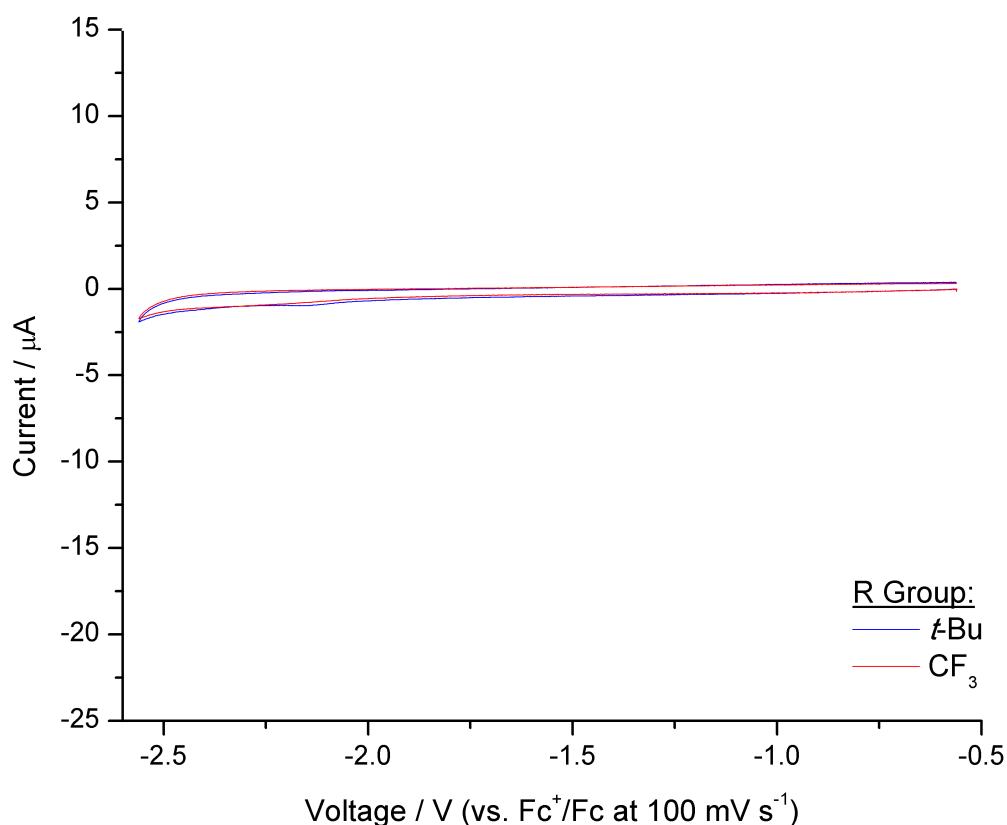


Fig. 4.10 Superimposed cyclic voltammograms of two *para*-substituted mercury *m*-terphenyl complexes (R-Ar)₂Hg (R = *t*-Bu, **4.3**; CF₃, **4.12**) showing no reduction processes on scanning to -2.5 V (vs. Fc⁺/Fc). Samples measured in THF (1.0 mM) containing [nBu₄N][BF₄] (0.5 M) at 298 K. Only scans at 100 mV s⁻¹ are shown.

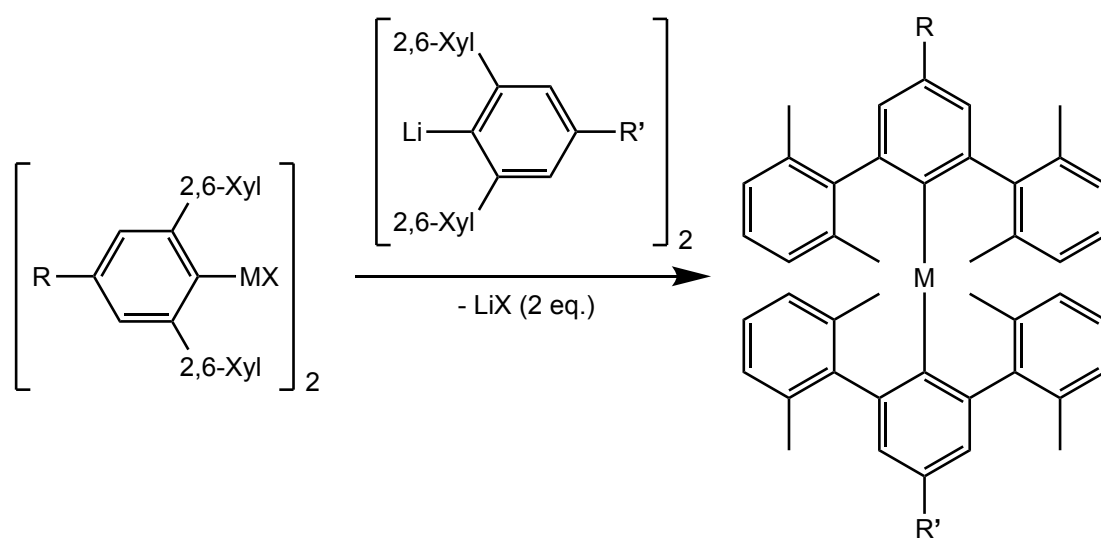
4.3 Conclusions

Four series of *para*-functionalised Group 12 *m*-terphenyl complexes **4.1** – **4.12**, featuring ligand substituents of varying electron-donating and -withdrawing strengths, have been reported. From a crystallographic perspective, the complexes are structurally identical, since the C–M–C bond lengths and angles remain essentially invariant across the series. However, NMR spectroscopic studies reveal considerable electronic differences within the ligand framework and, consequently, at the metal centre, as emphasised by the linear correlation of the ^{113}Cd and ^{199}Hg NMR chemical shifts with the literature Hammett constants of the *para*-substituents. Moreover, the flanking methyl protons, H-9, exhibit similar shifts in their ^1H NMR spectra, suggesting the occurrence of through-space $\text{M}\cdots\text{H}-\text{C}$ contacts. In all cases, the NMR trends proceed in the opposite direction to that expected, such that electron-withdrawing substituents cause an upfield peak shift. Future computational modelling will aim to address these phenomena and offer elucidation into the electronic nature of these complexes.

Overall, these Group 12 systems confirm that *para*-functionalisation directly influences the electronic properties at the metal centre, with minimal structural or steric impact on the coordination sphere. This is promising for the later synthesis of open-shell transition metal complexes aimed at investigating the role of these electronic effects on both the magnetic properties and small molecule reactivity of such low-coordinate systems.

4.4 Future Work

Aside from performing the computational calculations on the Group 12 systems, a potential future project could involve the syntheses of the unsymmetrical, heteroleptic analogues of the two-coordinate complexes, $(R-Ar)M(Ar-R')$. This concept would involve binding a metal, M, to two distinct *m*-terphenyl ligands featuring different *para*-substituents, R and R', to form complexes containing, for example, both an electron-donating and an electron-withdrawing group (e.g. R = *t*-Bu and R' = CF₃). Such modifications could allow for greater control of the electronic environment at the metal centre. While it would be of primary interest to study the electronic properties of these systems, specifically by measuring the NMR chemical shifts to determine if the Hammett substituent effects are additive, they may also present applications as charge-transfer complexes. The synthesis of these unsymmetrical complexes could be attempted via a standard metathesis route (**Scheme 4.2**). This method has previously been employed within the Kays group to isolate a series of mercury diaryls $(2,6-TmpC_6H_3)Hg(2,6-Ar_2C_6H_3)$ (Ar = 2,6-Xyl, Dcp, Pmp; Dcp = 2,6-Cl₂C₆H₃).²⁷⁰

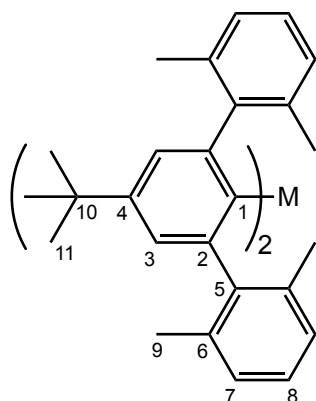


Scheme 4.2 Proposed route to unsymmetrical, heteroleptic, two-coordinate complexes featuring *m*-terphenyl ligands with *para*-substituents, R and R'.

4.5 Experimental

4.5.1 Metal Complex Synthesis: Group 12 ($M = \text{Zn, Cd, Hg}$)

4.5.1.1 ($t\text{-Bu-Ar}$)₂ M ($M = \text{Zn, 4.1; Cd, 4.2; Hg, 4.3}$)

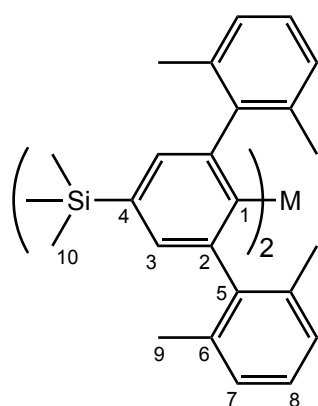


A mixture of [$t\text{-Bu-Ar-Li}$]₂ (**3.9**) (100 mg, 0.14 mmol) and MX_2 (0.14 mmol, $\text{MX}_2 = \text{ZnCl}_2, \text{CdCl}_2, \text{HgBr}_2$) in toluene (10 mL) and THF (1 mL) was stirred for 16 h at room temperature. After this time, the solvent was removed under vacuum to yield a white solid, which was dried at 60 °C under vacuum for 4 h, then extracted into

hexane (3 x 10 mL). Concentration of the resultant colourless solution under vacuum, followed by storage at -30 °C, resulted in clear, colourless crystals of **4.1** – **4.3** with isolated yields of 35.0 mg (33%), 17.2 mg (15%) and 39.1 mg (31%) respectively. Data for **4.1**: $^1\text{H NMR } \delta_{\text{H}}$ (400 MHz; C_6D_6): 7.05 (12H, m, 8 x H-7 and 4 x H-8), 6.93 (4H, s, 4 x H-3), 1.83 (24H, s, 24 x H-9), 1.14 (18H, s, 18 x H-11); $^{13}\text{C NMR } \delta_{\text{C}}$ (101 MHz; C_6D_6): 151.9 (C-4), 149.8 (C-2), 148.5 (C-1), 146.6 (C-5), 136.3 (C-6), 128.1 (C-7), 127.2 (C-8), 122.4 (C-3), 34.6 (C-10), 31.4 (C-11), 21.9 (C-9); HRMS (EI), m/z : (Found: 746.38172. Calc. for $\text{C}_{52}\text{H}_{58}\text{Zn}_1$: 746.38245.) Data for **4.2**: $^1\text{H NMR } \delta_{\text{H}}$ (400 MHz; C_6D_6): 7.08-7.04 (4H, m, 4 x H-8), 7.03-7.01 (8H, m, 8 x H-7), 7.02 (4H, s, 4 x H-3), 1.84 (24H, s, 24 x H-9), 1.18 (18H, s, 18 x H-11); $^{13}\text{C NMR } \delta_{\text{C}}$ (101 MHz; C_6D_6): 158.3 (C-1), 151.4 (C-4), 149.4 (C-2), 147.4 (C-5), 136.1 (C-6), 128.0 (C-7), 127.1 (C-8), 122.0 (C-3), 34.7 (C-10), 31.5 (C-11), 21.5 (C-9); $^{113}\text{Cd NMR } \delta_{\text{Cd}}$ (88.8 MHz; C_6D_6): -225.89 (m); HRMS (EI), m/z : (Found: 796.35767. Calc. for $\text{C}_{52}\text{H}_{58}\text{Cd}_1$: 796.35666.) Data for **4.3**: Elemental analysis: (Found: C, 70.4; H, 6.8. Calc. for $\text{C}_{52}\text{H}_{58}\text{Hg}$: C, 70.7; H, 6.6%); $^1\text{H NMR } \delta_{\text{H}}$ (400 MHz; C_6D_6): 7.10-7.06 (4H, m, 4 x H-8), 7.09 (4H, s, 4 x H-3), 7.05-7.03 (8H, m, 8 x H-7), 1.83 (24H, s, 24 x H-9),

1.15 (18H, s, 18 x H-11); ^{13}C NMR δ_{C} (101 MHz; C_6D_6): 169.1 (C-1), 151.4 (C-4), 148.4 (C-2), 145.5 (C-5), 136.4 (C-6), 127.8 (C-7), 127.2 (C-8), 123.7 (C-3), 34.6 (C-10), 31.5 (C-11), 21.5 (C-9); ^{199}Hg NMR δ_{Hg} (71.7 MHz; C_6D_6): -642.81 (s); HRMS (EI), m/z: (Found: 884.42443. Calc. for $\text{C}_{52}\text{H}_{58}\text{Hg}_1$: 884.42393.)

4.5.1.2 ($\text{Me}_3\text{Si-Ar}$) $_2\text{M}$ ($\text{M} = \text{Zn}$, 4.4; Cd , 4.5; Hg , 4.6)

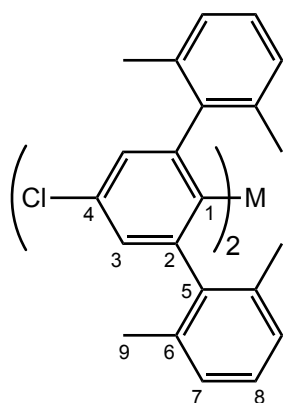


A mixture of $[\text{Me}_3\text{Si-Ar-Li}]_2$ (**3.10**) (100 mg, 0.14 mmol) and MX_2 (0.14 mmol, $\text{MX}_2 = \text{ZnCl}_2, \text{CdCl}_2, \text{HgBr}_2$) in toluene (10 mL) and THF (1 mL) was stirred for 16 h at room temperature. After this time, the solvent was removed under vacuum to yield a white solid, which was dried at 60 °C under vacuum for 4 h, then extracted into

hexane (3 x 10 mL). Concentration of the resultant colourless solution under vacuum, followed by storage at -30 °C, resulted in clear, colourless crystals of **4.4** – **4.6** with isolated yields of 43.8 mg (41%), 29.2 mg (26%) and 35.0 mg (29%) respectively. Data for **4.4**: ^1H NMR δ_{H} (400 MHz; C_6D_6): 7.14 (4H, s, 4 x H-3), 7.06-7.03 (4H, m, 4 x H-8), 7.03-7.00 (8H, m, 8 x H-7), 1.82 (24H, s, 24 x H-9), 0.13 (18H, s, 18 x H-10); ^{13}C NMR δ_{C} (101 MHz; C_6D_6): 152.8 (C-1), 149.3 (C-2), 146.3 (C-5), 140.7 (C-4), 136.3 (C-6), 130.2 (C-3), 128.2 (C-7), 127.3 (C-8), 22.0 (C-9), -1.1 (C-10); ^{29}Si NMR δ_{Si} (79.5 MHz; C_6D_6): -4.76 (s); HRMS (EI), m/z: (Found: 778.33407. Calc. for $\text{C}_{50}\text{H}_{58}\text{Si}_2\text{Zn}_1$: 778.33630.) Data for **4.5**: ^1H NMR δ_{H} (400 MHz; C_6D_6): 7.22 (4H, s, 4 x H-3), 7.06-7.02 (4H, m, 4 x H-8), 7.02-6.99 (8H, m, 8 x H-7), 1.82 (24H, s, 24 x H-9), 0.17 (18H, s, 18 x H-10); ^{13}C NMR δ_{C} (101 MHz; C_6D_6): 162.9 (C-1), 149.1 (C-2), 147.2 (C-5), 140.0 (C-4), 136.1 (C-6), 129.7 (C-3), 128.1 (C-7), 127.2 (C-8), 21.6 (C-9), -0.9 (C-10); ^{29}Si NMR δ_{Si} (79.5 MHz; C_6D_6): -4.76 (s); ^{113}Cd NMR δ_{Cd}

(88.8 MHz; C₆D₆): -239.07 (m); HRMS (FD), m/z: (Found: 828.3119. Calc. for C₅₀H₅₈Si₂Cd₁: 828.3118.) Data for **4.6**: ¹H NMR δ_H (400 MHz; C₆D₆): 7.30 (4H, s, 4 x H-3), 7.08-7.05 (4H, m, 4 x H-8), 7.03-7.01 (8H, m, 8 x H-7), 1.81 (24H, s, 24 x H-9), 0.14 (18H, s, 18 x H-10); ¹³C NMR δ_C (101 MHz; C₆D₆): 173.0 (C-1), 148.1 (C-2), 145.2 (C-5), 140.2 (C-4), 136.4 (C-6), 131.5 (C-3), 127.9 (C-7), 127.3 (C-8), 21.5 (C-9), -1.0 (C-10); ²⁹Si NMR δ_{Si} (79.5 MHz; C₆D₆): -4.69 (s); ¹⁹⁹Hg NMR δ_{Hg} (71.7 MHz; C₆D₆): -674.91 (s); HRMS (FD), m/z: (Found: 916.3789. Calc. for C₅₀H₅₈Si₂Hg₁: 916.3778.)

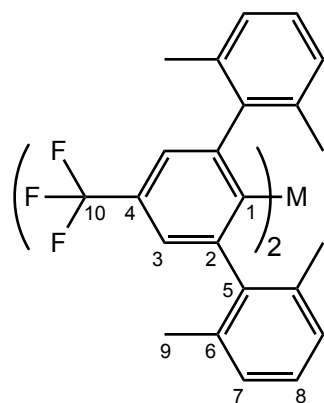
4.5.1.3 (Cl-Ar)₂M (M = Zn, 4.7; Cd, 4.8; Hg, 4.9)



A mixture of [Cl-Ar-Li]₂ (**3.12**) (200 mg, 0.31 mmol) and MX₂ (0.31 mmol, MX₂ = ZnCl₂, CdCl₂, HgBr₂) in toluene (10 mL) and THF (1 mL) was stirred for 16 h at room temperature. After this time, the solvent was removed under vacuum to yield a white solid, which was dried at 60 °C under vacuum for 4 h, then extracted into toluene (2 x 15 mL). Concentration of the resultant colourless solution under vacuum, followed by storage at -30 °C, resulted in clear, colourless crystals of **4.7** – **4.9** with isolated yields of 59.2 mg (27%), 79.3 mg (34%) and 70.8 mg (28%) respectively. Data for **4.7**: Elemental analysis: (Found: C, 74.7; H, 5.9. Calc. for C₄₄H₄₀Cl₂Zn: C, 75.0; H, 5.7%); ¹H NMR δ_H (400 MHz; C₆D₆): 6.99 (4H, t, *J* 7.6 Hz, 4 x H-8), 6.90 (8H, d, *J* 7.6 Hz, 8 x H-7), 6.78 (4H, s, 4 x H-3), 1.61 (24H, s, 24 x H-9); ¹³C NMR δ_C (101 MHz; C₆D₆): 151.6 (C-2), 150.2 (C-1), 144.3 (C-5), 136.0 (C-6), 135.4 (C-4), 128.2 (C-7), 127.7 (C-8), 125.7 (C-3), 21.6 (C-9); HRMS (EI), m/z: (Found: 702.18018. Calc. for C₄₄H₄₀Cl₂Zn₁: 702.17930.) Data for **4.8**: Elemental analysis: (Found:

C, 70.05; H, 5.35. Calc. for $C_{44}H_{40}Cl_2Cd$: C, 70.3; H, 5.4%; 1H NMR δ_H (400 MHz; C_6D_6): 6.98 (4H, t, J 7.5 Hz, 4 x H-8), 6.89 (8H, d, J 7.5 Hz, 8 x H-7), 6.88 (4H, s, 4 x H-3), 1.63 (24H, s, 24 x H-9); ^{13}C NMR δ_C (101 MHz; C_6D_6): 160.1 (C-1), 151.1 (C-2), 145.3 (C-5), 135.8 (C-6), 134.8 (C-4), 128.1 (C-7), 127.5 (C-8), 125.4 (C-3), 21.2 (C-9); ^{113}Cd NMR δ_{Cd} (88.8 MHz; C_6D_6): -246.03 (m); HRMS (EI), m/z : (Found: 752.15463. Calc. for $C_{44}H_{40}Cl_2Cd$: 752.15352.) Data for **4.9**: 1H NMR δ_H (400 MHz; C_6D_6): 7.00 (4H, t, J 7.4 Hz, 4 x H-8), 6.92 (4H, s, 4 x H-3), 6.91 (8H, d, J 7.4 Hz, 8 x H-7), 1.61 (24H, s, 24 x H-9); ^{13}C NMR δ_C (101 MHz; C_6D_6): 170.2 (C-1), 150.1 (C-2), 143.4 (C-5), 136.1 (C-6), 134.7 (C-4), 127.9 (C-7), 127.6 (C-8), 127.0 (C-3), 21.2 (C-9); ^{199}Hg NMR δ_{Hg} (71.7 MHz; C_6D_6): -695.04 (s); HRMS (FD), m/z : (Found: 840.22486. Calc. for $C_{44}H_{40}Cl_2Hg$: 840.22078.)

4.5.1.4 (F_3C-Ar) $_2M$ ($M = Zn, 4.10; Cd, 4.11; Hg, 4.12$)



A mixture of $[F_3C-Ar-Li]_2$ (**3.13**) (100 mg, 0.14 mmol) and MX_2 (0.14 mmol, $MX_2 = ZnCl_2, CdCl_2, HgBr_2$) in toluene (10 mL) and THF (1 mL) was stirred for 16 h at room temperature. After this time, the solvent was removed under vacuum to yield a white solid, which was dried at 60 °C under vacuum for 4 h, then extracted into

hexane (3 x 10 mL). Concentration of the resultant colourless solution under vacuum, followed by storage at -30 °C, resulted in clear, colourless crystals of **4.10** – **4.12** with isolated yields of 43.7 mg (41%), 48.0 mg (42%) and 56.0 mg (44%) respectively. Data for **4.10**: Elemental analysis: (Found: C, 71.3; H, 5.3. Calc. for $C_{46}H_{40}F_6Zn$: C, 71.6; H, 5.2%); 1H NMR δ_H (400 MHz; C_6D_6): 7.05 (4H, s, 4 x H-3), 6.99 (4H, t, J 7.5 Hz, 4 x H-8), 6.89 (8H, d, J 7.5 Hz, 8 x H-7), 1.55 (24H, s, 24 x H-9); ^{13}C NMR

δ_C (101 MHz; C_6D_6): 156.8 (C-1), 150.7 (C-2), 144.2 (C-5), 136.0 (C-6), 131.5 (q, J 31.7 Hz, C-4), 128.3 (C-7), 127.9 (C-8), 125.1 (q, J 272.4 Hz, C-10), 122.1 (q, J 3.5 Hz, C-3), 21.6 (C-9); ^{19}F NMR δ_F (376 MHz; C_6D_6): -62.05 (s); HRMS (FD), m/z : (Found: 770.2294. Calc. for $C_{46}H_{40}F_6Zn_1$: 770.2320.) Data for **4.11**: Elemental analysis: (Found: C, 67.55; H, 5.05. Calc. for $C_{46}H_{40}F_6Cd$: C, 67.4; H, 4.9%); 1H NMR δ_H (400 MHz; C_6D_6): 7.14 (4H, s, 4 x H-3), 6.98 (4H, t, J 7.5 Hz, 4 x H-8), 6.88 (8H, d, J 7.5 Hz, 8 x H-7), 1.56 (24H, s, 24 x H-9); ^{13}C NMR δ_C (101 MHz; C_6D_6): 167.0 (C-1), 150.2 (C-2), 145.3 (C-5), 135.8 (C-6), 131.1 (q, J 31.5 Hz, C-4), 128.2 (C-7), 127.7 (C-8), 125.3 (q, J 272.3 Hz, C-10), 121.7 (q, J 3.4 Hz, C-3), 21.3 (C-9); ^{19}F NMR δ_F (376 MHz; C_6D_6): -61.82 (s); ^{113}Cd NMR δ_{Cd} (88.8 MHz; C_6D_6): -265.21 (m); HRMS (FD), m/z : (Found: 820.2092. Calc. for $C_{46}H_{40}F_6Cd_1$: 820.2062.) Data for **4.12**: 1H NMR δ_H (400 MHz; C_6D_6): 7.20 (4H, s, 4 x H-3), 7.00 (4H, t, J 7.4 Hz, 4 x H-8), 6.89 (8H, d, J 7.4 Hz, 8 x H-7), 1.54 (24H, s, 24 x H-9); ^{13}C NMR δ_C (101 MHz; C_6D_6): 176.0 (C-1), 149.3 (C-2), 143.2 (C-5), 136.1 (C-6), 131.1 (q, J 31.8 Hz, C-4), 128.0 (C-7), 127.9 (C-8), 125.1 (q, J 272.5 Hz, C-10), 123.6 (q, J 3.5 Hz, C-3), 21.2 (C-9); ^{19}F NMR δ_F (376 MHz; C_6D_6): -61.88 (s); ^{199}Hg NMR δ_{Hg} (71.7 MHz; C_6D_6): -745.00 (s); HRMS (FD), m/z : (Found: 908.27762. Calc. for $C_{46}H_{40}F_6Hg_1$: 908.27350.)

Chapter V

Open-Shell Complexes

5.1 Introduction

The stabilisation of low-coordinate transition metal complexes exhibiting novel bonding modes and geometries has been explored via the use of sterically demanding ligands.^{61,109,271–274} To prevent the formation of aryl-bridged oligomers^{67–69,275–279} or donor/acceptor complexes,^{280–282} the bulky *m*-terphenyl unit has been adopted to isolate strictly two-coordinate systems, such as $(2,6\text{-Mes}_2\text{C}_6\text{H}_3)_2\text{M}$ ($\text{M} = \text{Mn}, \text{Fe}, \text{Co}$) (**Fig. 5.1**).^{71,107,283} Other notable examples include the first Cr–Cr quintuply bonded species $[2,6\text{-Dipp}_2\text{C}_6\text{H}_3\text{Cr}]_2$,¹⁰⁶ in addition to a series of heteroleptic complexes $(2,6\text{-Dipp}_2\text{C}_6\text{H}_3)\text{M}(\text{NHC}_6\text{H}_3\{2,6\text{-Mes}\}_2)$ ($\text{M} = \text{Mn}, \text{Fe}, \text{Co}$).²⁸⁴

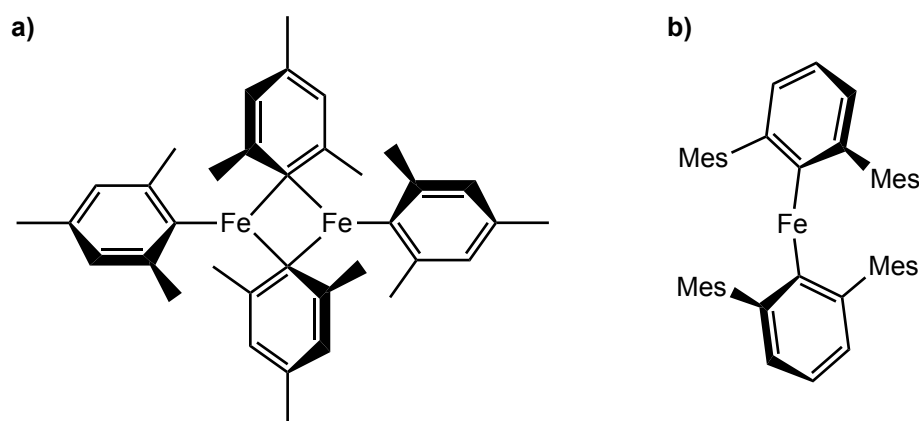


Fig. 5.1 Solid-state structures of a) the mesityl-bridged $[(\text{Mes})_2\text{Fe}]_2$ dimer, and b) the $(2,6\text{-Mes}_2\text{C}_6\text{H}_3)_2\text{Fe}$ monomer featuring the bulkier *m*-terphenyl ligand.^{107,277}

Low-coordinate transition metal complexes present a range of potential applications in catalysis and materials chemistry, notably for cross-coupling processes,¹¹² alkyne/olefin polymerisations,^{116–118} the making of nanoparticles with precise morphologies,^{124–126} and as grafting precursors for preparing catalytically-active surfaces.^{285–287} More recently, their roles as precatalysts for hydrophosphination,²⁸⁸ cyclotrimerization²⁸⁹ and dehydrocoupling⁷⁷ reactions have also been reported.

However, it is the magnetic properties of these open-shell complexes that attract particular interest owing to their ability to behave as single-molecule magnets (SMMs). Specifically, two-coordinate systems in linear or near-linear geometries generally exhibit SMM characteristics; this is a result of their weak ligand field that generates unquenched orbital angular momentum and a large axial magnetic anisotropy which, together, leads to a high relaxation barrier to spin inversion, U_{eff} .^{28,46,290,291} A prominent example is the linear iron(I) system $[\text{Fe}(\text{C}(\text{SiMe}_3)_3)_2][\text{K}(2,2,2\text{-crypt})]$ that showed an extremely large barrier ($U_{\text{eff}} = 325.2$ K) under zero applied magnetic field.⁵⁴⁻⁵⁶

One advantage of SMMs is the option to tailor their magnetic properties via modification of the chemical structure. Numerous studies on the lanthanides have revealed that ligand substitution can vary the relaxation barrier,²⁹²⁻²⁹⁵ for example, in the complex $[\text{Dy}_2(\text{valdien})_2(\text{L})_2]$ ($\text{H}_2\text{valdien} = \text{N}1,\text{N}3\text{-bis}(3\text{-methoxysalicylidene})\text{diethylenetriamine}$; $\text{L} = \text{NO}_3^-$, MeCOO^- , $\text{ClCH}_2\text{COO}^-$, $\text{Cl}_2\text{CHCOO}^-$, $\{\text{MeCO}\}_2\text{CH}^-$, $\{\text{CF}_3\text{CO}\}_2\text{CH}^-$), the incorporation of electron-withdrawing groups can cause a 7-fold increase of the U_{eff} barrier.²⁹⁶ For the transition metals, several *m*-terphenyl SMMs have also been reported, where the magnetism is studied as structural changes are implemented on the flanking aryl groups, see *Chapter 1.2.8*.^{58,136,297} However, changing the flanking groups can induce bent geometries and result in the formation of secondary metal-ligand contacts, both of which can be detrimental to the magnetism by quenching the orbital angular momentum, as demonstrated by a series of two-coordinate iron(II) complexes $(2,6\text{-Ar}_2\text{C}_6\text{H}_3\text{-}\{\text{H}\}\text{N})_2\text{Fe}$ ($\text{Ar} = \text{Dipp}$, Tripp , Mes).^{135,137} Thus, it is instead of interest to probe the magnetic behaviour by introducing electronic substituents onto the ligand periphery such that minimal structural change can be ensured.

Following our work on *para*-substituted *m*-terphenyl Group 12 complexes, concluding that *para*-functionalisation does indeed systematically influence the electronics at the metal centre without steric impact on the coordination sphere, we have sought to apply the same ligand systems to the transition metals for structural, electronic and magnetic investigation. Herein, a series of novel *para*-substituted, two-coordinate, *m*-terphenyl iron complexes of the form $(R-Ar)_2Fe$ ($Ar = 2,6-(2,6-Xyl)_2C_6H_2$; $R = t-Bu, SiMe_3, H, Cl, CF_3$) are reported. A structural study is provided through a crystallographic analysis, while electronic elucidation is performed via a combination of NMR, IR, UV/Vis and X-ray photoelectron spectroscopies and cyclic voltammetry. Finally, the magnetic properties are examined by direct current (dc) and alternating current (ac) susceptibility measurements using a SQUID magnetometer. The general structure of the ligands used in this research is shown below (Fig. 5.2).

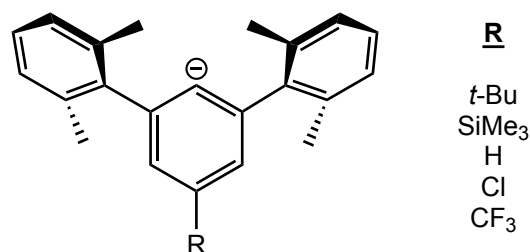


Fig. 5.2 General structure of the *para*-substituted *m*-terphenyl ligands discussed herein for the synthesis of open-shell transition metal complexes.

5.2.1.2 Crystallographic Analysis

To analyse the structural properties of the *para*-substituted *m*-terphenyl iron complexes **5.1** – **5.5**, the compounds were crystallographically characterised after recrystallisation from *s*-hexane (**5.1**, **5.2**, **5.5**) or toluene (**5.4**) at $-30\text{ }^{\circ}\text{C}$, except for $(\text{H-Ar})_2\text{Fe}$ (**5.3**) which has already been reported.^{81,298} Single crystal X-ray diffraction data of $(\text{R-Ar})_2\text{Fe}$ ($\text{R} = t\text{-Bu}$, **5.1**; SiMe_3 , **5.2**; Cl , **5.4**; CF_3 , **5.5**) showed that these complexes are all two-coordinate and monomeric in the solid-state, each featuring a single metal centre stabilised by two σ -bonded *m*-terphenyl ligands in a bent geometry (**Fig. 5.3** – **5.4**), see **Table 5.1**. Owing to the steric demands of the bulky *m*-terphenyl ligands, the nearest $\text{Fe}\cdots\text{Fe}$ separations are $d(\text{Fe}\cdots\text{Fe}) = 10.4\text{ \AA}$ (for **5.4**), suggesting that there are no interactions between adjacent metal centres. The closest metal-ligand secondary contacts occur for **5.1** [$\text{Fe}(1)\text{--C}(29) = 2.834(4)\text{ \AA}$] between iron and the *ipso*-carbon of a flanking aryl; these distances lie within the sum of their van der Waals radii (*ca.* 3.75 \AA).²⁹⁹ Akin to the lithium species **3.9** – **3.13** in *Chapter 3.2.2.2*, $\text{Fe}\cdots\text{H}\text{--C}$ anagostic interactions are formed to the hydrogens of the flanking methyl groups [$2.6706(9)\text{--}3.1425(4)\text{ \AA}$]. The absence of these contacts in the Group 12 analogues **4.1** – **4.12** is possibly due to the smaller van der Waals radii assumed for Zn (1.39 \AA), Cd (1.58 \AA) and Hg (1.55 \AA) relative to that of Fe (*ca.* 2.05 \AA).^{184,185,299} However, the difficulties in determining the van der Waals radii of metal atoms could mean that the values used for the Group 12 elements may be underestimated by *ca.* 0.5 \AA .³⁰⁰ Despite this, the presence of $\text{Fe}\cdots\text{H}\text{--C}$ contacts could contribute to the bending of these iron structures. Relevant bond lengths and angles are given in **Table 5.1**.

Table 5.1 Relevant bond lengths (Å) and angles (°) for the *m*-terphenyl iron complexes, (R-Ar)₂Fe (**5.1**, **5.2**, **5.4** and **5.5**), featuring *para*-substituent, R. The unsubstituted analogue, (H-Ar)₂Fe (**5.3**), is reported elsewhere.^{81,298}

M = Fe	Bond Lengths (Å) and Angles (°)			
	5.1 ^a (R = <i>t</i> -Bu)	5.2 ^b (R = SiMe ₃)	5.4 ^{b,c} (R = Cl)	5.5 (R = CF ₃)
Fe(1)–C(1)	2.041(4)	2.026(4) {2.019(4)}	2.031(2) {2.0230(18)} [2.041(2)]	2.038(4)
Fe(1)–C(23)	2.019(4)	2.018(4) {-}	2.0301(18) {2.0338(18)} [2.0327(18)]	2.042(4)
C(1)–Fe(1)–C(23)	169.92(17)	172.24(17) {174.9(3)}	170.50(8) {170.74(8)} [168.30(8)]	170.57(16)
C(1)-aryl plane ···C(23)plane	80.22(14)	80.37(13) {79.77(18)}	83.69(7) {89.79(6)} [85.26(6)]	82.22(14)
C(1)-aryl plane ···flanking aryl plane	80.37(14) 89.2(10) ^a 87.8(5) ^a	72.03(14) 78.69(14) {79.69(14)} {68.05(14)}	86.89(7) 78.65(8) {79.03(7)} {71.40(7)} [77.56(7)] [86.10(7)]	79.31(16) 84.67(19)
C(23)-aryl plane ···flanking aryl plane	86.17(15) 82.17(15)	68.04(14) 80.37(14) {-} {-}	72.81(7) 76.60(7) {81.28(7)} {89.90(7)} [76.75(7)] [68.56(7)]	80.69(15) 89.94(15)

^a For **5.1**, two ‘C(1)plane···flanking aryl plane’ values due to disordered flanking ring.

^b For **5.2** and **5.4**, molecule 2 of the asymmetric unit is in curly brackets.

^c For **5.4**, molecule 3 of the asymmetric unit is in square brackets.

The *para*-substituted iron complexes show no significant change in Fe–C bond length as the functional group is varied. All Fe–C_{ipso} bond distances occur within a narrow range [2.018(4)–2.042(4) Å], where any minor structural deviations are likely due to crystal packing effects. For example, in **5.4**, the bond lengths vary between crystallographically independent molecules in the asymmetric unit [Fe(1)–C(1) = 2.0230(18) vs. 2.041(2) Å for molecules 2 and 3, respectively], suggesting that their structures are susceptible to minor deformation by crystal packing forces. Overall, the Fe–C bond distances are comparable to the unsubstituted analogue **5.3** [Fe(1)–C(1) = 2.028(2) Å, Fe(1)–C(23) = 2.029(2) Å], as well as other iron diaryls in the literature, whose Fe–C bond lengths range between 2.03–2.06 Å.^{70,81,107,108,138,298}

A narrow range of C–Fe–C angles for **5.1**, **5.2**, **5.4** and **5.5** [168.30(8)–174.9(3)°] are observed that exhibit small variations as the *para*-group is changed, and are comparable to the unsubstituted derivative **5.3** [C(1)–Fe(1)–C(23) = 167.70(9)°].^{81,298} It appears that the bulkier substituents produce more linear structures [C(1)–Fe(1)–C(23) = 174.9(3) vs 167.70(9)° for **5.2** (R = SiMe₃) and **5.3** (R = H) respectively], although this could be a consequence of crystal packing effects. This has been rationalised by a shallow potential energy well for C–M–C bending that results in easier distortion of the complex by crystal packing forces, as demonstrated by (2,6-Mes₂C₆H₃)₂Fe whose two crystallographically independent molecules display significantly different C–Fe–C angles of 164.4(1)° and 171(1)°.^{107,109} The iron diaryls **5.1** – **5.5** exhibit more bent geometries than the Group 12 series **4.1** – **4.12** described in *Chapter 4.2.1.2*, possibly due to the presence of secondary metal-ligand contacts. However, the angles are similar to other iron diaryls in the literature, and more linear than (2,6-Dipp₂C₆H₃)₂Fe [150.34(6)°], which could prove advantageous from a magnetic standpoint.^{107,108,138}

To reduce the steric strain between the *m*-terphenyl ligands in complexes **5.1** – **5.5**, the two metal-substituted central aryl rings on each ligand are orientated approximately orthogonal to one another. This results in torsion angles between the planes of these 6-membered central rings, C(1)-aryl and C(23)-aryl, that vary with the *para*-group; the *t*-Bu, SiMe₃ and CF₃ iron complexes [79.77(18)–82.22(14)°] are less perpendicular than the Cl derivative [83.69(7)–89.79(6)°]. However, this could be due to crystal packing effects or the steric size of the *para*-substituent. In spite of this, the torsion angles are similar to that of the unsubstituted analogue **5.3** [83.36(8)°], showing that these angles generally fall within a reasonably narrow 10° range.^{81,298}

Finally, for **5.1** – **5.5**, the torsion angles between the planes of the central aryl rings, C(1)-aryl and C(23)-aryl, and the flanking 2,6-Xyl groups [68.04(14)–89.94(15)°] occur within a similar range to the Group 12 species **4.1** – **4.12** [69.52(7)–88.63(13)°] in *Chapter 4.2.1.2*. Here, the 2,6-Xyl flanking groups adopt a near-orthogonal orientation, likely to minimise steric interactions between the *ortho*-methyl groups on each *m*-terphenyl ligand.

In summary, the crystal structures of the *m*-terphenyl iron complexes **5.1** – **5.5** show little structural variation as the *para*-substituent is changed, which suggests that *para*-functionalisation has minimal steric influence on the geometry, possibly because the *para*-group is directed away from the coordination sphere. Moreover, Fe⋯H–C anagostic interactions are identified between the metal centre and the flanking methyl groups. However, although structurally similar, further studies are required to probe the electronic and magnetic properties of these systems.

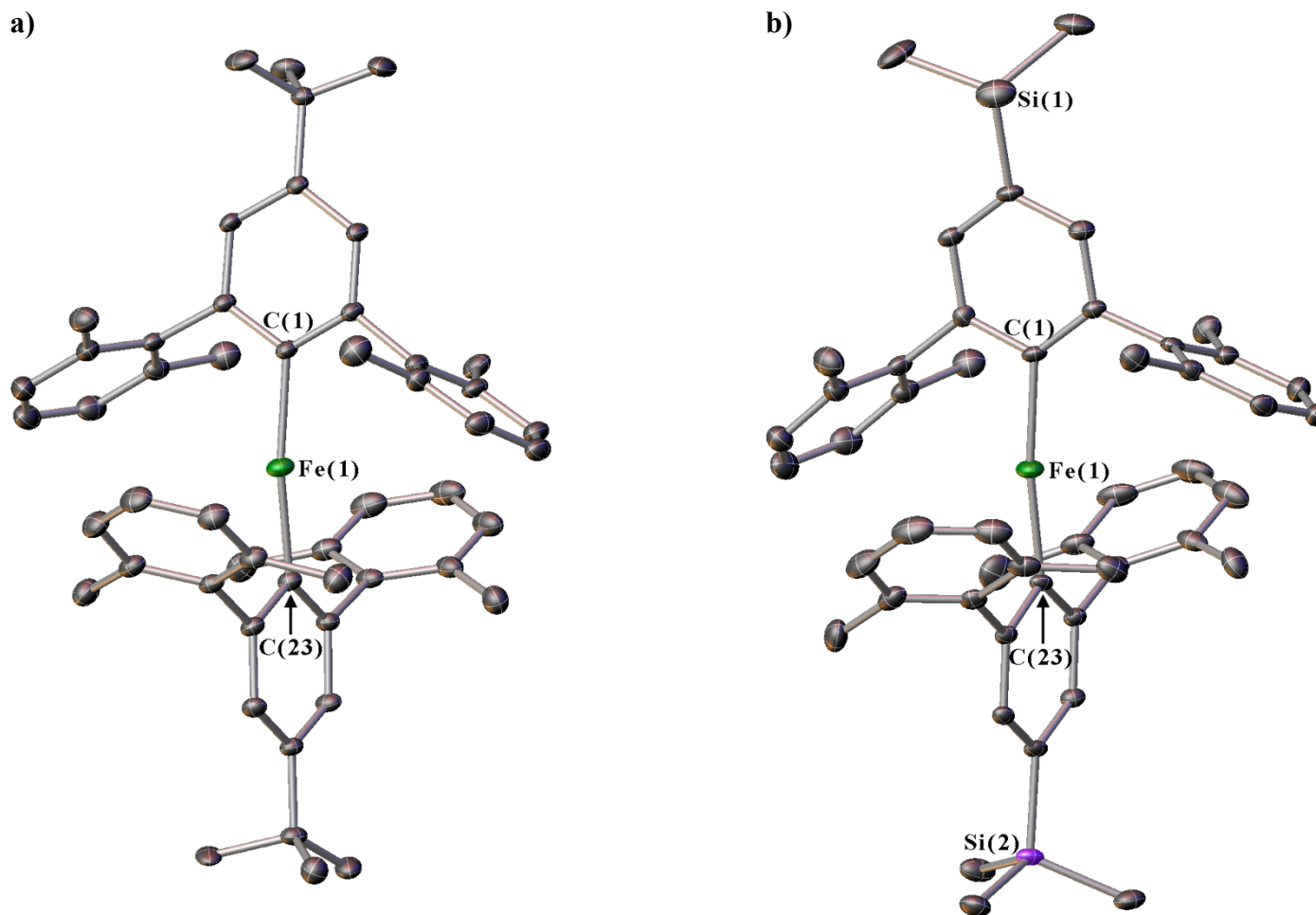


Fig. 5.3 Crystal structures of the *m*-terphenyl iron complexes, (R-Ar)₂Fe, where a) R = *t*-Bu (**5.1**) and b) R = SiMe₃ (**5.2**). Ellipsoids set at 9% and 34% probability respectively. Hydrogen atoms and residual solvent molecules are omitted for clarity. When necessary, only one molecule from the asymmetric unit is shown. The unsubstituted analogue, (H-Ar)₂Fe (**5.3**), is reported elsewhere.^{81,298}

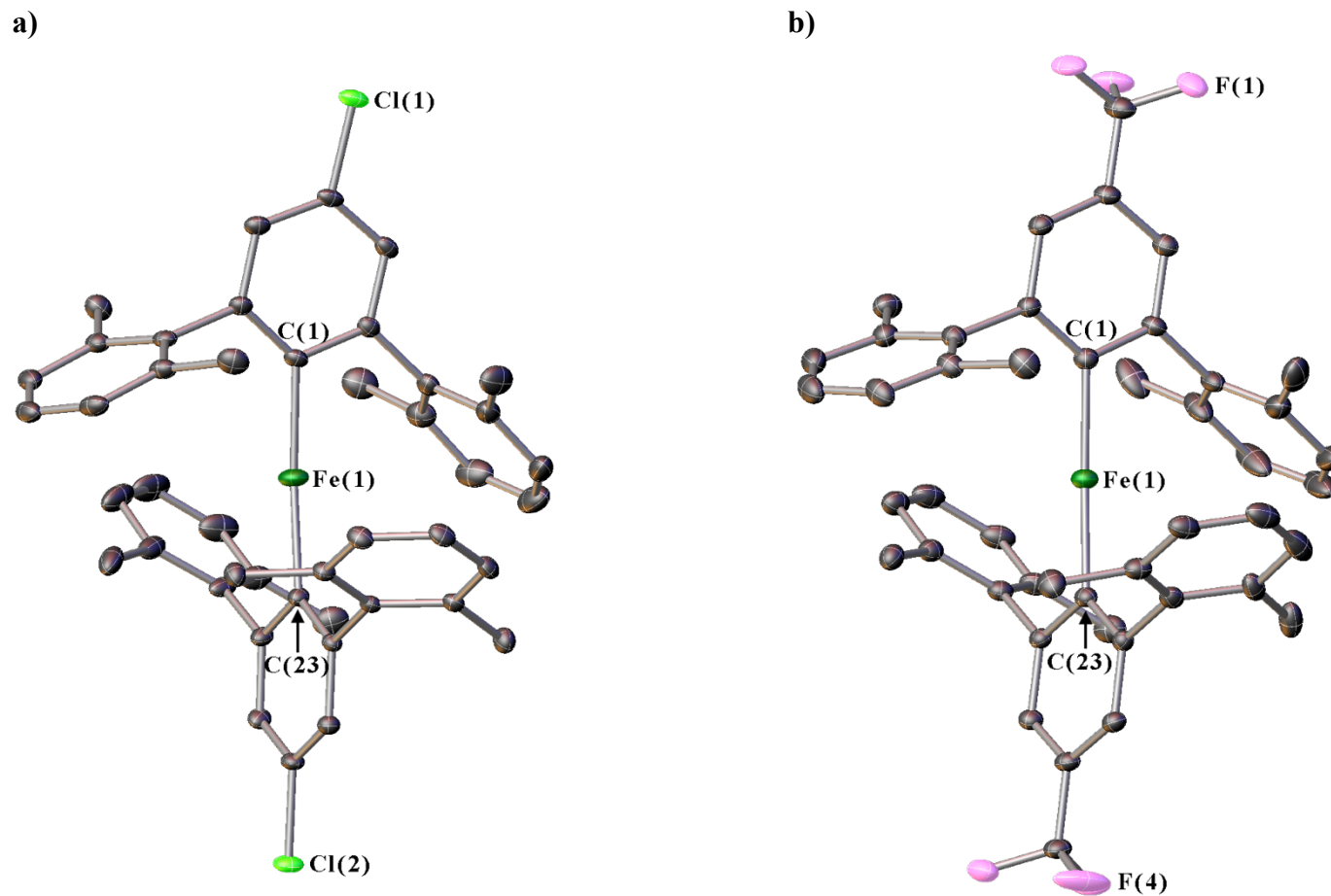


Fig. 5.4 Crystal structures of the *m*-terphenyl iron complexes, (R-Ar)₂Fe, where a) R = Cl (**5.4**) and b) R = CF₃ (**5.5**). Ellipsoids set at 30% and 14% probability respectively. Hydrogen atoms and residual solvent molecules are omitted for clarity. When necessary, only one molecule from the asymmetric unit is shown. The unsubstituted analogue, (H-Ar)₂Fe (**5.3**), is reported elsewhere.^{81,298}

5.2.1.3 NMR Analysis

The electronic properties of the *para*-substituted *m*-terphenyl iron diaryls **5.1** – **5.5** were studied by ^1H NMR spectroscopy in *d*-benzene. These high-spin d^6 iron(II) complexes ($S = 2$) are paramagnetic and therefore exhibit broadened and shifted signals over a wide chemical shift range.^{301–303} Nonetheless, spectral assignment is possible by rough integration of the NMR signals, using the *m*-terphenyl numbering scheme (**Fig. 5.7**). In all cases, four characteristic peaks occur: one for the central ring *meta*-hydrogens (H-3), two for the flanking ring *meta*-/*para*-hydrogens (H-7 and H-8), and one for the flanking methyl groups (H-9). Additional singlets are observed for **5.1**, **5.2** and **5.3** due to the *t*-Bu, SiMe_3 and H *para*-substituents respectively (**Fig. 5.5**). The results reflect a study where protons in the ligand plane go downfield, while those out-of-plane go upfield.³⁰⁴ For **5.1** – **5.5**, this plane is defined by the central ring of the *m*-terphenyl ligand.

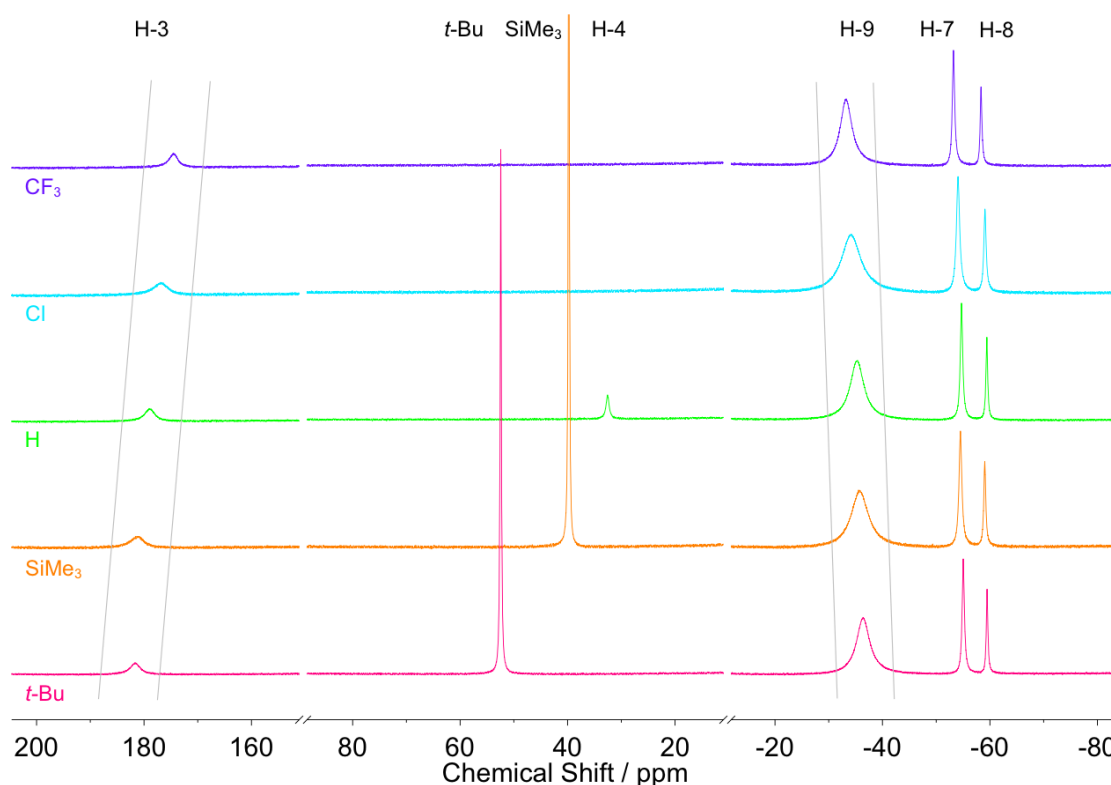


Fig. 5.5 Stacked wide-scan ^1H NMR spectra of the paramagnetic *m*-terphenyl iron complexes, $(\text{R-Ar})_2\text{Fe}$, **5.1** – **5.5**, showing peak shifts for H-3 and H-9.

A comparison of the ^1H NMR spectra reveals several features. Firstly, the 2,6-Xyl aryl protons, H-7 (-53.2 to -55.0 ppm) and H-8 (-58.4 to -59.5 ppm), remain relatively unshifted across the series. Secondly, the central ring hydrogens, H-3, and the flanking methyl groups, H-9, are both shifted towards zero by increased electron-withdrawing strength of the *para*-substituent, see **Table 5.2**. Here, the H-9 peak shifts in the opposite direction than that for **3.9 – 3.13** in *Chapter 3.2.2.3* and **4.1 – 4.12** in *Chapter 4.2.1.3*.

Table 5.2 Wide-scan ^1H NMR chemical shifts, δ , for $(\text{R-Ar})_2\text{Fe}$ (**5.1 – 5.5**), where R is the *para*-substituent, for relevant atoms on the *m*-terphenyl iron complexes. The flanking aryl atoms remain unshifted so have been omitted.¹³⁹

$(\text{R-Ar})_2\text{Fe}$	R Group	Hammett Constant, σ_{para}	^1H NMR Chemical Shifts, δ (ppm)	
			H-3	H-9
5.1	<i>t</i> -Bu	-0.20	181.6	-36.4
5.2	SiMe ₃	-0.07	181.2	-35.8
5.3	H	0.00	178.9	-35.3
5.4	Cl	0.23	176.8	-34.2
5.5	CF ₃	0.54	174.5	-33.2

Plotting a graph of the chemical shifts, δ , against the Hammett constants, σ_{para} , gives a linear correlation for each trend (**Fig. 5.6**).¹³⁹ This implies that *para*-substitution directly influences the electronic properties of the *m*-terphenyl ligands. Here, the shifting of the flanking methyl peaks, H-9, is likely due to weak interactions with the metal centre, as evidenced by the formation of $\text{Fe}\cdots\text{H-C}$ anagostic contacts in the crystal structures. The trend for H-3, however, was unobserved in complexes **3.9 – 3.13** and **4.1 – 4.12**; this could possibly be rationalised in terms of a field generated by the paramagnetic iron centre, whose strength varies depending on the *para*-group, that extends to the nearby H-3 protons and influences their chemical shifts.

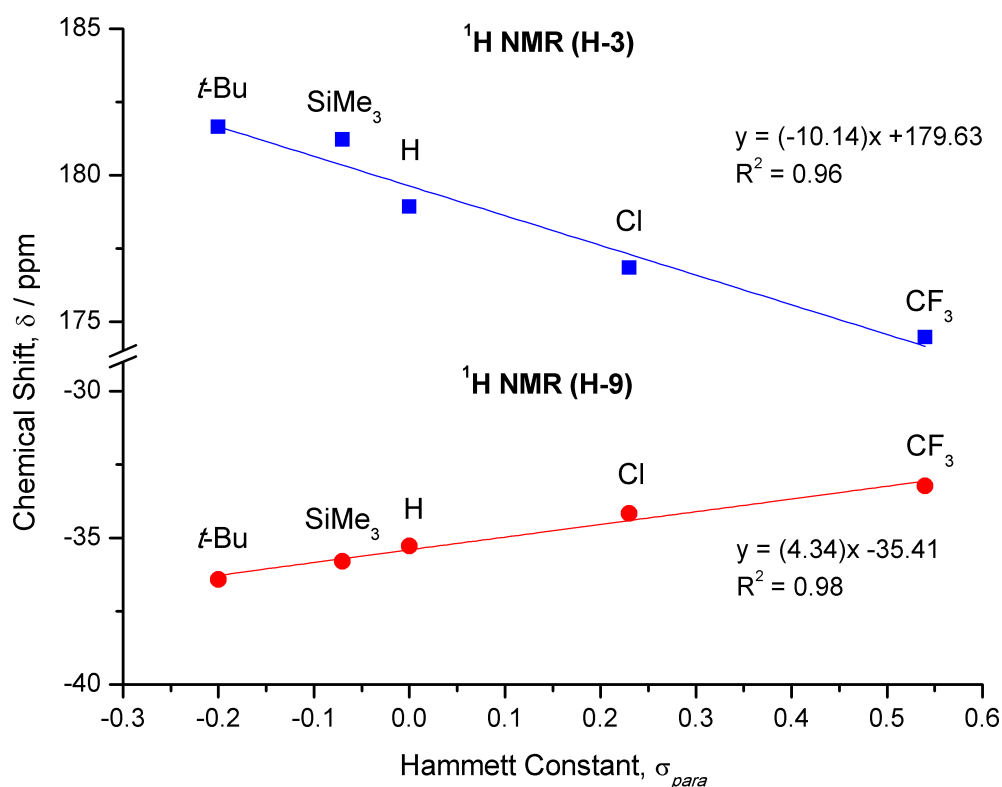


Fig. 5.6 Plot of the ^1H NMR chemical shifts, δ , for the central ring protons, H-3, and the flanking methyl protons, H-9, of the *para*-substituted iron complexes $(\text{R-Ar})_2\text{Fe}$, **5.1** – **5.5**, versus their literature Hammett constants, σ_{para} .¹³⁹

In summary, while wide-scan ^1H NMR provides a characteristic fingerprint of the iron complexes, the spectra for **5.1** – **5.5** reveal only ligand-based electronic trends; it does not describe the properties at the iron centre. In the absence of ^{57}Fe NMR, other techniques must thus be adopted to measure the electronic differences at the metal.

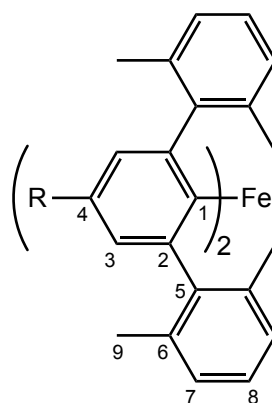


Fig. 5.7 NMR numbering scheme for the iron diaryls, $(\text{R-Ar})_2\text{Fe}$.

5.2.1.4 IR Analysis

The electronic properties of the *para*-substituted *m*-terphenyl iron complexes **5.1** – **5.5** were further studied by IR spectroscopy as 6.4 mM solutions in benzene. A general fingerprint can be identified across the series; all systems exhibit similar peaks between 2734–2919 cm^{-1} , 1431–1437 cm^{-1} , and 1377–1378 cm^{-1} , possibly due to C–H stretches, C=C stretches and C–C–H bending modes respectively (**Fig. 5.8**).³⁰⁵ However, no discernible peak shifts are observed between the complexes. Nonetheless, the IR spectra could enable the electronic structures of **5.1** – **5.5** to be probed via the binding of an infrared-active species to the metal centre. This is explored in *Chapter 6.2.1.3* with a detailed analysis of isocyanide reactivity.

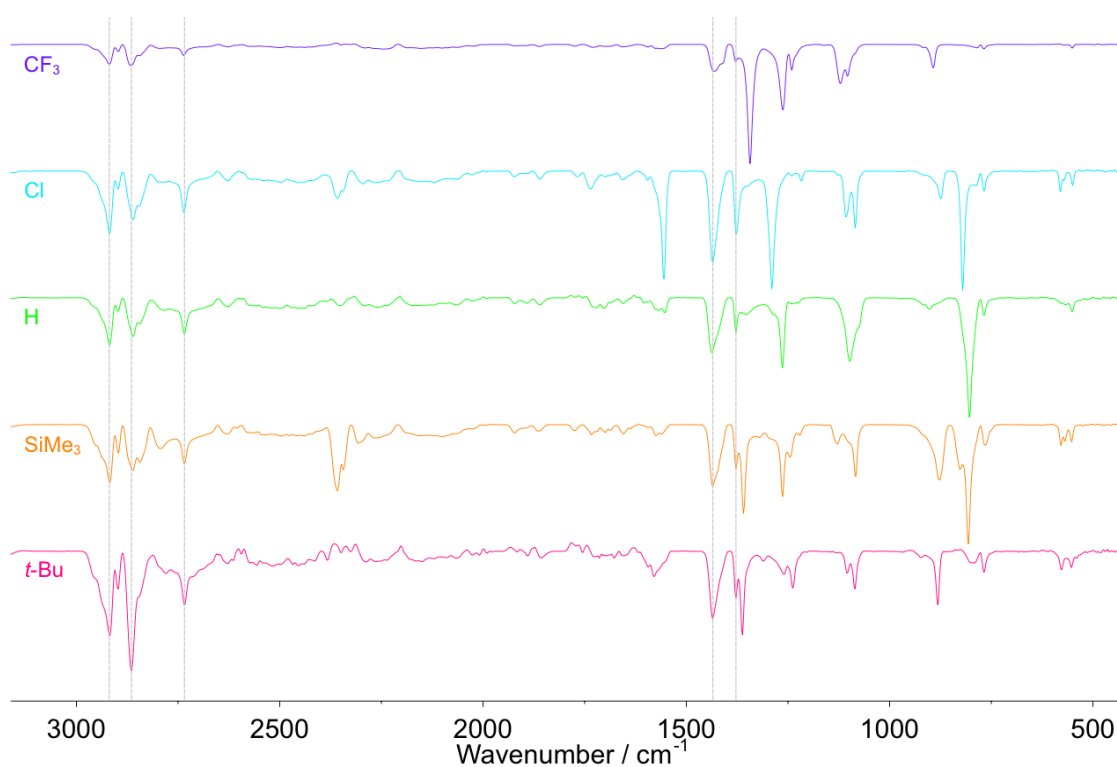


Fig. 5.8 Stacked IR spectra of the *m*-terphenyl iron complexes, $(\text{R-Ar})_2\text{Fe}$, **5.1** – **5.5**, showing similarities across the series but no discernible trends.

5.2.1.5 UV/Vis Analysis

The *para*-substituted *m*-terphenyl iron systems **5.1** – **5.5** were also analysed by UV/Vis spectroscopy as 0.6 mM solutions in toluene, after attempts in hexane and THF presented problems due to solubility or solvatochromic effects.³⁰⁶ In all cases, broad absorption bands are observed below 500 nm with molar extinction coefficients ranging *ca.* 500–1656 mol⁻¹ dm³ cm⁻¹, giving the complexes their yellow-green colours. These bands exhibit a general fingerprint consisting of four transitions that shift in wavelength depending on the *para*-substituent, although with no identifiable trend (**Fig. 5.9**). Regarding their intensities, however, the extinction coefficients seemingly decrease for *para*-groups with greater electron-withdrawing strengths, barring the Cl analogue. Despite this, since the absorptions reside in the shoulder of the intense ligand band below 350 nm, the results are difficult to interpret and would require computational calculations for a fuller explanation.

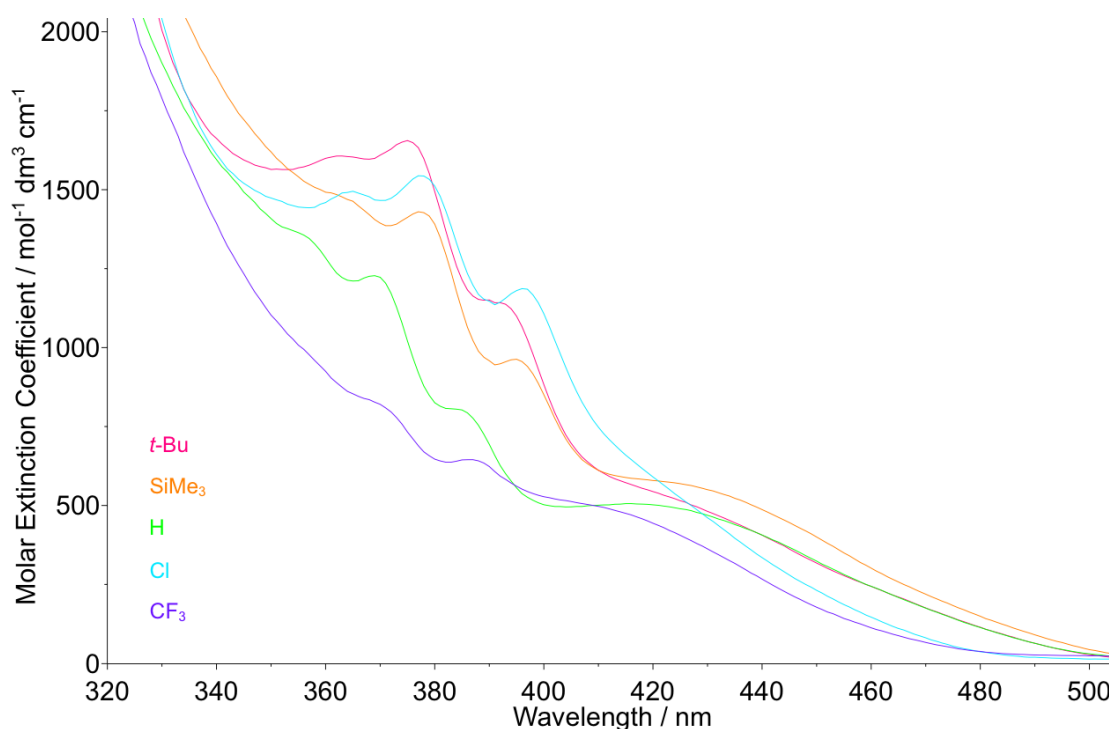


Fig. 5.9 Superimposed UV/Vis spectra of the *m*-terphenyl iron complexes, (R-Ar)₂Fe, **5.1** – **5.5**, showing similar peak shapes but no discernable trends.

5.2.1.6 XPS Analysis

The *t*-Bu and CF₃ *para*-substituted *m*-terphenyl iron complexes, **5.1** and **5.5**, were studied by X-ray photoelectron spectroscopy (XPS). This surface-sensitive technique analyses the elemental composition of a sample and provides information on an atom's chemical environment via its measured binding energy.³⁰⁷ These energies generally increase for complexes featuring electron-withdrawing groups.^{308–317} For **5.1** and **5.5**, wide-scan spectra reveal C 1s and Fe 2p electron peaks, plus a F 1s signal in **5.5** for the CF₃ group (**Fig. 5.10**). In **5.1**, the unexpected O 1s and Si 2p peaks are likely due to silicone grease contaminants, although XPS will detect oxidised surface defects absent in the bulk material. A comparison of the Fe 2p signals reveals that, while both peaks exhibit similar shapes with binding energies indicative of a +2 oxidation state, changing the *para*-substituent causes no discernible peak shifts.^{318,319} Hence, XPS fails to detect any electronic differences at the iron centre.

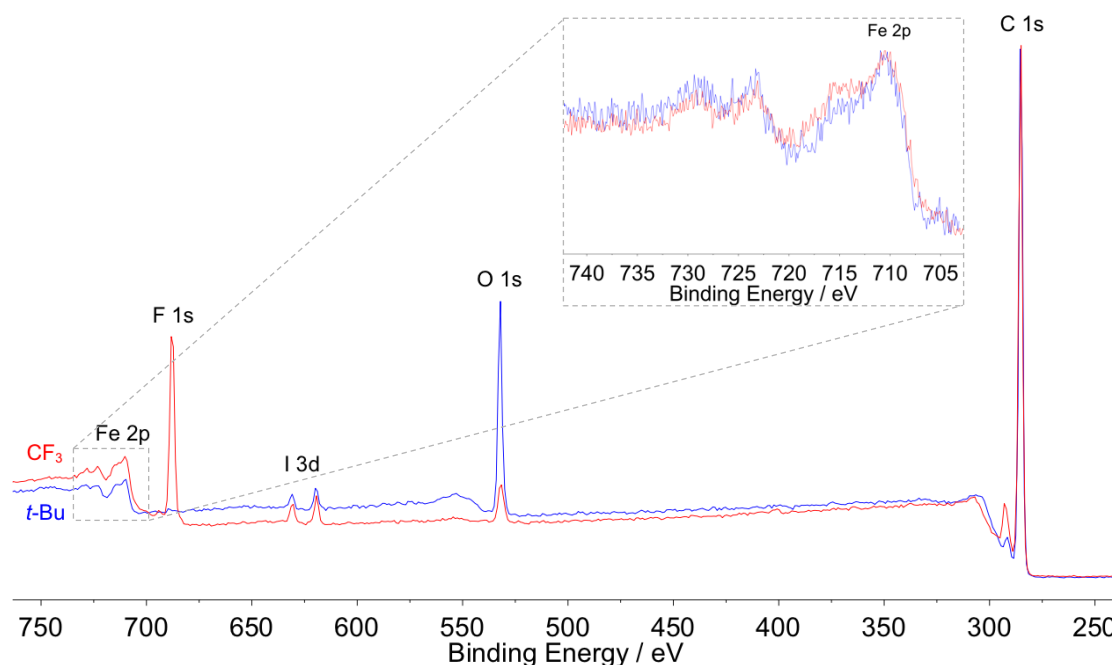


Fig. 5.10 Superimposed X-ray photoelectron spectra of the *t*-Bu and CF₃ *m*-terphenyl iron complexes, (R-Ar)₂Fe, **5.1** and **5.5**, showing similar signals for the Fe 2p peaks as shown by their normalized high-resolution spectra (inset).

5.2.1.7 Cyclic Voltammetry Analysis

The electronic properties of the *para*-substituted *m*-terphenyl iron complexes **5.1** – **5.5** were next investigated by cyclic voltammetry (CV) as 1.0 mM solutions in THF containing 0.5 M [ⁿBu₄N][BF₄] electrolyte.³²⁰ All samples show a single reduction process occurring at cathodic peak potentials, $E_{p,c}$, ranging between -2.01 and -2.28 V (vs. Fc⁺/Fc at 100 mV s⁻¹) (Fig. 5.11 – 5.13). Here, conventional $E_{1/2}$ potentials have not been quoted as not all complexes yield a return wave. To help deduce the nature of the redox process, a number of scan rates were measured between 20–500 mV s⁻¹. Relevant data from the cyclic voltammograms are summarised in Table 5.3.

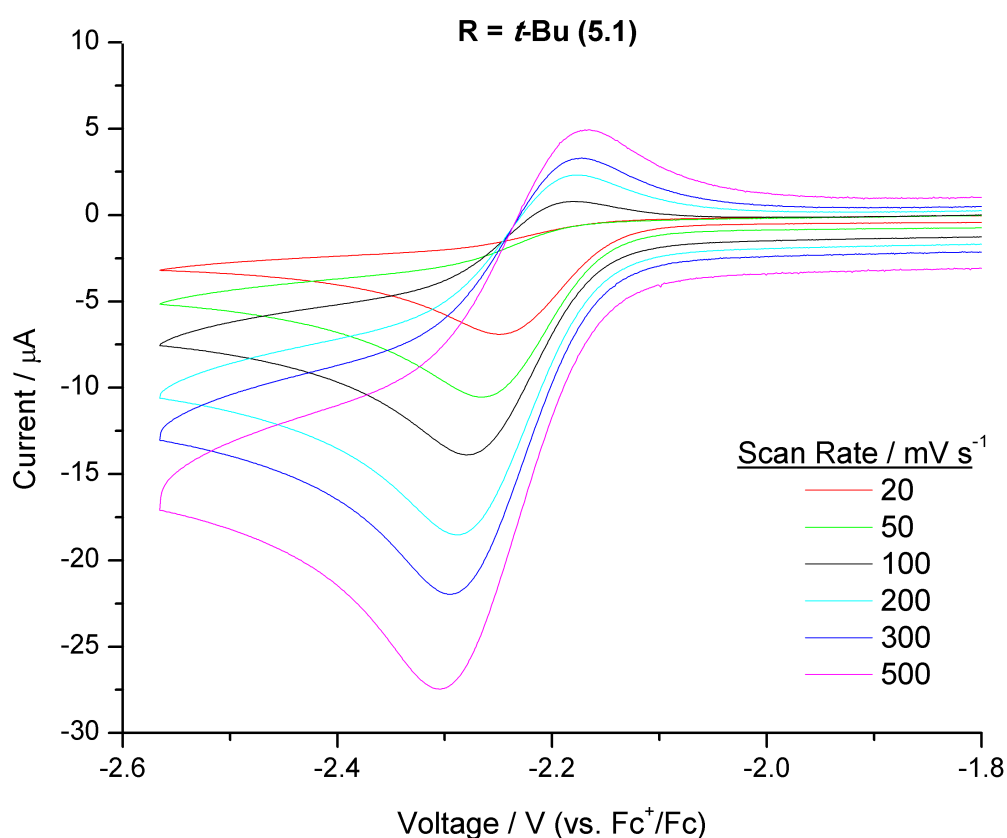


Fig. 5.11 Cyclic voltammograms of the *m*-terphenyl iron complex, (R-Ar)₂Fe, in THF containing 0.5 M [ⁿBu₄N][BF₄], where a) R = *t*-Bu (**5.1**).

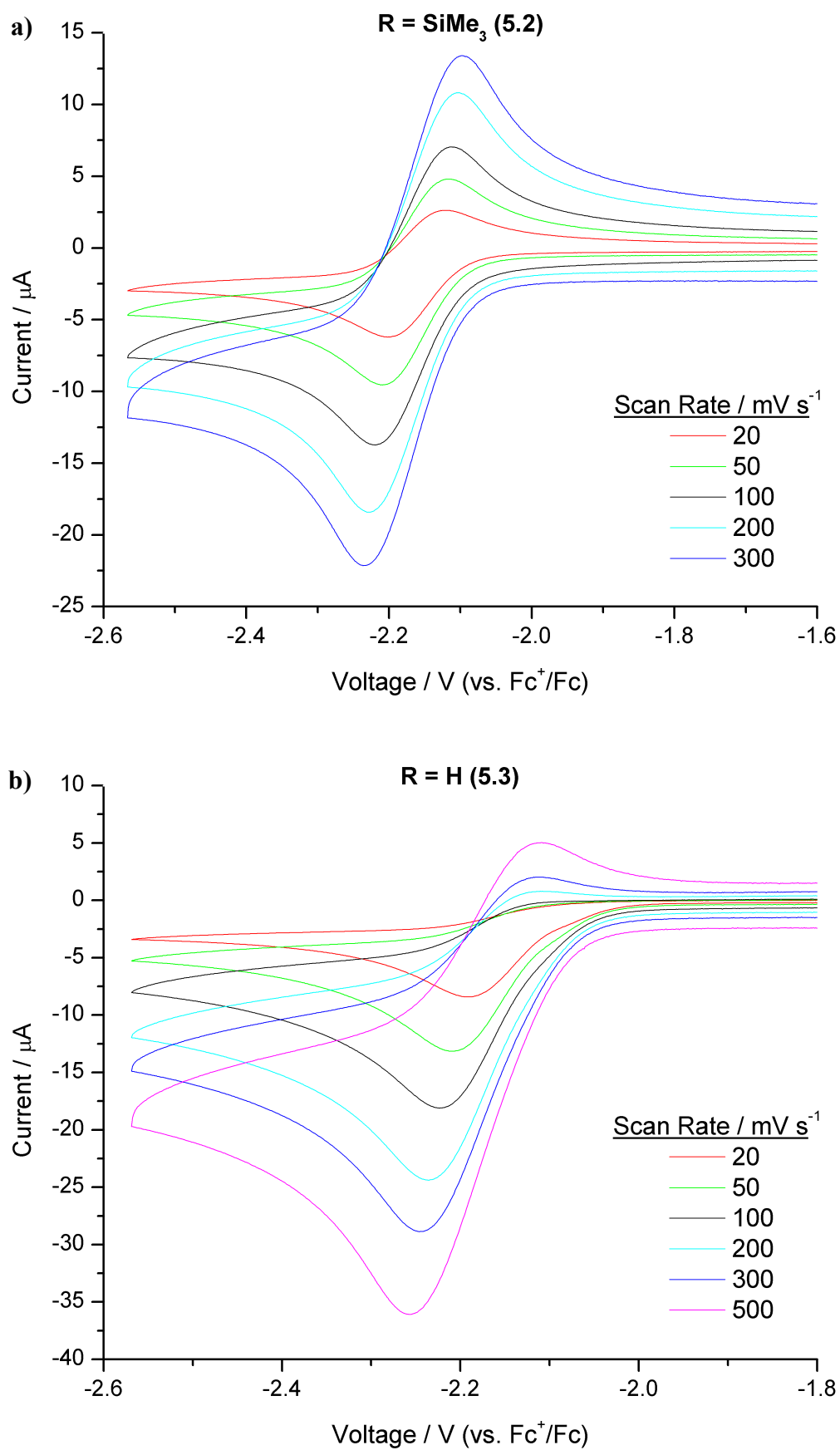


Fig. 5.12 Cyclic voltammograms of the *m*-terphenyl iron complexes, $(\text{R-Ar})_2\text{Fe}$, in THF containing 0.5 M $[\text{nBu}_4\text{N}][\text{BF}_4]$, where a) $\text{R} = \text{SiMe}_3$ (**5.2**) and b) $\text{R} = \text{H}$ (**5.3**).

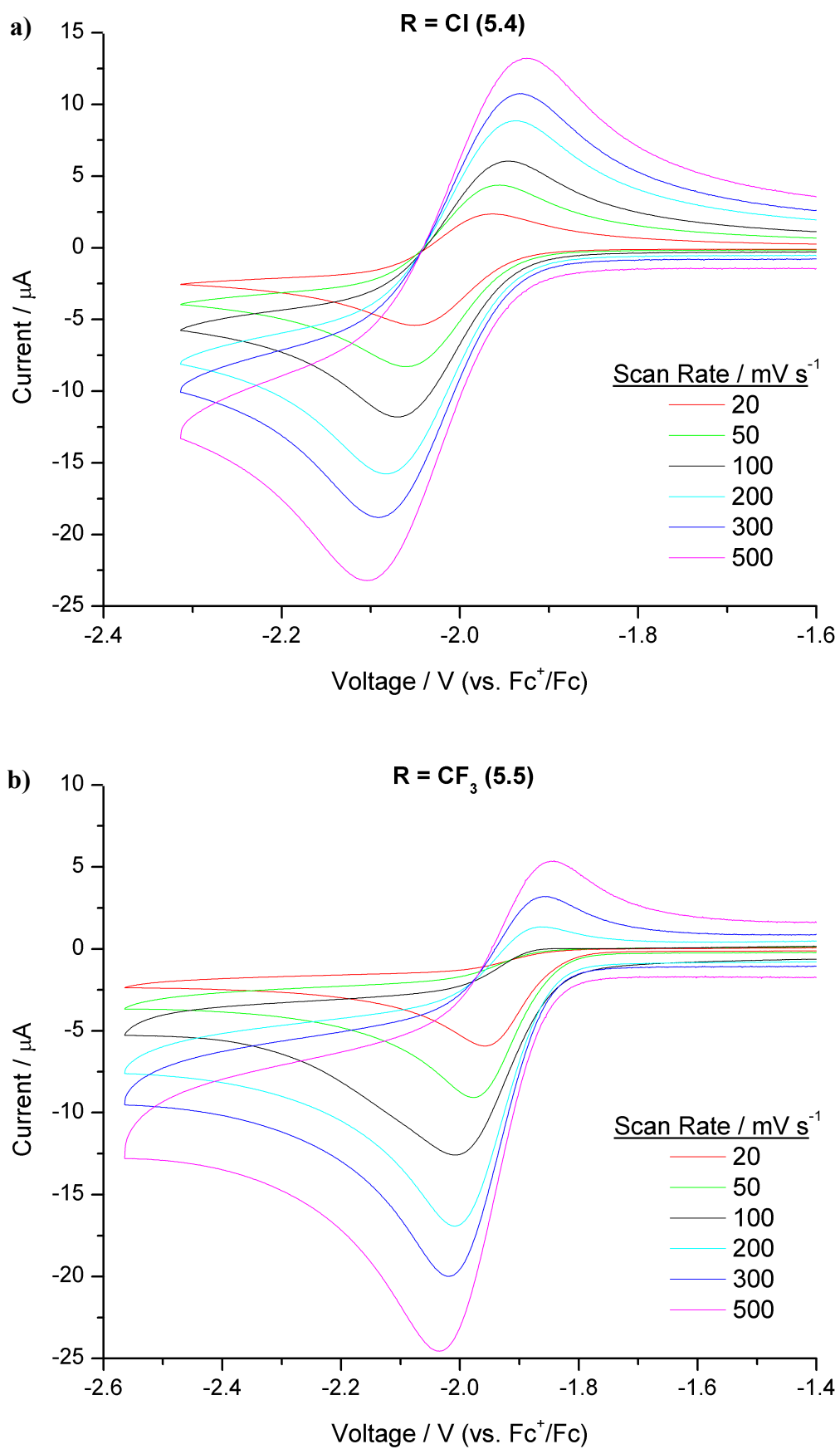


Fig. 5.13 Cyclic voltammograms of the *m*-terphenyl iron complexes, $(R-Ar)_2Fe$, in THF containing 0.5 M $[nBu_4N][BF_4]$, where a) R = Cl (5.4) and b) R = CF_3 (5.5).

Table 5.3 Cyclic voltammetry data for (R-Ar)₂Fe, **5.1** – **5.5**, with *para*-substituent, R.

	Scan Rate, ν / mV s ⁻¹	E _{p,c} / V	E _{p,a} / V	E _{1/2} / V	ΔE / mV	I _{p,c} / μ A	I _{p,a} / μ A	$\left \frac{I_{p,a}}{I_{p,c}} \right $
R = <i>t</i> -Bu (5.1)	20	-2.25	-	-	-	-6.33	-	-
	50	-2.27	-	-	-	-9.59	-	-
	100	-2.28	-2.18	-2.23	100	-12.14	3.91	0.32
	200	-2.29	-2.18	-2.23	110	-16.30	6.55	0.40
	300	-2.30	-2.17	-2.23	120	-19.29	8.29	0.43
	500	-2.30	-2.17	-2.24	140	-23.77	11.13	0.47
	100 (Fc ⁺ /Fc)	0.52	0.61	0.56	90	-8.50	9.50	0.90 ^a
R = SiMe ₃ (5.2)	20	-2.20	-2.12	-2.16	80	-5.89	4.16	0.71
	50	-2.21	-2.12	-2.16	90	-8.98	6.92	0.77
	100	-2.22	-2.11	-2.17	110	-12.77	9.51	0.74
	200	-2.23	-2.10	-2.17	120	-16.69	13.85	0.83
	300	-2.23	-2.10	-2.17	140	-19.84	16.74	0.84
	500	-2.23	-2.10	-2.17	140	-19.84	16.74	0.84
	100 (Fc ⁺ /Fc)	0.52	0.62	0.57	100	-9.93	12.83	0.77 ^a
R = H (5.3)	20	-2.19	-	-	-	-8.15	-	-
	50	-2.21	-	-	-	-12.70	-	-
	100	-2.22	-	-	-	-17.32	-	-
	200	-2.24	-2.11	-2.17	130	-23.19	5.91	0.26
	300	-2.24	-2.11	-2.18	130	-27.23	8.26	0.30
	500	-2.26	-2.11	-2.18	150	-33.48	12.97	0.39
	100 (Fc ⁺ /Fc)	0.50	0.64	0.57	140	-26.97	29.78	0.91 ^a
R = Cl (5.4)	20	-2.05	-1.96	-2.01	90	-5.30	3.74	0.71
	50	-2.06	-1.96	-2.01	100	-8.07	6.17	0.76
	100	-2.07	-1.95	-2.01	120	-11.37	8.20	0.72
	200	-2.08	-1.94	-2.01	150	-15.03	11.42	0.76
	300	-2.09	-1.93	-2.01	160	-17.84	13.25	0.74
	500	-2.10	-1.92	-2.01	180	-21.61	15.64	0.72
	100 (Fc ⁺ /Fc)	0.52	0.61	0.56	90	-9.91	10.28	0.96 ^a
R = CF ₃ (5.5)	20	-1.96	-	-	-	-5.76	-	-
	50	-1.98	-	-	-	-8.81	-	-
	100	-2.01	-	-	-	-11.76	-	-
	200	-2.01	-1.86	-1.94	150	-15.93	4.13	0.26
	300	-2.02	-1.86	-1.94	160	-18.79	6.32	0.34
	500	-2.04	-1.84	-1.94	190	-22.78	8.76	0.38
	100 (Fc ⁺ /Fc)	0.51	0.62	0.56	100	-12.65	14.15	0.89 ^a

^a For the Fc⁺/Fc reference, $|I_{p,c}/I_{p,a}|$ values are quoted.

The redox activity for **5.1** – **5.5** cannot be described as reversible since, for reversibility, the peak-to-peak separation, ΔE , should equal 57 mV, the peak current ratio, $|I_{p,a}/I_{p,c}|$, should be 1, and the peak positions should be independent of scan rate, v .³²¹ However, a plot of the cathodic peak currents, $I_{p,c}$, versus $v^{1/2}$, reveals a linear trend that suggests the process is diffusion controlled (Fig. 5.14).³²⁰ It also appears that **5.2** and **5.4** are more reversible than **5.1**, **5.3** and **5.5** where, for the latter three, the absence of a return wave indicates that the reduced species decomposes before it can be re-oxidised; at faster scan rates, however, re-oxidation is observed as shown by the emerging return signal. This behaviour can be justified by chemical reaction of the reduced intermediate causing its removal from the diffusion layer. The reduction mechanisms can thus be tentatively assigned as ‘E’ type for **5.2** and **5.4**, and as ‘EC’ type for **5.1**, **5.3** and **5.5**.³²⁰

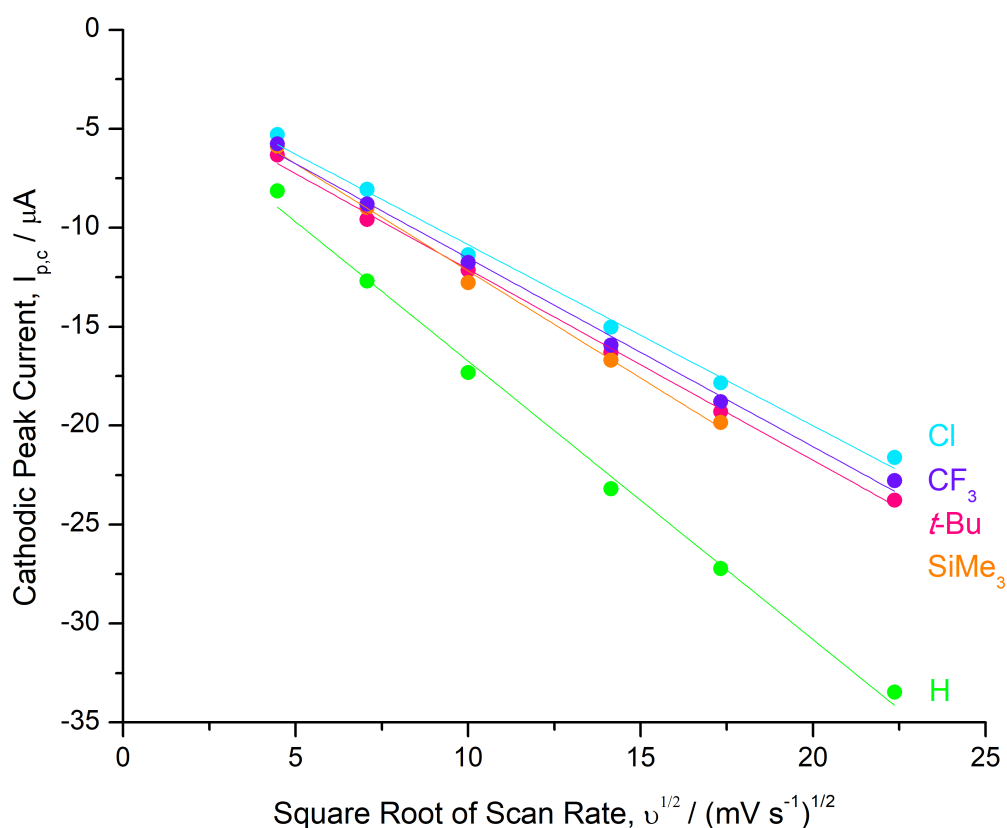


Fig. 5.14 Linear plots of the cathodic peak currents, $I_{p,c}$, versus the square root of the scan rate, $v^{1/2}$, for the *para*-substituted iron complexes (R-Ar)₂Fe, **5.1** – **5.5**.

The observed redox behaviour is likely metal-based, corresponding to a single-electron reduction at the iron centre, from Fe(II) \rightarrow Fe(I). This is supported by CV data of the mercury complexes, (R-Ar)₂Hg (R = *t*-Bu, **4.3**; CF₃, **4.12**), discussed previously in Chapter 4.2.1.4, where no reduction processes were detected. This suggests that neither the mercury centre nor the *m*-terphenyl ligand are redox active and, therefore, that the reduction of **5.1** – **5.5** occurs at the iron centre. Hence, cyclic voltammetry enables direct measurement of the electronic properties at the metal which, in turn, allows the effects of *para*-substitution on the iron centres to be studied. A comparison of the cathodic reduction potentials, E_{p,c}, reveals a peak shift towards less negative potentials (–2.28, –2.22, –2.22, –2.07, –2.01 V vs. Fc⁺/Fc at 100 mV s^{–1}, for **5.1** – **5.5** respectively) as electron-withdrawing strength of the *para*-substituent is increased (**Fig. 5.15**).

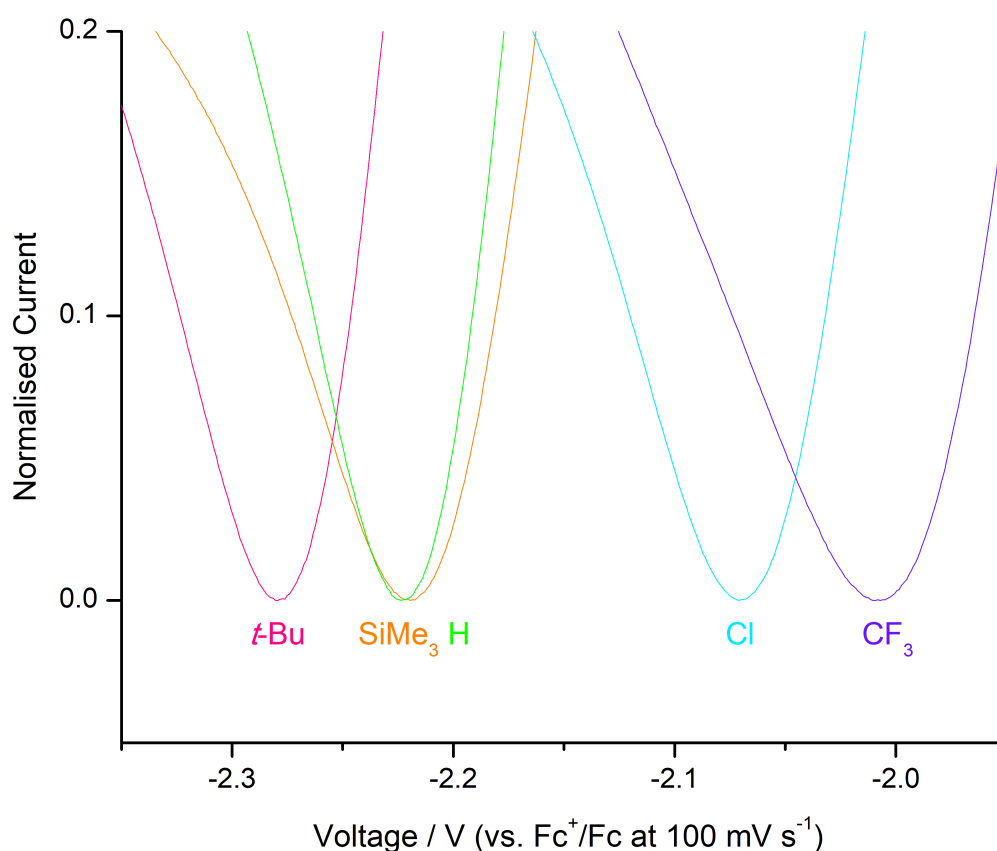


Fig. 5.15 Superimposed reduction signals of the *m*-terphenyl iron complexes (R-Ar)₂Fe, **5.1** – **5.5**, showing the shift of cathodic reduction potential, E_{p,c}.

This peak shift is likely due to the decreased electron density at the metal centre associated with electron-withdrawing groups; such an effect destabilises the Fe(II) species and makes gaining an electron to Fe(I) more favourable, shifting the reduction potential to lower energies. Moreover, plotting a graph of the cathodic reduction potentials, $E_{p,c}$, against the Hammett constants for the *para*-groups, σ_{para} , reveals a linear correlation (**Fig. 5.16**).¹³⁹ This implies that *para*-substitution directly influences the electronic properties at the iron centre. Similar trends have also been reported for other functionalised iron systems,^{322–324} including substituted ferrocenes^{325–328} and substituted porphyrin complexes.^{329,330}

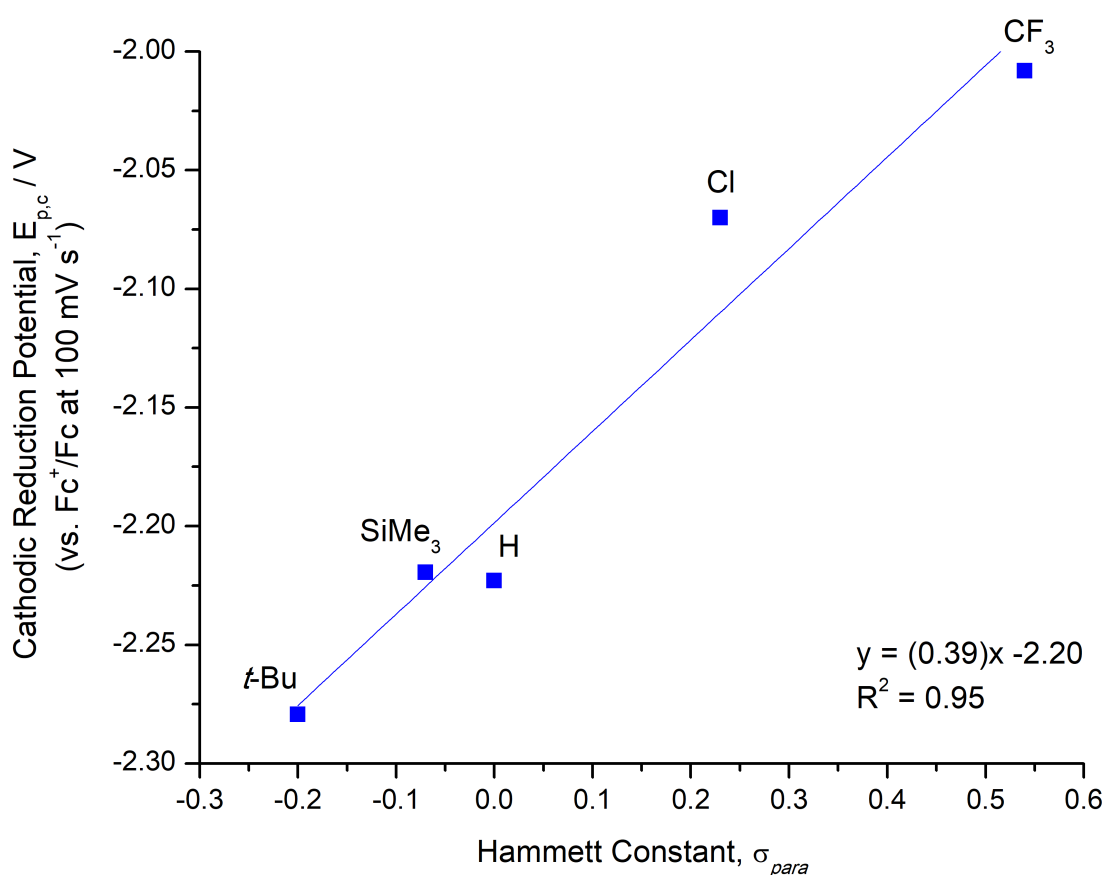


Fig. 5.16 Plot of the cathodic reduction potentials, $E_{p,c}$, for the *para*-substituted iron complexes (R-Ar)₂Fe, **5.1** – **5.5**, versus their literature Hammett constants, σ_{para} .¹³⁹

The cyclic voltammograms of complexes **5.1** – **5.5** also revealed the occurrence of oxidative processes between +0.50 and +1.25 V (vs. Fc^+/Fc at 100 mV s^{-1}) (**Fig. 5.17**), after which decomposition occurs due to a multi-electron oxidation. While two peaks are observed for **5.1** – **5.4**, the CF_3 analogue **5.5** only exhibits one oxidation signal; this could be related to the solvatochromic differences of **5.5** encountered by UV/Vis spectroscopy in THF solutions. In all cases, a return wave is not observed at scan rates of 100 mV s^{-1} , suggesting that the oxidised species decomposes before it can be re-reduced. Overall, no electronic trends are immediately apparent with respect to the *para*-substituents, although further CV experiments could be performed to study the spectroelectrochemical behaviour of these iron systems.

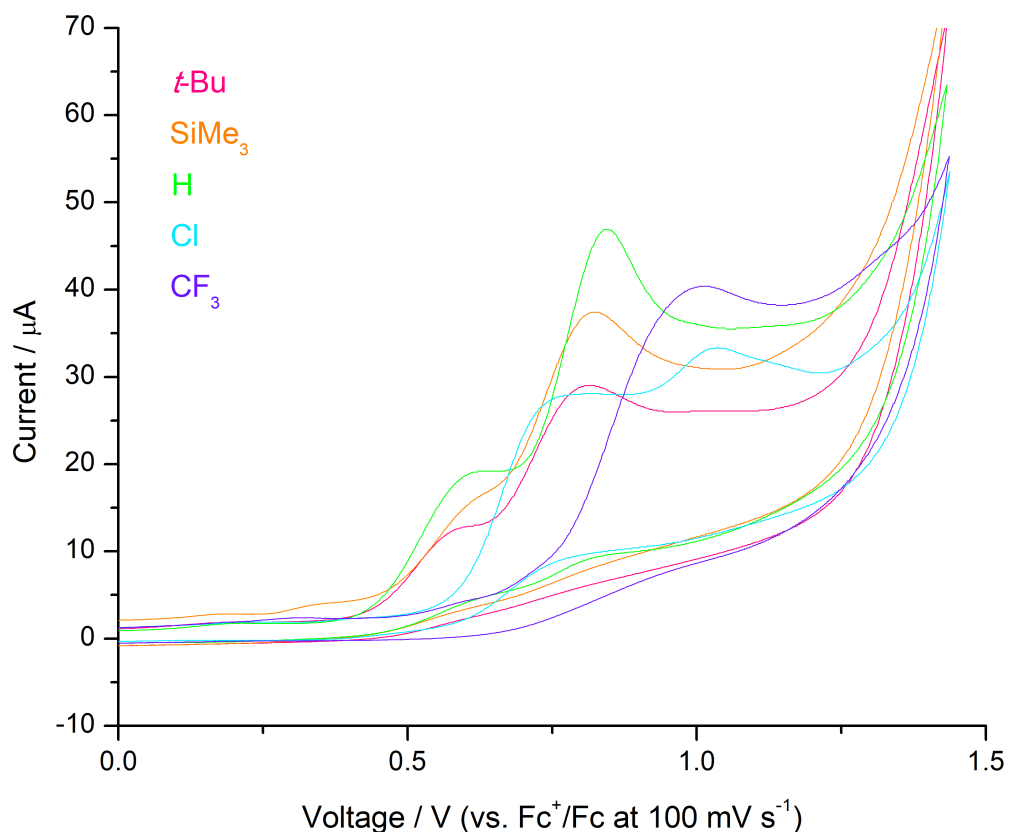


Fig. 5.17 Superimposed cyclic voltammograms of the *m*-terphenyl iron complexes, $(\text{R-Ar})_2\text{Fe}$, **5.1** – **5.5**, in THF containing $0.5 \text{ M } [\text{nBu}_4\text{N}][\text{BF}_4]$, demonstrating the occurrence of oxidation processes at anodic peak potentials.

5.2.1.8 Magnetic Analysis

The magnetic properties of the *para*-substituted *m*-terphenyl iron complexes **5.1** – **5.5** were investigated using a SQUID magnetometer by recording their direct current (dc) and alternating current (ac) magnetic susceptibility behaviour. The analysis of these measurements is still ongoing and requires further interpretation in conjunction with the collaborator. However, the preliminary results are presented below, and compared to those for **5.3** that were previously recorded within the Kays group.⁸¹

From the ac susceptibility studies, the relaxation time of the magnetisation, τ , was measured, then its temperature dependence, T , was determined. This data was used to construct an Arrhenius plot for each complex of $\ln(\tau)$ versus $1/T$ (**Fig. 5.18**), where the gradient of each line represents the effective spin-reversal barrier of that complex, U_{eff} , discussed in *Chapter 1.2.2*. Hence, the iron diaryls **5.1** – **5.5** were found to exhibit single-molecule magnet behaviour under an applied magnetic field, with U_{eff} barriers of 25.4, 20.5, 31.5, 21.2 and 35.3 K for the *t*-Bu, SiMe₃, H, Cl and CF₃ *para*-groups, respectively. While no discernible trends are immediately apparent with respect to the Hammett constants, σ_{para} , of the *para*-substituents, the CF₃ derivative, **5.1**, clearly presents the largest U_{eff} barrier of the series, although the reasons for this are unknown at the present moment. Furthermore, the U_{eff} barriers are considerably smaller than those reported for the amido *m*-terphenyl iron(II) complexes (2,6-Ar₂C₆H₃-{H}N)₂Fe of 156.8 K (Ar = Dipp) and 149.6 K (Ar = Tripp).¹³⁵ Further work will therefore be required to fully interpret the magnetic behaviour of systems **5.1** – **5.5** and a broader analysis of the full data set is intended. Despite this, a computational study will likely be necessary to rationalise the magnetic results.

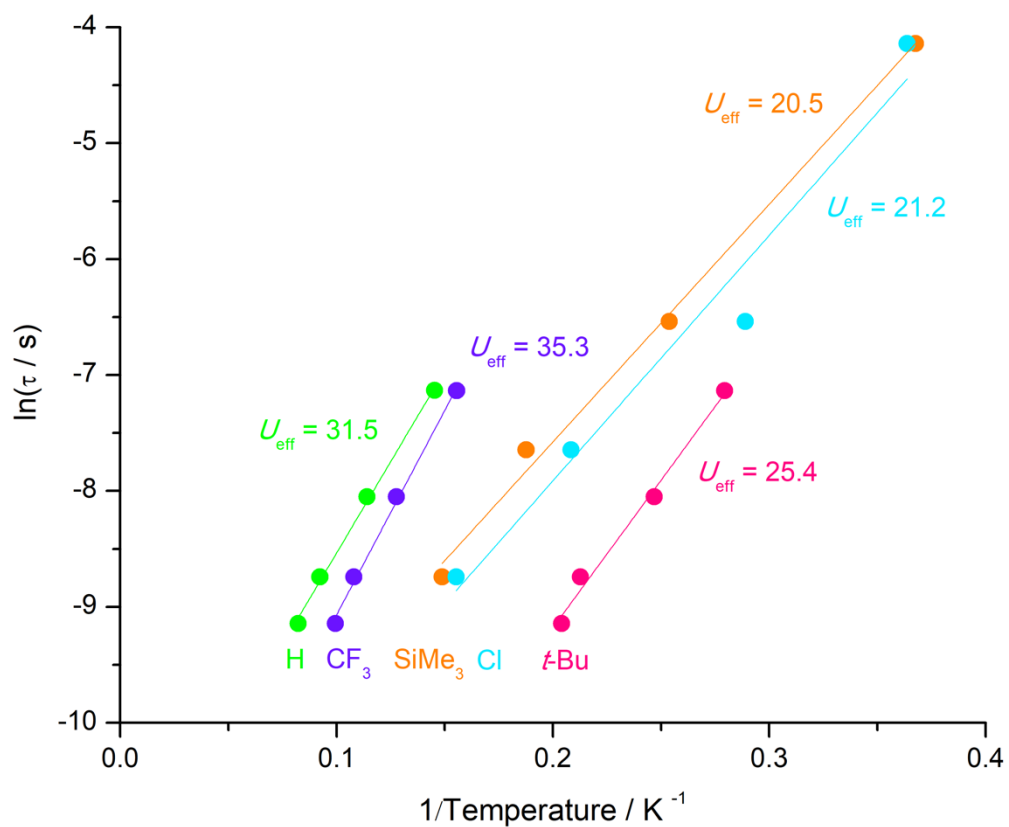


Fig. 5.18 Arrhenius plots showing the temperature dependence, T , of the relaxation times, τ , for the *para*-substituted iron complexes $(\text{R-Ar})_2\text{Fe}$, **5.1** – **5.5**, from which their spin-reversal barriers, U_{eff} , can be deduced.

5.3 Conclusions

A series of *para*-functionalised iron *m*-terphenyl complexes, **5.1**, **5.2**, **5.4** and **5.5**, have been reported. From a structural perspective, these complexes are similar, with a narrow range of C–M–C bond lengths and angles across the series, and the formation of Fe···H–C anagostic contacts between the metal centre and the flanking methyl groups. From an electronic viewpoint, the ¹H NMR spectra of **5.1** – **5.5** exhibit chemical shifts for the central ring hydrogens, H-3, and the flanking methyl groups, H-9, that shift linearly with the Hammett constant of their *para*-substituents. This was rationalised by a possible field generated by the paramagnetic iron centre that influences the chemical shifts of H-3 and H-9, where the field strength varies depending on the *para*-group. However, ¹H NMR spectroscopy only describes the ligand-based trends, rather than the electronic environment at the metal. Alternative analytical techniques were therefore attempted. While IR, UV/Vis and X-Ray photoelectron spectroscopies proved to be inadequate at probing the electronic structure at iron, cyclic voltammetry revealed an Fe(II) → Fe(I) reduction process at the metal centre. Here, a linear correlation is observed between the cathodic peak potentials, E_{p,c}, and the Hammett constants of the *para*-substituents, where electron-withdrawing groups result in peak shifts to lower potentials. This implies that *para*-substitution directly influences the electronic properties at the iron centre. Therefore, to investigate the effect of these electronic changes upon the magnetic properties of these iron diaryls, SQUID magnetometry measurements were undertaken. Although this work is currently ongoing, complexes **5.1** – **5.5** do exhibit single-molecule magnetism, where the magnetic properties and effective spin-reversal barrier, U_{eff}, vary depending on the *para*-substituent. However, further magnetic and computational analyses are required to conclude this topic.

5.4 Future Work

Following from the studies of the iron diaryls **5.1** – **5.5**, future work will involve the synthesis of an analogous series of *para*-substituted *m*-terphenyl cobalt complexes $(R-Ar)_2Co$ ($R = t-Bu, SiMe_3, H, Cl, CF_3$) that incorporate the ligands described in this research (**Fig. 5.19**). The structural and electronic properties of these cobalt systems can again be investigated by X-ray crystallography, NMR spectroscopy and cyclic voltammetry such that the effects of *para*-substitution can be determined. A comparison of the iron and cobalt complexes may then reveal which metal is more prone to the electronic effects of the *para*-groups. For example, if the cobalt diaryls also exhibit reduction potentials that, when plotted against their Hammett constants, σ_{para} , display a linear correlation, then the gradient of this plot can be compared with that reported for **5.1** – **5.5** in *Chapter 5.2.1.7*. Here, a steeper gradient may suggest that the metal centre is more susceptible to electronic change by the *para*-substituent. Furthermore, the magnetic properties of the cobalt diaryl series can be studied to compare their potential single-molecule magnet behaviour.

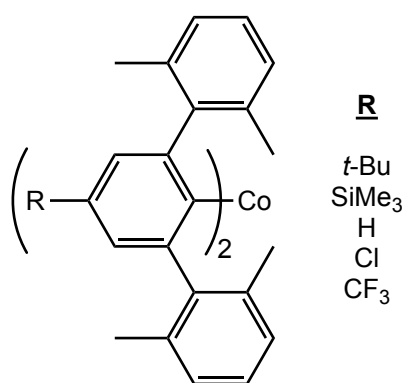
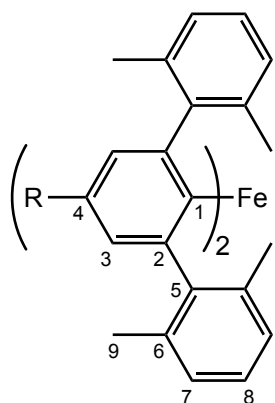


Fig. 5.19 Proposed series of *para*-substituted *m*-terphenyl cobalt complexes $(R-Ar)_2Co$ ($R = t-Bu, SiMe_3, H, Cl, CF_3$).

5.5 Experimental

5.5.1 Metal Complex Synthesis: Iron

5.5.1.1 (R-Ar)₂Fe (R = *t*-Bu, **5.1**; SiMe₃, **5.2**; H, **5.3**; Cl, **5.4**; CF₃, **5.5**)



A green mixture of [R-Ar-Li]₂ (1 eq.) (R = *t*-Bu, **3.9**: 500 mg, 0.72 mmol; R = SiMe₃, **3.10**: 500 mg, 0.69 mmol; R = H, **3.11**: 500 mg, 0.86 mmol; R = Cl, **3.12**: 500 mg, 0.77 mmol; R = CF₃, **3.13**: 400 mg, 0.56 mmol) and FeCl₂(THF)_{1.5} (1 eq.) in toluene (20 mL) and THF (2 mL) was stirred for 16 h at room temperature. After this time, the solvent was removed under vacuum to yield a yellow-green solid that was dried at 60 °C under vacuum for 4 h. The solid was then extracted into either hexane (2 x 15 mL) for **5.1**, **5.2** and **5.5**, or into toluene (2 x 15 mL) for **5.3** and **5.4**, to give a solution ranging in colour between yellow and dark green. Concentration of this solution under vacuum, followed by its storage at -30 °C, resulted in yellow-green crystals of **5.1** – **5.5** in isolated yields of 308 mg (58%), 303 mg (57%), 251 mg (47%), 229 mg (43%) and 154 mg (36%) respectively. Data for **5.1**: Elemental analysis: (Found: C, 84.5; H, 8.05. Calc. for C₅₂H₅₈Fe: C, 84.5; H, 7.9%); UV/Vis (toluene) λ_{max}/nm (ε/mol⁻¹ dm³ cm⁻¹): 363 (1606.8), 375 (1655.7), 392 (1142.8), 427sh (501.7); IR ν_{max}(benzene)/cm⁻¹ 2918(m), 2898(w), 2865(m), 2734(w), 1579(w), 1435(m), 1378(w), 1362(m), 1260(w), 1238(w), 1104(w), 1086(w); 882(w), 768(w), 577(w), 553(w); ¹H NMR δ_H (400 MHz; C₆D₆): 181.64 (4H, s, br, Δν_{1/2} = 933 Hz, 4 x H-3), 52.44 (18H, s, br, Δν_{1/2} = 99 Hz, 18 x H-11 {*t*-Bu}), -36.39 (24H, s, br, Δν_{1/2} = 1186 Hz, 24 x H-9), -55.02 (8H, s, br, Δν_{1/2} = 175 Hz, 8 x H-7), -59.47 (4H, s, br, Δν_{1/2} = 132 Hz, 4 x H-8); HRMS (ASAP), m/z: (Found: 739.3958. Calc. for C₅₂H₅₈FeH₁ [M+H]: 739.3967.) Data for **5.2**: UV/Vis (toluene) λ_{max}/nm (ε/mol⁻¹ dm³ cm⁻¹): 361sh (1490.0), 377 (1430.4), 394.69 (963.5),

427sh (563.2); IR $\nu_{\max}(\text{benzene})/\text{cm}^{-1}$ 2918(m), 2897(w), 2861(m), 2844(m), 2793(w), 2734(m), 2358(m), 2344(m), 1435(m), 1378(m), 1359(s), 1263(m), 1245(m), 1128(w), 1084(m), 878(m), 827(m), 807(s), 765(w), 578(w), 569(w), 552(w); ^1H NMR δ_{H} (400 MHz; C_6D_6): 181.24 (4H, s, br, $\Delta\nu_{1/2} = 1216$ Hz, 4 x H-3), 39.77 (18H, s, br, $\Delta\nu_{1/2} = 83$ Hz, 18 x H-10 {SiMe₃}), -35.75 (24H, s, br, $\Delta\nu_{1/2} = 1567$ Hz, 24 x H-9), -54.51 (8H, s, br, $\Delta\nu_{1/2} = 254$ Hz, 8 x H-7), -59.04 (4H, s, br, $\Delta\nu_{1/2} = 164$ Hz, 4 x H-8); HRMS (ASAP), m/z : (Found: 771.3505. Calc. for $\text{C}_{50}\text{H}_{58}\text{Si}_2\text{FeH}_1$ [M+H]: 771.3505.)

Data for **5.3**: UV/Vis (toluene) λ_{\max}/nm ($\epsilon/\text{mol}^{-1} \text{ dm}^3 \text{ cm}^{-1}$): 354sh (1370.4), 369 (1227.8), 384sh (805.0), 416 (506.0); IR $\nu_{\max}(\text{benzene})/\text{cm}^{-1}$ 2918(m), 2861(m), 2844(w), 2735(m), 1437(m), 1378(m), 1353(w), 1264(m), 1098(m), 804(s), 768(w), 551(w); ^1H NMR δ_{H} (400 MHz; C_6D_6): 178.94 (4H, s, br, $\Delta\nu_{1/2} = 923$ Hz, 4 x H-3), 32.55 (2H, s, br, $\Delta\nu_{1/2} = 265$ Hz, 2 x H-4), -35.28 (24H, s, br, $\Delta\nu_{1/2} = 1213$ Hz, 24 x H-9), -54.72 (8H, s, br, $\Delta\nu_{1/2} = 200$ Hz, 8 x H-7), -59.42 (4H, s, br, $\Delta\nu_{1/2} = 150$ Hz, 4 x H-8). Data for **5.4**: Elemental analysis: (Found: C, 75.8; H, 5.9. Calc. for $\text{C}_{44}\text{H}_{40}\text{Cl}_2\text{Fe}$: C, 76.0; H, 5.8%); UV/Vis (toluene) λ_{\max}/nm ($\epsilon/\text{mol}^{-1} \text{ dm}^3 \text{ cm}^{-1}$): 365 (1495.1), 377 (1545.2), 396 (1186.9); IR $\nu_{\max}(\text{benzene})/\text{cm}^{-1}$ 2919(m), 2898(w), 2860(m), 2846(m), 2736(m), 2357(w), 2345(w), 1735(w), 1555(s), 1435(s), 1377(m), 1289(s), 1107(m), 1084(m), 874(w), 820(s), 768(w), 580(w), 550(w); ^1H NMR δ_{H} (400 MHz; C_6D_6): 176.84 (4H, s, br, $\Delta\nu_{1/2} = 1317$ Hz, 4 x H-3), -34.17 (24H, s, br, $\Delta\nu_{1/2} = 1769$ Hz, 24 x H-9), -54.07 (8H, s, br, $\Delta\nu_{1/2} = 289$ Hz, 8 x H-7), -59.08 (4H, s, br, $\Delta\nu_{1/2} = 199$ Hz, 4 x H-8); HRMS (ASAP), m/z : (Found: 693.1979. Calc. for $\text{C}_{44}\text{H}_{40}\text{Cl}_2\text{FeH}_1$ [M+H]: 693.1981.)

Data for **5.5**: UV/Vis (toluene) λ_{\max}/nm ($\epsilon/\text{mol}^{-1} \text{ dm}^3 \text{ cm}^{-1}$): 369sh (827.1), 387 (645.4), 410sh (500.2); IR $\nu_{\max}(\text{benzene})/\text{cm}^{-1}$ 2919(w), 2897(w), 2866(w), 2845(w), 2736(w),

1431(w), 1378(w), 1343(s), 1263(m), 1241(w), 1121(m), 1104(w), 893(w); ^1H NMR δ_{H} (400 MHz; C_6D_6): 174.53 (4H, s, br, $\Delta\nu_{1/2} = 805$ Hz, 4 x H-3), -33.24 (24H, s, br, $\Delta\nu_{1/2} = 1008$ Hz, 24 x H-9), -53.22 (8H, s, br, $\Delta\nu_{1/2} = 204$ Hz, 8 x H-7), -58.35 (4H, s, br, $\Delta\nu_{1/2} = 151$ Hz, 4 x H-8); ^{19}F NMR δ_{F} (376 MHz; C_6D_6): -61.97 (s); HRMS (ASAP), m/z : (Found: 762.2377. Calc. for $\text{C}_{46}\text{H}_{40}\text{F}_6\text{Fe}$ [M]: 762.2385.)

Chapter VI

Small Molecule Reactivity

6.1 Introduction

The bonding and reactivity of small molecules towards low-coordinate metal complexes has remained a central theme in organometallic chemistry, providing insight into the fundamental interactions facilitated by coordinatively unsaturated metal centres. Such systems promote a wealth of chemical behaviour, including addition, elimination and insertion processes, which together afford applications of catalytic, industrial and biological importance.^{331–337} In the ongoing pursuit to develop potential candidates for small molecule activation, the *m*-terphenyl framework has received particular interest owing to the reactivity of its main-group^{130–132,338–363} and transition metal^{77,108,127,128,288,289,298,364–368} compounds. Examples include the hydrogenation of the digermine ArGeGeAr (Ar = 2,6-Dipp₂C₆H₃) to form a digermane ArH₂GeGeH₂Ar,³⁴⁴ and the cleavage of ammonia by (2,6-Dipp₂C₆H₃)₂M (M = Mn, Fe) to yield the amido complexes [(2,6-Dipp₂C₆H₃)M(μ-NH₂)(NH₃)_{*n*}]₂ (M = Mn {*n* = 1}, Fe {*n* = 0}).¹²⁷

Recent studies have explored the structural influences of *m*-terphenyl systems on small molecule reactivity, notably in mediating a pathway towards CO activation. A series of *m*-terphenyl cobalt complexes, for instance, has highlighted the significance of ligand bulk in determining the CO reaction product formed. Here, the half-sandwich species (Ar)Co(*η*⁶-C₇H₈) (Ar = 2,6-Tripp_{2-3,5-*i*}-Pr₂C₆H) reacts to give an acyl-carbonyl moiety [(Ar{O}C)Co(CO)],³⁶⁴ while the metal diaryls (2,6-Ar'₂C₆H₃)₂Co(OEt₂)_{*n*} (Ar' = Naph {*n* = 1}, Mes {*n* = 0}) yield the sterically-encumbered ketones shown in *Chapter 1.2.8 (Scheme 1.7)*.¹²⁸ Similarly, the iron analogues (2,6-Ar₂C₆H₃)₂Fe activate CO either via insertion to form an acyl-carbonyl complex (Ar = Dipp),¹⁰⁸ or via complete C≡O bond scission to afford an organic 1,3-squaraine (Ar = Mes, 2,6-Xyl), which again underlines the steric importance of the flanking aryl groups (**Fig. 6.1**).²⁹⁸

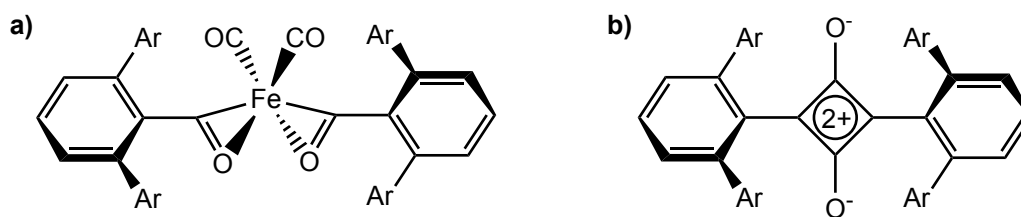


Fig. 6.1 Products from the reaction of $(2,6\text{-Ar}_2\text{C}_6\text{H}_3)_2\text{Fe}$ with CO to form either a) an acyl-carbonyl complex (Ar = Dipp), or b) a 1,3-squaraine (Ar = Mes, 2,6-Xyl).^{108,298}

In contrast, the electronic effects of *m*-terphenyl complexes upon their small molecule reactivity have yet to be investigated. Such an understanding is vital for elucidating key chemical information, including reaction pathways, kinetic rates and mechanisms, all of which are essential for optimising experimental conditions, product yields or catalytic activities.^{369–372} Moreover, by exploiting an infrared-active molecule, a handle could be provided through which the electronic structure at the metal centre can be probed via an analysis of the infrared stretching frequencies.^{373–375} This approach is particularly useful for iron complexes where ^{57}Fe NMR spectroscopy is not readily available. It is therefore of interest to develop a system to explore this concept further.

A series of *para*-substituted, two-coordinate, *m*-terphenyl iron complexes $(\text{R-Ar})_2\text{Fe}$ (Ar = 2,6-(2,6-Xyl) $_2\text{C}_6\text{H}_2$; R = *t*-Bu, SiMe₃, H, Cl, CF₃) have been shown to possess electronic structures that vary with the *para*-group, R, see *Chapter V*. However, an infrared-active species that coordinates to the iron centre in these systems without further reaction is yet to be established; CO is not ideal due to its multiple insertion products and eventual degradation of the metal complex.²⁹⁸ New candidates must thus be screened using the unsubstituted parent diaryl, $(\text{H-Ar})_2\text{Fe}$, to explore the underlying chemistry behind their reactivities, and to enable the measurement of their electronic properties by infrared spectroscopy. Once optimised, this approach can be extended to probe the electronic structures of the full *para*-substituted series $(\text{R-Ar})_2\text{Fe}$.

Herein, the small molecule reactivity of the unsubstituted *m*-terphenyl iron complex $(\text{Ar})_2\text{Fe}$ ($\text{Ar} = 2,6\text{-}(2,6\text{-Xyl})_2\text{C}_6\text{H}_3$) towards functionalised isocyanides ($\text{R}'\text{-NC}$) ($\text{R}' = t\text{-Bu}$, 2-Naph, 4-F-C₆H₄) is reported, resulting in the formation of several coordination-insertion products. Monitoring the early phases of the reactions is provided by NMR and IR spectroscopic studies in order to optimise the conditions, including the solvent system and reagent stoichiometry, while structural characterisation of the reaction products is performed by X-ray crystallographic analysis. The general structure of the unsubstituted metal diaryl complexes used within this work is presented below (**Fig. 6.2**).

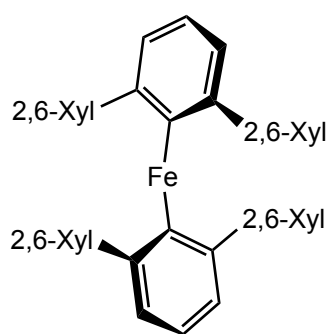


Fig. 6.2 Structure of the *m*-terphenyl iron complex trialled for small molecule reactivity with functionalised isocyanides.

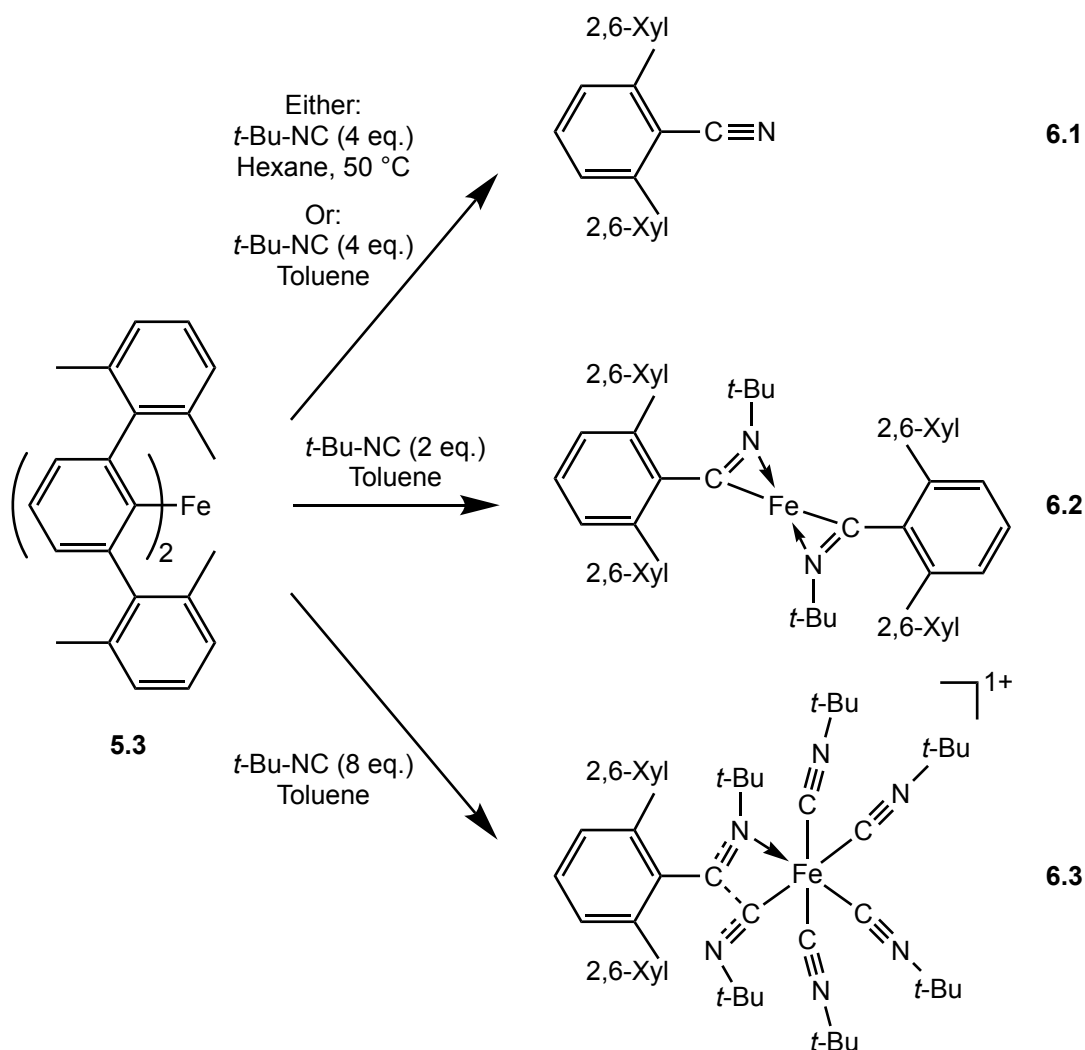
6.2 Discussion

6.2.1 Reactivity: Isocyanides ($R'-NC$)

6.2.1.1 Synthesis

The small molecule reactivity of the unsubstituted *m*-terphenyl iron complex (Ar)₂Fe ($Ar = 2,6-(2,6-Xyl)_2C_6H_3$), **5.3**, was investigated towards a number of functionalised isocyanides ($R'-NC$) ($R' = t\text{-Bu}, 2\text{-Naph}, 4\text{-F-C}_6\text{H}_4$). Preliminary NMR studies in *d*-benzene indicated that reactions had occurred in all cases. This was evidenced by an initial colour change of solution from yellow to dark red, as well as the disappearance of starting material peaks in the ¹H NMR spectra with the emergence of new wide-scan signals, suggesting the formation of paramagnetic species. The experiments were thus repeated in an attempt to isolate crystalline products by trialling a range of conditions. Despite this, success was only met with the *t*-Bu isocyanide; the 2-Naph and 4-F-C₆H₄ derivatives yielded no characterisable products.

Reactions of **5.3** with the *t*-Bu isocyanide (*t*-Bu-NC) were attempted under varied conditions (**Scheme 6.1**). At first, a 1:4 ratio of **5.3** to *t*-Bu-NC was tested, using hexane as the solvent. However, solubility issues immediately became apparent and, therefore, the mixture was sonicated at 50 °C until a dark green solution was observed. Storage of this solution at -30 °C subsequently resulted in colourless needles that were identified crystallographically as an *m*-terphenyl nitrile, Ar-CN, **6.1**, in which the *t*-Bu group had been cleaved (**Scheme 6.1**). While the decomposition product **6.1** reveals that a reaction did occur, possibly via the insertion of *t*-Bu-NC into the Fe-*C*_{ipso} bond, it also suggests that the isocyanide was in excess, likely due to the insolubility of **5.3** in hexane. Hence, all future experiments were performed in toluene.



Scheme 6.1 Reactivity of the *m*-terphenyl iron complex, **5.3**, with the *t*-Bu isocyanide (*t*-Bu-NC) under varying reaction conditions to form products **6.1**, **6.2** and **6.3**.

To counter the poor solubility, the reaction was repeated in toluene, again using a 1:4 ratio of **5.3** to *t*-Bu-NC but without heating or sonication. Unlike the previous reaction in hexane, the now fully-dissolved solution exhibited an immediate colour change from yellow to dark red. However, extraction into hexane and recrystallisation at $-30\text{ }^{\circ}\text{C}$ yielded colourless needles of the same decomposition product, **6.1** (**Scheme 6.1**). From this, it was concluded that the four-fold excess of *t*-Bu-NC might be driving the reaction towards the decomposition material, **6.1**. Hence, further adjustment of the reagent stoichiometry was required.

Thus, the reaction involving a 1:2 ratio of **5.3** to *t*-Bu-NC in toluene was investigated. This led to the formation of a dark red solution that was extracted into hexane and recrystallised at $-30\text{ }^{\circ}\text{C}$ to form red needles. Analysis by X-ray crystallography confirmed the sample to be a *bis*-insertion product, $(\text{Ar}-\{t\text{-Bu-N}\}\text{C})_2\text{Fe}$, **6.2**, in which a single *t*-Bu-NC had inserted into each of the $\text{Fe}-\text{C}_{\text{ipso}}$ bonds (**Scheme 6.1**). Although this reaction could successfully be repeated to give crystalline solids with the same structure, scale-up attempts failed to yield a pure product that could be analysed by NMR spectroscopy. Moreover, mass spectrometry was unable to detect the expected ions of **6.2**. Therefore, further work is required to characterise the metal complex fully.

Reactions were also trialled using a larger excess of *t*-Bu-NC to study the stoichiometric effects. Accordingly, a 1:8 ratio of **5.3** to *t*-Bu-NC was reacted in toluene to give a red solution that, following extraction into hexane, was stored at $-30\text{ }^{\circ}\text{C}$ to yield colourless crystals of $[(t\text{-Bu-NC}^*-\text{C}\{\text{Ar}\}\text{N}^*\{t\text{-Bu}\})\text{Fe}(\text{CN-}t\text{-Bu})_4]^+$, **6.3**, where the asterisk denotes an atom bonded to the metal (**Scheme 6.1**). The crystallographic data for **6.3** is of low-resolution so, while the structure can be modelled, bond parameters cannot be reported with precision. Product **6.3** likely features a positive charge stabilised by a counter-anion such as CN^- , although this could not be located in the crystal structure. It consists of an iron centre coordinated to four terminal *t*-Bu-NC molecules, plus two interacting *t*-Bu-NC moieties inserted into the $\text{Fe}-\text{C}_{\text{ipso}}$ bond of the *m*-terphenyl ligand. The complex appears to resemble a double-insertion product. The other *m*-terphenyl unit has been lost completely; perhaps to yield the *m*-terphenyl nitrile, **6.1**. This suggests that the remaining $(\text{Ar}-\{t\text{-Bu-N}\}\text{C})$ ligand could similarly detach from the metal centre to produce $(t\text{-Bu-NC})_5\text{Fe}$. In summary, a variety of coordination and insertion processes are observed.

6.2.1.2 Crystallographic Analysis

The structures of products **6.1** – **6.3**, obtained from the reaction of $(\text{Ar})_2\text{Fe}$, **5.3**, with 4, 2 and 8 equivalents of *t*-Bu isocyanide (*t*-Bu-NC), respectively, were analysed by X-ray crystallography. The products were recrystallised from hexane at $-30\text{ }^\circ\text{C}$ as either colourless needles (**6.1**), red needles (**6.2**), or low-quality colourless crystals that appeared to degrade on handling (**6.3**), seemingly via a melting or dissolution process.

Single crystal X-ray data of the *m*-terphenyl nitrile product, Ar-CN, **6.1**, shows an *m*-terphenyl moiety bound via its *ipso*-carbon to a terminal cyano group (**Fig. 6.3**). The C–N bond length [C(13)–N(1) = 1.146(2) Å] is indicative of a triple bond and is comparable to that of benzonitrile [1.137(14) Å]³⁷⁶ and other reported aromatic nitriles [avg. 1.138 Å].³⁷⁷ Similarly, the C_{ipso} –CN bond length [C(1)–C(13) = 1.441(2) Å] agrees with the average literature value [avg. 1.443 Å],³⁷⁷ suggesting partial double bond character due to resonance effects with the CN unit and the aromatic framework. The linear C_{ipso} –C–N bond angle [C(1)–(C(13)–N(1) = 180.0(0)°] supports a formal triple bond for the C–N unit. Akin to the *m*-terphenyl iodides **3.2** – **3.8** in *Chapter 3.2.1.2*, the dihedral angles between the planes of the central ring and the *ortho*-2,6-Xyl flanking groups for **6.1** are near-orthogonal [87.95(3)°]. Overall, product **6.1** confirms that a reaction occurred with the isocyanide, likely via its insertion into the Fe– C_{ipso} bond, and reveals that the *t*-Bu group is cleaved in the process. The loss of this *t*-Bu group has previously been ascribed to C–H bond activation in an *m*-terphenyl germanium isocyanide complex $(2,6\text{-Mes}_2\text{C}_6\text{H}_3)_2\text{Ge}(\text{CN-}t\text{-Bu})$ to form a metal hydride and isobutylene gas.^{130,132}

Crystallographic analysis of the *bis*-insertion product, $(\text{Ar}-\{t\text{-Bu-N}\}\text{C})_2\text{Fe}$, **6.2**, reveals a monomeric complex comprised of two *m*-terphenyl ligands each bridged via a single *t*-Bu-NC to an iron(II) centre (**Fig. 6.3**), see **Table 6.1**. The nearest $\text{Fe}\cdots\text{Fe}$ separations are smaller than those in $(\text{Ar})_2\text{Fe}$ [$d(\text{Fe}\cdots\text{Fe}) = 9.1$ vs 10.4 Å for **6.2** and **5.3**, respectively] but suggest that adjacent metal centres do not interact.⁸¹ Weak $\text{Fe}\cdots\text{H}-\text{C}$ anagostic interactions are formed to the hydrogens of the flanking methyl groups on the *m*-terphenyl ligand [$2.9817(4)$ – $3.0529(4)$ Å], see **Table 6.1**. The insertion of *t*-Bu-NC into the $\text{Fe}-\text{C}_{\text{ipso}}$ bonds yields a planar $(\text{C}_{\text{ipso}}\text{CN})_2\text{Fe}$ core, within which new $\text{C}_{\text{ipso}}-\text{CN}$ single bonds [$\text{C}(1)-\text{C}(23) = 1.519(9)$ Å] are formed, along with conversion of the C–N triple bonds to longer C–N double bonds [$\text{C}(23)-\text{N}(1) = 1.279(10)$ Å] that are similar to other double-bonded isocyanide iron complexes in the literature, whose C–N bond lengths range between 1.26 – 1.30 Å.^{278,378–382} In comparison, the $\text{N}-\text{CMe}_3$ group is only single-bonded [$\text{C}(24)-\text{N}(1) = 1.491(11)$ Å]. Coordination of the isocyanide ligands to the iron centre in **6.2** occurs via an η^2 -bonding mode, involving an $\text{Fe}-\text{C}$ [$\text{Fe}(1)-\text{C}(23) = 1.917(7)$ Å] and an $\text{Fe}-\text{N}$ bond [$\text{Fe}(1)-\text{N}(1) = 1.887(7)$ Å]. The $\text{Fe}-\text{C}$ bonds are shorter than those in **5.3**, [$\text{Fe}-\text{C}_{\text{ipso}} = 2.028(2)$ and $2.029(2)$ Å],⁸¹ most likely due to steric effects and the carbenoid character of the coordinated carbon.³⁸³ Moreover, the $\text{Fe}-\text{C}$ bond lengths are similar to those found in the η^2 -bonded isocyanide iron complex $(\text{Mes}-\{t\text{-Bu-N}^*\}\text{C}^*)_2\text{Fe}_2(\mu\text{-C}(\text{N}-t\text{-Bu})\text{-Mes})_2$ [$\text{Fe}-\text{C}^* = 1.921(3)$ Å and $\text{Fe}-\text{N}^* = 2.007(4)$ Å].²⁷⁸ However, for **6.2**, the $\text{Fe}-\text{C}$ and $\text{Fe}-\text{N}$ bond lengths are essentially identical to one another (within error). This suggests that the C–N units bind to the metal in a side-on, π -bonded mode.³⁸⁴ Hence, **6.2** can be denoted as an η^2 -iminoacyl or η^2 -imidoyl system.³⁸⁵ Moreover, although formally four-coordinate, **6.2** may be described as a pseudo two-coordinate species.

Table 6.1 Relevant bond lengths (Å) and angles (°) for the planar ($C_{ipso}CN$)₂Fe core within the *bis*-insertion product, (Ar-*t*-Bu-N)C₂Fe, **6.2**.

Bond Lengths (Å)		Bond Angles (°)	
Fe(1)–C(23)	1.917(7)	C(23)–Fe(1)–C(23) ^a	180.00(8)
Fe(1)–N(1)	1.887(7)	N(1)–Fe(1)–N(1) ^a	180.00(1)
C(1)–C(23)	1.519(9)	C(23)–Fe(1)–N(1) ^a	39.3(3)
C(23)–N(1)	1.279(10)	Fe(1)–C(23)–N(1) ^a	69.1(4)
N(1)–C(24)	1.491(11)	Fe(1)–N(1)–C(23)	71.6(5)
Fe(1)···H(14C)	3.0529(4)	C(1)–C(23)–Fe(1)	158.9(7)
Fe(1)···H(21A)	2.9817(4)	C(1)–C(23)–N(1)	132.0(8)
		C(24)–N(1)–Fe(1)	151.3(4)
		C(24)–N(1)–C(23)	137.1(6)

^a For **6.2**, there is only half a molecule in the asymmetric unit.

The ($C_{ipso}CN$)₂Fe core is comprised of two triangular (CN)Fe planes that lie on opposite sides of the iron centre. These are separated by linear C–Fe–C and N–Fe–N bond angles of exactly 180°, resulting in a planar (CN)Fe(CN) moiety with a distorted square planar geometry. This arrangement could suggest possible electron delocalisation across the central system via conjugation of the out-of-plane C–N π -orbitals on the π -bound isocyanide ligands, into an out-of-plane orbital on the metal. The angles within these (CN)Fe triangles sum to 180° [C(23)–Fe(1)–N(1) = 39.3(3)°, Fe(1)–C(23)–N(1) = 69.1(4)° and Fe(1)–N(1)–C(23) = 71.6(5)°], where the Fe–C–N and Fe–N–C angles are very similar to one another, further supporting a model for side-on isocyanide binding. The angles measured from the C–N bonds to the adjacent *m*-terphenyl *ipso*-carbons [C(1)–C(23)–N(1) = 132.0(8)°] or to the *t*-Bu groups [C(24)–N(1)–C(23) = 137.1(6)°] are similar to those found in the complex (Mes-*t*-Bu-N*)C*₂Fe₂(μ -C(N-*t*-Bu)-Mes)₂ [C_{ipso} -C*–N* = 132.2(3)° and *t*-Bu–N*–C* = 131.9(3)°].²⁷⁸ Here, **6.2** exhibits a more obtuse *t*-Bu–N– C_{ipso} angle [137.1(6)°], perhaps due to the greater steric bulk of the *m*-terphenyl ligand, or a shorter Fe–N bond versus the literature complex.²⁷⁸ Nonetheless, these angles provide extra evidence for a double-bonded C–N group.

The dihedral angle between the triangular (CN)Fe plane and the C(1)-aryl plane of the central ring of the *m*-terphenyl ligand [85.2(4)°] is near-orthogonal and likely minimises the steric strain between the flanking 2,6-Xyl groups and the *t*-Bu moieties. As a consequence, the C(1)-aryl planes of the two *m*-terphenyl units become parallel to one another [0.0(9)°], unlike in the parent complex (Ar)₂Fe, **5.3**, where these planes are almost perpendicular [86.36(8)°].⁸¹ Thus, the insertion of *t*-Bu-NC in **6.2** causes the *m*-terphenyl frameworks to twist, relative to one another, in order to accommodate the changing steric demands; this can be attributed to the increased inter-ligand distance in **6.2** [*C*_{ipso}⋯*C*_{ipso} = 6.758(13) vs. 4.033(3) Å for **6.2** and **5.3**, respectively] that reduces the steric interactions between two *m*-terphenyl groups.⁸¹ Furthermore, the torsion angles between the C(1)-aryl plane of the central ring of each *m*-terphenyl ligand in **6.2** and the planes of the flanking 2,6-Xyl groups [73.4(3)° and 71.5(3)° for **6.2**] are less orthogonal than those in the parent complex **5.3** [82.76(9)–89.47(8)°].⁸¹ Thus, it appears that the 2,6-Xyl groups twist away from the nearby *t*-Bu units to minimise steric interactions in **6.2**.

Overall, the structure of **6.2** confirms that *t*-Bu-NC reacts with (Ar)₂Fe, **5.3**, to form a *bis*-insertion product. This likely proceeds via the initial coordination of a *t*-Bu-NC molecule, followed by its migratory insertion into the Fe–*C*_{ipso} bond, in a similar manner to that described for (2,6-Mes₂C₆H₃-{MeN}C)Ge(2,6-Mes₂C₆H₃).^{131,132} However, future experimental work and calculations would be required to provide a full mechanistic explanation. Moreover, the effects of sequential isocyanide insertions are of further interest, as shown by the addition of excess *t*-Bu isocyanide to yield **6.3**.

The pseudo double-insertion product **6.3** [(*t*-Bu-NC*–C{Ar}N*{*t*-Bu})Fe(CN-*t*-Bu)₄]⁺ adopts a monomeric structure comprised of an *m*-terphenyl ligand bridged via two interacting *t*-Bu-NC units to an iron(II) centre, whose coordination sphere is completed by four terminal *t*-Bu-NC ligands (**Fig. 6.3**), see **Table 6.2**. The complex possibly features a positive charge, stabilised by a counter-anion such as CN[−], similar to the iron system reported by Riera *et al.* [(PhN*=C{Me}₃–C*=NPh)Fe(CNPh)₂(dppe)]⁺(ClO₄)[−] (dppe = Ph₂P–C₂H₄–PPh₂; where the asterisk denotes an atom bonded to the metal).³⁸⁶ Due to the low-quality crystallographic data for **6.3**, the bond lengths and angles for this complex cannot be reported with precision. Nevertheless, bond orders for the C–N bonds can be approximated using the bond parameters in **Table 6.2**. Thus, on binding to the iron centre, the four terminal *t*-Bu-NC ligands appear to maintain their C–N triple bonds [1.13(4)–1.17(3) Å] and N–CMe₃ single bonds [1.48(4)–1.50(3) Å], as found for (*t*-Bu-NC)₅Fe [C–N = 1.16(1)–1.22(1) Å and N–CMe₃ = 1.39(1)–1.48(1) Å].³⁸⁷ In **6.3**, the terminal isocyanide C–N–CMe₃ bond angles remain near-linear [159(2)–177(3)°], except for C(33)–N(3)–C(34) [162(2)°] and C(48)–N(6)–C(49) [159(2)°] that bend away from the *m*-terphenyl ligand, presumably to minimise steric clash. However, more substantial bending was found in (*t*-Bu-NC)₅Fe [C–N–CMe₃ = 133.1(8)–177.1(8)°], although this was attributed to π-backbonding effects.³⁸⁷ For the bridging isocyanides, C–N triple bonds [C(23)–N(1) = 1.13(5) Å, C(28)–N(2) = 1.10(5) Å] and N–CMe₃ single bonds [C(24)–N(1) = 1.56(5) Å, C(29)–N(2) = 1.54(5) Å] are observed. Such bond orders usually indicate that the inserted isocyanides are discrete, individual species detached from one another. Conversely, the bent C–N–CMe₃ bond angles [C(23)–N(1)–C(24) = 129(3)°, C(28)–N(2)–C(29) = 110(3)] suggest otherwise; that the C–N groups are double-bonded and that the N atoms are formally sp²-hybridised. However, this would result in unstable trivalent carbon atoms [C(23) and C(28)].

Table 6.2 Relevant bond lengths (Å) and angles (°) for the pseudo double-insertion product, $[(t\text{-Bu-NC}^*\text{-C}\{\text{Ar}\}\text{N}^*\{t\text{-Bu}\})\text{Fe}(\text{CN-}t\text{-Bu})_4]^+$, **6.3**.

Bond Lengths (Å) and Angles (°)				
Iron Coordination Sphere	Fe(1)–N(1)	2.11(3)	Fe(1)–C(38)	1.88(3)
	Fe(1)–C(28)	1.88(4)	Fe(1)–C(43)	1.84(3)
	Fe(1)–C(33)	1.858(18)	Fe(1)–C(48)	1.85(2)
	N(1)–Fe(1)–C(28)	70.0(16)	C(28)–Fe(1)–C(48)	95.1(17)
	N(1)–Fe(1)–C(33)	91.2(13)	C(33)–Fe(1)–C(38)	89.3(18)
	N(1)–Fe(1)–C(38)	169.9(13)	C(33)–Fe(1)–C(43)	89.8(14)
	N(1)–Fe(1)–C(43)	103.3(13)	C(33)–Fe(1)–C(48)	171.8(15)
	N(1)–Fe(1)–C(48)	91.9(13)	C(38)–Fe(1)–C(43)	86.9(13)
	C(28)–Fe(1)–C(33)	93.1(17)	C(38)–Fe(1)–C(48)	89.0(18)
	C(28)–Fe(1)–C(38)	99.9(17)	C(43)–Fe(1)–C(48)	82.0(14)
	C(28)–Fe(1)–C(43)	172.7(17)		
Bridging Isocyanides	N(1)–C(23)	1.13(5)	N(2)⋯H(13A)	2.19(3)
	N(1)–C(24)	1.56(5)	N(2)⋯H(22C)	1.82(3)
	N(2)–C(28)	1.10(5)	C(23)–C(1)	1.57(4)
	N(2)–C(29)	1.54(5)	C(23)⋯C(28)	1.84(6)
	Fe(1)–N(1)–C(23)	103(3)	N(1)–C(23)–C(28)	99(3)
	Fe(1)–N(1)–C(24)	128.4(19)	C(23)–N(1)–C(24)	129(3)
	Fe(1)–C(28)–N(2)	171(4)	C(23)–C(28)–N(2)	99(3)
	Fe(1)–C(28)–C(23)	89(2)	C(28)–N(2)–C(29)	110(3)
	N(1)–C(23)–C(1)	145(3)	C(28)–C(23)–C(1)	116(2)
Terminal Isocyanides	N(3)–C(33)	1.15(3)	N(5)–C(43)	1.15(4)
	N(3)–C(34)	1.49(3)	N(5)–C(44)	1.49(3)
	N(4)–C(38)	1.13(4)	N(6)–C(48)	1.17(3)
	N(4)–C(39)	1.48(4)	N(6)–C(49)	1.50(3)
	Fe(1)–C(33)–N(3)	164(2)	C(33)–N(3)–C(34)	162(2)
	Fe(1)–C(38)–N(4)	172(3)	C(38)–N(4)–C(39)	176(3)
	Fe(1)–C(43)–N(5)	172(3)	C(43)–N(5)–C(44)	177(3)
	Fe(1)–C(48)–N(6)	167(3)	C(48)–N(6)–C(49)	159(2)

Therefore, it is proposed that the C–N groups have partial triple bond character, stabilised by the interaction of the two isocyanide units via the formation of an intramolecular N–C \cdots C–N bond [C(23) \cdots C(28) = 1.84(6) Å], plus short N \cdots H–C contacts between one of the N atoms and the H atoms of the flanking methyl groups [N(2) \cdots H(13A) = 2.19(3) Å and N(2) \cdots H(22C) = 1.82(3) Å]. These distances fall within the sum of the Van der Waals radii for the relevant atoms (2.75 Å).^{184,185} The ligand in **6.3** thus appears to feature a delocalised N \equiv C \cdots C \equiv N unit that is conjugated through its out-of-plane p-orbitals on the sp²-hybridised atoms, as shown earlier (**Scheme 6.1**). This differs from the aforementioned complex by Riera *et al.* [(PhN^{*}=C{Me}–C^{*}=NPh)Fe(CNPh)₂(dppe)]⁺(ClO₄)⁻, in which the N=C–C=N moiety features longer, double-bonded N–C groups [C–N = 1.27(1) and 1.30(1) Å] and a shorter C–C single bond [C–C = 1.46(2) Å].³⁸⁶ In spite of this, the author still suggests a degree of electron delocalisation along the N=C–C=N chain.

Complex **6.3** can be described as a pseudo double-insertion product, resulting from the successive insertion of two isocyanides into one of the Fe–C_{ipso} bonds of the parent complex **5.3**. Similarly to **6.2**, a new C_{ipso}–CN single bond [C(1)–C(23) = 1.57(4) Å] is formed from the insertion of *t*-Bu–NC into the *m*-terphenyl framework. Hence, the overall ligand can be described as an *m*-terphenyl diiminoacyl system. This ligand chelates to iron in a bidentate fashion, via a κ^2 -bonding mode, to form a planar four-membered ring denoted by (C^{*} \cdots C \equiv N^{*})Fe, where the asterisks indicate an atom bound to the metal; specifically, a carbon on one isocyanide and a nitrogen on the other. The angles in this ring sum to 360° [C(28)–Fe(1)–N(1) = 70(2)°, Fe(1)–C(28)–C(23) = 89(2)°, C(28)–C(23)–N(1) = 99(3)° and C(23)–N(1)–Fe(1) = 103(3)°].

Coordination of the six isocyanide units to the iron centre results in an overall six-coordinate complex with a distorted octahedral geometry. All Fe–C bonds lengths in **6.3** [1.84(3)–1.88(4) Å] are approximately the same as those in **6.2** [1.917(7) Å] (within error). However, the Fe–N bond in **6.3** [Fe(1)–N(1) = 2.11(3) Å] is significantly longer than that in **6.2** [1.887(7) Å]. This could possibly be due to the increased triple bond character of the coordinated C–N group in **6.3** that decreases the availability of the nitrogen lone pair for bonding, or because the isocyanide unit is no longer side-on, π -bonded to the iron centre. Nonetheless, the longer bond in **6.3** is comparable to that in the complex by Riera *et al.* [(PhN^{*}=C{Me}₃–C^{*}=NPh)Fe(CNPh)₂(dppe)]⁺(ClO₄)⁻.³⁸⁶

The dihedral angle between the four-membered (C^{*}⋯C≡N^{*})Fe plane and the C(1)-aryl plane of the central ring of the *m*-terphenyl ligand [88.5(13)°] is near-orthogonal as found for **6.2**. This likely minimises the steric interaction between the flanking 2,6-Xyl groups and the *t*-Bu moieties. The torsion angles between the central C(1)-aryl plane and the planes of the flanking 2,6-Xyl groups of the *m*-terphenyl ligand [83.0(10)° and 85.2(10)°] are comparable to those in the parent complex **5.3** [82.76(9)–89.47(8)°].⁸¹

Overall, the crystal structure of **6.3** confirms that (Ar)₂Fe, **5.3**, reacts with an excess of *t*-Bu-NC to form a pseudo double-insertion product. This likely results from the successive coordination and migratory insertion of two isocyanide molecules into the Fe–C_{ipso} bond of the parent complex.^{131,132} However, owing to the poor quality of the crystallographic data collected for **6.3**, the experiment should ideally be repeated to obtain better crystals. This could be attempted in the presence of AgClO₄ to provide a counter-anion for preferential product formation.³⁸⁶

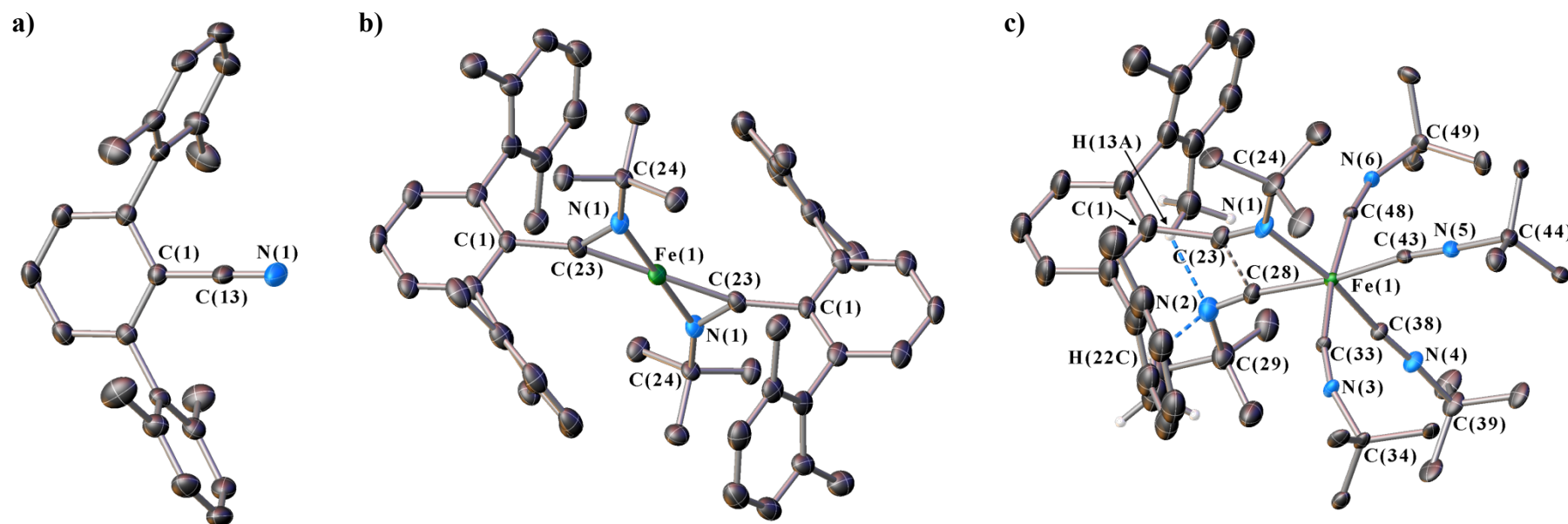


Fig. 6.3 Crystal structures showing the reactivity products of the *m*-terphenyl iron complex $(\text{Ar})_2\text{Fe}$ (**5.3**) with *t*-Bu isocyanide (*t*-Bu-NC) under varying reaction conditions to form either a) an organic *m*-terphenyl nitrile Ar-CN (**6.1**), b) a *bis*-insertion complex $(\text{Ar}-\{\textit{t}\text{-Bu-N}\}\text{C})_2\text{Fe}$ (**6.2**), or c) a pseudo double-insertion complex $[(\textit{t}\text{-Bu-NC}^*-\text{C}\{\text{Ar}\}\text{N}^*\{\textit{t}\text{-Bu}\})\text{Fe}(\text{CN-}\textit{t}\text{-Bu})_4]^+$ (**6.3**). Dashed lines indicate short-range contacts. Ellipsoids set at 45%, 35% and 10% probability for **6.1**, **6.2** and **6.3**. All irrelevant hydrogen atoms and residual solvent molecules are omitted for clarity.

6.2.1.3 IR Analysis

The reactions of $(Ar)_2Fe$, **5.3**, with *t*-Bu-NC, in 1:2 or 1:8 ratios, were monitored by IR spectroscopy using 6.4 mM solutions of **5.3** in toluene. Previous IR analysis of **5.3** in Chapter 5.2.1.4 showed no IR absorption between 2400–1600 cm^{-1} , while free *t*-Bu-NC exhibits a C–N stretch at 2133 cm^{-1} that agrees with previous reports.^{130,388,389} The reaction of **5.3** with two equivalents of *t*-Bu-NC causes, after 1.5 h, the disappearance of the free isocyanide peak (2133 cm^{-1}) and the emergence of two new bands at lower wavenumbers (2049 cm^{-1} and 2085 cm^{-1}), indicating that the compounds react rapidly (Fig. 6.4). After 26 h, little change is observed, except that the peak at 2085 cm^{-1} shifts to 2092 cm^{-1} and decreases in intensity. This could perhaps correspond to the initial coordination of a *t*-Bu-NC ligand, producing a similar peak to that in the terminally-bound isocyanide complex $(t\text{-Bu-NC})_5Fe$ (2110 cm^{-1}).³⁸⁷

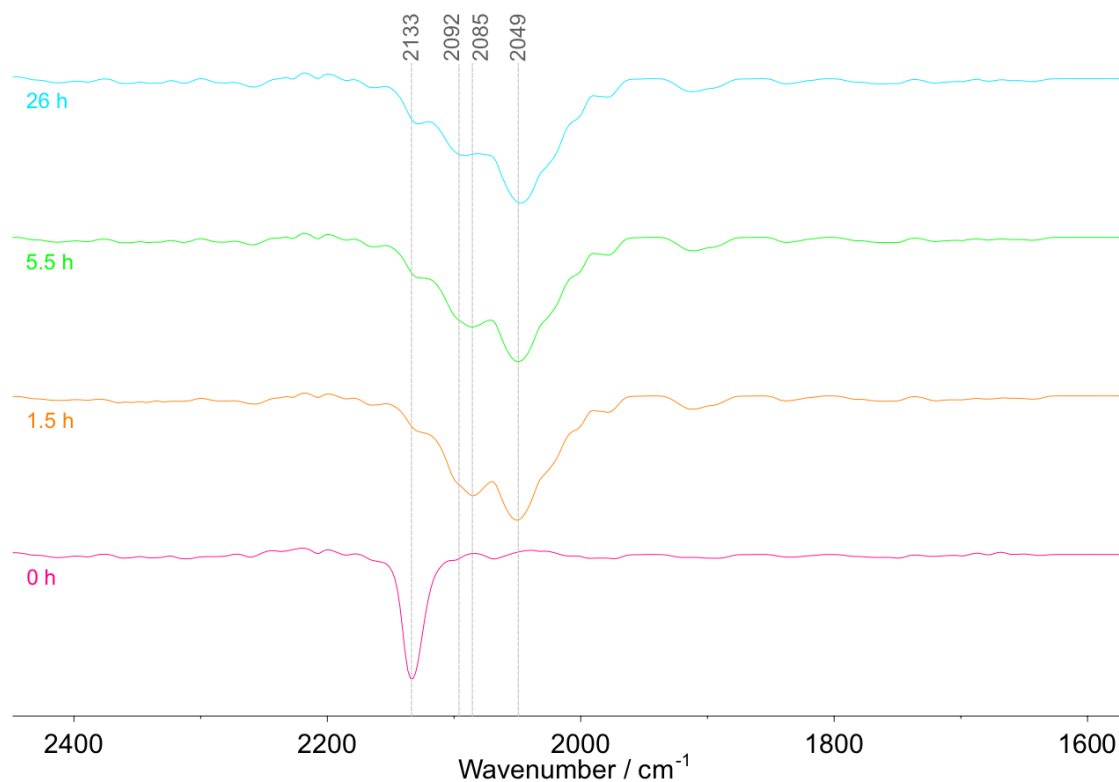


Fig. 6.4 Stacked IR spectra for the reaction of $(Ar)_2Fe$, **5.3**, with two equivalents of *t*-Bu isocyanide (*t*-Bu-NC) in toluene over 26 h.

Following the reaction of **5.3** with *t*-Bu-NC, the C–N stretch shifts to lower energy, corresponding to a weakening of the C–N bond on forming the *bis*-insertion product, (Ar-*t*-Bu-N}C)₂Fe, **6.2**. This corroborates the crystallographic results where the partial triple C–N bond of the free isocyanide [1.1674(14) Å]³⁹⁰ is lengthened towards that of a C–N double bond in **6.2** [1.279(10) Å]. However, the new C–N bands observed (2049–2092 cm⁻¹) occur at somewhat higher wavenumbers than other double-bonded isocyanide iron complexes, including [(Me-*t*-Bu-N}C)Fe(CO)₂(PMe₃)₂]⁺(BPh₄)⁻ (1753 cm⁻¹)^{391,392} and (Mes-*t*-Bu-N}C)₂Fe₂(μ-C(N-*t*-Bu)-Mes)₂ (1601 cm⁻¹).²⁷⁸ These differences could possibly be attributed to the stabilising effect of a delocalised, planar (CN)Fe(CN) core in **6.2**, as suggested in *Chapter 6.2.1.2*, or to the degree of bending of the C–N–CMe₃ angle in the isocyanide ligands.³⁸⁷ In any case, future computational calculations would be required for a more in-depth understanding of the IR results.

The reaction of **5.3** with eight equivalents of *t*-Bu-NC similarly causes rapid change of the free isocyanide peak (2133 cm⁻¹) with the immediate appearance of two new bands at lower wavenumber (2053 cm⁻¹ and 2099 cm⁻¹) within 0.5 h (**Fig. 6.5**). After 22 h, the peak at 2099 cm⁻¹ diminishes in intensity, while the band at 2053 cm⁻¹ grows more intense and shifts towards 2047 cm⁻¹. Overall, these findings are comparable to those in the above IR experiment; the reaction causes the C–N stretch to shift lower in energy due to a weakening of the C–N bond. Here, the band at 2099 cm⁻¹ could correspond to a terminally-coordinated isocyanide and the peak at 2047 cm⁻¹ could arise from isocyanide insertion. However, the reaction of **5.3** with eight equivalents of *t*-Bu-NC also results in the formation of two additional bands (2247 cm⁻¹ and 2269 cm⁻¹) that were not observed in the two-equivalent reaction. These peaks emerge after 3 h with a greater wavenumber than the free isocyanide (2133 cm⁻¹).

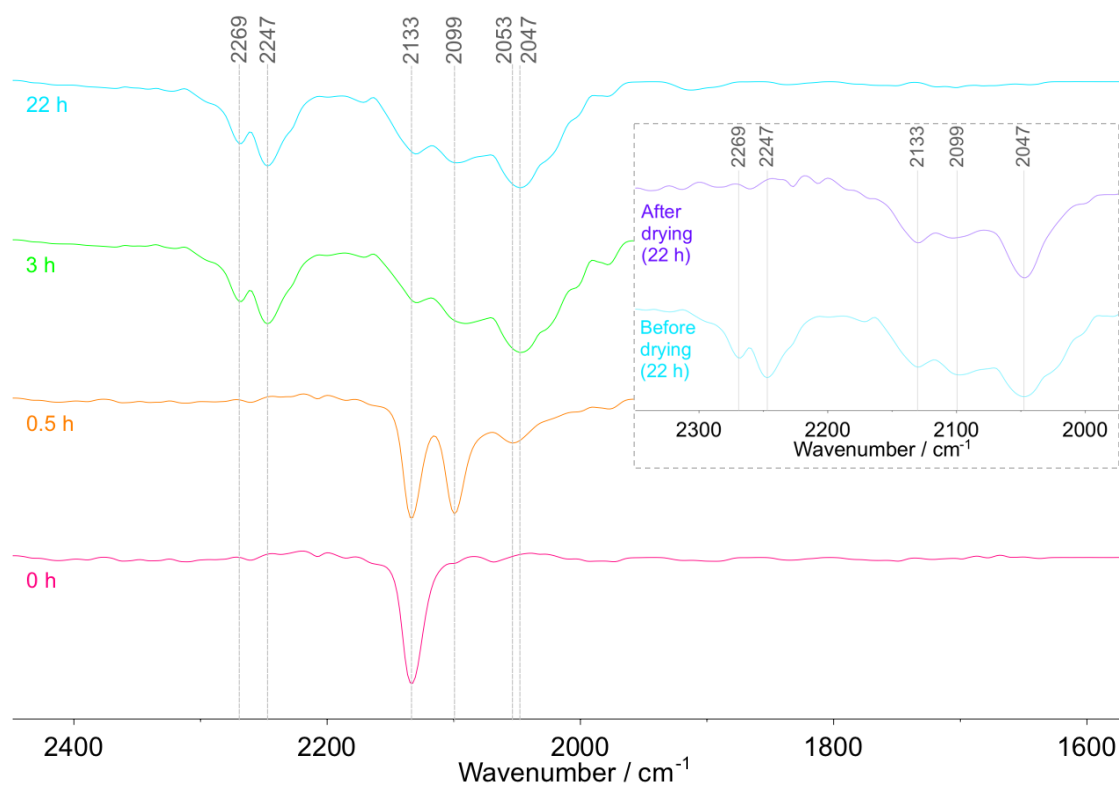


Fig. 6.5 Stacked IR spectra for the reaction of $(\text{Ar})_2\text{Fe}$, **5.3**, with eight equivalents of *t*-Bu isocyanide (*t*-Bu-NC) in toluene over 22 h, showing removal of the IR bands at 2247 cm^{-1} and 2269 cm^{-1} by drying the sample under vacuum for *ca.* 30 mins (inset).

Drying the sample (from the reaction with eight equivalents of *t*-Bu-NC) under vacuum for *ca.* 30 mins results in the loss of the two new IR bands (2247 cm^{-1} and 2269 cm^{-1}) (**Fig. 6.5**). This suggests that these bands originate from a volatile species that is independent of **6.3** and, hence, that a mixture of products is formed from the reaction. It is unlikely that the volatile species is an iron cyanide complex, whose C–N vibrations generally occur at lower wavenumbers, for example $[\text{Fe}(\text{CN})_6]\text{K}_3$ (2117 cm^{-1}) and $[\text{Fe}(\text{CN})_6]\text{K}_4$ ($2044\text{--}2050\text{ cm}^{-1}$).³⁹³ For similar reasons, a cyanide anion, CN^- , is improbable ($2054\text{--}2079\text{ cm}^{-1}$)^{394,395} and isobutylene shows no IR absorptions between $2700\text{--}1800\text{ cm}^{-1}$.³⁹⁶ However, nitrile compounds, that are often volatile, can produce an intense C–N stretching band in the $2270\text{--}2210\text{ cm}^{-1}$ region³⁹⁷ and could yield multiple peaks if weakly-coordinated to a metal centre.³⁹⁸ Even so, future computational work would be required to fully elucidate the IR data.

6.3 Conclusions

The small molecule reactivity of $(\text{Ar})_2\text{Fe}$, **5.3**, towards a number of functionalised isocyanides ($\text{R}'\text{-NC}$) ($\text{R}' = t\text{-Bu}$, 2-Naph, 4-F- C_6H_4) has been investigated. Preliminary NMR studies suggested that **5.3** reacted in all cases, however, the nature of the products was only elucidated for the reactions involving $t\text{-Bu}$ isocyanide ($t\text{-Bu-NC}$). Thus, the reaction conditions of **5.3** with $t\text{-Bu-NC}$ were optimised, trialling 1:4, 1:2 and 1:8 reagent ratios, to yield crystalline materials of an *m*-terphenyl nitrile, Ar-CN , **6.1**, a *bis*-insertion product $(\text{Ar}\{-t\text{-Bu-N}\}\text{C})_2\text{Fe}$, **6.2**, and a pseudo double-insertion product $[(t\text{-Bu-NC}^*\text{-C}\{\text{Ar}\}\text{N}^*\{t\text{-Bu}\})\text{Fe}(\text{CN-}t\text{-Bu})_4]^+$, **6.3**, respectively. IR reaction monitoring showed these reactions to occur rapidly, with the appearance of new IR bands at lower wavenumber that indicate a weakening of the isocyanide C–N bond.

The crystal structures of **6.1** – **6.3** revealed that both coordination and insertion processes occur, including *bis*- and double-insertion, through which mechanistic details can be postulated. It was suggested that the reactions proceed via the initial coordination of $t\text{-Bu}$ isocyanide, followed by migratory insertion into the $\text{Fe-C}_{\text{ipso}}$ bonds, to form **6.2** as the primary product. In the presence of excess isocyanide, it is possible that multiple insertions can occur until the *m*-terphenyl isocyanide moiety cleaves from the metal centre as the nitrile **6.1**, leaving an intermediate that is prone to further reaction to yield compounds such as **6.3**. As a consequence, a mixture of products may be generated during the reaction, which might explain why scale-up and characterisation proved unsuccessful. Future reactivity studies and computational work would therefore be required to elucidate the mechanisms involved in generating these complexes.

6.4 Future Work

Despite having covered the groundwork of isocyanide reactivity towards $(\text{Ar})_2\text{Fe}$, **5.3**, continued experimental and computational work is required to elucidate the underlying processes and reaction mechanisms occurring, where optimisation of the reaction conditions would be necessary to isolate pure samples for characterisation. Specifically, the reaction to form **6.3** could be repeated in the presence of a counter-anion like AgClO_4 to encourage preferential product formation.³⁸⁶

Once the reactivity of the unsubstituted system **5.3** has been optimised, the electronic effects of the functionalised diaryls $(\text{R-Ar})_2\text{Fe}$ ($\text{R} = t\text{-Bu, SiMe}_3, \text{H, Cl, CF}_3$), **5.1 – 5.5**, upon their isocyanide reactivity could be studied to provide insight into the reaction pathways, kinetic rates and mechanisms. It would be of particular interest to investigate how *m*-terphenyl *para*-substituents impact product formation to yield coordination or insertion species, together with their influence in controlling the strength of the isocyanide C–N bonding. Here, IR spectroscopy could be employed to probe the effects of *para*-substitution upon the C–N stretching frequencies to provide insight into the electronic structure at the metal centre.

6.5 Experimental

6.5.1 Reactivity: Isocyanides (*t*-Bu-NC)

6.5.1.1 *Ar*-CN (6.1)

A mixture of (Ar)₂Fe (**5.3**) (20 mg, 0.03 mmol) and *t*-butyl isocyanide (14.4 μL, 0.13 mmol) in hexane (20 mL) was sonicated at 50 °C for 30 mins to give a dark green solution. This solution was stirred for 16 h at room temperature to precipitate a green solid. The resultant mixture was filtered, and the filtrate was stored at –30 °C to yield colourless needles that were crystallographically characterised to be **6.1**.

Alternatively, (Ar)₂Fe (**5.3**) (20 mg, 0.03 mmol) and *t*-butyl isocyanide (14.4 μL, 0.13 mmol) in toluene (20 mL) was stirred for 16 h at room temperature as a dark red solution. The solvent was reduced under vacuum, and the resultant solid was extracted into hexane (2 x 10 mL) and stored at –30 °C to again yield colourless needles of **6.1**.

However, due to the impure nature of the bulk samples, attempts to fully characterise the compound were unsuccessful.

6.5.1.2 (*Ar*-*t*-Bu-NC)₂Fe (6.2)

A solution of (Ar)₂Fe (**5.3**) (20 mg, 0.03 mmol) and *t*-butyl isocyanide (7.95 μL, 0.07 mmol) in toluene (5 mL) was stirred for 16 h at room temperature to give a dark red colour. The solvent was reduced under vacuum, and the resultant dark red oily solid was extracted into hexane (2 x 5 mL) and stored at –30 °C to yield red needles of **6.2**.

Again, despite repeated attempts, full characterisation was prevented by bulk sample impurity, and mass spectrometry failed to detect the complex.

6.5.1.3 [(*t*-Bu-NC*–C{Ar}N*{*t*-Bu})Fe(CN-*t*-Bu)₄]⁺ (6.3)

A mixture of (Ar)₂Fe (**5.3**) (20 mg, 0.03 mmol) and *t*-butyl isocyanide (28.9 μL, 0.26 mmol) was dissolved in toluene (20 mL) to give a dark red solution that was stirred for 48 h at room temperature. After this time, the solution was dark green. The solvent was reduced under vacuum, then the solid was extracted into hexane (2 x 10 mL) and stored at –30 °C to precipitate an orange solid. The mixture was filtered, and the orange filtrate was stored at –30 °C to yield poor-quality colourless crystals of **6.3**. Again, full characterisation could not be achieved.

Chapter VII

Global Conclusions

7.1 Concluding Remarks

The purpose of this research sought to expand the library of low-coordinate *m*-terphenyl metal complexes suitable for electronic investigation, by overcoming the considerable synthetic challenges presented by these highly air- and moisture-sensitive systems. This was achieved through the design and synthesis of a new series of *para*-substituted *m*-terphenyl ligands featuring electron-donating and -withdrawing groups, whose electronic strengths can be quantified by literature Hammett constants, σ_{para} . Here, the same flanking aryl groups, 2,6-Xyl, were employed in all ligand frameworks to minimise structural variations due to steric effects. The influence of the ligand architecture was then studied with respect to the structural, electronic and magnetic properties of the resulting metal complexes. Furthermore, the groundwork has been established for understanding the reactivity of these low-coordinate systems towards small molecules.

Firstly, a series of *para*-functionalised *m*-terphenyl iodide ligand precursors, R-Ar-I, **3.2** – **3.8**, was synthesised via the modification of various literature procedures. From a crystallographic perspective, these compounds are structurally similar, with comparable C–I bond lengths and little change in the dihedral angles between their central C(1)-aryl ring and the 2,6-Xyl groups. However, ^1H and ^{13}C NMR spectroscopy revealed that, while *para*-substitution has negligible effect on the 2,6-Xyl flanking groups, it does cause significant electronic change in the central ring, notably at the *ipso*-carbon position. Overall, all iodides were synthesised on a large scale feasible for the future syntheses of metal complexes, except for the OMe compound, **3.7**, which was too low-yielding to be practically carried forwards within this research.

Lithiation of the iodide precursors yielded a series of *para*-substituted *m*-terphenyl lithium complexes, $[\text{R-Ar-Li}]_2$, **3.9** – **3.13**, except for that of iodide **3.8**, which failed to yield any substantial products. In the solid-state, these lithium systems are structurally similar, forming dimers with weak $\text{Li}\cdots\text{H-C}$ anagostic contacts between the lithium ions and the flanking methyl groups. In solution, the complexes retain their dimeric structures as evidenced by DOSY experiments and optimised ^{13}C NMR spectroscopy. Furthermore, ^1H , ^{13}C and ^7Li NMR spectroscopies revealed significant electronic differences both in the ligand framework and at the metal centre. In particular, a linear correlation was identified between the ^7Li NMR chemical shifts and the Hammett constants of the *para*-substituents. A similar correlation was found for the ^1H NMR chemical shifts of the flanking methyl protons, H-9, possibly due to the through-space $\text{Li}\cdots\text{H}$ interactions observed by ^7Li - ^1H HOESY experiments. In all cases, the NMR trends proceed in the opposite direction to that expected, where electron-withdrawing substituents cause an upfield peak shift.

The lithium precursors were then used to prepare four series of *para*-functionalised Group 12 *m*-terphenyl complexes, $(\text{R-Ar})_2\text{M}$ ($\text{M} = \text{Zn}, \text{Cd}, \text{Hg}$), **4.1** – **4.12**. X-ray crystallography showed these complexes to be structurally similar, since the C–M–C bond lengths and angles remain essentially invariant across the series. However, NMR spectroscopic studies revealed electronic differences within the ligand framework and at the metal centre, as emphasised by the linear correlation of the ^{113}Cd and ^{199}Hg NMR chemical shifts with the Hammett constants of the *para*-substituents. A similar trend was identified with the ^1H NMR chemical shifts of the flanking methyl protons, H-9, suggesting the occurrence of through-space $\text{M}\cdots\text{H-C}$ contacts. Akin to the lithium complexes, the NMR trends proceed in the opposite direction to that expected.

The lithium precursors were also used to synthesise a series of *para*-substituted iron *m*-terphenyl complexes (R-Ar)₂Fe, **5.1** – **5.5**. Structurally, these complexes show a narrow range of C–M–C bond lengths and angles, as well as Fe···H–C contacts between the metal and the flanking methyl groups. From an electronic viewpoint, the ¹H NMR spectra of **5.1** – **5.5** exhibit chemical shifts for the central ring hydrogens, H-3, and the flanking methyl groups, H-9, that shift linearly with the Hammett constant of their *para*-substituents. While IR, UV/Vis and X-Ray photoelectron spectroscopies proved inadequate at probing the electronic nature of the iron centre, cyclic voltammetry revealed an Fe(II) → Fe(I) reduction process, with a linear correlation between the cathodic peak potentials, E_{p,c}, and the Hammett constants of the *para*-substituents. Finally, SQUID magnetometry of **5.1** – **5.5** showed that the iron diaryls can exhibit single-molecule magnet behaviour, where the effective spin-reversal barrier, U_{eff}, varies with the *para*-substituent although with no discernible trend.

Finally, the small molecule reactivity of the unsubstituted iron diaryl, (Ar)₂Fe, **5.3**, was investigated towards a number of isocyanides (R'-NC) (R' = *t*-Bu, 2-Naph, 4-F-C₆H₄). Preliminary NMR studies suggested that **5.3** reacted in all cases, however, crystals were only isolated for the reactions with *t*-Bu-NC. Thus, the reaction conditions of **5.3** with *t*-Bu-NC were optimised using 1:4, 1:2 and 1:8 reagent ratios, to give an *m*-terphenyl nitrile, Ar-CN, **6.1**, a *bis*-insertion species (Ar-{*t*-Bu-N}C)₂Fe, **6.2**, and a pseudo double-insertion product [(*t*-Bu-NC*–C{Ar}N*{*t*-Bu})Fe(CN-*t*-Bu)₄]⁺, **6.3**, respectively. The crystal structures of **6.1** – **6.3** revealed that both coordination and insertion processes occur, including *bis*- and double-insertion. Furthermore, IR reaction monitoring showed that these reactions occur rapidly, with the appearance of new IR bands at lower wavenumber indicating a weakening of the isocyanide C–N bond.

Appendices

Crystallographic Tables

	3.2	3.3	3.5	3.6	3.7
Internal Code	OAJVLB	OAJVLC	KEWJMA	OAJVLE	OAJVLA
Formula	C ₂₆ H ₂₉ I	C ₂₅ H ₂₉ ISi	C ₂₂ H ₂₀ ClI	C ₂₃ H ₂₀ F ₃ I	C ₂₃ H ₂₃ OI
<i>M_w</i>	468.39	484.47	446.73	480.29	442.31
<i>T</i> (K)	120(2)	120(2)	120(2)	120(2)	119.9(2)
Crystal system	monoclinic	monoclinic	monoclinic	monoclinic	triclinic
Space Group	P2 ₁ /n	P2 ₁ /c	P2 ₁ /n	P2 ₁ /n	P-1
<i>a</i> (Å)	13.1749(2)	6.3663(4)	8.3499(2)	8.51060(10)	8.3720(4)
<i>b</i> (Å)	13.2712(2)	17.8142(9)	34.7269(7)	35.0225(4)	13.7244(6)
<i>c</i> (Å)	13.8896(2)	20.5558(14)	13.4766(3)	13.61300(10)	18.1728(8)
α (°)	90	90	90	90	105.436(4)
β (°)	109.910(2)	96.860(6)	100.064(2)	99.1350(10)	96.680(4)
γ (°)	90	90	90	90	100.238(4)
<i>V</i> (Å ³)	2283.39(6)	2314.6(2)	3847.63(15)	4006.06(7)	1951.00(16)
<i>Z</i>	4	4	8	8	4
<i>D_{calc}</i> (g cm ⁻³)	1.363	1.39	1.542	1.593	1.506
μ (mm ⁻¹)	11.046	11.395	14.332	12.836	12.934
<i>F₀₀₀</i>	952	984	1776	1904	888
Crystal size (mm ³)	0.14 × 0.08 × 0.05	0.48 × 0.26 × 0.07	0.65 × 0.11 × 0.08	0.46 × 0.22 × 0.10	0.24 × 0.08 × 0.03
λ (Å)	1.54184	1.54184	1.54184	1.54184	1.54184
2 θ range for data collection (°)	7.992 to 147.16	6.586 to 149.004	7.132 to 147.398	7.044 to 147.47	6.846 to 149.508
Reflections collected	8955	9764	16211	61599	23056
Independent reflections	4473	4520	7564	8032	7815
<i>R_{int}</i>	0.0240	0.0505	0.0427	0.0535	0.0691
<i>Goof</i> on <i>F</i> ²	1.025	1.054	1.034	1.123	1.147
<i>R</i> ₁ , <i>wR</i> ₂ [<i>I</i> > 2 σ (<i>I</i>)]	0.0271, 0.0660	0.0580, 0.1477	0.0399, 0.1019	0.0459, 0.0936	0.2079, 0.5027
<i>R</i> ₁ , <i>wR</i> ₂ (all data)	0.0314, 0.0685	0.0648, 0.1524	0.0436, 0.1055	0.0474, 0.0941	0.2135, 0.5051
Largest diff. peak/hole (e Å ⁻³)	1.80/-0.83	3.02/-1.49	1.17/-1.32	2.04/-1.02	10.84/-7.83

Crystallographic Tables

	3.8	3.9	3.10	3.12	3.13
Internal Code	OAJVLD	LIAJVB	LIAJVG	KEWJMB	LIAJVF
Formula	C _{47.5} H ₄₄ I ₂	C ₅₈ H ₆₄ Li ₂	C ₅₀ H ₅₈ Li ₂ Si ₂	C ₄₇ H ₄₇ Cl ₂ Li ₂	C ₄₆ H ₄₀ F ₆ Li ₂
<i>M</i> _w	868.62	774.97	729.02	696.62	720.66
<i>T</i> (K)	120(2)	119.98(10)	120(2)	120(2)	120(2)
Crystal system	triclinic	triclinic	triclinic	monoclinic	monoclinic
Space Group	P-1	P-1	P-1	P2 ₁ /c	C2/c
<i>a</i> (Å)	7.2288(11)	11.9982(4)	11.7845(5)	12.1125(11)	16.2343(6)
<i>b</i> (Å)	12.5109(11)	15.2538(10)	13.7778(6)	16.8343(14)	16.3983(5)
<i>c</i> (Å)	12.9447(12)	15.4697(9)	16.2675(8)	19.6420(14)	15.5748(5)
α (°)	112.206(9)	113.742(6)	69.756(4)	90	90
β (°)	93.048(10)	101.077(4)	85.404(4)	103.471(9)	115.087(4)
γ (°)	99.021(10)	104.484(4)	64.756(4)	90	90
<i>V</i> (Å ³)	1062.3(2)	2368.3(2)	2234.36(19)	3894.9(6)	3755.1(2)
<i>Z</i>	1	2	2	4	4
<i>D</i> _{calc} (g cm ⁻³)	1.358	1.087	1.084	1.188	1.275
μ (mm ⁻¹)	11.832	0.445	0.938	1.72	0.763
<i>F</i> ₀₀₀	435	836	784	1476	1504
Crystal size (mm ³)	0.15 × 0.11 × 0.03	0.62 × 0.35 × 0.22	0.20 × 0.14 × 0.07	0.25 × 0.13 × 0.10	0.49 × 0.11 × 0.09
λ (Å)	1.54184	1.54184	1.54184	1.54184	1.54184
2θ range for data collection (°)	7.432 to 148.016	6.614 to 148.726	5.808 to 147.602	7 to 151.612	8.076 to 149.072
Reflections collected	8304	18075	16819	20656	21864
Independent reflections	4128	9364	8737	7768	3818
<i>R</i> _{int}	0.0574	0.0213	0.0335	0.0560	0.0275
<i>Goof</i> on <i>F</i> ²	1.056	1.886	1.066	1.032	1.039
<i>R</i> ₁ , <i>wR</i> ₂ [<i>I</i> > 2σ(<i>I</i>)]	0.0851, 0.2238	0.0760, 0.2378	0.0482, 0.1149	0.0705, 0.1573	0.0390, 0.1038
<i>R</i> ₁ , <i>wR</i> ₂ (all data)	0.0971, 0.2340	0.0844, 0.2497	0.0598, 0.1212	0.1286, 0.1945	0.0430, 0.1076
Largest diff. peak/hole (e Å ⁻³)	2.51/-1.55	0.82/-0.46	0.33/-0.30	0.26/-0.38	0.28/-0.24

Crystallographic Tables

	4.1	4.2	4.3	4.4	4.5
Internal Code	ZNAJVA	CDAJVA	HGAJVA	ZNAJVB	CDAJVB
Formula	C ₅₂ H ₅₈ Zn	C ₅₂ H ₅₈ Cd	C ₅₂ H ₅₈ Hg	C ₅₀ H ₅₈ Si ₂ Zn	C ₅₀ H ₅₈ Si ₂ Cd
<i>M</i> _w	748.35	795.38	883.57	780.51	827.54
<i>T</i> (K)	120.00(11)	120.00(12)	120.01(10)	120(2)	120(2)
Crystal system	triclinic	triclinic	triclinic	Triclinic	Triclinic
Space Group	P-1	P-1	P-1	<i>P</i> -1	<i>P</i> -1
<i>a</i> (Å)	12.1182(4)	12.1241(4)	12.0934(3)	11.658(3)	11.5086(5)
<i>b</i> (Å)	15.1384(5)	15.2935(5)	15.2550(4)	13.804(4)	13.9916(7)
<i>c</i> (Å)	15.2972(5)	15.4933(5)	15.5470(5)	16.423(4)	16.5734(13)
α (°)	113.284(3)	112.638(3)	113.054(3)	70.32(2)	107.205(6)
β (°)	101.454(3)	102.448(3)	102.333(2)	85.79(2)	94.247(5)
γ (°)	103.427(3)	104.576(3)	104.184(2)	65.06(3)	114.241(5)
<i>V</i> (Å ³)	2371.15(15)	2404.03(15)	2399.68(13)	2249.2(11)	2265.2(3)
<i>Z</i>	2	2	2	2	2
<i>D</i> _{calc} (g cm ⁻³)	1.048	1.099	1.223	1.152	1.213
μ (mm ⁻¹)	0.928	3.845	5.96	1.491	4.589
<i>F</i> ₀₀₀	800	836	900	832.0	868.0
Crystal size (mm ³)	0.44 × 0.16 × 0.15	0.16 × 0.08 × 0.07	0.49 × 0.28 × 0.08	0.10 x 0.07 x 0.02	0.16 x 0.10 x 0.02
λ (Å)	1.54184	1.54184	1.54184	1.54184	1.54184
2θ range for data collection (°)	6.958 to 147.238	6.744 to 147.308	6.766 to 148.232	7.504 to 149.406	7.424 to 133.154
Reflections collected	18044	23029	18437	8994	8009
Independent reflections	9297	9448	9426	8994	8009
<i>R</i> _{int}	0.0351	0.0281	0.0453	-	-
<i>Goof</i> on <i>F</i> ²	1.889	1.114	1.08	1.016	1.190
<i>R</i> ₁ , <i>wR</i> ₂ [<i>I</i> > 2σ(<i>I</i>)]	0.0871, 0.2514	0.0389, 0.1168	0.0485, 0.1343	0.1374, 0.3180	0.1140, 0.2929
<i>R</i> ₁ , <i>wR</i> ₂ (all data)	0.0964, 0.2621	0.0412, 0.1191	0.0513, 0.1377	0.2536, 0.4007	0.1283, 0.2996
Largest diff. peak/hole (e Å ⁻³)	1.60/-0.76	1.51/-0.70	2.92/-2.39	1.56/-1.42	4.18/-2.48

Crystallographic Tables

	4.6	4.7	4.8	4.9	4.10
Internal Code	HGAJVB	KEWJME	KEWJMF	KEWJMD	ZNAJVC
Formula	C ₅₀ H ₅₈ Si ₂ Hg	C ₄₄ H ₄₀ Cl ₂ Zn	C ₄₄ H ₄₀ Cl ₂ Cd	C ₄₄ H ₄₀ Cl ₂ Hg	C ₄₉ H ₄₆ F ₆ Zn
<i>M</i> _w	915.73	705.03	752.06	840.25	814.23
<i>T</i> (K)	120(2)	120(2)	120(2)	120(2)	120(2)
Crystal system	triclinic	Monoclinic	Monoclinic	Monoclinic	monoclinic
Space Group	P-1	<i>P</i> 2 ₁ / <i>n</i>	<i>P</i> 2 ₁ / <i>c</i>	<i>P</i> 2 ₁ / <i>c</i>	<i>P</i> 2 ₁ / <i>c</i>
<i>a</i> (Å)	11.5548(8)	17.8312(2)	10.4856(3)	10.4595(2)	11.59590(10)
<i>b</i> (Å)	13.9247(7)	19.6421(3)	19.5184(5)	19.5671(6)	17.77240(10)
<i>c</i> (Å)	16.6732(11)	20.8076(3)	17.9884(5)	18.0162(4)	20.6031(2)
α (°)	69.107(6)	90	90	90	90
β (°)	85.782(6)	100.9640(10)	98.895(2)	99.208(2)	100.6780(10)
γ (°)	65.508(6)	90	90	90	90
<i>V</i> (Å ³)	2272.0(3)	7154.68(17)	3637.27(17)	3639.72(16)	4172.51(6)
<i>Z</i>	2	8	4	4	4
<i>D</i> _{calc} (g cm ⁻³)	1.339	1.309	1.373	1.533	1.296
μ (mm ⁻¹)	6.802	2.544	6.374	9.150	1.315
<i>F</i> ₀₀₀	932	2944.0	1544.0	1672.0	1696
Crystal size (mm ³)	0.11 × 0.08 × 0.01	0.09 × 0.05 × 0.04	0.33 × 0.18 × 0.14	0.24 × 0.09 × 0.07	0.59 × 0.43 × 0.37
λ (Å)	1.54184	1.54184	1.54184	1.54184	1.54184
2θ range for data collection (°)	7.476 to 147.32	6.764 to 147.226	6.726 to 149.632	6.716 to 148.878	6.618 to 149.172
Reflections collected	17836	47824	15158	26249	135433
Independent reflections	8873	14178	7217	7305	8496
<i>R</i> _{int}	0.0833	0.0422	0.0282	0.0357	0.0524
<i>Goof</i> on <i>F</i> ²	1.161	1.016	1.035	1.016	1.036
<i>R</i> ₁ , <i>wR</i> ₂ [<i>I</i> > 2σ(<i>I</i>)]	0.1388, 0.3698	0.0352, 0.0789	0.0326, 0.0844	0.0273, 0.0671	0.0438, 0.1160
<i>R</i> ₁ , <i>wR</i> ₂ (all data)	0.1459, 0.3737	0.0517, 0.0860	0.0363, 0.0876	0.0343, 0.0709	0.0448, 0.1171
Largest diff. peak/hole (e Å ⁻³)	11.99/-5.18	0.29/-0.38	1.03/-0.88	0.77/-0.62	0.81/-0.74

Crystallographic Tables

	4.11	4.12	5.1	5.2	5.4
Internal Code	CDAJVC	HGAJVC	FEAJVA	FEAJVB	KEWJMC
Formula	C ₄₆ H ₄₀ F ₆ Cd	C ₄₉ H ₄₇ F ₆ Hg	C ₅₂ H ₅₈ Fe	C ₅₀ H ₅₈ FeSi ₂	C ₄₄ H ₄₀ Cl ₂ Fe
<i>M_w</i>	819.18	950.45	739.94	770.99	695.51
<i>T</i> (K)	120.00(10)	120(2)	120(2)	120(2)	120(2)
Crystal system	monoclinic	monoclinic	monoclinic	monoclinic	monoclinic
Space Group	P2 ₁ /c	P2 ₁ /c	P2 ₁ /c	C2/c	P2 ₁ /c
<i>a</i> (Å)	11.5314(2)	11.6029(2)	12.9758(15)	25.4389(10)	22.1189(2)
<i>b</i> (Å)	17.9866(2)	17.9140(3)	16.9439(16)	11.5117(4)	19.6861(2)
<i>c</i> (Å)	20.5675(3)	20.5582(3)	20.2267(14)	47.1469(18)	24.7347(2)
α (°)	90	90	90	90	90
β (°)	100.422(2)	100.899(2)	96.776(8)	102.414(4)	95.9930(10)
γ (°)	90	90	90	90	90
<i>V</i> (Å ³)	4195.54(11)	4196.03(12)	4416.0(7)	13483.9(9)	10711.49(17)
<i>Z</i>	4	4	4	12	12
<i>D</i> _{calc} (g cm ⁻³)	1.297	1.505	1.113	1.139	1.294
μ (mm ⁻¹)	4.638	7.076	2.964	3.424	4.981
<i>F</i> ₀₀₀	1672	1900	1586	4944	4368
Crystal size (mm ³)	0.30 × 0.14 × 0.07	0.03 × 0.08 × 0.10	0.26 × 0.22 × 0.054	0.44 × 0.14 × 0.07	0.55 × 0.49 × 0.31
λ (Å)	1.54184	1.54184	1.54184	1.54184	1.54184
2 θ range for data collection (°)	6.576 to 149.012	6.596 to 147.404	6.826 to 165.504	7.116 to 149.312	6.798 to 147.918
Reflections collected	63011	22223	61007	79133	92429
Independent reflections	8543	8282	9098	13471	21283
<i>R</i> _{int}	0.0312	0.0322	0.3579	0.1280	0.0554
<i>Goof</i> on <i>F</i> ²	0.572	1.018	0.879	1.062	1.055
<i>R</i> ₁ , <i>wR</i> ₂ [<i>I</i> > 2 σ (<i>I</i>)]	0.0267, 0.0749	0.0332, 0.0697	0.0738, 0.1479	0.0844, 0.1952	0.0522, 0.1509
<i>R</i> ₁ , <i>wR</i> ₂ (all data)	0.0323, 0.0854	0.0526, 0.0771	0.2274, 0.1965	0.1103, 0.2115	0.0558, 0.1558
Largest diff. peak/hole (e Å ⁻³)	0.45/-0.51	1.27/-0.77	0.27/-0.28	0.77/-0.75	1.15/-0.72

Crystallographic Tables

	5.5	6.1	6.2	6.3
Internal Code	FEAJVC	ECTJMA	ECTJME	ECTJMC
Formula	C ₄₆ H ₄₀ F ₆ Fe	C ₂₃ H ₂₁ N	C ₅₇ H ₆₇ FeN ₂	C ₅₂ H ₇₅ N ₆ Fe
<i>M_w</i>	762.63	311.41	835.97	840.03
<i>T</i> (K)	120.15	120(2)	120(2)	120(2)
Crystal system	monoclinic	monoclinic	triclinic	orthorhombic
Space Group	P2 ₁ /c	C2/c	P-1	Aea2
<i>a</i> (Å)	11.3274(3)	14.1035(7)	9.1009(10)	45.920(9)
<i>b</i> (Å)	18.0368(5)	8.8755(3)	11.7395(18)	13.9958(19)
<i>c</i> (Å)	20.6315(4)	15.5339(7)	12.8585(18)	16.367(3)
α (°)	90	90	79.779(12)	90
β (°)	98.775(2)	111.188(5)	74.539(11)	90
γ (°)	90	90	72.784(12)	90
<i>V</i> (Å ³)	4165.89(19)	1813.02(15)	1257.5(3)	10519(3)
<i>Z</i>	4	4	1	8
<i>D</i> _{calc} (g cm ⁻³)	1.216	1.141	1.104	1.061
μ (mm ⁻¹)	3.375	0.497	2.665	2.568
<i>F</i> ₀₀₀	1584	664	449	3640
Crystal size (mm ³)	0.10 x 0.14 x 0.28	0.50 × 0.43 × 0.26	0.08 × 0.05 × 0.03	0.16 × 0.07 × 0.03
λ (Å)	1.54184	1.54184	1.54184	1.54184
2 θ range for data collection (°)	7.898 to 155.106	12.03 to 146.01	7.174 to 133.2	3.848 to 148.432
Reflections collected	32739	3124	9508	27305
Independent reflections	8612	1754	4420	8253
<i>R</i> _{int}	0.0514	0.0169	0.0924	0.2706
<i>Goof</i> on <i>F</i> ²	1.224	1.082	1.076	1.324
<i>R</i> ₁ , <i>wR</i> ₂ [<i>I</i> > 2 σ (<i>I</i>)]	0.1029, 0.2991	0.0405, 0.1106	0.1202, 0.3328	0.2535, 0.5157
<i>R</i> ₁ , <i>wR</i> ₂ (all data)	0.1235, 0.3203	0.0425, 0.1128	0.1521, 0.3607	0.3821, 0.6134
Largest diff. peak/hole (e Å ⁻³)	1.95/-0.60	0.17/-0.18	1.64/-0.77	3.90/-0.68

References

References

- 1 M. Hilbert and P. López, *Science*, 2011, **332**, 60–65.
- 2 M. Hilbert, in *Encyclopedia of Big Data*, eds. L. A. Schintler and C. L. McNeely, Springer International Publishing, Cham, Switzerland, 2017, pp. 1–4.
- 3 *Digital Economy Compass 2019*, Statista, 2019.
- 4 R. E. Simpson, *Nat. Nanotechnol.*, 2019, **14**, 643–644.
- 5 O. Cador and F. Pointillart, in *Topics in Organometallic Chemistry*, Springer, Berlin, Heidelberg, 2018.
- 6 B. Bhushan, *Microsyst. Technol.*, 2018, **24**, 4423–4436.
- 7 J. D. Cressler, in *Silicon Earth Introduction to Microelectronics and Nanotechnology, Second Edition*, CRC Press, Florida, 2nd edn., 2016, pp. 164–165.
- 8 J. E. Monson, in *Magnetic Recording: The First 100 Years*, eds. E. D. Daniel, C. D. Mee and M. H. Clark, Wiley-IEEE Press, New York, 1999, pp. 230–233.
- 9 F. J. Himpsel, A. Kirakosian, J. N. Crain, J. L. Lin and D. Y. Petrovykh, *Solid State Commun.*, 2001, **117**, 149–157.
- 10 R. L. Comstock, *J. Mater. Sci. Mater. Electron.*, 2002, **13**, 509–523.
- 11 M. Affronte, *J. Mater. Chem.*, 2009, **19**, 1731–1737.
- 12 H. Wu, L. Zhang and Y. Song, in *High Density Data Storage - Principle, Technology, and Materials*, eds. Y. Song and D. Zhu, World Scientific, Singapore, 2009, pp. 1–3.
- 13 J. W. Lu, E. Chen, M. Kabir, M. R. Stan and S. A. Wolf, *Int. Mater. Rev.*, 2016, **61**, 456–472.
- 14 S. Maat and A. C. Marley, in *Handbook of Spintronics*, eds. Y. Xu, D.

References

- Awschalom and J. Nitta, Springer, Dordrecht, The Netherlands, 1st edn., 2014, pp. 1–45.
- 15 E. E. Fullerton and J. R. Childress, *Proc. IEEE*, 2016, **104**, 1787–1795.
- 16 W. A. Bhat, *Int. J. Inf. Technol.*, 2018.
- 17 M. Affronte and F. Troiani, in *Molecular Magnets: Physics and Applications*, eds. J. Bartolomé, F. Luis and J. F. Fernández, Springer, Berlin, Heidelberg, 2014, pp. 249–273.
- 18 G. Christou, D. Gatteschi, D. N. Hendrickson and R. Sessoli, *MRS Bull.*, 2000, **25**, 66–71.
- 19 T. Thomson, L. Abelmann and H. Groenland, in *Magnetic Nanostructures in Modern Technology*, eds. B. Azzerboni, G. Asti, L. Pareti and M. Ghidini, Springer, Dordrecht, The Netherlands, 2008, pp. 237–306.
- 20 M. Ganzhorn and W. Wernsdorfer, in *Molecular Magnets: Physics and Applications*, eds. J. Bartolomé, F. Luis and J. F. Fernández, Springer, Berlin, Heidelberg, 2014, pp. 319–364.
- 21 S. K. RITTER, *Chem. Eng. News Arch.*, 2004, **82**, 29–32.
- 22 A. F. Orchard, in *Magnetochemistry*, ed. A. F. Orchard, Oxford University Press, Oxford, UK, 2003, pp. 6–13.
- 23 N. E. Chakov, M. Soler, W. Wernsdorfer, K. A. Abboud and G. Christou, *Inorg. Chem.*, 2005, **44**, 5304–5321.
- 24 D. Gatteschi, R. Sessoli and J. Villain, *Molecular Nanomagnets*, Oxford University Press, Oxford, UK, 2006.
- 25 S. F. A. Kettle, in *Physical Inorganic Chemistry: A Coordination Chemistry Approach*, ed. S. F. A. Kettle, Springer, Berlin, Heidelberg, 1996, pp. 185–210.
- 26 O. Kahn, *Molecular Magnetism*, VCH Publishers, New York, 1993.

- 27 N. Izarova and P. Kögerler, in *Trends in Polyoxometalates Research*, eds. L. Ruhlmann and D. Schaming, Nova Science Publishers, U.S.A., 2015, pp. 121–149.
- 28 G. A. Craig and M. Murrie, *Chem. Soc. Rev.*, 2015, **44**, 2135–2147.
- 29 H. L. C. Feltham and S. Brooker, *Coord. Chem. Rev.*, 2014, **276**, 1–33.
- 30 G. Aromí and E. K. Brechin, in *Single-Molecule Magnets and Related Phenomena*, ed. R. Winpenny, Springer, Berlin, Heidelberg, 2006, pp. 1–67.
- 31 T. Glaser, *Chem. Commun.*, 2011, **47**, 116–130.
- 32 F. Neese and D. A. Pantazis, *Faraday Discuss.*, 2011, **148**, 229–238.
- 33 S. Goswami, A. K. Mondal and S. Konar, *Inorg. Chem. Front.*, 2015, **2**, 687–712.
- 34 D. Gatteschi and R. Sessoli, *Angew. Chem. Int. Ed.*, 2003, **42**, 268–297.
- 35 J. R. Long, in *The Chemistry of Nanostructured Materials*, ed. P. Yang, WORLD SCIENTIFIC, Hong Kong, 2003, pp. 291–315.
- 36 K. A. Lippert, C. Mukherjee, J. P. Broschinski, Y. Lippert, S. Walleck, A. Stammer, H. Bögge, J. Schnack and T. Glaser, *Inorg. Chem.*, 2017, **56**, 15119–15129.
- 37 G. Aromí, E. McInnes and R. Winpenny, in *Molecular Cluster Magnets*, ed. R. Winpenny, World Scientific Publishing, Singapore, 2011, pp. 59–108.
- 38 C. Chappert, A. Fert and F. N. Van Dau, *Nat. Mater.*, 2007, **6**, 813.
- 39 C. A. P. Goodwin, F. Ortu, D. Reta, N. F. Chilton and D. P. Mills, *Nature*, 2017, **548**, 439.
- 40 F.-S. Guo, B. M. Day, Y.-C. Chen, M.-L. Tong, A. Mansikkamäki and R. A. Layfield, *Angew. Chem. Int. Ed.*, 2017, **56**, 11445–11449.
- 41 F.-S. Guo, B. M. Day, Y.-C. Chen, M.-L. Tong, A. Mansikkamäki and R. A.

References

- Layfield, *Science*, 2018, **362**, 1400–1403.
- 42 T. Lis, *Acta Crystallogr. Sect. B*, 1980, **36**, 2042–2046.
- 43 A. Caneschi, D. Gatteschi, R. Sessoli, A. L. Barra, L. C. Brunel and M. Guillot, *J. Am. Chem. Soc.*, 1991, **113**, 5873–5874.
- 44 R. Sessoli, H. L. Tsai, A. R. Schake, S. Wang, J. B. Vincent, K. Folting, D. Gatteschi, G. Christou and D. N. Hendrickson, *J. Am. Chem. Soc.*, 1993, **115**, 1804–1816.
- 45 R. Sessoli, D. Gatteschi, A. Caneschi and M. A. Novak, *Nature*, 1993, **365**, 141–143.
- 46 J. M. Frost, K. L. M. Harriman and M. Murugesu, *Chem. Sci.*, 2016, **7**, 2470–2491.
- 47 C. J. Milios, A. Vinslava, W. Wernsdorfer, S. Moggach, S. Parsons, S. P. Perlepes, G. Christou and E. K. Brechin, *J. Am. Chem. Soc.*, 2007, **129**, 2754–2755.
- 48 R. Bagai and G. Christou, *Chem. Soc. Rev.*, 2009, **38**, 1011–1026.
- 49 E. Ruiz, J. Cirera, J. Cano, S. Alvarez, C. Loose and J. Kortus, *Chem. Commun.*, 2008, 52–54.
- 50 O. Waldmann, *Inorg. Chem.*, 2007, **46**, 10035–10037.
- 51 P. Parois, S. A. Moggach, J. Sanchez-Benitez, K. V Kamenev, A. R. Lennie, J. E. Warren, E. K. Brechin, S. Parsons and M. Murrie, *Chem. Commun.*, 2010, **46**, 1881–1883.
- 52 N. Ishikawa, M. Sugita, T. Ishikawa, S. Koshihara and Y. Kaizu, *J. Am. Chem. Soc.*, 2003, **125**, 8694–8695.
- 53 D. N. Woodruff, R. E. P. Winpenny and R. A. Layfield, *Chem. Rev.*, 2013, **113**, 5110–5148.

- 54 J. M. Zadrozny, D. J. Xiao, M. Atanasov, G. J. Long, F. Grandjean, F. Neese and J. R. Long, *Nat. Chem.*, 2013, **5**, 577.
- 55 J. M. Zadrozny, D. J. Xiao, J. R. Long, M. Atanasov, F. Neese, F. Grandjean and G. J. Long, *Inorg. Chem.*, 2013, **52**, 13123–13131.
- 56 M. K. Thomsen, A. Nyvang, J. P. S. Walsh, P. C. Bunting, J. R. Long, F. Neese, M. Atanasov, A. Genoni and J. Overgaard, *Inorg. Chem.*, 2019, **58**, 3211–3218.
- 57 H. A. Kramers, *Proc. R. Acad. Sci. Amsterdam*, 1930, **33**, 959–972.
- 58 C. Ni, T. A. Stich, G. J. Long and P. P. Power, *Chem. Commun.*, 2010, **46**, 4466–4468.
- 59 J. J. Le Roy, M. Jeletic, S. I. Gorelsky, I. Korobkov, L. Ungur, L. F. Chibotaru and M. Murugesu, *J. Am. Chem. Soc.*, 2013, **135**, 3502–3510.
- 60 J. J. Le Roy, L. Ungur, I. Korobkov, L. F. Chibotaru and M. Murugesu, *J. Am. Chem. Soc.*, 2014, **136**, 8003–8010.
- 61 P. P. Power, *J. Organomet. Chem.*, 2004, **689**, 3904–3919.
- 62 H. Bürger and U. Wannagat, *Monatsh. Chem.*, 1963, **94**, 1007–1012.
- 63 H. Bürger and U. Wannagat, *Monatsh. Chem.*, 1964, **95**, 1099–1102.
- 64 H. H. Jaffé and G. O. Doak, *J. Chem. Phys.*, 1953, **21**, 196–200.
- 65 R. R. Schrock and G. W. Parshall, *Chem. Rev.*, 1976, **76**, 243–268.
- 66 N. H. Buttrus, C. Eaborn, P. B. Hitchcock, J. D. Smith and A. C. Sullivan, *J. Chem. Soc. Chem. Commun.*, 1985, 1380–1381.
- 67 R. Fischer, H. Görls, M. Friedrich and M. Westerhausen, *J. Organomet. Chem.*, 2009, **694**, 1107–1111.
- 68 S. Gambarotta, C. Floriani, A. Chiesi-Villa and C. Guastini, *J. Chem. Soc. Chem. Commun.*, 1983, 1128–1129.

References

- 69 C. Ni, J. C. Fettinger, G. J. Long and P. P. Power, *Dalton Trans.*, 2010, **39**, 10664–10670.
- 70 R. Wehmschulte and P. P. Power, *Organometallics*, 1995, **14**, 3264–3267.
- 71 D. L. Kays, *Organomet. Chem.*, 2010, **36**, 56–76.
- 72 C. A. Tolman, *Chem. Rev.*, 1977, **77**, 313–348.
- 73 A. C. Hillier, W. J. Sommer, B. S. Yong, J. L. Petersen, L. Cavallo and S. P. Nolan, *Organometallics*, 2003, **22**, 4322–4326.
- 74 L. Cavallo, A. Correa, C. Costabile and H. Jacobsen, *ChemInform*, 2006, **37**.
- 75 A. Poater, F. Ragone, S. Giudice, C. Costabile, R. Dorta, S. P. Nolan and L. Cavallo, *Organometallics*, 2008, **27**, 2679–2681.
- 76 A. Poater, B. Cosenza, A. Correa, S. Giudice, F. Ragone, V. Scarano and L. Cavallo, *Eur. J. Inorg. Chem.*, 2009, **2009**, 1759–1766.
- 77 H. R. Sharpe, A. M. Geer, T. J. Blundell, F. R. Hastings, M. W. Fay, G. A. Rance, W. Lewis, A. J. Blake and D. L. Kays, *Catal. Sci. Technol.*, 2018, **8**, 229–235.
- 78 L. Falivene, R. Credendino, A. Poater, A. Petta, L. Serra, R. Oliva, V. Scarano and L. Cavallo, *Organometallics*, 2016, **35**, 2286–2293.
- 79 A. Poater, F. Ragone, R. Mariz, R. Dorta and L. Cavallo, *Chem. – A Eur. J.*, 2010, **16**, 14348–14353.
- 80 T. J. Blundell, F. R. Hastings, B. M. Gridley, G. J. Moxey, W. Lewis, A. J. Blake and D. L. Kays, *Dalton Trans.*, 2014, **43**, 14257–14264.
- 81 T. J. Blundell, Ph.D, University of Nottingham, 2015.
- 82 K. V Bukhryakov, R. R. Schrock, A. H. Hoveyda, P. Müller and J. Becker, *Org. Lett.*, 2017, **19**, 2607–2609.
- 83 L. G. Perla, J. M. Kulenkampff, J. C. Fettinger and P. P. Power,

- Organometallics*, 2018, **37**, 4048–4054.
- 84 B. Schiemenz and P. P. Power, *Organometallics*, 1996, **15**, 958–964.
- 85 Z. Zhu, R. C. Fischer, B. D. Ellis, E. Rivard, W. A. Merrill, M. M. Olmstead, P. P. Power, J. D. Guo, S. Nagase and L. Pu, *Chem. Eur. J.*, 2009, **15**, 5263–5272.
- 86 C. Stanciu, A. F. Richards, J. C. Fettinger, M. Brynda and P. P. Power, *J. Organomet. Chem.*, 2006, **691**, 2540–2545.
- 87 N. J. Hardman, R. J. Wright, A. D. Phillips and P. P. Power, *Angew. Chem.*, 2002, **114**, 2966–2968.
- 88 N. J. Hardman, R. J. Wright, A. D. Phillips and P. P. Power, *J. Am. Chem. Soc.*, 2003, **125**, 2667–2679.
- 89 R. Wolf, C. Ni, T. Nguyen, M. Brynda, G. J. Long, A. D. Sutton, R. C. Fischer, J. C. Fettinger, M. Hellman, L. Pu and P. P. Power, *Inorg. Chem.*, 2007, **46**, 11277–11290.
- 90 E. Rivard, R. C. Fischer, R. Wolf, Y. Peng, W. A. Merrill, N. D. Schley, Z. Zhu, L. Pu, J. C. Fettinger, S. J. Teat, I. Nowik, R. H. Herber, N. Takagi, S. Nagase and P. P. Power, *J. Am. Chem. Soc.*, 2007, **129**, 16197–16208.
- 91 R. S. Simons, L. Pu, M. M. Olmstead and P. P. Power, *Organometallics*, 1997, **16**, 1920–1925.
- 92 P. Wilfling, K. Schittelkopf, M. Flock, R. H. Herber, P. P. Power and R. C. Fischer, *Organometallics*, 2015, **34**, 2222–2232.
- 93 R. C. Fischer, L. Pu, J. C. Fettinger, M. A. Brynda and P. P. Power, *J. Am. Chem. Soc.*, 2006, **128**, 11366–11367.
- 94 Y. Peng, R. C. Fischer, W. A. Merrill, J. Fischer, L. Pu, B. D. Ellis, J. C. Fettinger, R. H. Herber and P. P. Power, *Chem. Sci.*, 2010, **1**, 461–468.

References

- 95 C. J. F. Du, H. Hart and K. K. D. Ng, *J. Org. Chem.*, 1986, **51**, 3162–3165.
- 96 A. Saednya and H. Hart, *Synthesis (Stuttg.)*, 1996, **12**, 1455–1458.
- 97 K. Ruhlandt-Senge, J. J. Ellison, R. J. Wehmschulte, F. Pauer and P. P. Power, *J. Am. Chem. Soc.*, 1993, **115**, 11353–11357.
- 98 B. Schiemenz and P. P. Power, *Angew. Chem. Int. Ed. Eng*, 1996, **35**, 2150–2152.
- 99 G. W. Rabe, R. D. Sommer and A. L. Rheingold, *Organometallics*, 2000, **19**, 5537–5540.
- 100 S. Hino, M. M. Olmstead, J. C. Fettinger and P. P. Power, *J. Organomet. Chem.*, 2005, **690**, 1638–1644.
- 101 B. Twamley, S. T. Haubrich and P. P. Power, *Adv. Organomet. Chem.*, 1999, **44**, 1–65.
- 102 J. A. C. Clyburne and N. McMullen, *Coord. Chem. Rev.*, 2000, **210**, 73–99.
- 103 A. D. Sutton, T. Ngyuen, J. C. Fettinger, M. M. Olmstead, G. J. Long and P. P. Power, *Inorg. Chem.*, 2007, **46**, 4809–4814.
- 104 T. Nguyen, W. A. Merrill, C. Ni, H. Lei, J. C. Fettinger, B. D. Ellis, G. J. Long, M. Brynda and P. P. Power, *Angew. Chem. Int. Ed.*, 2008, **47**, 9115–9117.
- 105 Z. Zhu, M. Brynda, R. J. Wright, R. C. Fischer, W. A. Merrill, E. Rivard, R. Wolf, J. C. Fettinger, M. M. Olmstead and P. P. Power, *J. Am. Chem. Soc.*, 2007, **129**, 10847–10857.
- 106 T. Nguyen, A. D. Sutton, M. Brynda, J. C. Fettinger, G. J. Long and P. P. Power, *Science*, 2005, **310**, 844–847.
- 107 D. L. Kays and A. R. Cowley, *Chem. Commun.*, 2007, **0**, 1053–1055.
- 108 C. Ni and P. P. Power, *Chem. Commun.*, 2009, **0**, 5543–5545.
- 109 P. P. Power, *Chem. Rev.*, 2012, **112**, 3482–3507.

- 110 A. L. Companion and M. A. Komarynsky, *J. Chem. Educ.*, 1964, **41**, 257.
- 111 R. Krishnamurthy and W. B. Schaap, *J. Chem. Educ.*, 1969, **46**, 799.
- 112 D. Noda, Y. Sunada, T. Hatakeyama, M. Nakamura and H. Nagashima, *J. Am. Chem. Soc.*, 2009, **131**, 6078–6079.
- 113 D. H. Hill, M. A. Parvez and A. Sen, *J. Am. Chem. Soc.*, 1994, **116**, 2889–2901.
- 114 E. Negishi, K. Akiyoshi, B. O'Connor, K. Takagi and G. Wu, *J. Am. Chem. Soc.*, 1989, **111**, 3089–3091.
- 115 J. Langer, S. Krieck, H. Görls and M. Westerhausen, *Angew. Chem. Int. Ed.*, 2009, **48**, 5741–5744.
- 116 R. A. Layfield, *Chem. Soc. Rev.*, 2008, **37**, 1098–1107.
- 117 G. W. Coates, *J. Chem. Soc. Dalton Trans.*, 2002, 467–475.
- 118 V. C. Gibson and S. K. Spitzmesser, *Chem. Rev.*, 2003, **103**, 283–316.
- 119 A. Zambelli, L. Oliva and C. Pellecchia, *Macromolecules*, 1989, **22**, 2129–2130.
- 120 G. M. Whitesides and W. J. Ehmman, *J. Am. Chem. Soc.*, 1969, **91**, 3800–3807.
- 121 S. Wang, B. R. Jarrett, S. M. Kauzlarich and A. Y. Louie, *J. Am. Chem. Soc.*, 2007, **129**, 3848–3856.
- 122 L. Zu, D. J. Norris, T. A. Kennedy, S. C. Erwin and A. L. Efros, *Nano Lett.*, 2006, **6**, 334–340.
- 123 D. J. Norris, N. Yao, F. T. Charnock and T. A. Kennedy, *Nano Lett.*, 2001, **1**, 3–7.
- 124 B. A. Hernandez-Sanchez, T. J. Boyle, H. D. Pratt, M. A. Rodriguez, L. N. Brewer and D. R. Dunphy, *Chem. Mater.*, 2008, **20**, 6643–6656.
- 125 T. J. Boyle, H. D. Pratt, B. A. Hernandez-Sanchez, T. N. Lambert and T. J.

References

- Headley, *J. Mater. Sci.*, 2007, **42**, 2792–2795.
- 126 S. D. Bunge, T. J. Boyle and T. J. Headley, *Nano Lett.*, 2003, **3**, 901–905.
- 127 C. Ni, H. Lei and P. P. Power, *Organometallics*, 2010, **29**, 1988–1991.
- 128 B. M. Gridley, A. J. Blake, A. L. Davis, W. Lewis, G. J. Moxey and D. L. Kays, *Chem. Commun.*, 2012, **48**, 8910–8912.
- 129 B. Zhou, M. S. Denning, D. L. Kays and J. M. Goicoechea, *J. Am. Chem. Soc.*, 2009, **131**, 2802–2803.
- 130 Z. D. Brown, P. Vasko, J. C. Fettinger, H. M. Tuononen and P. P. Power, *J. Am. Chem. Soc.*, 2012, **134**, 4045–4048.
- 131 Z. D. Brown, P. Vasko, J. D. Erickson, J. C. Fettinger, H. M. Tuononen and P. P. Power, *J. Am. Chem. Soc.*, 2013, **135**, 6257–6261.
- 132 Z. D. Brown and P. P. Power, *Inorg. Chem.*, 2013, **52**, 6248–6259.
- 133 W. M. Reiff, A. M. LaPointe and E. H. Witten, *J. Am. Chem. Soc.*, 2004, **126**, 10206–10207.
- 134 N. F. Chilton, H. Lei, A. M. Bryan, F. Grandjean, G. J. Long and P. P. Power, *Dalton Trans.*, 2015, **44**, 11202–11211.
- 135 J. M. Zadrozny, M. Atanasov, A. M. Bryan, C.-Y. Lin, B. D. Rekker, P. P. Power, F. Neese and J. R. Long, *Chem. Sci.*, 2013, **4**, 125–138.
- 136 W. A. Merrill, T. A. Stich, M. Brynda, G. J. Yeagle, J. C. Fettinger, R. De Hont, W. M. Reiff, C. E. Schulz, R. D. Britt and P. P. Power, *J. Am. Chem. Soc.*, 2009, **131**, 12693–12702.
- 137 M. Atanasov, J. M. Zadrozny, J. R. Long and F. Neese, *Chem. Sci.*, 2013, **4**, 139–156.
- 138 W. Seidel, H. Müller and H. Görls, *Angew. Chem. Int. Ed. English*, 1995, **34**, 325–327.

- 139 C. Hansch, A. Leo and R. W. Taft, *Chem. Rev.*, 1991, **91**, 165–195.
- 140 P. Muller, *Pure Appl. Chem.*, 1994, **66**, 1077–1184.
- 141 J. Cosier and A. M. Glazer, *J. Appl. Crystallogr.*, 1986, **19**, 105–107.
- 142 *CrysAlisPRO*, Oxford Diffraction/Agilent Technologies UK Ltd, Yarnton, England.
- 143 A. L. Spek, *Acta Crystallogr. Sect. D*, 2009, **65**, 148–155.
- 144 O. V Dolomanov, L. J. Bourhis, R. J. Gildea, J. A. K. Howard and H. Puschmann, *J. Appl. Crystallogr.*, 2009, **42**, 339–341.
- 145 G. M. Sheldrick, *Acta Crystallogr. Sect. A*, 2015, **71**, 3–8.
- 146 G. M. Sheldrick, *Acta Crystallogr. Sect. C*, 2015, **71**, 3–8.
- 147 CheckCIF Online, <http://checkcif.iucr.org/>, (accessed July 2019).
- 148 *TopSpin*, Bruker.
- 149 W. Bauer, *Magn. Reson. Chem.*, 1996, **34**, 532–537.
- 150 C. Yu and G. C. Levy, *J. Am. Chem. Soc.*, 1984, **106**, 6533–6537.
- 151 *OPUS*, Bruker.
- 152 *WINEPR SimFonia*, Bruker.
- 153 *CasaXPS*, Casa Software Ltd, Teignmouth, UK.
- 154 H. Y. Liu, B. Scharbert and R. H. Holm, *J. Am. Chem. Soc.*, 1991, **113**, 9529–9539.
- 155 G. W. A. Fowles, D. A. Rice and R. A. Walton, *J. Inorg. Nucl. Chem.*, 1969, **31**, 3119–3131.
- 156 E. Rivard and P. P. Power, *Inorg. Chem.*, 2007, **46**, 10047–10064.
- 157 C. Ni and P. P. Power, in *Metal-Metal Bonding*, ed. G. Parkin, Springer Berlin Heidelberg, Berlin, Heidelberg, 2010, pp. 59–111.
- 158 J. Su, X. W. Li, R. C. Crittendon and G. H. Robinson, *J. Am. Chem. Soc.*, 1997,

References

- 119**, 5471–5472.
- 159 R. J. Wehmschulte, W. J. Grigsby, B. Schiemenz, R. A. Bartlett and P. P. Power, *Inorg. Chem.*, 1996, **35**, 6694–6702.
- 160 B. Twamley, C. D. Sofield, M. M. Olmstead and P. P. Power, *J. Am. Chem. Soc.*, 1999, **121**, 3357–3367.
- 161 S. Wang, M. L. McCrea-Hendrick, C. M. Weinstein, C. A. Caputo, E. Hoppe, J. C. Fettinger, M. M. Olmstead and P. P. Power, *J. Am. Chem. Soc.*, 2017, **139**, 6586–6595.
- 162 S. Shah, M. C. Simpson, R. C. Smith and J. D. Protasiewicz, *J. Am. Chem. Soc.*, 2001, **123**, 6925–6926.
- 163 B. M. Gridley, T. J. Blundell, G. J. Moxey, W. Lewis, A. J. Blake and D. L. Kays, *Chem. Commun.*, 2013, **49**, 9752–9754.
- 164 S. Watanabe, K. Goto, T. Kawashima and R. Okazaki, *Tetrahedron Lett.*, 1995, **36**, 7677–7680.
- 165 M. Tian, L. Liu, Y. Li, R. Hu, T. Liu, H. Liu, S. Wang and Y. Li, *Chem. Commun.*, 2014, **50**, 2055–2057.
- 166 T. C. Bedard and J. S. Moore, *J. Am. Chem. Soc.*, 1995, **117**, 10662–10671.
- 167 J. Clayden, N. Greeves, S. Warren and P. Wothers, in *Organic Chemistry*, Oxford University Press, New York, 1st edn., 2009, pp. 597–598.
- 168 D. Wrobel and U. Wannagat, *J. Organomet. Chem.*, 1982, **225**, 203–210.
- 169 D. K. Miller, C. A. Bailey and R. E. Sammelson, *Synthesis (Stuttg.)*, 2015, **47**, 2791–2798.
- 170 Y. B. Malysheva, S. Combes, A. Y. Fedorov, P. Knochel and A. E. Gavryushin, *Synlett*, 2012, **23**, 1205–1208.
- 171 F. L. W. van Roosmalen, *Recl. des Trav. Chim. des Pays-Bas*, 1934, **53**, 359–

- 379.
- 172 A. Sattler and G. Parkin, *J. Am. Chem. Soc.*, 2012, **134**, 2355–2366.
- 173 M. Niemeyer, *Organometallics*, 1998, **17**, 4649–4656.
- 174 M. Olaru, S. Rosca and C. I. Rat, *Acta Crystallogr. Sect. E*, 2011, **67**, o213.
- 175 B. Twamley, N. J. Hardman and P. P. Power, *Acta Crystallogr. Sect. C*, 2000, **56**, e514.
- 176 D. A. Dickie, D. Abeysekera, I. D. McKenzie, H. A. Jenkins and J. A. C. Clyburne, *Cryst. Eng.*, 2003, **6**, 79–86.
- 177 C. Stanciu, A. R. Fox, A. F. Richards, J. C. Fettinger and P. P. Power, *J. Organomet. Chem.*, 2006, **691**, 2546–2553.
- 178 J. Clayden, N. Greeves, S. Warren and P. Wothers, in *Organic Chemistry*, Oxford University Press, New York, 1st edn., 2009, pp. 271–272.
- 179 H. Spiessicke and W. G. Schneider, *J. Chem. Phys.*, 1961, **35**, 731–738.
- 180 P. C. Lauterbur, *J. Chem. Phys.*, 1963, **38**, 1406–1414.
- 181 A. Marker, D. Doddrell and N. V Riggs, *J. Chem. Soc. Chem. Commun.*, 1972, **0**, 724–725.
- 182 L. Laitem, L. Christiaens and M. Renson, *Org. Magn. Reson.*, 1980, **13**, 319–322.
- 183 D. Doddrell, M. Barfield, W. Adcock, M. Aurangzeb and D. Jordan, *J. Chem. Soc. Perkin Trans. 2*, 1976, **0**, 402–412.
- 184 A. Bondi, *J. Phys. Chem.*, 1964, **68**, 441–451.
- 185 In *Mercury User Guide and Tutorials*, Cambridge Crystallographic Data Centre, 2018, pp. 306–307.
- 186 T. D. W. Claridge, in *High-Resolution NMR Techniques in Organic Chemistry*, ed. T. D. W. Claridge, Elsevier, 2nd edn., 2009, vol. 27, pp. 303–334.

References

- 187 I. Keresztes and P. G. Williard, *J. Am. Chem. Soc.*, 2000, **122**, 10228–10229.
- 188 L. Allouche, A. Marquis and J. M. Lehn, *Chem. Eur. J.*, 2006, **12**, 7520–7525.
- 189 D. Seebach, R. Hässig and J. Gabriel, *Helv. Chim. Acta*, 1983, **66**, 308–337.
- 190 W. Bauer, W. R. Winchester and P. v R. Schleyer, *Organometallics*, 1987, **6**, 2371–2379.
- 191 S. Berger, U. Fleischer, C. Geletneky and J. C. W. Lohrenz, *Chem. Ber.*, 1995, **128**, 1183–1186.
- 192 H. Dahn, *J. Chem. Educ.*, 2000, **77**, 905.
- 193 J. T. B. H. Jastrzebski, G. van Koten, M. Konijn and C. H. Stam, *J. Am. Chem. Soc.*, 1982, **104**, 5490–5492.
- 194 M. H. P. Rietveld, I. C. M. Wehman-Ooyevaar, G. M. Kapteijn, D. M. Grove, W. J. J. Smeets, H. Kooijman, A. L. Spek and G. van Koten, *Organometallics*, 1994, **13**, 3782–3787.
- 195 E. Wehman, J. T. B. H. Jastrzebski, J. M. Ernsting, D. M. Grove and G. van Koten, *J. Organomet. Chem.*, 1988, **353**, 133–143.
- 196 E. Wehman, J. T. B. H. Jastrzebski, J. M. Ernsting, D. M. Grove and G. van Koten, *J. Organomet. Chem.*, 1988, **353**, 145–155.
- 197 P. A. Scherr, R. J. Hogan and J. P. Oliver, *J. Am. Chem. Soc.*, 1974, **96**, 6055–6059.
- 198 H. Günther, D. Moskau, P. Bast and D. Schmalz, *Angew. Chem. Int. Ed. English*, 1987, **26**, 1212–1220.
- 199 H. Günther, *eMagRes*, 2007, 1–21.
- 200 J. A. Ladd, *Spectrochim. Acta*, 1966, **22**, 1157–1163.
- 201 J. Parker and J. A. Ladd, *J. Organomet. Chem.*, 1969, **19**, 1–7.
- 202 J. A. Ladd and J. Parker, *J. Chem. Soc. Dalton Trans.*, 1972, **0**, 930–934.

- 203 P. West and R. Waack, *J. Am. Chem. Soc.*, 1967, **89**, 4395–4399.
- 204 J. A. Ladd and J. Parker, *J. Organomet. Chem.*, 1971, **28**, 1–4.
- 205 L. M. Jackman and L. M. Scarmoutzos, *J. Am. Chem. Soc.*, 1984, **106**, 4627–4629.
- 206 O. Eppers and H. Günther, *Helv. Chim. Acta*, 1992, **75**, 2553–2562.
- 207 H. J. Reich, D. P. Green, M. A. Medina, W. S. Goldenberg, B. Ö. Gudmundsson, R. R. Dykstra and N. H. Phillips, *J. Am. Chem. Soc.*, 1998, **120**, 7201–7210.
- 208 A. Harrison-Marchand and F. Mongin, *Chem. Rev.*, 2013, **113**, 7470–7562.
- 209 W. Bauer, G. Müller, R. Pi and P. von Ragué Schleyer, *Angew. Chem. Int. Ed. English*, 1986, **25**, 1103–1104.
- 210 W. Bauer, M. Feigel, G. Mueller and P. v. R. Schleyer, *J. Am. Chem. Soc.*, 1988, **110**, 6033–6046.
- 211 W. Bauer, P. A. A. Klusener, S. Harder, J. A. Kanters, A. J. M. Duisenberg, L. Brandsma and P. v. R. Schleyer, *Organometallics*, 1988, **7**, 552–555.
- 212 C.-T. Chen and J. S. Siegel, *J. Am. Chem. Soc.*, 1994, **116**, 5959–5960.
- 213 P. Romanato, S. Duttwyler, A. Linden, K. K. Baldrige and J. S. Siegel, *J. Phys. Org. Chem.*, 2014, **27**, 277–283.
- 214 B. I. Kharisov, O. V. Kharissova, A. Vázquez Dimas, I. Gómez De La Fuente and Y. Peña Méndez, *J. Coord. Chem.*, 2016, **69**, 1125–1151.
- 215 N. Kumagai and M. Shibasaki, *Isr. J. Chem.*, 2017, **57**, 270–278.
- 216 B. Reuillard, K. H. Ly, T. E. Rosser, M. F. Kuehnel, I. Zebger and E. Reisner, *J. Am. Chem. Soc.*, 2017, **139**, 14425–14435.
- 217 A. A. Tregubov, D. B. Walker, K. Q. Vuong, J. J. Gooding and B. A. Messerle, *Dalton Trans.*, 2015, **44**, 7917–7926.

References

- 218 R. J. Wehmschulte, A. A. Diaz and M. A. Khan, *Organometallics*, 2003, **22**, 83–92.
- 219 H. Bürger, W. Sawodny and U. Wannagat, *J. Organomet. Chem.*, 1965, **3**, 113–120.
- 220 H. Schumann, J. Gottfriedsen and F. Girgsdies, *Z. Anorg. Allg. Chem.*, 1997, **623**, 1881–1884.
- 221 W. S. Rees, O. Just, H. Schumann and R. Weimann, *Polyhedron*, 1998, **17**, 1001–1004.
- 222 H. Schumann, J. Gottfriedsen, S. Dechert and F. Girgsdies, *Z. Anorg. Allg. Chem.*, 2000, **626**, 747–758.
- 223 O. Just, D. A. Gaul and W. S. Rees, *Polyhedron*, 2001, **20**, 815–821.
- 224 J. Hicks, E. J. Underhill, C. E. Kefalidis, L. Maron and C. Jones, *Angew. Chem. Int. Ed.*, 2015, **54**, 10000–10004.
- 225 P. R. Markies, G. Schat, O. S. Akkerman, F. Bickelhaupt, W. J. J. Smeets and A. L. Spek, *Organometallics*, 1990, **9**, 2243–2247.
- 226 T. Alsina, W. Clegg, K. A. Fraser and J. Sola, *J. Chem. Soc. Dalton Trans.*, 1992, 1393–1399.
- 227 S. C. Cole, M. P. Coles and P. B. Hitchcock, *Dalton Trans.*, 2003, 3663–3664.
- 228 M. Hayashi, M. Bolte, M. Wagner and H.-W. Lerner, *Z. Anorg. Allg. Chem.*, 2011, **637**, 646–649.
- 229 M. Niemeyer and P. P. Power, *Organometallics*, 1997, **16**, 3258–3260.
- 230 L. Enno and B. Jens, *Main Gr. Met. Chem.*, 2014, **37**, 155.
- 231 Z. Zhu, R. J. Wright, M. M. Olmstead, E. Rivard, M. Brynda and P. P. Power, *Angew. Chem. Int. Ed.*, 2006, **45**, 5807–5810.
- 232 Y. Wang, B. Quillian, C. S. Wannere, P. Wei, P. v. R. Schleyer and G. H.

- Robinson, *Organometallics*, 2007, **26**, 3054–3056.
- 233 E. Negishi, X. Zeng, Z. Tan, M. Qian, Q. Hu and Z. Huang, in *Metal-Catalyzed Cross-Coupling Reactions*, eds. A. de Meijere and F. Diederich, Wiley-VCH, Weinheim, Germany, 2004, p. 815.
- 234 Z. Rappoport and I. Marek, Eds., *The Chemistry of Organozinc Compounds*, Wiley, Chichester, UK, 2006.
- 235 A. R. Kennedy, J. Klett, R. E. Mulvey and D. S. Wright, *Science*, 2009, **326**, 706–708.
- 236 D. R. Armstrong, W. Clegg, S. H. Dale, E. Hevia, L. M. Hogg, G. W. Honeyman and R. E. Mulvey, *Angew. Chem. Int. Ed.*, 2006, **45**, 3775–3778.
- 237 G. W. Coates and D. R. Moore, *Angew. Chem. Int. Ed.*, 2004, **43**, 6618–6639.
- 238 H. Sugimoto and S. Inoue, *J. Polym. Sci. Part A Polym. Chem.*, 2004, **42**, 5561–5573.
- 239 T. J. Boyle, S. D. Bunge, T. M. Alam, G. P. Holland, T. J. Headley and G. Avilucea, *Inorg. Chem.*, 2005, **44**, 1309–1318.
- 240 M. Bochmann, K. Webb, M. Harman and M. B. Hursthouse, *Angew. Chem. Int. Ed. English*, 1990, **29**, 638–639.
- 241 B. Luo and W. L. Gladfelter, *Inorg. Chem.*, 2002, **41**, 590–597.
- 242 I. Castillo and T. D. Tilley, *J. Am. Chem. Soc.*, 2001, **123**, 10526–10534.
- 243 B. M. Gridley, G. J. Moxey, W. Lewis, A. J. Blake and D. L. Kays, *Chem. – Eur. J.*, 2013, **19**, 11446–11453.
- 244 Y. Sun, W. E. Piers and M. Parvez, *Can. J. Chem.*, 1998, **76**, 513–517.
- 245 M. H. Chisholm, J. C. Gallucci, H. Yin and H. Zhen, *Inorg. Chem.*, 2005, **44**, 4777–4785.
- 246 M. Westerhausen, M. W. Oßberger, J. S. Alexander and K. Ruhlandt-Senge, Z.

References

- Anorg. Allg. Chem.*, 2005, **631**, 2836–2841.
- 247 U. Braun, B. Böck, H. Nöth, I. Schwab, M. Schwartz, S. Weber and U. Wietelmann, *Eur. J. Inorg. Chem.*, 2004, **2004**, 3612–3628.
- 248 H. Strasdeit, I. Büsching, A.-K. Duhme and S. Pohl, *Acta Crystallogr. Sect. C*, 1993, **49**, 576–578.
- 249 C. Glidewell, J. N. Low and J. L. Wardell, *Acta Crystallogr. Sect. C*, 2005, **61**, m107–m108.
- 250 J. C. Huffman, W. A. Nugent and J. K. Kochi, *Inorg. Chem.*, 1980, **19**, 2749–2755.
- 251 S. Brooker, N. Bertel, D. Stalke, M. Noltemeyer, H. W. Roesky, G. M. Sheldrick and F. T. Edelman, *Organometallics*, 1992, **11**, 192–195.
- 252 B. Cordero, V. Gómez, A. E. Platero-Prats, M. Revés, J. Echeverría, E. Cremades, F. Barragán and S. Alvarez, *Dalton Trans.*, 2008, 2832–2838.
- 253 T. Ziegler, J. G. Snijders and E. J. Baerends, *J. Chem. Phys.*, 1981, **74**, 1271–1284.
- 254 P. Pyykko, *Chem. Rev.*, 1988, **88**, 563–594.
- 255 A. L. Allred, *J. Inorg. Nucl. Chem.*, 1961, **17**, 215–221.
- 256 D. M. Heinekey and S. R. Stobart, *Inorg. Chem.*, 1978, **17**, 1463–1466.
- 257 J. Arnold, T. D. Tilley, A. L. Rheingold and S. J. Geib, *Inorg. Chem.*, 1987, **26**, 2106–2109.
- 258 M. Summers, *113Cd NMR Spectroscopy of Coordination Compounds and Proteins*, 1988, vol. 86.
- 259 M. Munataka, S. Kitagawa and F. Yagi, *Inorg. Chem.*, 1986, **25**, 964–970.
- 260 M. A. Sens, N. K. Wilson, P. D. Ellis and J. D. Odom, *J. Magn. Reson.*, 1975, **19**, 323–336.

- 261 A. D. Cardin, P. D. Ellis, J. D. Odom and J. W. Howard, *J. Am. Chem. Soc.*, 1975, **97**, 1672–1679.
- 262 K. E. Rowland and R. D. Thomas, *Magn. Reson. Chem.*, 1985, **23**, 916–919.
- 263 B. Wrackmeyer and R. Contreras, ed. G. A. Webb, Academic Press, 1992, vol. 24, pp. 267–329.
- 264 M. Borzo and G. E. Maciel, *J. Magn. Reson.*, 1975, **19**, 279–282.
- 265 P. R. Wells and D. W. Hawker, *Org. Magn. Reson.*, 1981, **17**, 26–27.
- 266 D. J. Craik, in *Annual Reports on NMR Spectroscopy*, ed. G. A. Webb, Academic Press, 1984, vol. 15, pp. 91–92.
- 267 R. L. DeKock, E. J. Baerends, P. M. Boerrigter and R. Hengelmolen, *J. Am. Chem. Soc.*, 1984, **106**, 3387–3396.
- 268 L. A. Fedorov, B. A. Faingor, L. S. Golovchenko and D. N. Kravtsov, *J. Struct. Chem.*, 1979, **19**, 549–554.
- 269 H. Nakatsuji, K. Kand, K. Endo and T. Yonezawa, *J. Am. Chem. Soc.*, 1984, **106**, 4653–4660.
- 270 G. Ashworth, Ph.D, University of Nottingham, 2018.
- 271 F. A. Cotton, *Chem. Rev.*, 1955, **55**, 551–594.
- 272 G. Wilkinson, *Science*, 1974, **185**, 109–112.
- 273 P. J. Davidson, M. F. Lappert and R. Pearce, *Acc. Chem. Res.*, 1974, **7**, 209–217.
- 274 S. U. Koschmieder and G. Wilkinson, *Polyhedron*, 1991, **10**, 135–173.
- 275 E. Solari, F. Musso, E. Gallo, C. Floriani, N. Re, A. Chiesi-Villa and C. Rizzoli, *Organometallics*, 1995, **14**, 2265–2276.
- 276 B. Z. Machelett, *Z. Chem.*, 1976, **16**, 116.
- 277 H. Müller, W. Seidel and H. Görls, *J. Organomet. Chem.*, 1993, **445**, 133–136.

References

- 278 A. Klose, E. Solari, C. Floriani, A. Chiesi-Villa, C. Rizzoli and N. Re, *J. Am. Chem. Soc.*, 1994, **116**, 9123–9135.
- 279 K. H. Theopold, J. Silvestre, E. K. Byrne and D. S. Richeson, *Organometallics*, 1989, **8**, 2001–2009.
- 280 A. R. Hermes and G. S. Girolami, *Organometallics*, 1987, **6**, 763–768.
- 281 L. Falvello and M. Gerloch, *Acta Crystallogr. Sect. B*, 1979, **35**, 2547–2550.
- 282 L. J. Radonovich, K. J. Klabunde, C. B. Behrens, D. P. McCollor and B. B. Anderson, *Inorg. Chem.*, 1980, **19**, 1221–1226.
- 283 D. L. Kays, *Dalton Trans.*, 2011, **40**, 769–778.
- 284 C. Ni, J. C. Fettingner, G. J. Long and P. P. Power, *Inorg. Chem.*, 2009, **48**, 2443–2448.
- 285 T. Deschner, K. W. Törnroos and R. Anwänder, *Inorg. Chem.*, 2011, **50**, 7217–7228.
- 286 A. W. Holland, G. Li, A. M. Shahin, G. J. Long, A. T. Bell and T. D. Tilley, *J. Catal.*, 2005, **235**, 150–163.
- 287 C. Roukoss, J.-M. Basset, C. Copéret, C. Lucas and E. Kuntz, *Comptes Rendus Chim.*, 2008, **11**, 620–627.
- 288 H. R. Sharpe, A. M. Geer, W. Lewis, A. J. Blake and D. L. Kays, *Angew. Chem. Int. Ed.*, 2017, **56**, 4845–4848.
- 289 H. R. Sharpe, A. M. Geer, H. E. L. Williams, T. J. Blundell, W. Lewis, A. J. Blake and D. L. Kays, *Chem. Commun.*, 2017, **53**, 937–940.
- 290 R. A. Layfield, *Organometallics*, 2014, **33**, 1084–1099.
- 291 M. Feng and M. Tong, *Chem. – A Eur. J.*, 2018, **24**, 7574–7594.
- 292 A. Baniodeh, V. Mereacre, N. Magnani, Y. Lan, J. A. Wolny, V. Schünemann, C. E. Anson and A. K. Powell, *Chem. Commun.*, 2013, **49**, 9666–9668.

- 293 D. Zhang, Y.-M. Tian, W.-B. Sun, H.-F. Li, P. Chen, Y.-Q. Zhang and P.-F. Yan, *Dalton Trans.*, 2016, **45**, 2674–2680.
- 294 S. K. Langley, D. P. Wielechowski, B. Moubaraki and K. S. Murray, *Chem. Commun.*, 2016, **52**, 10976–10979.
- 295 Y. Li, Q. Shang, Y.-Q. Zhang, E.-C. Yang and X.-J. Zhao, *Chem. – A Eur. J.*, 2016, **22**, 18840–18849.
- 296 F. Habib, G. Brunet, V. Vieru, I. Korobkov, L. F. Chibotaru and M. Murugesu, *J. Am. Chem. Soc.*, 2013, **135**, 13242–13245.
- 297 J. Pratt, A. M. Bryan, M. Faust, J. N. Boynton, P. Vasko, B. D. Rekker, A. Mansikkamäki, J. C. Fettinger, H. M. Tuononen and P. P. Power, *Inorg. Chem.*, 2018, **57**, 6491–6502.
- 298 H. R. Sharpe, A. M. Geer, L. J. Taylor, B. M. Gridley, T. J. Blundell, A. J. Blake, E. S. Davies, W. Lewis, J. McMaster, D. Robinson and D. L. Kays, *Nat. Commun.*, 2018, **9**, 3757.
- 299 S. S. Batsanov, *Inorg. Mater.*, 2001, **37**, 871–885.
- 300 S.-Z. Hu, Z.-H. Zhoul and B. E. Robertson, *Z. Kristallogr.*, 2009, **224**, 375–383.
- 301 K. E. Schwarzhans, *Angew. Chem. Int. Ed. English*, 1970, **9**, 946–953.
- 302 F. H. Köhler, *eMagRes*, 2011.
- 303 A. J. Pell, G. Pintacuda and C. P. Grey, *Prog. Nucl. Magn. Reson. Spectrosc.*, 2019, **111**, 1–271.
- 304 P. L. Holland, *Acc. Chem. Res.*, 2008, **41**, 905–914.
- 305 G. Socrates, *Infrared and Raman characteristic group frequencies: tables and charts*, John Wiley & Sons, Chichester, 3rd ed., 2001.
- 306 C. Reichardt, *Chem. Rev.*, 1994, **94**, 2319–2358.

References

- 307 J. F. Watts, *An introduction to surface analysis by XPS and AES*, J. Wiley, Chichester, 2003.
- 308 S. O. Grim and L. J. Matienzo, *Inorg. Chem.*, 1975, **14**, 1014–1018.
- 309 R. D. Feltham and P. Brant, *J. Am. Chem. Soc.*, 1982, **104**, 641–645.
- 310 P. Brant and R. D. Feltham, *J. Electron Spectros. Relat. Phenomena*, 1983, **32**, 205–221.
- 311 S. Srivastava, S. Badrinarayanan and A. J. Mukhedkar, *Polyhedron*, 1985, **4**, 409–414.
- 312 P. G. Gassman, D. W. Macomber and J. W. Hershberger, *Organometallics*, 1983, **2**, 1470–1472.
- 313 P. G. Gassman and C. H. Winter, *J. Am. Chem. Soc.*, 1986, **108**, 4228–4229.
- 314 P. G. Gassman, P. A. Deck, C. H. Winter, D. A. Dobbs and D. H. Cao, *Organometallics*, 1992, **11**, 959–960.
- 315 P. G. Gassman, J. W. Mickelson and J. R. Sowa, *J. Am. Chem. Soc.*, 1992, **114**, 6942–6944.
- 316 Y. Yokota, Y. Mino, Y. Kanai, T. Utsunomiya, A. Imanishi, M. A. Wolak, R. Schlaf and K. Fukui, *J. Phys. Chem. C*, 2014, **118**, 10936–10943.
- 317 J. Conradie and E. Erasmus, *Polyhedron*, 2016, **119**, 142–150.
- 318 Thermo Scientific XPS Notes, <https://xpssimplified.com/elements/iron.php>, (accessed June 2019).
- 319 A. P. Grosvenor, B. A. Kobe, M. C. Biesinger and N. S. McIntyre, *Surf. Interface Anal.*, 2004, **36**, 1564–1574.
- 320 N. Elgrishi, K. J. Rountree, B. D. McCarthy, E. S. Rountree, T. T. Eisenhart and J. L. Dempsey, *J. Chem. Educ.*, 2018, **95**, 197–206.
- 321 A. J. Bard and L. R. Faulkner, *Electrochemical methods: fundamentals and*

- applications*, John Wiley & Sons, New York, 2nd ed., 2001.
- 322 M. Lanznaster, A. Neves, A. J. Bortoluzzi, A. M. C. Assumpção, I. Vencato, S. P. Machado and S. M. Drechsel, *Inorg. Chem.*, 2006, **45**, 1005–1011.
- 323 R. Manchanda, *Inorganica Chim. Acta*, 1996, **245**, 91–95.
- 324 C. A. Joseph, M. S. Lee, A. V Iretskii, G. Wu and P. C. Ford, *Inorg. Chem.*, 2006, **45**, 2075–2082.
- 325 S. P. Gubin, *Pure Appl. Chem.*, 1970, **23**, 463–487.
- 326 G. L. K. Hoh, W. E. McEwen and J. Kleinberg, *J. Am. Chem. Soc.*, 1961, **83**, 3949–3953.
- 327 W. F. Little, C. N. Reilley, J. D. Johnson, K. N. Lynn and A. P. Sanders, *J. Am. Chem. Soc.*, 1964, **86**, 1376–1381.
- 328 A. G. Nagy and S. Toma, *J. Organomet. Chem.*, 1984, **266**, 257–268.
- 329 K. M. Kadish and M. M. Morrison, *J. Am. Chem. Soc.*, 1976, **98**, 3326–3328.
- 330 K. M. Kadish and M. M. Morrison, *Bioinorg. Chem.*, 1977, **7**, 107–115.
- 331 W. B. Tolman, *Activation of Small Molecules: Organometallic and Bioinorganic Perspectives*, Wiley-VCH, Weinheim, Germany, 2006.
- 332 S. Yadav, S. Saha and S. S. Sen, *ChemCatChem*, 2016, **8**, 486–501.
- 333 C. Weetman and S. Inoue, *ChemCatChem*, 2018, **10**, 4213–4228.
- 334 J.-D. Guo and T. Sasamori, *Chem. – An Asian J.*, 2018, **13**, 3800–3817.
- 335 K. L. Haas and K. J. Franz, *Chem. Rev.*, 2009, **109**, 4921–4960.
- 336 A. Virtanen, *The Biological Fixation of Nitrogen and the Preservation of Fodder in Agriculture, and Their Importance to Human Nutrition*, Nobel Lecture, 1945.
- 337 J. R. Jennings, Ed., *Catalytic Ammonia Synthesis*, Springer US, New York, 1991.

References

- 338 L. Pu, N. J. Hardman and P. P. Power, *Organometallics*, 2001, **20**, 5105–5109.
- 339 G. L. Wegner, R. J. F. Berger, A. Schier and H. Schmidbaur, *Organometallics*, 2001, **20**, 418–423.
- 340 R. J. Wehmschulte, J. M. Steele and M. A. Khan, *Organometallics*, 2003, **22**, 4678–4684.
- 341 A. F. Richards, A. D. Phillips, M. M. Olmstead and P. P. Power, *J. Am. Chem. Soc.*, 2003, **125**, 3204–3205.
- 342 C. Cui, M. M. Olmstead and P. P. Power, *J. Am. Chem. Soc.*, 2004, **126**, 5062–5063.
- 343 C. Cui, M. Brynda, M. M. Olmstead and P. P. Power, *J. Am. Chem. Soc.*, 2004, **126**, 6510–6511.
- 344 G. H. Spikes, J. C. Fettinger and P. P. Power, *J. Am. Chem. Soc.*, 2005, **127**, 12232–12233.
- 345 J. D. Young, M. A. Khan, D. R. Powell and R. J. Wehmschulte, *Eur. J. Inorg. Chem.*, 2007, **2007**, 1671–1681.
- 346 X. Wang, Z. Zhu, Y. Peng, H. Lei, J. C. Fettinger and P. P. Power, *J. Am. Chem. Soc.*, 2009, **131**, 6912–6913.
- 347 Y. Peng, M. Brynda, B. D. Ellis, J. C. Fettinger, E. Rivard and P. P. Power, *Chem. Commun.*, 2008, 6042–6044.
- 348 Y. Peng, B. D. Ellis, X. Wang and P. P. Power, *J. Am. Chem. Soc.*, 2008, **130**, 12268–12269.
- 349 Z. Zhu, X. Wang, Y. Peng, H. Lei, J. C. Fettinger, E. Rivard and P. P. Power, *Angew. Chem. Int. Ed.*, 2009, **48**, 2031–2034.
- 350 Y. Peng, J.-D. Guo, B. D. Ellis, Z. Zhu, J. C. Fettinger, S. Nagase and P. P. Power, *J. Am. Chem. Soc.*, 2009, **131**, 16272–16282.

- 351 Y. Peng, B. D. Ellis, X. Wang, J. C. Fettinger and P. P. Power, *Science*, 2009, **325**, 1668–1670.
- 352 C. A. Caputo, Z. Zhu, Z. D. Brown, J. C. Fettinger and P. P. Power, *Chem. Commun.*, 2011, **47**, 7506–7508.
- 353 P. P. Power, *Acc. Chem. Res.*, 2011, **44**, 627–637.
- 354 P. P. Power, *Chem. Rec.*, 2012, **12**, 238–255.
- 355 Z. D. Brown, J.-D. Guo, S. Nagase and P. P. Power, *Organometallics*, 2012, **31**, 3768–3772.
- 356 Z. D. Brown, J. D. Erickson, J. C. Fettinger and P. P. Power, *Organometallics*, 2013, **32**, 617–622.
- 357 J. D. Erickson, J. C. Fettinger and P. P. Power, *Inorg. Chem.*, 2015, **54**, 1940–1948.
- 358 J. D. Erickson, P. Vasko, R. D. Riparetti, J. C. Fettinger, H. M. Tuononen and P. P. Power, *Organometallics*, 2015, **34**, 5785–5791.
- 359 A. Hinz and J. M. Goicoechea, *Angew. Chem. Int. Ed.*, 2016, **55**, 15515–15519.
- 360 J. D. Erickson, R. D. Riparetti, J. C. Fettinger and P. P. Power, *Organometallics*, 2016, **35**, 2124–2128.
- 361 T. Y. Lai, J. C. Fettinger and P. P. Power, *J. Am. Chem. Soc.*, 2018, **140**, 5674–5677.
- 362 T. Y. Lai, J.-D. Guo, J. C. Fettinger, S. Nagase and P. P. Power, *Chem. Commun.*, 2019, **55**, 405–407.
- 363 K. L. Gullett, T. Y. Lai, C.-Y. Chen, J. C. Fettinger and P. P. Power, *Organometallics*, 2019, **38**, 1425–1428.
- 364 H. Lei, B. D. Ellis, C. Ni, F. Grandjean, G. J. Long and P. P. Power, *Inorg. Chem.*, 2008, **47**, 10205–10207.

References

- 365 C. Ni, B. D. Ellis, G. J. Long and P. P. Power, *Chem. Commun.*, 2009, 2332–2334.
- 366 C. Ni and P. P. Power, *Organometallics*, 2009, **28**, 6541–6545.
- 367 H. Lei, J. C. Fettinger and P. P. Power, *Inorg. Chem.*, 2012, **51**, 1821–1826.
- 368 P. Zhao, H. Lei, C. Ni, J.-D. Guo, S. Kamali, J. C. Fettinger, F. Grandjean, G. J. Long, S. Nagase and P. P. Power, *Inorg. Chem.*, 2015, **54**, 8914–8922.
- 369 W. von Philipsborn, *Chem. Soc. Rev.*, 1999, **28**, 95–105.
- 370 M. Cheong and F. Basolo, *Organometallics*, 1988, **7**, 2041–2044.
- 371 D. Wang and R. J. Angelici, *Inorg. Chem.*, 1996, **35**, 1321–1331.
- 372 C. Nataro, L. M. Thomas and R. J. Angelici, *Inorg. Chem.*, 1997, **36**, 6000–6008.
- 373 K. Nakamoto, *Handb. Vib. Spectrosc.*, 2006, **1**, 1872–1892.
- 374 K. Sridharan, in *Spectral Methods in Transition Metal Complexes*, ed. K. Sridharan, Elsevier, Cambridge, 2016, pp. 69–97.
- 375 C. Pettinari and C. Santini, in *Encyclopedia of Spectroscopy and Spectrometry*, eds. J. C. Lindon, G. E. Tranter and D. W. Koppenaal, Academic Press, Oxford, 3rd edn., 2017, pp. 347–358.
- 376 G. Fauvet, M. Massaux and R. Chevalier, *Acta Crystallogr. Sect. B*, 1978, **34**, 1376–1378.
- 377 F. H. Allen, O. Kennard, D. G. Watson, L. Brammer, A. G. Orpen and R. Taylor, *J. Chem. Soc. Perkin Trans. 2*, 1987, S1–S19.
- 378 A. Klose, E. Solari, R. Ferguson, C. Floriani, A. Chiesi-Villa and C. Rizzoli, *Organometallics*, 1993, **12**, 2414–2416.
- 379 L.-C. Song, G.-L. Lu, Q.-M. Hu, X.-D. Qin, C.-X. Sun, J. Yang and J. Sun, *J. Organomet. Chem.*, 1998, **571**, 55–63.

- 380 C.-G. Yan, J. Sun and J. Sun, *J. Organomet. Chem.*, 1999, **585**, 63–67.
- 381 L.-C. Song, S.-Z. Mei, C.-P. Feng, F.-H. Gong, J.-H. Ge and Q.-M. Hu, *Organometallics*, 2010, **29**, 5050–5056.
- 382 Y.-C. Shi, Y. Shi and W. Yang, *J. Organomet. Chem.*, 2014, **772–773**, 131–138.
- 383 L. D. Durfee and I. P. Rothwell, *Chem. Rev.*, 1988, **88**, 1059–1079.
- 384 A. K. McMullen, I. P. Rothwell and J. C. Huffman, *J. Am. Chem. Soc.*, 1985, **107**, 1072–1073.
- 385 V. P. Boyarskiy, N. A. Bokach, K. V. Luzyanin and V. Y. Kukushkin, *Chem. Rev.*, 2015, **115**, 2698–2779.
- 386 V. Riera, J. Ruiz, Y. Jeannin and M. Philoche-Levisalles, *J. Chem. Soc. Dalton Trans.*, 1988, 1591–1597.
- 387 J.-M. Bassett, D. E. Berry, G. K. Barker, M. Green, J. A. K. Howard and F. G. A. Stone, *J. Chem. Soc. Dalton Trans.*, 1979, 1003–1011.
- 388 W. D. Horrocks and R. H. Mann, *Spectrochim. Acta*, 1963, **19**, 1375–1384.
- 389 R. W. Stephany, M. J. A. de Bie and W. Drenth, *Org. Magn. Reson.*, 1974, **6**, 45–47.
- 390 N. W. Howard, A. C. Legon, C. A. Rego and A. L. Wallwork, *J. Mol. Struct.*, 1989, **197**, 181–191.
- 391 G. Cardaci, G. Bellachioma and P. Zanazzi, *Polyhedron*, 1983, **2**, 967–968.
- 392 G. Bellachioma, G. Cardaci and P. Zanazzi, *Inorg. Chem.*, 1987, **26**, 84–91.
- 393 Y. A. Klyuev, *J. Appl. Spectrosc.*, 1965, **3**, 30–34.
- 394 M. K. Georgieva and E. A. Velcheva, *Int. J. Quantum Chem.*, 2006, **106**, 1316–1322.
- 395 M. Finze, E. Bernhardt, H. Willner and C. W. Lehmann, *J. Am. Chem. Soc.*,

References

- 2005, **127**, 10712–10722.
- 396 W. E. Wallace, in *NIST Chemistry WebBook, NIST Standard Reference Database Number 69*, eds. P. Linstrom and W. Mallard, National Institute of Standards and Technology, Gaithersburg MD.
- 397 D. Lin-Vien, N. B. Colthup, W. G. Fateley and J. G. Grasselli, eds. D. Lin-Vien, N. B. Colthup, W. G. Fateley and J. G. B. T.-T. H. of I. and R. C. F. of O. M. Grasselli, Academic Press, San Diego, 1991, pp. 105–115.
- 398 A. Raba, M. Cokoja, S. Ewald, K. Riener, E. Herdtweck, A. Pöthig, W. A. Herrmann and F. E. Kühn, *Organometallics*, 2012, **31**, 2793–2800.